Doctoral Dissertation

Size Dependent Plastic Deformations of Single Crystalline, Bi-crystalline, and Amorphous Finite Micro-pillars

BO PAN

July 2016

Graduate School of Engineering,
Osaka University

Table of Contents

Chapter 1

Introduction

1.1 Research background of size dependent plasticity in small scaled metallic pillars

The enormous development of experimental fabrication processes with advanced operating and viewing equipment brings the processing of material in critical dimensions down to micron- and nanometer level into existence. In the past decade, this development of experimental equipment and characterization methods has greatly affected the investigations on mechanical characters and microstructure evolution of metallic materials, especially for the area of structural materials. Differing from relying on the classical strengthening techniques applied on bulk scaled metallic specimens, the precise system for small scaled specimens can achieve the experimental characterization at micron and nano scales. It is possible to design the appropriate small dimensions of specimens in order to enlarge the effect of the intrinsic and extrinsic structures on the mechanical characters, which will result in the possibility of the vastly superior properties than the current bulk materials. Recent computational modeling such as molecular dynamics has the capability to achieve the simulation and prediction of the material behavior at the same small scaled dimensions. These aforementioned developments provide us some deep

understanding of mechanical characters and deformation mechanisms with reduced dimensions.

For the case of polycrystalline materials and metallic glasses, surface/boundary of the specimen influences the dislocations motion, nucleation or interaction, or the propagation of shear bands, respectively. As the bi-crystalline material is one most simple case in their polycrystalline form, the interaction between dislocations and grain boundary (GB) is of interest in recent studies. In the bulk polycrystalline metals, the GBs are regarded as obstacles to hinder dislocation motions which form a classical Hall-Petch relation describing the increasing yield strength accompany with decreasing obstacle distance down to the grain sizes of ~40nm [1-3]. However, the interaction between the dislocations and GBs such as dislocations transfer across the GB in bi-crystalline or polycrystalline materials, is widely involved in the plastic deformation of such materials [4-7]. Furthermore, when the grain sizes are reduced to ~40nm, the multiple lattice dislocations cannot be generated from GBs, and grain-boundary sliding, partial dislocation emission and absorption at GBs can be found [8-20]. When the grain sizes become below 20nm, the Hall-Petch relations are performed as “inverse” Hall-Petch, which goes through softening with decreasing grain size resulting from the activation of grain boundary-assisted deformation. Although the grain size and the dislocation-related grain mechanism is one controversial kind of the plasticity mechanism in nanocrystalline metals, the GB affecting dislocation motion and evolution is still one effective research view in micro-scaled and nanocrystalline metals, as shown in Figure 1-1 [21].

In recent years, another size effect different from the size-dependent plasticity has been reported: the strength of single crystalline materials inversely accompanies with external geometrical specimen dimensions of micro- or nano- pillars. The material

strength of such material may be due to the defect interactions with free surfaces [22, 23]. For the size effect of micro-samples, the strain gradient plasticity does believe that the inner local strain gradient stores a number of geometrically necessary dislocations in small local zone and constraints the plastic strain, and this means the plastic strain needs larger back stresses to be activated [24-28].

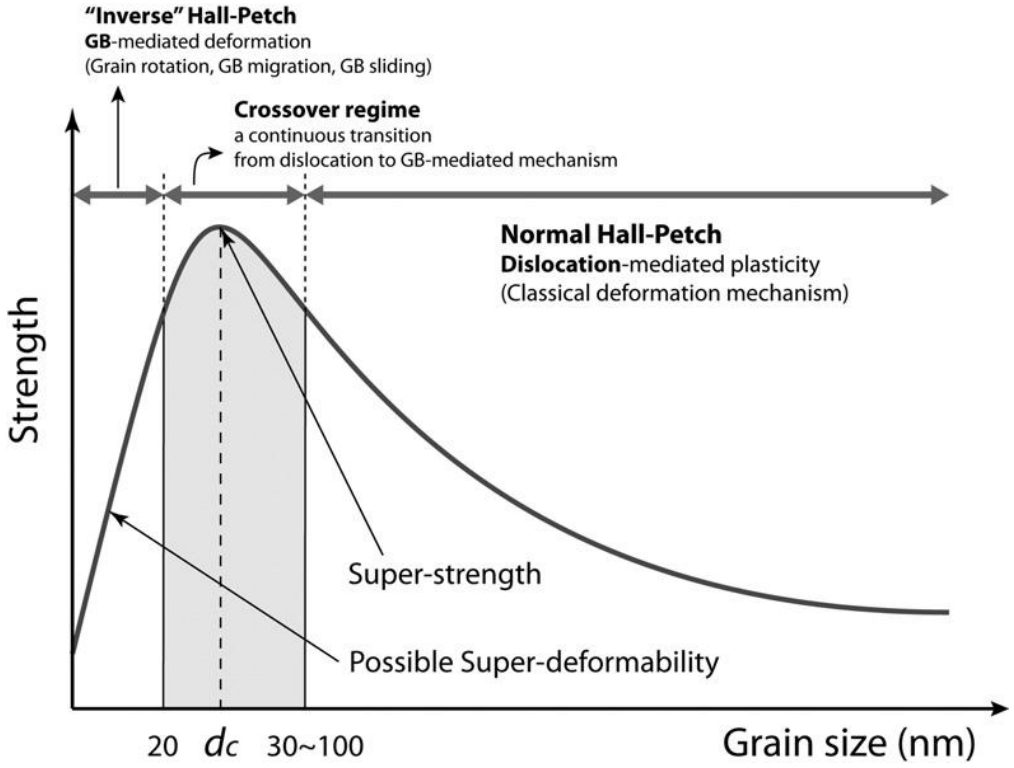

Figure 1-1. Strength of polycrystalline materials as a function of grain size: Hall – Petch relation and transition to "inverse" Hall – Petch [21].

However, uniaxial compression with a flat punch methodology first introduced by Uchic et al. where the flat punch was used to compress the micro-scaled pillars in order to strictly control the average deviation of strain gradient has been widely used to study the micro the no strain gradient size effect [22]. More recently through uniaxial flat compression experiments, understanding of plasticity in small volumes has been enriched for different kinds of fcc single crystals including Ni [29, 30, 31],

Au [32-35], Cu [36-43] and Al [44, 45], micro bi-crystalline Al [46] and Cu [4], nano-crystalline metals (Ni [47,48] and Cu [49]), and micro and nano scaled metallic glass [50-66]. It is found that the uniaxial compression strengths are much higher than those of bulk forms [29-45, 67-75]. Moreover, the single crystalline micro- and nano-pillars exhibit a stress-strain curve with intermittent discrete random strain bursts, which is also a different deformation mechanism from bulk. This size effect includes the following information that the plastic response is related to the external geometrical gain size or specimen size, and the microstructures such as defect is boundary-inside. It suggests that the interplay of the internal defects and external size has the probability of relate new deformation mechanism. This is developing the understanding of size effect.

For some simple kinds of polycrystals such as bi-crystal, the size effect in micro- or nano-pillars is link to the GB influence and the interplay of the internal defects and external size like single crystalline pillar. For the amorphous material, the research of size effect is few, and the reports about size effect of micro-scaled pillars are conflict whether the size effect is similar to or completely contrary to that of the crystalline materials [51, 52, 54, 55, 76]. And furthermore, the rapid cooling from liquid state to crystallization makes the lattice into the amorphous state [77] and the obvious GB with two different orientations couldn't be found. Therefore, the deformation mechanism and its relationship with external size may be the key factors for the size effect. This methodology is similar to the investigation of size effect of single crystalline micro- and nano-pillars. Thereby, the size effect of micro- and nano- scaled materials can be regarded as the intrinsic and extrinsic character length size effect. The physics of this size effect is the significant extension for the understanding of deformation mechanism.

This dissertation presents a trial on the interaction between relevant length scales and size effects on crystalline and amorphous metallic pillars. Relevant intrinsic characteristic length effect is regarded as a function of decreasing grain size of a pure single crystal or polycrystalline materials, characteristic length of internal defects of the crystalline materials, and shear transformation zones in metallic glasses. Apart from the recent studies on this field focusing on the superior mechanical properties resulting from the interaction between the internal defects and the external dimensions of the metallic materials by experiments, how this phenomenon could be understand physically and be mathematically described is also centered on here. The question of what is the maximum effective factors on the size dependent superior plastic properties of engineering metallic materials is concentrated on.

1.2 Related research on the size dependent plasticity

1.2.1 Yielding for small scaled crystalline materials

Proposal of efficient models for explanation of size effect on the single crystalline (SC) material from the physics view has been a subject of interest for a long time. Two decides before, the strain gradient plasticity did believe that the constraint of plastic strain results in the size effect: the inner local strain gradient makes a sum of geometrically necessary dislocations be assembled in small local zone, and the strain gradient plasticity implies that the dislocations need stronger image back stress to active the constraint of inner local strain gradients [24-29]. However, recent experiments have challenged the strain gradient plasticity as the process of the experiments has strictly controlled the average deviation of strain gradient [29-45]. Therefore, the theory of dislocations starvation firstly provided that dislocations tended to move towards to the surface under the effect of image forces and annihilate

there [30]. Some discrete dislocation simulation results have proved that the quasi ideal SC micro-pillars (SCMs) exhibit much greater strength and hardening relative to the defective ones at an equivalent diameter [78]. However, the strain rate in the simulation is so high that dislocations have no time to form the dislocation group, and the dominant effect is from the GB. Recently, it is shown that viable route that can smoothen the plastic flow of SC materials is by increasing the density of preexisting defects, such as dislocations [79-81] and solute atom clusters [82]. These aforementioned results indicate that the deformation of SC pillars can become more controllable when dislocations are trapped inside them. Therefore, intentionally preventing mobile dislocations from annihilation such as introducing (several) defect clusters into small-scaled SC pillars to hinder the dislocation motion should induce a fundamentally different mechanical performance. From this view, the dislocation pile-up effect initiated by inner dislocation source was provided for describing the size effect in SC pillars for exploring the relationship between the number of dislocation sources and the effect of dislocation pileup [83, 84]. And these studies explicitly expressed the size effect resulting from the source exhaustion [83, 85-87]. In addition, disperse dislocation dynamics simulation focused on the dislocation source truncation on the plastic strength [88], treated the improvement of strength as a result of the small scale constrains of the length of dislocation sources [89, 90]. Therefore, the dislocation source exhaustion, dislocation pile-up and length of dislocation sources are important factors for the size effect.

The stochastic nature of the plastic deformation corresponding to the size-dependent yield strength mentioned above is explained by low dislocation content or dislocation source number in the microcrystal, so that the usual mean-field conditions for forest hardening are destroyed [30, 91]. In these models, the

boundary/surface of the micropillars plays a key role in the size effect because it not only determines the dislocation source lengths but also acts as a sink for dislocations. It has been shown that the boundary/surface of the micropillars can significantly affect the measured stiffness values [92]. Moreover, Fan et al. have inserted boundaries inside solid pillars to construct a model of hollow pillars in three-dimensional discrete dislocation dynamics simulations, and the results have shown that the boundary condition affects the strength of the hollow pillars via the wall thickness [93]. Until now, however, there have been almost no experiments conducted on hollow pillars. Recently, the physics of the surface energy has been considered in the description of the surface effect of nanowires and naonosprings [94, 95]. In crystalline materials, the surface energy/stress on yield point, phase transformation and pseudo-elastic behavior has also been reported [96-104]. But, at present, little work has been done to link the size effect of SC micro- and nanopillars to the surface energy, and few studies have been done on hollow pillars.

The other interest in crystal strength has been focused on a single crystal yield surface for plastic deformation [105-115]. A smooth single yield surface for a crystalline material reduces the computational ambiguity and also overcomes the problem of multiple slip systems in the crystal plasticity case. The initial single crystal yield function proposed for a single crystal was expressed as a power type yield function [105] and it has been modified to the simpler current logarithmic-exponential configuration recently [115]. The yield function proposed by Gambin [110, 112, 113], which considered the degree of the nonlinearity of the yield function, was defined by the stacking fault energy (SFE) of materials. Then, a rigid plastic computational function was developed for Gambin's single crystal yield surface [116]. Recently, Zamiri et al. [114, 115] introduced an optimization method to establish an

elastic–plastic integration function for this single crystal yield function with a small modification for the Gambin's single crystal yield surface model, and this model improves the simplicity and efficiency of single yield function. All these phenomenological yield functions based on the single crystal plasticity can be easily used to describe the actual metal forming processes [116]. Although all these single crystal yield functions have been very successful in representing the characteristics of crystals, they are all expressed as a phenomenological form. Micro and nano-sized SC material shows the strong size effect which is affected by the inner defect effect, such as dislocation starvation [30], source exhaustion [85] and dislocation pile-up [83]. To describe the size effect and also to physically explain the effects of dislocations, a single crystal yield function considering the dislocation physics should be considered.

1.2.2 Constitutive of crystalline plasticity

Constitutive laws, kinematics, homogenization, physical analyses, and multiscale calculations in crystal plasticity finite-element (CPFE) modeling are widely used to describe elastic–plastic deformation of anisotropic heterogeneous crystalline matter [117-122]. The CPFE model can describe both shape changes (symmetric part) and lattice rotations (skew-symmetric part) [119, 123]. The CPFE model might be improved by using the extensive knowledge gained from experimental and theoretical studies of single crystalline deformation and introducing the further development of continuum field theories [118, 120]. Therefore, the CPFE method can be used to investigate the size-dependent plastic behavior of single crystalline micropillars (SCMs) by considering lattice deformation and the crystallographic system.

In terms of the plasticity of SCMs, the size-dependent mechanical response (size effect), including extremely high strength and unsmooth hardening [29, 31], should be

considered. There are some micromechanisms of size-dependent yield strength of the SCMs, which are commonly based on the inner defects, such as source truncation [40, 41], dislocation starvation [30], source starvation and inner dislocation pile-up [83, 85]. According to these considerations, prediction of the yield strength for the SCMs has been studied and these theories, such as the single-arm source (SAS) model, are different from conventional scale-free solid mechanics [83, 85]. These considerations can be extended to describe the plastic flow based on the evolution of the corresponding defects such as dislocations. The geometric necessary dislocations (GNDs) is also used to describe the size dependent plasticity. However, the size effect found by uniaxial compression test with a flat punch tends to be resulted from the dislocation truncation, dislocation starvation, source starvation and inner dislocation pile-up. As known, the CPFE method has also been used to describe the anomalous hardening by adding experimental data, such as the recent studies of displacement burst [124-127] and dislocation starvation [128-131]. However, the hardening model and constitutive laws used in these studies did not involve any physical size-dependent considerations. If the inner defects considerations are combined with the hardening model, the physical hardening can be linked to the constitutive law. The physical hardening model can affect the constitutive law because of the mechanical effect on dislocation motion. Therefore, it is necessary to build the CPFE framework by combining the physical model of the yield stress and the dislocation-based hardening model to obtain the constitutive law with the size effect. The size dependent plastic flow of single crystalline and bi-crystalline micro pillars will be described in Chapter 4, and the deformation mechanism will also be discussed.

1.2.3 Size dependent plasticity of metallic glass

Metallic glass (MG), also known as amorphous alloy, is manufactured with rapid cooling from the liquid quasi-static state, so the regular crystalline lattice cannot be formed [77, 132]. The metallic glass has extracted board attention due to the interests in fundamental study of superb combined mechanical properties [133] and great potential for the applications in the future [134].

Some tensile and compressive experiments have been conducted to study the mechanical properties of bulk metallic glasses (BMGs). At room temperature, BMG represents extremely high elastic limit (around 1600MPa) with 2% strain limit (much higher yield strength than crystalline materials) [135]. At high temperature ($>0.7T_g$, T_g is the glass transition temperature), the elastic limit decreases down to several hundred MPa. For the deformation as known [136], their deformation behaviors are classified into two forms, namely homogeneous deformation at high temperature ($>0.7T_g$) and inhomogeneous deformation at low temperature ($<0.7T_g$) [137]. At room temperature, metallic glasses are found to exhibit negligible macroscopic plastic strain before the formation of localized shear bands, which is followed by rapid propagation and catastrophically fracture during deformation [138]. The local shear bands are affected by the aspect ratio [139] and the reducing size [59, 101]. When the temperature is near to the T_g, the viscoplastic deformation behaviors can be obtained [136, 140]. The modulus and yield strength (elastic limit) at high temperature are much smaller than them at room temperature, and the plastic elongation can reach more than 40~50%. Therefore, the yield strength and plastic deformation should be studied.

Like the characteristic of the strength in crystalline materials, the strength of metallic glass also shows size dependence to some extent. If the sample size is reduced to 100nm, Zr-based MG pillars attain high strength of 2.25GPa, and the yield

strength (100~1000nm) presents slightly similar tendency as SC “smaller is stronger” [59, 136]. They correlated the shear band propagation stress with the pillar size by analogously applying Griffith’s criterion. The size dependent strength below 100nm is described by utilizing atomic simulations and provided the model with Mohr-Coulomb criterion [141]. Experiments of $Pd_{40}Ni_{40}P_{20}$ and $Zr_{41.2}Ti_{13.8}Cu_{12.5}Ni_{10}Be_{22.5}$ using pillars 2-20μm and 0.3-3μm in size, respectively are conducted and concluded that the yield strength is insensitive to the pillar size [142, 143]. It is argued that the yield stress of pillars over 1μm may follow the “smaller is stronger” tendency derived by a Griffith-like model, but the experiments showed yield strength would slightly increase with the increase of pillar size [59]. The size effect of the yield strength in metallic glasses is still an open issue

Computational studies of the plastic deformation of the MG at high and room temperature have received considerable attention in the last years. The description of the plastic deformation in metallic glasses has been reported by introducing the concept of free volume and shear transformation, which is regarded as the potential defects promote yielding and plastic deformation [144]. Because of the non-regular structure in amorphous material, the motion of atomic defects in the shear transformation zone (STZ) accompanies with the variance of volume [144, 145]. And this local Spaepen’s free volume is introduced as special kinds of “flow defects” and related to the formation of shear bands [136]. Based on the creation and annihilation of the above free volume, the constitution of elastic-plastic mechanism deforms the phenomenon of STZ of metallic glasses [145-149]. Meanwhile, the metal yield criterions such as Mises (VM) criterion, Tresca criterion, Drucker-Prager criterion and Mohr-Coulomb criterion have been tried to link with elastic-plastic mechanics [150-153]. However, few current plasticity can describe both the mechanical

deformations at room and high temperature. Furthermore, the research on the plastic behavior of small scaled BMGs is also absent.

1.3 Objectives and scopes of this research

The objective of this dissertation is to have an insight into the size dependent plasticity of the crystalline materials and amorphous materials. The intrinsic defect scales, external geometrical scales, interaction of GB and defects and "flow defects" will be investigated to understand the physics of the deformation mechanism. The main tasks of this dissertation are (i) to study the relationship among the size dependent yielding (surface), defects and surface in pure single crystalline micro-pillars; (ii) to develop the dislocation-nature-base plasticity to describe the plastic deformation of single-crystalline and bi-crystalline micro-pillars, and study the deformation inside the pillars and near the GB; (iii) to summarize the size effect of crystalline material and amorphous material, preform the temperature-based constitution to study the plastic deformation without classical dislocations motion.

The present dissertation is composed of 6 chapters. The dissertation flow chart is shown in Figure 1-2. Firstly, general introduction has been present in this Chapter 1. Then Chapter 2 provides the detailed experimental procedures employed in this dissertation, and experimental results of single-crystalline, bi-crystalline, and metallic glass micro-pillars by uniaxial compression test with a flat punch. In Chapter 3, the physical model considering dislocations pile-up, source starvation, and surface energy is established to explain the size dependent yielding shown in Chapter 2. The size dependent crystalline yield surface is provided in order to understand the size effect well. In Chapter 4, a dislocation-based constitution is provided by combining the dislocation physics with the crystal plasticity to describe the plastic flow of

single-crystalline and bi-crystalline micro-pillars in Chapter 2. Grain boundary effect on the slip deformation is studied from simulations. In Chapter 5, the size dependence of yielding in metallic glass is examined based on the results in Chapter 2. The size effect of crystalline materials and amorphous materials is summarized and compared. The constitution based on free volume theory is provided to study the plastic deformation of metallic glasses. The relationship between the formation of STZs and plastic response (yielding, flow) is discussed in Chapter 5. Finally, the entire research works are summarized in Chapter 6.

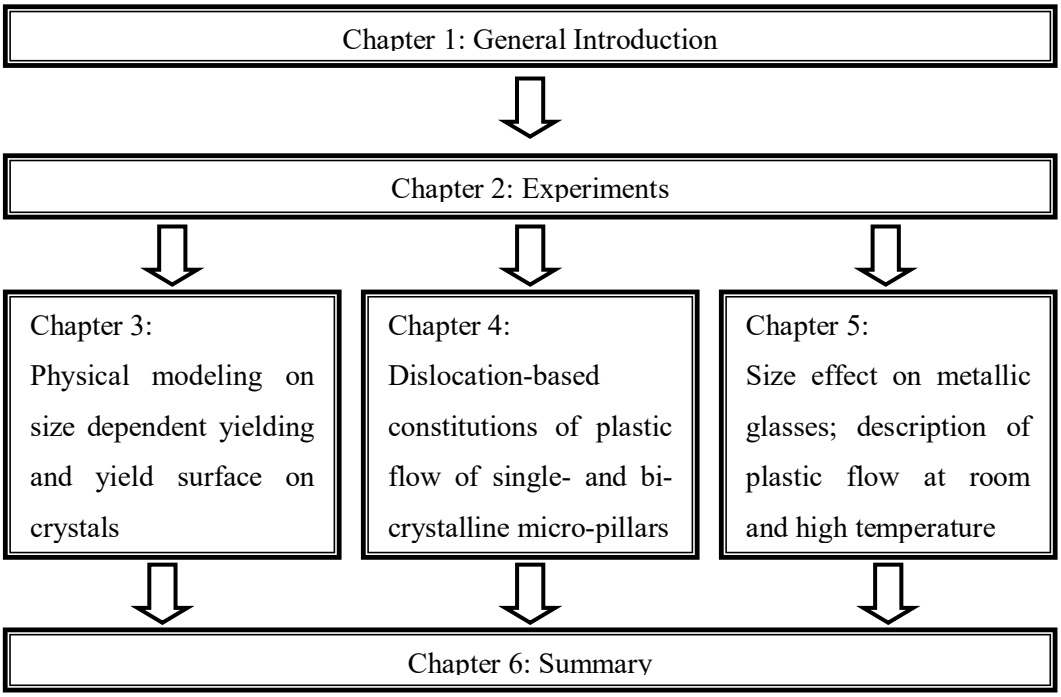

Figure 1-2. Flow chat of this doctoral dissertation.

Reference

[1] Hall EO. The deformation and ageing of mild steel. 3. Discussion of results. Proc Phys Soc Lond Sect B 1951 (64) 747-753.

[2] Petch NJ. The cleavage strength of polycrystals. J Iron Steel Inst 1953 (174) 25-28.

[3] Agena ASM. A study of flow characteristics of nanostructured Al-6082 alloy produced by ECAP under upsetting test. J Mater Process Technol 2009 (209) 856-863.

[4] Hirouchi T, Shibutani Y. Mechanical Responses of Copper Bicrystalline Micro Pillars with $\Sigma 3$ Coherent Twin Boundaries by Uniaxial Compression Tests. Mater Trans 2014 (55) 52-57.

[5] Tsuru T, Shibutani Y, Hirouchi T. A predictive model for transferability of plastic deformation through grain boundaries. AIP Adv. 2016 (6) 015004.

[6] Tsuru T, Kaji Y, Shibutani Y. Incipient plasticity of twin and stable/unstable grain boundaries during nanoindentation in copper. Physical Review B 2010 (82) 024101.

[7] Tsuru T, Kaji Y, Shibutani Y. Minimum Energy Motion and Core Structure of Pure Edge and Screw Dislocations in Aluminum. J Comp Sci Tech 2010 (4) 185-193.

[8] Ke M, Hackney SA, Milligan WW, Aifantis EC. Observation and measurement of grain rotation and plastic strain in nanostructured metal thin-films. Nanostruct Mater 1995 (5) 689-697.

[9] Wang YB, Li BQ, Sui ML, Mao SX. Deformation-induced grain rotation and growth in nanocrystalline Ni. Appl Phys Lett 2008 (92) 011903.

[10] Farkas D, Mohanty S, Monk J. Strain-driven grain boundary motion in nanocrystalline materials. Mater Sci Eng A 2008 (493) 33-40.

[11] Van Swygenhoven H, Derlet PA. Grain-boundary sliding in nanocrystalline fcc metals. Phys Rev B 2001 (64) 224105.

[12] Van Swygenhoven H, Derlet PM, Hasnaoui A. Atomic mechanism for dislocation emission from nanosized grain boundaries. Phys Rev B 2002 (66) 024101.

[13] Yamakov V, Wolf D, Phillpot SR, Mukherjee AK, Gleiter H. Dislocation processes in the deformation of nanocrystalline aluminium by molecular-dynamics simulation. Nat Mater 2002 (1) 45-48.

[14] Yamakov V, Wolf D, Phillpot SR, Gleiter H. Grain-boundary diffusion creep in nanocrystalline palladium by molecular dynamics simulation. Acta Mater 2002 (50) 61-73.

[15] Yin WM, Whang SH. The creep and fracture in nanostructured metals and alloys. JOM J Minerals Met Mater Soc 2005 (57) 63-70.

[16] Legros M, Gianola DS, Hemker KJ. In situ TEM observations of fast grain-boundary motion in stressed nanocrystalline aluminum films. Acta Mater 2008

(56) 3380-3393.
[17] Gianola DS, Van Petegem S, Legros M, Brandstetter S, Van Swygenhoven H, Hemker KJ. Stress-assisted discontinuous grain growth and its effect on the deformation behavior of nanocrystalline aluminum thin films. Acta Mater 2006 (54) 2253-2263.
[18] Gianola DS, Eberl C, Cheng XM, Hemker KJ. Stress-driven surface topography evolution in nanocrystalline Al thin films. Adv Mater 2008 (20) 303-308.
[19] Gianola DS, Mendis BG, Cheng XM, Hemker KJ. Grain-size stabilization by impurities and effect on stress-coupled grain growth in nanocrystalline Al thin films. Mater Sci Eng A 2008 (483) 637-640.
[20] Gianola DS, Warner DH, Molinari JF, Hemker KJ. Increased strain rate sensitivity due to stress-coupled grain growth in nanocrystalline Al. Scr Mater 2006 (55) 649-652.
[21] Greer JR, De Hosson JTM. Plasticity in small-sized metallic systems: Intrinsic versus extrinsic size effect. Prog Mater Sci 2011 (56) 654-724.
[22] Uchic MD, Shade PA, Dimiduk DM. Plasticity of micrometer-scale single crystals in compression. Annu Rev Mater Res 2009 (39) 361-386.
[23] Kraft O, Gruber PA, Monig R, Weygand D. Plasticity in confined dimensions. Annu Rev Mater Res 2010 (40) 293-317.
[24] Fleck NA, Hutchinson JW. A phenomenological theory for strain gradient effects in plasticity. J Mech Phys Solids 1993 (41) 1825-1857.
[25] Fleck NA, Hutchinson JW. Strain gradient plasticity (1997), Academic Press.
[26] Gao H, Huang Y, Nix WD, Hutchinson JW. Mechanism-based strain gradient plasticity—I. Theory. J Mech Phys Solids 1999 (47) 1239-1263.
[27] Huang Y, Gao H, Nix WD, Hutchinson JW. Mechanism-based strain gradient plasticity—II. Analysis. J Mech Phys Solids 2000 (48) 99-128.
[28] Nix WD, Gao H. Indentation size effects in crystalline materials: a law for strain gradient plasticity. J Mech Phys Solids 1998 (46) 411-425.
[29] Uchic MD, Dimiduk DM, Florando JN, Nix WD. Sample dimensions influence strength and crystal plasticity. Science 2004 (305) 986-989.
[30] Shan ZW, Mishra R, Syed SA, Warren OL, Minor AM. Mechanical annealing and source-limited deformation in submicron diameter Ni crystals. Nature Mater 2008 (7) 115-119.
[31] Dimiduk DM, Uchic MD, Parthasarathy TA. Size-affected single-slip behavior of pure nickel microcrystals. Acta Mater 2005 (53) 4065-4077.
[32] Greer JR, Oliver WC, Nix WD. Size dependence of mechanical properties of gold at the micron scale in the absence of strain gradients. Acta Mater 2005 (53) 1821-1830.

[33] Greer JR, Nix WD. Nanoscale gold pillars strengthened through dislocation starvation. Phys Rev B 2006 (73) 245410-245416.
[34] Volkert CA, Lilleodden ET. Size effects in the deformation of sub-micron Au columns. Philos Mag 2006 (86) 5567-5579.
[35] Budiman A, Han S, Greer JR, Tamura N, Patel J, Nix WD. A search for evidence of strain gradient hardening in Au submicron pillars under uniaxial compression using synchrotron X-ray microdiffraction. Acta Mater 2007 (56) 602-608.
[36] Kiener D, Motz C, Rester M, Jenko M, Dehm G. FIB damage of Cu and possible consequences for miniaturized mechanical tests. Mater Sci Eng A 2006 (459) 262-272.
[37] Dehm G. Miniaturized single-crystalline fcc metals deformed in tension: New insights in size-dependent plasticity. Prog Mater Sci 2009 (54) 664-688.
[38] Kiener D, Motz C, Schoberl T, Jenko M, Dehm G. Determination of mechanical properties of copper at the micron scale. Adv Eng Mater 2006 (8) 1119-1125.
[39] Kiener D, Grosinger W, Dehm G, Pippan R. A further step towards an understanding of size-dependent crystal plasticity: in situ tension experiments of miniaturized single-crystal copper samples. Acta Mater 2008 (56) 580-592.
[40] Kiener D, Grosinger W, Dehm G. On the importance of sample compliance in uniaxial microtesting. Scr Mater 2009 (60) 148-151.
[41] Kiener D, Motz C, Dehm G. Micro-compression testing: a critical discussion of experimental constraints. Mater Sci Eng A 2009 (505) 79-87.
[42] Maass R, Van Petegem S, Grolimund D, Van Swygenhoven H, Kiener D, Dehm G. Crystal rotation in Cu single crystal micropillars: in situ Laue and electron backscatter diffraction. Appl Phys Lett 2008 (92) 071905
[43] Jennings AT, Greer JR. Tensile deformation of FIB-less single crystalline copper pillars. Philos Mag 2010 (91) 1-13
[44] Ng KS, Ngan AHW. Breakdown of Schmid's law in micropillars. Scr Mater 2008 (59) 796-799.
[45] Ng KS, Ngan AHW. Effects of trapping dislocations within small crystals on their deformation behavior. Acta Mater 2009 (57) 4902-4910.
[46] Ng KS, Ngan AHW. Deformation of micron-sized aluminum bi-crystal pillars. Philos Mag 2009 (89) 3013-3326.
[47] Rinaldi A, Peralta P, Friesen C, Sieradzki K. Sample-size effects in the yield behavior of nanocrystalline nickel. Acta Mater 2008 (56) 511-517.
[48] Jang D, Greer JR. Size-induced weakening and grain boundary-assisted deformation in 60nm-grained Ni nano-pillar. Scr Mater 2011 (64) 77-80.
[49] Jang D, Cai C, Greer JR. Influence of homogeneous interfaces on the strength of 500 nm diameter Cu nanopillars. Nano Lett 2011 (11) 1743–1746.

[50] Cheng S, Wang XL, Choo H, Liaw PK. Global melting of Zr57Ti5Ni8Cu20Al10 bulk metallic glass under microcompression. Appl Phys Lett 2007 (91) 201917.
[51] Lee CJ, Huang JC, Nieh TG. Sample size effect and microcompression of $Mg_{65}Cu_{25}Gd_{10}$ metallic glass. Appl Phys Lett 2007 (91) 161913.
[52] Lai YH, Lee CJ, Cheng YT, Chou HS, Chen HM, Du XH, et al. Bulk and microscale compressive behavior of a Zr-based metallic glass. Scr Mater 2008 (58) 890-893.
[53] Volkert CA, Donohue A, Spaepen F. Effect of sample size on deformation in amorphous metals. J Appl Phys 2008 (103) 083539.
[54] Schuster BE, Wei Q, Hufnagel TC, Ramesh KT. Size-independent strength and deformation mode in compression of a Pdbased metallic glass. Acta Mater 2008 (56) 5091-5100.
[55] Schuster BE, Wei Q, Ervin MH, Hruszkewycz SO, Miller MK, Hufnagel TC, et al. Bulk and microscale compressive properties of a Pd-based metallic glass. Scr Mater 2007 (57) 517-20.
[56] Shan ZW, Li J, Cheng YQ, Minor AM, Syed Asif SA et al. Plastic flow and failure resistance of metallic glass: Insight from in situ compression of nanopillars. Phys Rev B 2008 (77) 155419.
[57] Donohue A, Spaepen F, Hoagland RG, Mishra A. Suppression of the shear band instability during plastic flow of nanometer-scale confined metallic glasses. Appl Phys Lett 2007 (91) 241905.
[58] Wu XL, Guo YZ, Wei Q, Wang WH. Prevalence of shear banding in compression of Zr41Ti14Cu12.5Ni10Be22.5 pillars as small as 150 nm in diameter. Acta Mater 2009 (57) 3562-3571.
[59] Jang D, Greer JR. Transition from a strong-yet-brittle to a stronger-and-ductile state by size reduction of metallic glasses. Nat Mater 2010 (9) 215-219.
[60] Chen CQ, Pei YT, De Hosson JTM. Effects of size on the mechanical response of metallic glasses investigated through in situ TEM bending and compression experiments. Acta Mater 2010 (58) 189-200.
[61] De Hosson JTM. Advances in transmission electron microscopy: In situ straining and in situ compression experiments on metallic glasses. Microsc Res Tech 2009 (72) 250-260.
[62] Jang D, Gross C, Greer JR. Effects of size on the strength and deformation mechanism in Zr-based metallic glasses. Int J Plast 2011 (27) 858–867.
[63] Ye JC, Lu J, Yang Y, Liaw PK. Extraction of bulk metallic-glass yield strengths using tapered micropillars in microcompression experiments. Intermetallics 2010 (18) 385-393.
[64] Chen CQ, Pei YT, De Hosson JTM. Strength of submicrometer diameter pillars

of metallic glasses investigated with in situ transmission electron microscopy. Philos Mag Lett 2009 (89) 633-640.
[65] Wu Y, Li HX, Jiao ZB, Gao JE, Lu ZP. Size effects on the compressive deformation behaviour of a brittle Fe-based bulk metallic glass. Philos Mag Lett 2010 (90) 403-412.
[66] Wu FF, Zhang ZF, Mao SX. Size-dependent shear fracture and global tensile plasticity of metallic glasses. Acta Mater 2009 (57) 257-266.
[67] Han S-M, Bozorg-Grayeli T, Groves J, Nix WD. Size effects on strength and plasticity of vanadium nanopillars. Scr Mater 2010 (63) 1153-1156.
[68] Dou R, Derby B. A universal scaling law for the strength of metal micropillars and nanowires. Scr Mater 2009 (61) 524-527.
[69] Jennings AT, Burek MJ, Greer JR. Size effects in single crystalline cu nano-pillars fabricated without the use of focused ion beam. Phys Rev Lett 2010 (104) 135503.
[70] Lee S, Han S, Nix WD. Uniaxial compression of fcc Au nanopillars on an MgO substrate: The effects of prestraining and annealing. Acta Mater 2009(57) 4404-4415.
[71] Jennings AT, Greer JR. Emergence of strain rate effects in cu nano-pillars: transition from dislocation multiplication to dislocation nucleation. Acta Mater 2011 (59) 5627–5637.
[72] Brinckmann S, Kim J-Y, Greer JR. Fundamental differences in mechanical behavior between two types of crystals at nanoscale. Phys Rev Lett 2008 (100) 155502.
[73] Greer JR, Weinberger C, Cai W. Comparing strengths of FCC and BCC sub-micrometer pillars: compression experiments and dislocation dynamics simulations. Mater Sci Eng A 2008 (493) 21-25.
[74] Sun Q, Guo Q, Liao X, Greer JR, Sun J. Size effects in strength and plasticity of single crystalline titanium micro-pillars with prismatic slip orientation. Scr Mater 2011 (65) 473–476.
[75] Zhu T, Li J. Ultra-strength materials. Prog Mater Sci 2010 (55) 710-757.
[76] Kuzmin O, Pei Y, Chen C, De Hosson JTM. Intrinsic and extrinsic size effects in the deformation of metallic glass nanopillars. Acta Mater 2011 (60) 889-898.
[77] Webb TW, Zhu XH, Aifantis EC. A simple method for calculating shear band angles for pressure sensitive plastic materials. Mech Res Commun 1997 (24) 69-74.
[78] Tang H, Schwarz KW, Espinosa HD. Dislocation escape-related size effects in single-crystal micropillars under uniaxial compression. Acta Mater 2007 (55) 1607–1616.
[79] El-Awady JA, Uchic, MD, Shade PA, Kim SL, Rao SI, Dimiduk DM, Woodward C. Pre-straining effects on the power-law scaling of size dependent strengthening in

Ni single crystals. Scr Mater 2013 (68) 207–210.
[80] Bei H, Shim Pharr SGM, George EP. Effects of pre-strain on the compressive stress–strain response of Mo-alloy single-crystal micropillars. Acta Mater 2008 (56) 4762–4770.
[81] Schneider AS, Kiener D, Yakacki CM, Maier HJ, Gruber PA, Tamura N, Kunz M, Minor AM, Frick CP. Influence of bulk pre-straining on the size effect in nickel compression pillars. Mater Sci Eng A 2013 (559) 147–158.
[82] Xie KY, Shrestha S, Cao Y, Felfer PJ, Wang Y, Liao X, Cairney JM, Ringer SP. The effect of pre-existing defects on the strength and deformation behavior of a-Fe nanopillars. Acta Mater 2013 (61) 439–452.
[83] Pan B, Shibutani Y, Zhang X, Shang F. Effect of dislocation pile-up on size-dependent yield strength in finite single-crystal micro-samples. J Appl Phys 2015 (118) 014305.
[84] Senger J, Weygand D, Gumbsch P, Kraft O. Discrete dislocation simulations of the plasticity of micro-pillars under uniaxial loading. Scr Mater. 2008 (58) 587-590.
[85] Parthasarathy TA, Rao SI, Dimiduk DM, Uchic MD, Trinkle DR. Contribution to size effect of yield strength from the stochastics of dislocation source lengths in finite samples. Scr Mater 2007 (56) 313-316.
[86] Pan B, Shibutani Y, Tanaka H. Dislocation-based constitutive model of crystal plasticity for the size effect of single crystalline micropillar samples. Mech Eng J 2016 Doi: 10.1299/mej.15-00602. (Released January 28, 2016)
[87] Pan B, Tanaka H, Shibutani Y. Effect of surface energy upon size-dependent yield strength of single-crystalline hollow micro- and nanopillars. Mater Sci Eng A 2016 (659) 22-28.
[88] Rao SI, Dimiduk DM, Tang M, Uchic MD, Parthasarathy TA, Woodwar C. Estimating the strength of single-ended dislocation sources in micron-sized single crystals. Philos Mag 2007 (87) 4777-4794.
[89] El-Awady JA, Wen M, Ghoniem NM. The role of the weakest-link mechanism in controlling the plasticity of micropillars. J Mech Phys Solids 2009 (57) 32-50.
[90] Tang H, Schwarz KW, Espinosa HD. Dislocation-source shutdown and the plastic behavior of single-crystal micropillars. Phys Rev Lett 2008 (100) 185503.
[91] Norfleet DM, Dimiduk DM, Polasik SJ, Uchic MD, Mills MJ. Dislocation structures and their relationship to strength in deformed nickel microcrystals, Acta Mater 2008 (56) 2988–3001.
[92] Zhang G, ZhaoY. Mechanical Characteristics of Nano-Scale Springs. J Appl Phys 2004 (95) 267-271.
[93] Fan H, Li Z, Huang M. Size effect on the compressive strength of hollow micropillars governed by wall thickness, Scr Mater 2012 (67) 225-228.

[94] Hurtado DE, Ortiz M. Surface effects and the size-dependent hardening and strengthening of nickel micropillars. J Mech Phys Solids 2012 (60) 1432-1446.
[95] Wang D, Wang G. Influence of surface energy on the stiffness of nanosprings. Appl Phys Lett 2011(98) 083112.
[96] Diao J, Gall K, Dunn ML. Atomistic simulation of the structure and elastic properties of gold nanowires. J Mech Phys Solids 2004 (52) 1935-1962.
[97] Diao J, Gall K, Dunn ML.Surface-stress-induced phase transformation in metal nanowires. Nut Mater 2003 (2) 656-660.
[98] Diao J, Gall K, Dunn ML. Yield strength asymmetry in metal nanowires. Nano Lett 2004 (4) 1863-1867.
[99] Farkas D, Caro A, Bringa E, Crowson D. Mechanical response of nanoporous gold. Acta Mater 2006 (61) 3249-3256.
[100] Gioia G, Dai X. Surface stress and reversing size effect in the initial yielding of ultrathin films. J Appl Mech 2006 (73) 254-258.
[101] Guo H, Yan P, Wang Y, Tan J, Zhang Z, Sui M, Ma E. Tensile ductility and necking of metallic glass. Nut Mater 2007 (6) 735-739.
[102] Liang W, Zhou W. Surface-stress-driven Pseudoelasticity and Shape Memory Effect at the Nanoscale. Fracture of Nano and Engineering (2009), Spring.
[103] Yang Z, Lu Z, Zhao YP. Atomistic simulation on size-dependent yield strength and defects evolution of metal nanowires. Comp Mater Sci 2009 (46) 142-150.
[104] Zhang W, Wang T, Chen X. Effect of surface stress on the asymmetric yield strength of nanowires. J Appl Phys 2008 (103) 123527.
[105] Montheillet F, Gilormini P, Jonas JJ. Relation between axial stresses and texture development during torsion testing: a simplified theory. Acta Metall 1985 (33) 705-718.
[106] Houtte PV. Calculation of the yield locus of textured polycrystals using the Taylor and the related Taylor theories. Texture Microstrct 1987 (7) 29-72.
[107] Lequeu Ph, Gilormini P, Montheillet F, Bacroix B, Jonas JJ. Yield surfaces for textured polycrystals – I. Crystallographic approach. Acta Metall 1987 (35) 439-451.
[108] Lequeu Ph, Gilormini P, Montheillet F, Bacroix B, Jonas JJ. Yield surfaces for textured polycrystals – II. Analytical approach. Acta Metall 1987 (35) 1159-1174.
[109] Arminjon M. A regular form of the Schmid law. Application to the ambiguity problem. Texture Microstruct 1991 (14-18) 1121-1128.
[110] Darrieulat M, Piot D. A method of generating analytical yield surfaces of crystalline materials. Int J Plast 1996 (12) 575-610.
[111] Gambin W. Plasticity of crystals with interacting slip systems. Eng Trans 1991 (39) 303–324.
[112] Gambin W. Refined analysis of elastic–plastic crystals. Int J Solids Struct 1992

(29) 2013–2021.
[113] Gambin W, Barlat F. Modeling of deformation texture development based on rate independent crystal plasticity. Int J Plast 1997 (13) 75–85.
[114] Zamiri A, Pourboghrat F, Barlat F. An effective computational algorithm for rate-independent crystal plasticity based on a single crystal yield surface with an application to tube hydroforming. Int J Plast 2007 (23) 1126-1147.
[115] Zamiri A, Pourboghrat F. A novel yield function for single crystals based on combined constraints optimization. Int J Plast 2010 (26) 731-746.
[116] Guan Y, Pourboghrat F, Barlat F. Finite element modeling of tube hydroforming of polycrystalline aluminum alloy extrusions. Int J Plast 2006 (22) 2366-2393.
[117] Becker R. Effects of strain localization on surface roughening during sheet forming. Acta Mater 1998 (46) 1385–1401.
[118] Evers LP, Brekelmans WAM, Geers MGD. Scale dependent crystal plasticity framework with dislocation density and grain boundary effects. Int J Solids Struct 2004 (41) 5209–5230.
[119] Gerken JM Dawson PR. A crystal plasticity model that incorporates stresses and strains due to slip gradients, J Mech Phys Solids 2008 (56) 1651–1672.
[120] Gurtin ME, Anand L, Lele SP, Gradient single-crystal plasticity with free energy dependent on dislocation densities. J Mech Phys Solids 2007 (55) 1853–1878.
[121] Raabe D, Becker R. Coupling of a crystal plasticity finite element model with a probabilistic cellular automaton for simulating primary static recrystallization in aluminum. Model Simul Mater Sci Eng 2000 (8) 445–462.
[122] Roters F, Eisenlohr P, Hantcherli L, Tjahjanto D, Bieler T, Raabe D. Overview of constitutive laws, kinematics, homogenization and multiscale methods in crystal plasticity finite-element modeling: Theory, experiments, applications. Acta Mater 2010 (58) 1152–1211.
[123] Peirce D, Asaro RJ, Needleman A. An analysis of nonuniform and localized deformation in ductile single crystals. Acta Metall 1982 (30) 1087–1119.
[124] Zhang X, Pan B, Shang, FL. Scale-free behavior of displacement bursts: Lower limit and scaling exponent, Europhys Lett 2012 (100) 16005.
[125] Zhang X, Shang FL. A continuum model for intermittent deformation of single crystal micro pillars, Int J Solids Struct 2014 (51) 1859–1871.
[126] Zhang X, Shang FL, Yu Y, Yan YB, Yan SP. A stochastic model for the temporal aspects of flow intermittency in micro pillar compression, Int J Solids Struct Vol.51, 2014 (51) 4519–4530.
[127] Zhang X, Zhang XC, Shang FL, Li Q. Second-order work and strain burst in single-crystalline micropillar plasticity. Int J Plast 2016 (77) 192-213.
[128] Gao Y, Liu ZL, You, XC et al. A hybrid multiscale computational framework of

crystal plasticity at submicron scales. Comput Mater Sci 2010 (49) 672-681.
[129] Gao Y, Zhuang Z, Liu ZL et al. Characteristic sizes for exhaustion-hardening mechanism of compressed Cu single-crystal micropillars. Chin Phys Lett 2010 (27) 086103.
[130] Gao Y, Zhuang Z, Liu ZL et al. Investigations of pipe-diffusion-based dislocation climb by discrete dislocation dynamics. Int J Plast 2011 (27) 1055-1071.
[131] Cui YN, Lin P, Liu ZL, Zhuang Z. Theoretical and numerical investigations of single arm dislocation source controlled plastic flow in FCC micropillars. Int J Plast 2014 (55) 279-292.
[132] Petker A, Johnson WL. A highly processable metallic glass $Zr_{41.2}Ti_{13.8}Cu_{12.5}$-$Ni_{10.0}Be_{22.5}$. Appl Phys Lett 1993 (63) 2342-2344.
[133] Loffler JF. Bulk metallic glasses. Intermetallics 2003 (11) 529-540.
[134] Ashby MF, Greer AL. Metallic glasses as structural materials. Scr Mater 2006 (54) 321-326.
[135] Conner RD, Rosakis AJ, Johnson WL, Owen DM. Fracture toughness determination for a beryllium-bearing bulk metallic glass. Scr Mater 1997 (37) 1373-1378.
[136] Spaepen F. Microscopic mechanism for steady-state inhomogeneous flow in metallic glasses. Acta Metall 1977 (25) 407-415.
[137] Zhao M, Li M. Comparative study of elastoplastic constitutive models for deformation of metallic glasses. Metals 2012 (2) 488-507.
[138] Inoue A, Zhang W, Zhang T, Kurosaka K. High-strength Cu-based bulk glassy alloys in Cu-Zr-Ti and Cu-Hf-Ti ternary systems. Acta Mater 2001 (49) 2645-2652.
[139] Inoue A, Zhang W, Tsurui T, Yavari AR, Greer AL. Unusual room-temperature compressive plasticity in nanocrystal-toughened bulk copper-zirconium glass. Philos Mag Lett 2005 (85) 221-229
[140] Greer JR, De Hosson JTM. Plasticity in small-sized metallic systems: Intrinsic versus extrinsic size effect. Prog Mater Sci 2011 (56) 654 – 724
[141] Zhou X, Zhou H, Li X, Chen C. Size effects on tensile and compressive strengths in metallic glass nanowires J Mech Phys Solids 2015 (53) 130-144
[142] Schuster BE, Wei Q, Hufnagel TC, Ramesh KT. Size-independent strength and deformation mode in compression of a Pd-based metallic glass. 2008 (56) 5091-5100.
[143] Dubach A, Raghavan R, Löffler JF, Michler J, Ramamurty U. Micropillar compression studies on a bulk metallic glass in different structural states. Scr Mater 2009 (60) 567-570.
[144] Argon AS. Plastic-deformation in metallic glassed. Acta Metall 1979 (27) 47-58.
[145] Eckert J, Das J, Kim KB, Baier F, Tang MB, Wang WH, Zhang ZF. High

strength ductile Cu-base metallic glass. Intermetallics 2006 (14) 876-881.
[146] Wakeda M, Shibutani Y, Ogata S, Park J. Relationship between local geometrical factors and mechanical properties for Cu–Zr amorphous alloys. Intermetallics 2007 (15) 139-144.
[147] Steif PS, Spaepen F, Hutchinson JW. Strain localization in amorphous metals. Acta Metall 1982 (30) 447-455.
[148] Spaepen F. Homogeneous flow of metallic glasses: A free volume perspective. Scr Mater 2006 (54) 363-367
[149] Heggen M, Spaemen F, Feuerbacher M. Creation and annihilation of free volume during homogeneous flow of a metallic glass. J Appl Phys 2005 (97) 033506.
[150] Zhao M, Li M. A constitutive theory and modeling on deviation of shear band inclination angles in bulk metallic glass. J Mater Res 2009 (24) 2688-2696.
[151] Donovan PE. A yield criterion for $Pd_{40}Ni_{40}P_{20}$ metallic glass. Acta Metall 1989 (37) 445-456.
[152] Schuh CA, Lund AC. Atomistic basis for the plastic yield criterion of metallic glass. Nut Mater 2003(2) 449-452.
[153] Shibutani Y, Wakeda M, Yoshikawa T. Mechanics of Amorphous Metals (Elastic-Plastic Finite Element Analyses Using Inhomogeneous Defects Theory) [in Japanese]. Trans Jpn Soc Mech Eng Ser A 2013 (79) 1807-1817. (渋谷陽二，譯田真人，吉川高正，非晶性金属材料の材料力学 (不均質欠陥理論に基づく弾塑性有限要素解析).日本機械学会論文集（A 編），2013 (79) 1807-1817.)

Chapter 2

Uniaxial Compression Tests on Single Crystalline, Bi-crystalline and Metallic Glass Micro-pillars

In this chapter, uniaxial compression test will be conducted on the single crystalline, bi-crystalline and metallic glass micro-pillars by the flat punch. The background and objective the uniaxial flat compression, the procedure of the experiments, and results will be introduced in the following. In the Chapter 3, 4 and 5, the theoretical explanations, descriptions and discussion will be applied on these experiments.

2.1 Research background of mechanical properties in uniaxial compression tests

2.1.1 Single crystalline micro-pillars

In the last 10 years it was ubiquitously demonstrated that at the micron- and sub-micron scales, the sample size dramatically affects crystalline strength, as revealed by room-temperature uniaxial compression experiments on a wide range of single-crystalline metallic micro-pillars with non-zero initial dislocation densities [1, 2]. In these studies, cylindrical micro-pillars were fabricated mainly by the use of the Focused Ion Beam (FIB) with some FIB-less methodologies, as well, and remarkably, the results of all of these reports for face-centered cubic (fcc) metals show the increasing strengths accompanying with the decreasing diameter of the micro-pillars

[3, 4], which was called size effect of micro-samples.

For the size effect of micro-samples, the strain gradient plasticity did believe that the constraint of plastic strain results in the size effect: the inner local strain gradient makes a sum of geometrically necessary dislocations be assembled in small local zone, and this means that the dislocations need stronger image back stress to active the constraint of strain gradients [5-9]. However, uniaxial compression with a flat punch methodology to study small-scale mechanical behavior was first introduced by Uchic et al. where the flat punch was used to compress the micro-scaled pillars in order to strictly control the average deviation of strain gradient. The stress-strain responses and shape deformation are shown in Figure 2-1a, b, c, the strengths in small diameter micro-pillars are larger than those in large diameter micro-pillars. The flat punch and the test sketch is shown in Figure 2-1d, the diamond flat punch is parallel to the surface of the micro-sample. The result in Uchic's experiment challenged the strain gradient plasticity theory as there are no geometrically necessary dislocations cross the slip planes, or nearly no active dislocations inside the pillars. More recently, understanding of plasticity in small volumes has been enriched for different kinds of fcc single crystals through uniaxial flat compression experiments, including Ni [4, 10, 11], Au [12-15], Cu [16-23] and Al [24, 25]. For the Ni, Au and Al samples, the nano- and micro-scale pillars have been investigated to study the size dependent mechanical response. However, for the Cu samples, few micro-scale pillars were conducted in the uniaxial compression tests.

Therefore, in this chapter some micro-size Cu pillars (1-10μm) will be produced by FIB, and compressed by a flat punch to receive the mechanical response. The size dependent strength and plastic flow will be further studied on Chapter 3 and 4 based on these experimental results.

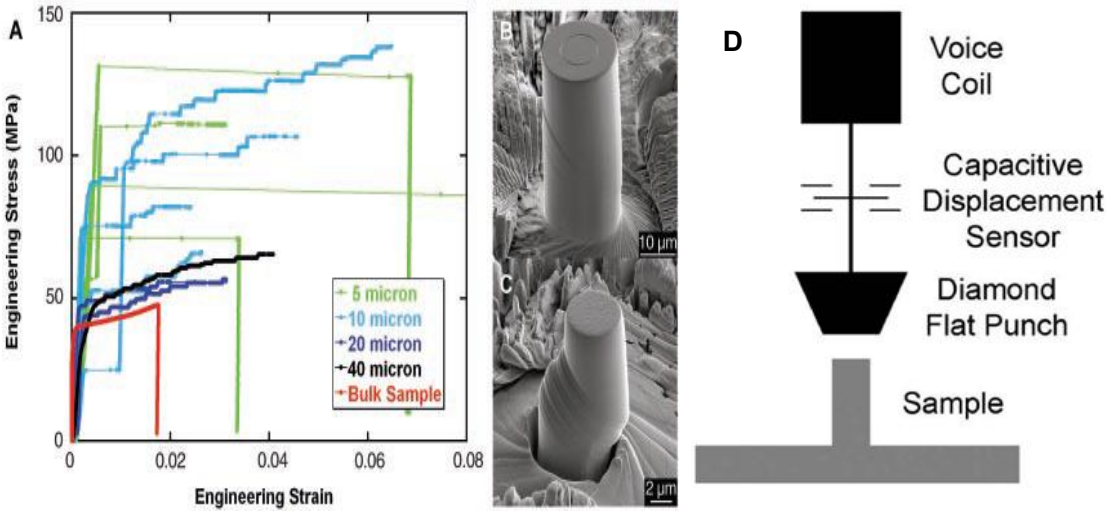

Figure 2-1. Mechanical behavior at room temperature for pure Ni microsamples having a〈134〉orientation. (**A**) Stress-strain curves for microsamples ranging in size from 40 to 5μm in diameter, as well as the stress-strain curve for a bulk single crystal having approximate dimensions 2.6 × 2.6 × 7.4 mm. (**B**) A scanning electron micrograph (SEM) image of a 20μm-diameter microsample tested to ~4% strain. The circle milled into the top surface of the microsample is a fiducial mark used during sample machining. (**C**) A SEM image of 5μm-diameter microsample after testing, where the sample achieved ~19% strain during a rapid burst of deformation that occurred in less than 0.2 s. (**D**) The sketch of the uniaxial compression test on micro samples by using a diamond flat punch.

2.1.2 Bi-crystalline micro-pillars

The size effect in the polycrystalline material is well-known as the Hall-Pecth relationship that grain boundaries/interfaces (GBs) pile up the gliding dislocations, providing effective barriers to transmission of dislocations from one grain to another. However, when the external specimen size is in the micro scale similar to the feature

internal length, the role of GBs differs from itself in the Hall-Pecth relationship in bulk scale specimen [26]. The interaction between dislocations and GB majorly affects the slip transfer across GBs and slip systems [26-29]. Physically, the local plastic deformation will be operated if a Nano-scope indenting applied on the surface of an individual grain or near GBs. Meanwhile, the mechanical response involving a sharp stress gradient to indent loading can be developed from the surrounding long-ranged elastic field [26, 27]. In this way, nanoindenting on the limited volume sample with a GB should be carried out in order to prevent local gradient effect from GBs and confirm the process of dislocations motion interacting with the GB under the more uniform stress condition. To improve in accuracy and avoid the strain gradient effect, a flat-punch indenter in the nanoindentation tests has been operated on single crystalline micro-pillars (SCMs) in order to enforce a uniform compression [1]. Even, thin film or nanometer-sized pillar [10, 30] was conducted in the uniaxial compression test to increase the effect of the emitted dislocations, which distribute imhomogeneously in the interior with more unexpected constraint than at the case for SCMs. Recent experiments [26, 31, 32] reported that Copper (Cu), aluminum (Al) and nickel (Ni) bi-crystalline micro-pillars (BCMs) containing high-angle GBs vertically oriented along the pillar axis have shown their strengthening effects of the GB. However, the BCM with a specific coincidence site lattice boundary (CSL) has been rarely investigated experimentally and the interaction between local strain and dislocations.

In this chapter, the Cu bi-crystalline micro-pillars will be compressed by a flat punch in order to study the interaction of local strain and dislocations near or cross the GBs.

2.1.3 Metallic glass micro-pillars

As mentioned in the previous section, the flow stresses and yield strengths of crystalline metals have been found to be highly size dependent. The strengthening is attributed to dislocation source-limited behavior in small volumes. Different from SCMs and BCMs, the deformation behavior of metallic glass (MG) pillars is not dependent on dislocation dynamics. And there remain conflicts in the literatures about the size effects on the strength and deformation mechanisms in MGs. When the specimen size is reduced to 100nm, the tensile strength of Zr-based MG pillar has a high value of 2.25GPa [33]. The relationship between the shear band propagation stress and the specimen size compares the Griffith's criterion, and the critical specimen size for the localized-to-homogeneous deformation transition is around 30-100nm [33]. The transition from the shear band to homogenous flow occurs at round 400nm [34, 35]. If the specimen size decreases from 600nm down to 90nm, the compressive yield stress will leads to a slight decrease [36]. This is one kind of the size effect but different from the size effect of crystalline material as above statement. For the micro-scaled MG pillars, the reports of the size effect has some conflicts that the increase yield strength accompanies with the increasing or decreasing size [36, 37]. The size effect of MG in micro size (over 1μm) is still an open issue. In order to investigate the size effect of MG, a similar uniaxial flat compression should be conducted like SCMs and BCMs.

In this chapter, we examine the influence of pillar size on the compressive stress-strain response of micro-pillars (1-10μm) of a Zr-based MG ($Zr_{55}Al_{10}Cu_{30}Ni_5$). The related mechanical properties will be physically studied in the Chapter 5.

2.2 Experimental setup

2.2.1 Sample preparation

2.2.1.1 Crystalline cell enlargement by recrystallization annealing

99.96% pure Oxygen Free Copper (OFC) plates with length 6 mm, width 3 mm and thickness 2 mm were prepared in the this experiment for production of SCMs and BCMs . The samples were annealed at 500 °C for 6 hours in vacuum and cooled down to room temperature in a converted scanning electron microscopy (SEM, JSM-5130) with a heat fatigue test device (STH-707S). A thermocouple was attached in the heating stage to monitor the heat treatment temperature. Above the recrystallization temperature, the crystalline cell will be enlarged.

2.2.1.2 Crystalline orientation analysis

Information on the crystal orientation, including grain size and the rotation angles of grain boundaries, was analyzed using the electron backscatter diffraction (EBSD) technique. The as-annealed samples were electronically polished in a solution containing 150 mL HNO_3 and 350 mL CH_3OH at temperature of -35°C for electron back scatter diffraction (EBSD) analyses. The apparatus of electrolytic polishing is shown in Figure 2-2. EBSD measurements were carried out using the program TSL Data Collection ver. 5.31 in a JSM-6510 scanning electron microscope (SEM) (JEOL) with tungsten (W) gun at accelerating voltage of 15kV. The polishing voltage and the electric current are 8V and 0.35-0.48A, respectively. The average recrystallized grain diameter was approximately given as 200μm, the same orientation samples can be fabricated in one suitable grain. During the EBSD progress, the orientation of each grain can be obtained, so a special orientation can be chosen to investigate the

properties of crystal.

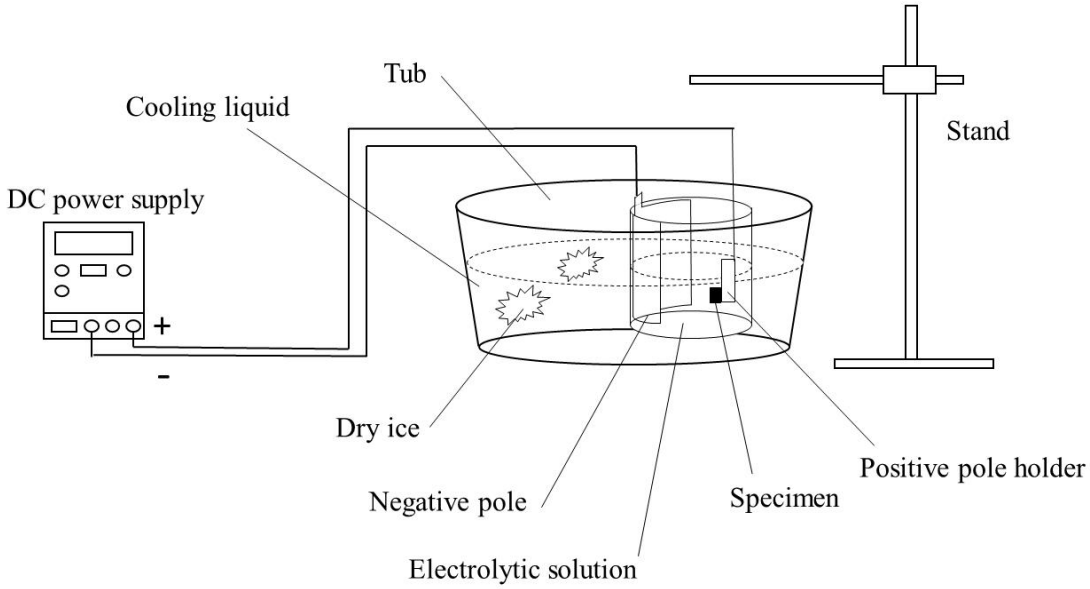

Figure 2-2. Experimental apparatus for electrolytic polishing.

2.2.1.3 SCMs, BCMs and MG pillars fabrication

SCMs, BCMs and MG pillars were fabricated by FIB milling in a JIB-4000 (JEOL) at accelerating voltage of 30 kV with gallium (Ga) ion source. For FIB milling, the following three steps of fabricating processes were employed to get the more proper cylindrical pillars. Two sets of larger beam currents of 3.8 and 1.3nA were initially adopted to mill a tapered pillar as rough finishing. Then, it turned down to the smaller ion current of 20pA as finer milling to remove the taper of pillar. The final tapering angle was successfully reduced to be less than about 2°. The grains for BCMs with almost the same crystallographic orientations were selected along the pillar axis. The final diameters at the half of height for SCMs, BCMs and MG pillars were 1-10μm (SCMs: approximately 1.3μm, 4.2μm and 8.7μm respectively; BCMs and SCMs of grain left (SCM (L) for short) and SCM of grain right (SCM (R) for short):

approximately 4.3μm and 7μm respectively; MG pillars: approximately 1μm, 2μm, 3μm, 4μm, 5μm 6μm 7μm 8μm and 10μm, respectively). The aspect ratio designed here was roughly 1:3.5. The milling depths of each sample in the same diameter were almost the same. The experiments on copper below 1μm have been investigated by researchers [38]. Therefore, in this study we choose the samples with the diameters arrange from 1μm to 10μm. Recalling that the FIB damage on Cu has been reported in recent study [38], the same amount of FIB damage could have been provided to all of the samples equally.

For the BCMs, the milling depths of two grains were almost same, refer to Hirouchi and Shibutani's previous experiment [26], and the similar orientations of two grains as the case in ref. [26] are shown in Figure 2-3a and b. The same amount of FIB damage could have been provided to all of the samples equally. The micro-pillars for Figure 2-3 are in the scale of 4μm. In order to avoid the influence of displacement bursts, the larger scaled pillar (7μm) are fabricated by FIB milling shown in Figure 2-4a and b, and the orientation information is shown in Table 2-1. The large scale micro-pillars such as the specimen shown in Figure 2-4 shows smooth plastic flow meanly representing the hardening of the metallic material. In order to study the grain effect, the triple crystalline micro-pillars were fabricated by FIB milling shown in Figure 2-4a and c.

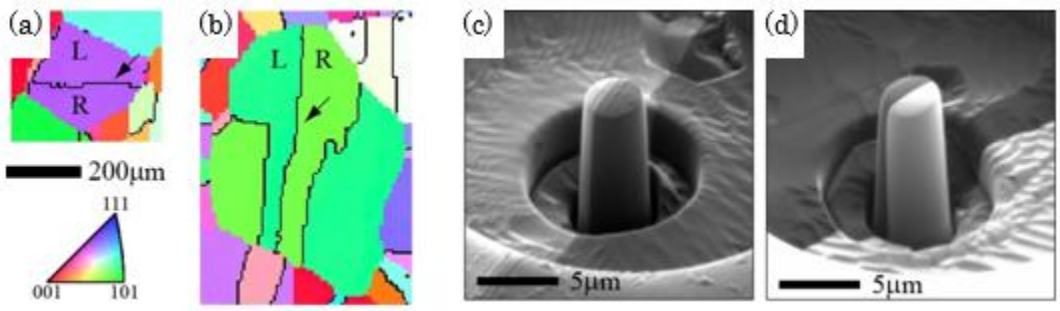

Figure 2-3. Inverse pole figures of groups A (a) and B (b) by EBSD shown by arrow. Also, FIB images of BCMs of Groups A (c) and B (d) [26].

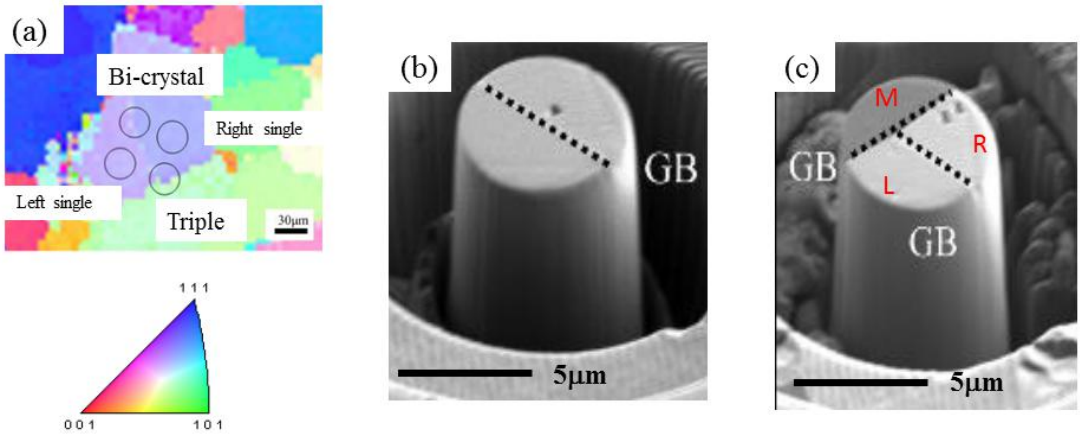

Figure 2-4. Inverse pole figures of groups C and D (a) by EBSD shown by circle. Also, FIB images of BCMs of Groups C (b) and D (Triple crystalline micro-pillars) (c).

Table 2-1 Orientation information for SCMs (L), SCMs (R), BCMs of Groups A-D

Group	Size (μm)	Normal direction to surface		
		L	R	M
A	4	[6 11 5]	[-12 13 25]	/
B	4	[1 -5 5]	[11 21 6]	/
C	7	[-25 -16 -9]	[4 7 -11]	/
D	7	[4 7 -11]	[-25 -16 -9]	[-5 3 1]

M is shown in Figure 2-4c.

2.2.2 Micro compression test

The micro compression test on the SCMs, BCMs and MG pillars is conducted by a Nano-indenter G200 (Agilent Technologies) equipped with a designed diamond flat-punch tip of 20μm diameter. The pillars were compressed in load-controlled mode at a constant loading rate of 1.0 μNs^{-1}.

2.3 Results

2.3.1 SCM

The selected copper experimental results of stress-strain curve are shown in Figure 2-4. The information of these yield stresses, normal crystalline orientations, the maximum Schmid Factor (SF), the corresponding slip system and critical resolved shear stress (CRSS) is shown in Table 2-2. Compared with the CRSS of each size, the CRSSs in 1μm, 4μm and 8μm scales are 63.3MPa, 28.6~38.1MPa and 19.2MPa, respectively. It shows a "smaller is stronger" relationship where pillars with smaller diameters accompany with larger strength. This size dependent CRSS-*d* (diameter) relationship has been reported [4, 10-25]. However, the physics of this phenomenon is still an open issue. In Figure 2-4a, it is shown that the emission of large strain bursts, which operate the catastrophically deformation, were observed in the samples with 1μm diameter. In Figure 2-4b and c, the plastic flow strain is involved by displacement bursts and flow deformation with 4~10μm diameter. For specimen c1, the plastic flow only represents the hardening influence. That is to say, the displacement burst is another size dependent characteristic.

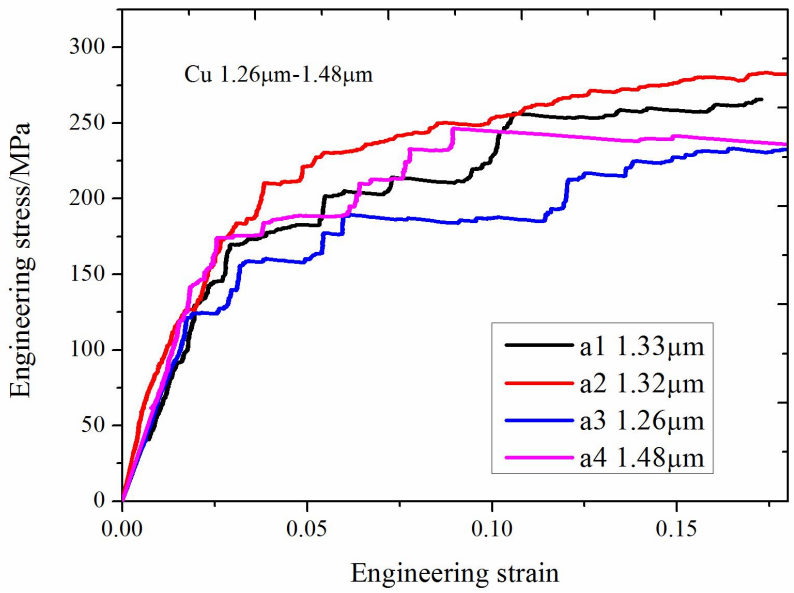

(a) Group a

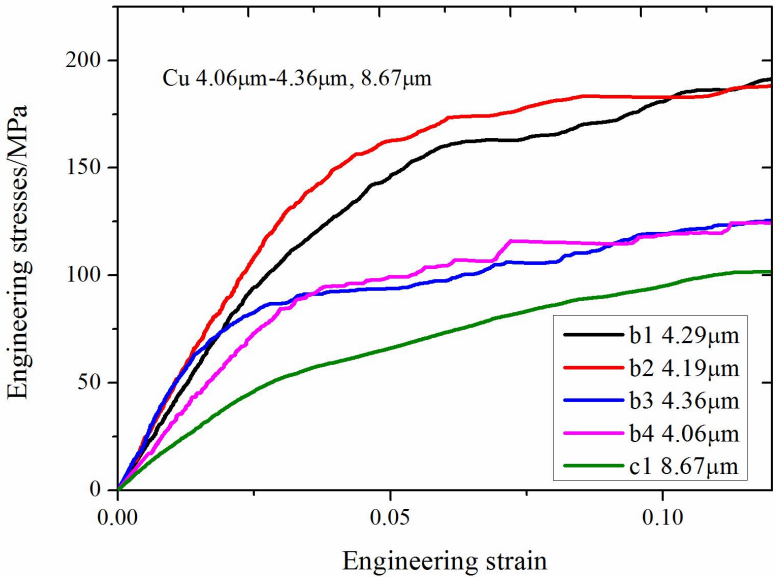

(b) Group b and c

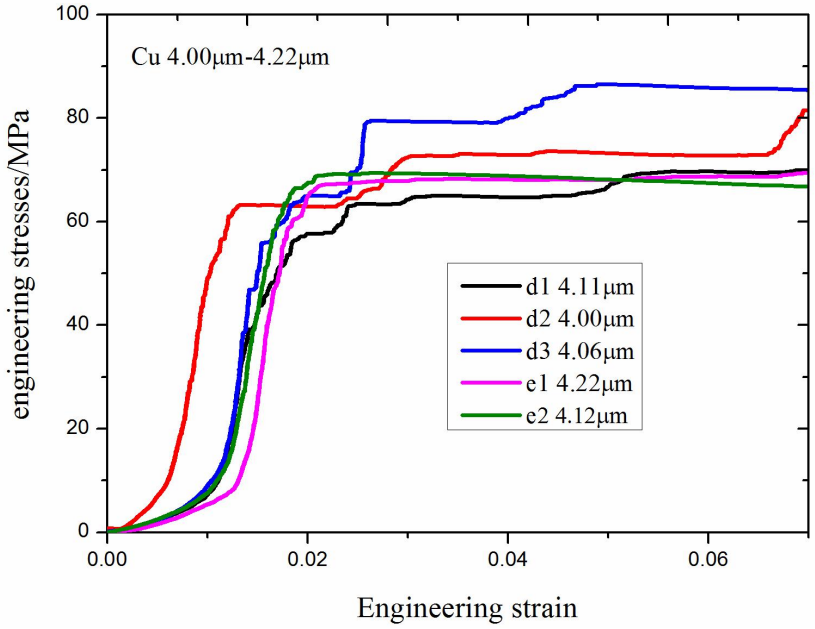

(c) Group d and e

Figure 2-4. Engineering stress and engineering strain experimental curves of copper specimens.

Table 2-2. The details about size, orientation and yield stresses of SCMs Group a-e

No.	yield/MPa	d/μm	h/μm	Normal orientation	slip plane	slip direction	SF	CRSS/Mpa
b1	112.1	4.29	12.53	[1 0 1]	(1 1 1)	[1 −1 0]	0.408	38.1
b2	139.3	4.19	11.14					
b3	80.02	4.36	16.4					
b4	87.5	4.06	14.3					
a1	167.3	1.33	4.46	[6 1 5]	(−1 −1 1)	[0 −1 −1]	0.433	63.3
a2	125.2	1.32	4.67					
a3	119.7	1.26	4.39					
a4	172.6	1.48	3.76					
c1	46.98	8.69	32	[1 0 1]	(1 1 1)	[1 −1 0]	0.408	19.2
d1	68.2	4.11	14.57	[1 −5 5]	(−1 −1 1)	[1 −1 0]	0.435	28.6
d2	63.2	4.00	13.91					
d3	64.94	4.06	14.59					
e1	68.19	4.22	13.24	[1 12 16]	(−1 1 1)	[−1 −1 0]	0.466	32.1
e2	68.99	4.12	14.27					

During the displacement burst process, the dislocation evolution has a large earthquake as displacement bursts vibrate the dislocation distribution [39-44]. Recently some continuum models are provided to describe displacement bursts during the plastic plow stage [40-41], and it has been found that the large strain burst accompanying with dislocations avalanche produced unstable local strain, which didn't distribute along the original slip system. Based on the method of dislocation simulation provided to describe the variance of the dislocations, it is believed that dislocations distribution would vibrate when displacement burst happened [42-44]. Therefore, the physical explanations on the relationship between the dislocations evolution and the macro strain need to include the displacement burst. At present, understandings on the displacement bursts are limited to the observation method in which the variance of the inner micro- and nano- structures cannot be seen during the plastic process. Large displacement bursts always accompany with dislocations avalanche, which results in unstable deformation and uncertain variance of dislocation evolution. Thereby large displacement bursts cannot be considered into the dislocation evolution consideration which would be studied in following.

The shape deformation of the SEM image of Cu SCMs in 4μm is shown in Figure 2-5. It shows that the deformed SCMs with orientations [6 11 5] and [1 0 1] have the characteristic of single slip with the largest SF. But for the deformed SCMs with orientations [1 $\bar{5}$ 5] and [1 12 16], it can be clearly seen that SCMs were deformed accompanying two different slip planes (two cross slip). When considering the sequence of these two kinds of slips, the slip nucleated at the upper side preferentially occurred as the stress of concentration around the surface edge of pillar [26]. The slide angles of the two slip plane are almost the same, which are the two of the slide angles with the largest three SFs. This kind of shear failure in the slip planes among the three largest slide angles, associated with the bursts frequently occurred via the activation of shear transformation zone [26].

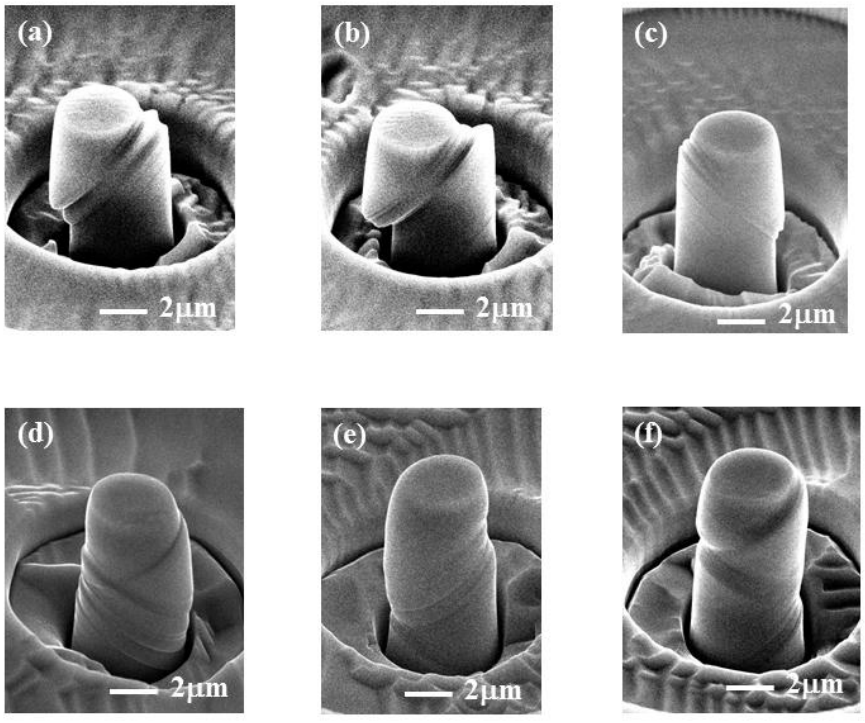

Figure 2-5. The SEM image of the deformed SCMs with normal orientations: (a) and (b) [6 11 5]-SCM (L) of group A; (c) [1 0 1]-SCM of group b and c; (d) [1 $\bar{5}$ 5]-SCM of group d; (e) and (f) [1 12 16]-SCM of group e.

2.3.2 BCM

The stress-strain responses of Groups A, B, C and D are plotted in Figure 2-6a, b and c, respectively. The solid line, dotted line and point line represent the stress-strain responses of BCM, SCM (L) and SCM (R), respectively. The stress-strain curve of 4μm before the linear stress-strain response involves a nonlinear deformed response because of the possible existing angular misalignment between a flat punch and the top surface of the specimen. For the Group A, yield stresses of BCM are around 70MPa, the corresponding yield stresses of SCM (L) and SCM (R) are 60-65MPa. There is almost no work hardening to be observed for BCMs and SCMs, even though some small displacement exists just after elastic strain. The large deformation of the catastrophically large displacement can be found. For Group B shown in Figure 2-6b, the distinct work hardening are observed during the strain is up to 4%. And the hardening consists of the repetition of small displacement bursts and hardening. After that, the SCM still continue this kind deformation until fracture. However, the BCM represents unstable deformations with large displacement bursts. In Figure 2-6c, the SCMs and BCMs of 7μm only show the plastic flow of work hardening. And relationship between the size and displacement is still unknown [39-44]. Figure 2-6a and b, the yielding stresses of BCMs are larger than those of SCMs, and this phenomenon can also be found in Figure 2-6c. The Triple crystalline micro-pillar shows not only large yielding stresses but also an obvious work hardening than SCMs and BCMs. That is to say, the grain boundary (GB) strengths the mechanical response of the micro-pillars. This phenomenon would be explained in chapter 4.

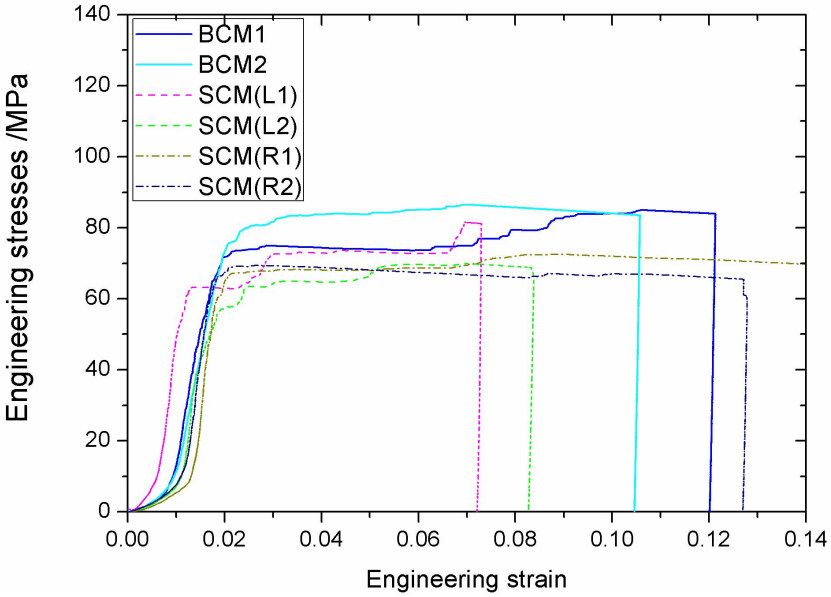

(a) Group A in Table 2-1.

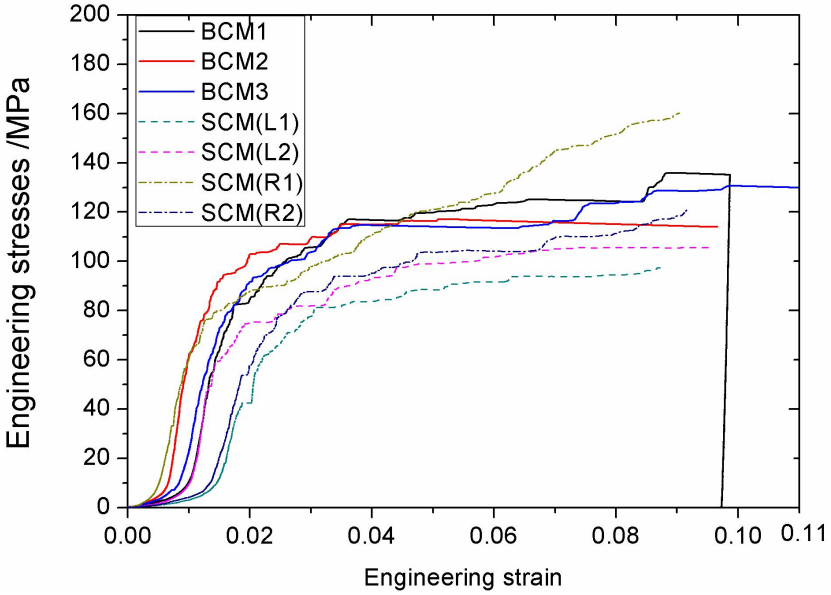

(b) Group B in Table 2-1.

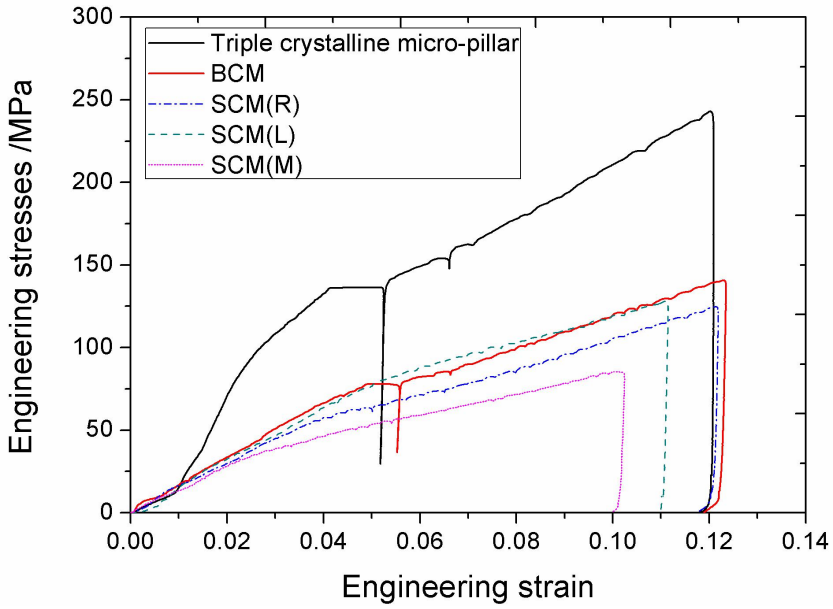

(c) Group C and D in Table 2-1.

Figure 2-6. The stress-strain curve of Group A, B, C and D in Table 2-1. The solid line, dotted line and point line represent the stress-strain curve of BCM, SCM (L) and SCM (R) (corresponding SCM to the left side and right side of BCM), respectively. The lines shows the mechanical responses of Group A (a), Group B (b), Group C (c) and Group D (c).

Figure 2-7a-h presents FIB/SEM micro-graphs of BCMs and corresponding SCMs of Group A and B in 4μm with the same crystallographic orientations after test from the lateral view. It is clearly revealed that the slip planes in each side of BCMs are almost the same as the slip planes of the corresponding SCMs. In Figure 2a-d, the BCMs and SCMs of Group A have the characteristic of single slip with the largest Schmid Factor (SF). But for Group B, it can be clearly seen that both BCMs and SCMs were deformed accompanying two different slip planes (two cross slip). The slip direction in both Group A and Group B is parallel to the GB, therefore the slip

band is along the GB. In Figure 2-8, the slip planes of BCM (Group C) are also almost the same as the slip planes of the corresponding SCMs, but the slip direction is not strictly parallel to the GB with a very small angle. The slip deformation of a triple crystalline micro-pillar is also studied shown in Figure 2-8g. The slip direction is almost along the GB between the left grain (L in Figure 2-8g) and right grain (R in Figure 2-8g).

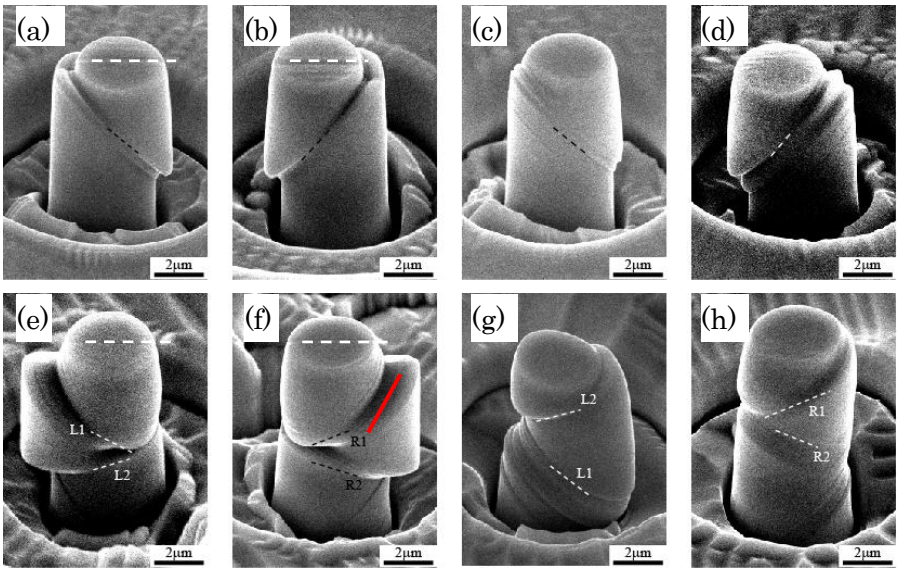

Figure 2-7. SEM images of group A and group B after compression with a tilt angle of 45°: (a) Left and (b) right sides of BCM of Group A, (c) left side of SCM(L), and (d) right side of SCM(R). (e) Left and (f) right sides of BCM in Group B, (g) left side of SCM(L), and (h) right side of SCM(R). Dashed lines show the slip lines for measurements of slip plane ((a)~(d) for group A, (e)~(h) for group B): (a) Left side of BCM, (b) right side of BCM, (c) left side of SCM(L), and (d) right side of SCM(R); (e) Left side of BCM, (f) right side of BCM, (g) left side of SCM(L), and (h) right side of SCM(R) [26].

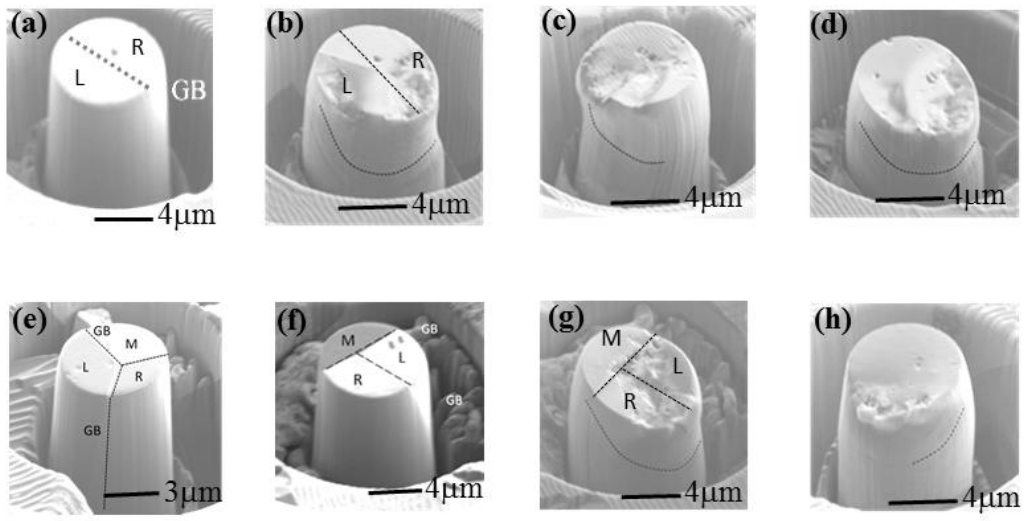

Figure 2-8. SEM images of group C and group D with a tilt angle of 45°: (a) Left and right sides of BCM of Group C before compression, (b) Left and right sides of BCM of Group C after compression, (c) left side of SCM (L), and (d) right side of SCM(R) after compression; (e) original shape of Triple crystalline micro-pillar Group D with a slide grain boundary (GB) between M side and L side, (f) original shape of Triple crystalline micro-pillar Group D from the view side of GB between L and R, (g) deformed shape of Triple crystalline micro-pillar Group D, and (h) middle side of SCM (M). Dashed lines show the slip lines for measurements of slip plane ((a)~(d) for group C, (e)~(h) for group D: (a) and (b) BCM, (c) left side of SCM(L), and (d) right side of SCM(R); (e), (f) and (g) Triple crystalline micro-pillar Group D, (h) middle side of SCM (M).

When considering the sequence of these two kinds of slips (single slip in Groups A and C; two cross slip in Group B), the slip nucleated at the upper side preferentially occurred as the stress of concentration around the surface edge of pillar [26]. The slide angles of the two slip plane are almost the same, which are the two of the slide angles

with the largest three SFs. This kind of shear failure in the slip planes among the three largest slide angles, associated with the bursts frequently occurred via the activation of shear transformation zone [26]. Under ultrahigh external mechanical stress, once a mesoscopic glide plane is formed, local shear can active macroscopic sliding and result in the evolution of defects, with strain bursts shown in stress-strain curve (see Figure 2-6). This mechanism operates the evolution of interior microstructures such as dislocations, the motion of that would result in the variance of the plastic strain [24-28, 41-44].

2.3.3 Metallic glass micro-pillar

The stress-strain responses of different scaled metallic glass (MG) micro-pillars (1μm, 2μm, 4μm, 6μm, 7μm, 8μm and 10μm) are plotted in Figure 2-9a~g, respectively. The same scaled two or three MG micro-pillars are compressed uniaxially in order to avoid the dispersiveness from the experiments. Compared with the results among all the figures, the elastic limits of the micro-pillars in 1μm and 2μm is around 1200-1400MPa, smaller those of the micro-pillars in 4-10μm. This unobvious size dependent elastic limit tendency is different from that of crystalline material. The plastic flow of the 1μm diameter MG micro-pillar involves much more elastic stress increase stages and represents more obvious stress increase tendency globally than that of large scaled MG micro-pillars. In the crystalline micro-pillars and amorphous micro-pillars, the elastic stress increase always accompanies with the phenomenon of displacement bursts. The catastrophically unstable plastic deformation is related to this kind of displacement bursts.

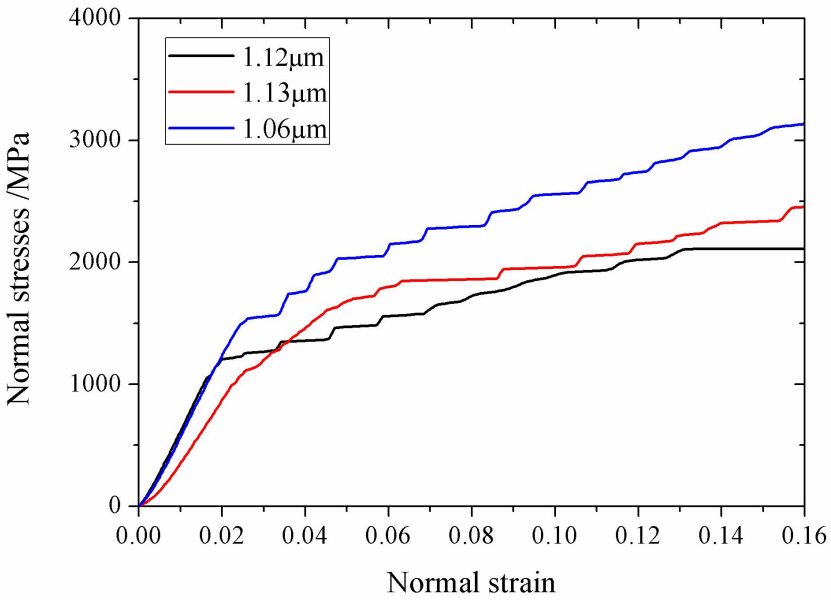

(a) 1μm diameter MG micro-pillars;

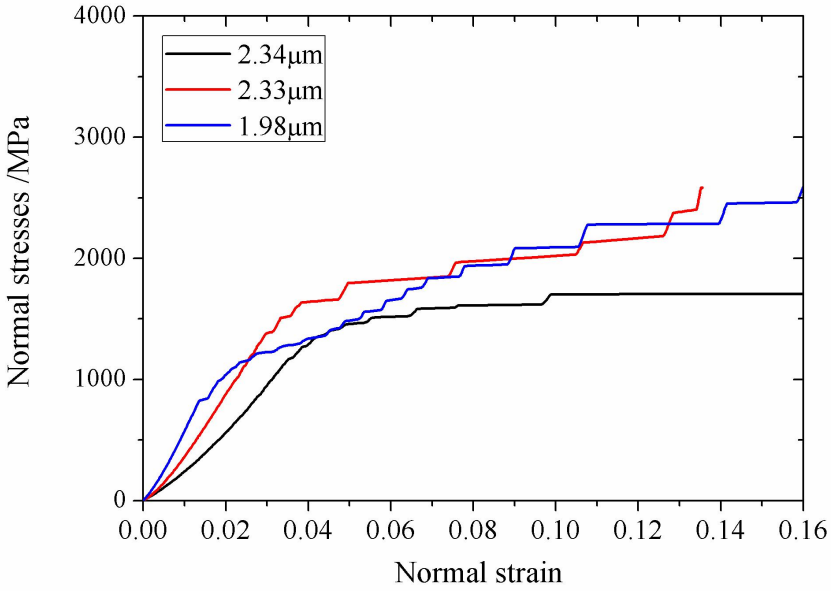

(b) 2μm diameter MG micro-pillars;

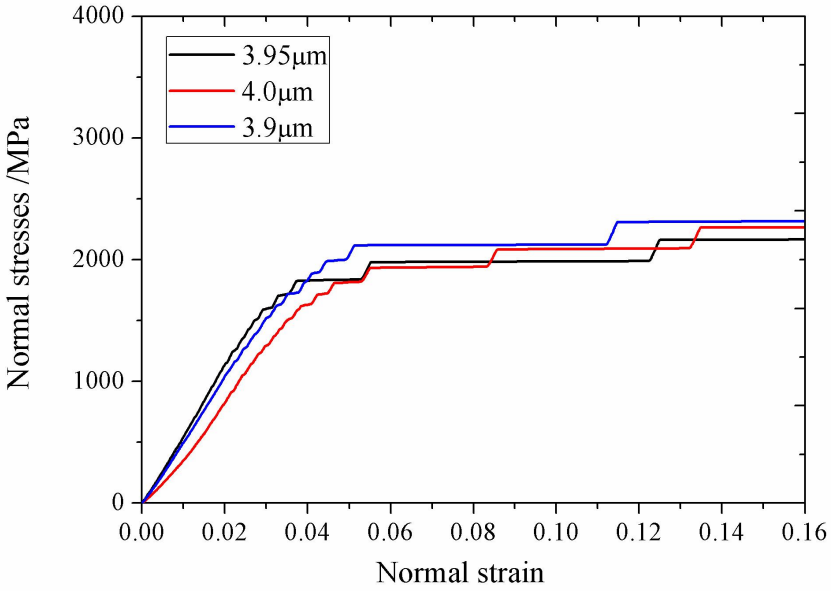

(c) 4μm diameter MG micro-pillars;

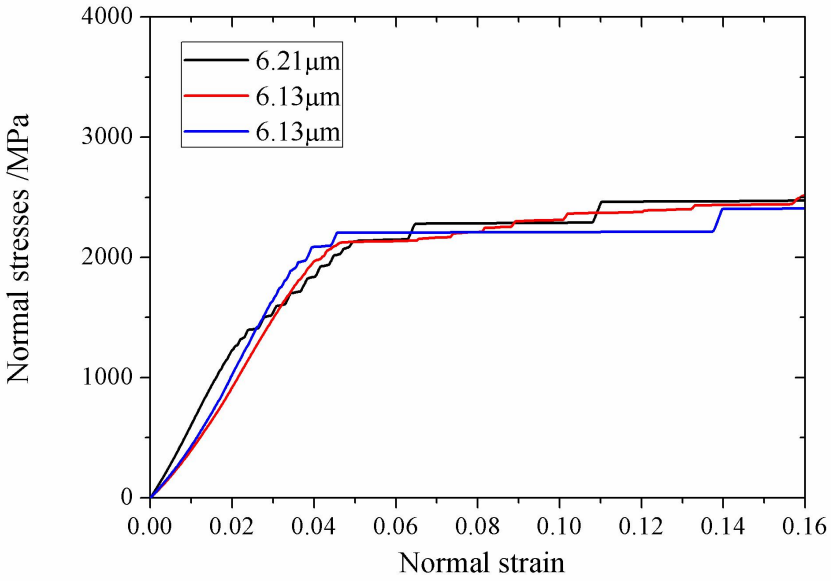

(d) 6μm diameter MG micro-pillars;

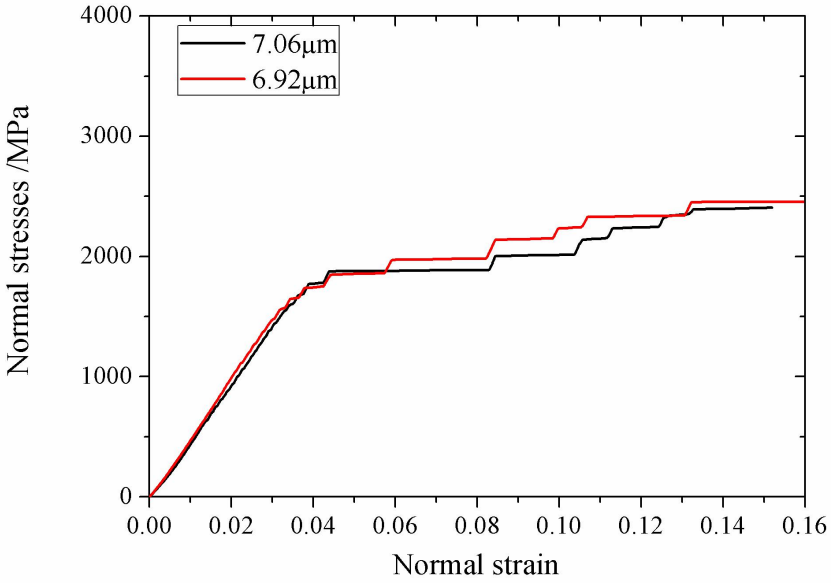

(e) 7μm diameter MG micro-pillars;

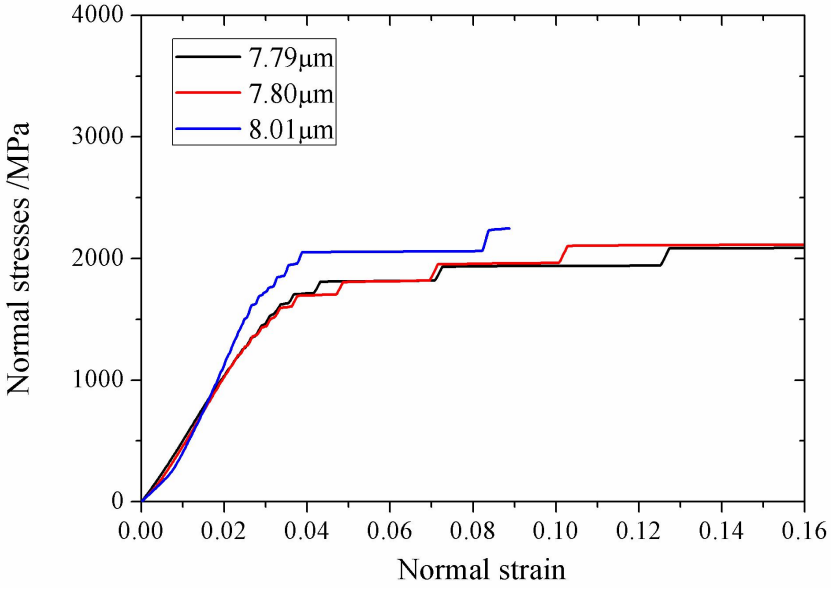

(f) 8μm diameter MG micro-pillars;

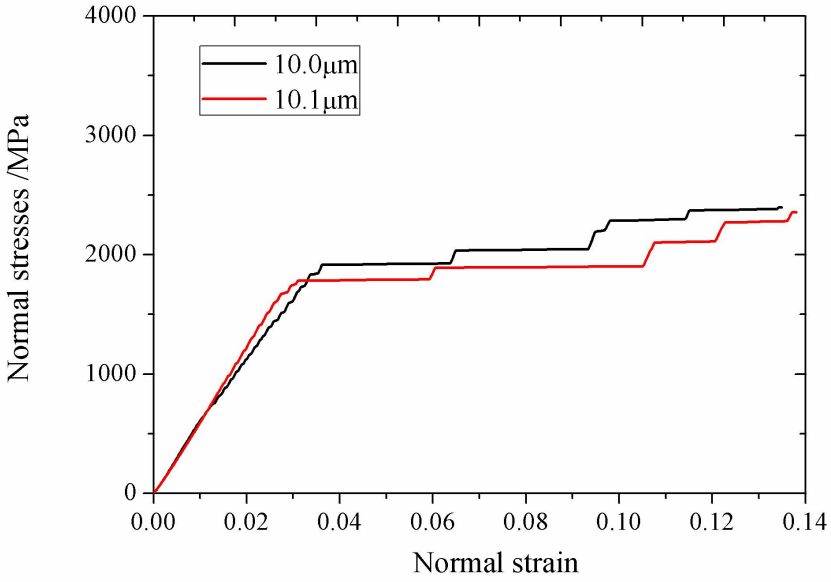

(g) 10μm diameter MG micro-pillars;

Figure 2-9. The stress-strain curve of metallic glass micro-pillars in different sizes: (a) 1μm; (b) 2μm; (c) 4μm; (d) 6μm; (e) 7μm; (f) 8μm; (g) 10μm.

In micro-pillars, the MGs also attracts high elastic limit, which is much higher than the crystalline materials, and obvious plastic flow at room temperature, which is different from the bulk MGs. The Bulk MGs shows the catastrophic failure after the elastic limit under tension and compression [33, 45]. However, it has been widely accepted that plastic deformation of the small scaled MGs such as nano-scaled MGs is carries by shear transformation zones (STZs) which are clusters of hundreds of atoms undergoing shear displacements under external loading. The shear bands of MGs are shown in Figure 2-10a~f. The angles between the shear plane and the loading axis are all at or very close to 45°. In Figure 2-10, the large scaled (4-10μm) MG micro-pillars have more obvious shear band than the small scaled (1-2μm) ones. When the stress state reaches the yield point, strain concentrates into some small regions. These localized regions start to propagate together and link to each other, and form a narrow

shear bands.

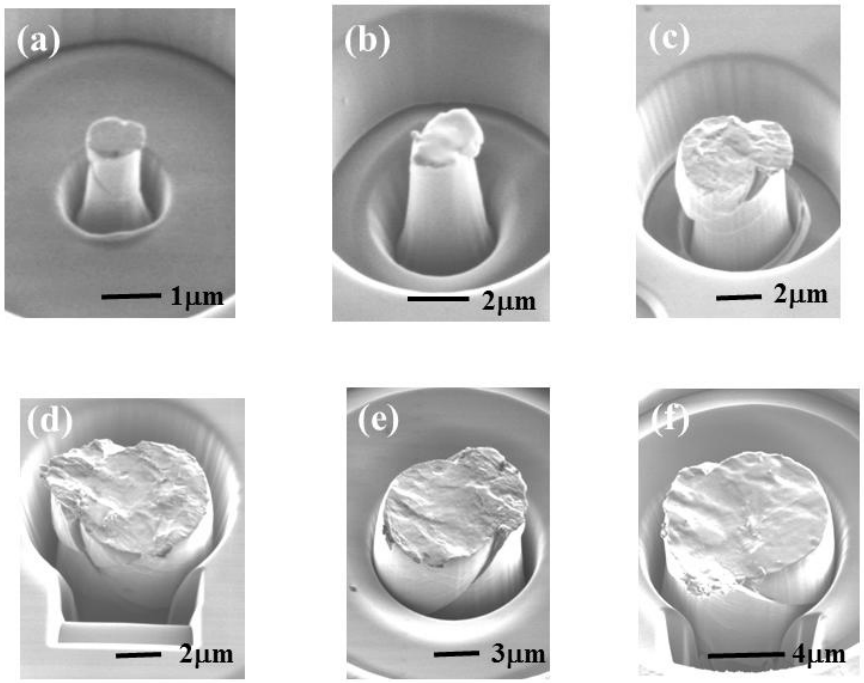

Figure 2-10. The SEM image of the deformed MG micro-pillars with different sizes: (a) 1μm; (b) 2μm; (c) 4μm; (d) 6μm; (e) 8μm and (f) 10μm.

2.4 Summary

In this chapter, the research background of the uniaxial compression test on the SCMs, BCMs and MG micro-pillars, and the targets of our conducted experiments are reviewed. The procedure of the experiments are introduced in the following. The results of SCMs shows strong size dependent mechanical characteristics such as size dependent CRSS and different plastic flow with varied scaled diameters. The physical explanations of these phenomenon will be stated in Chapter 3 and 4 based on the dislocation physics, surface energy theory and crystal plasticity. The BCM experiments shows the effect of grain boundary on the stress-strain response and slip deformation. The relationship between the dislocation motion and the grain boundary,

and the stress-strain behavior will be studied in Chapter 4. The MG micro-pillar experiments shows an unobvious size dependent elastic limit relationship, which will be deeply discussed in Chapter 5. The plastic flow will be described based on free volume theory in Chapter 5, and compared with the experiments in this chapter.

Reference

[1] Uchic MD, Shade PA, Dimiduk DM. Plasticity of micrometer-scale single crystals in compression. Annu Rev Mater Res 2009 (39) 361-386.
[2] Kraft O, Gruber PA, Monig R, Weygand D. Plasticity in confined dimensions. Annu Rev Mater Res 2010 (40) 293-317.
[3] Dou R, Derby B. A universal scaling law for the strength of metal micropillars and nanowires. Scr Mater 2009 (61) 524-527.
[4] Uchic MD, Dimiduk DM, Florando JN, Nix WD. Sample dimensions influence strength and crystal plasticity. Science 2004 (305) 986-989.
[5] Fleck NA, Hutchinson JW. A phenomenological theory for strain gradient effects in plasticity. J Mech Phys Solids 1993 (41) 1825-1857.
[6] Fleck NA, Hutchinson JW. Strain gradient plasticity. Academic Press, New York, 1997, p295.
[7] Gao H, Huang Y, Nix WD, Hutchinson JW. Mechanism-based strain gradient plasticity—I. Theory. J Mech Phys Solids 1999 (47) 1239-1263.
[8] Huang Y, Gao H, Nix WD, Hutchinson JW. Mechanism-based strain gradient plasticity—II. Analysis. J Mech Phys Solids 2000 (48) 99-128.
[9] Nix WD, Gao H. Indentation size effects in crystalline materials: a law for strain gradient plasticity. J Mech Phys Solids 1998 (46) 411-425.
[10] Shan ZW, Mishra R, Syed SA, Warren OL, Minor AM. Mechanical annealing and source-limited deformation in submicron diameter Ni crystals. Nat Mater 2008 (7) 115-119.
[11] Dimiduk DM, Uchic MD, Parthasarathy TA. Size-affected single-slip behavior of pure nickel microcrystals. Acta Mater 2005 (53) 4065-4077.
[12] Greer JR, Oliver WC, Nix WD. Size dependence of mechanical properties of gold at the micron scale in the absence of strain gradients. Acta Mater 2005 (53) 1821-1830.
[13] Greer JR, Nix WD. Nanoscale gold pillars strengthened through dislocation starvation. Phys Rev B 2006 (73) 245410-245416.
[14] Volkert CA, Lilleodden ET. Size effects in the deformation of sub-micron Au columns. Philos Mag 2006 (86) 5567-5579.
[15] Budiman A, Han S, Greer JR, Tamura N, Patel J, Nix WD. A search for evidence of strain gradient hardening in Au submicron pillars under uniaxial compression using synchrotron X-ray microdiffraction. Acta Mater 2007 (56) 602–608.
[16] Kiener D, Motz C, Rester M, Jenko M, Dehm G. FIB damage of Cu and possible consequences for miniaturized mechanical tests. Mater Sci Eng A 2006 (459)

262-272.
[17] Dehm G. Miniaturized single-crystalline fcc metals deformed in tension: New insights in size-dependent plasticity. Prog Mater Sci 2009 (54) 664-688.
[18] Kiener D, Motz C, Schoberl T, Jenko M, Dehm G. Determination of mechanical properties of copper at the micron scale. Adv Eng Mater 2006 (8) 1119-1125.
[19] Kiener D, Grosinger W, Dehm G, Pippan R. A further step towards an understanding of size-dependent crystal plasticity: in situ tension experiments of miniaturized single-crystal copper samples. Acta Mater 2008 (56) 580-592.
[20] Kiener D, Grosinger W, Dehm G. On the importance of sample compliance in uniaxial microtesting. Scr Mater 2009 (60) 148-151.
[21] Kiener D, Motz C, Dehm G. Micro-compression testing: a critical discussion of experimental constraints. Mater Sci Eng A 2009 (505) 79–87.
[22] Maass R, Van Petegem S, Grolimund D, Van Swygenhoven H, Kiener D, Dehm G. Crystal rotation in Cu single crystal micropillars: in situ Laue and electron backscatter diffraction. Appl Phys Lett 2008 (92) 071905
[23] Jennings AT, Greer JR. Tensile deformation of FIB-less single crystalline copper pillars. Philos Mag 2010 (91) 1-13
[24] Ng KS, Ngan AHW. Breakdown of Schmid's law in micropillars. Scr Mater 2008 (59) 796-799.
[25] Ng KS, Ngan AHW. Effects of trapping dislocations within small crystals on their deformation behavior. Acta Mater 2009 (57) 4902-4910.
[26] Hirouchi T, Shibutani Y. Mechanical Responses of Copper Bicrystalline Micro Pillars with $\Sigma 3$ Coherent Twin Boundaries by Uniaxial Compression Tests. Mater Trans 2014 (55) 52-57.
[27] Tsuru T, Shibutani Y, Hirouchi T. A predictive model for transferability of plastic deformation through grain boundaries. AIP Adv 2016 (6) 015004.
[28] Tsuru T, Kaji Y, Shibutani Y. Incipient plasticity of twin and stable/unstable grain boundaries during nanoindentation in copper. Phys Rev B 2010 (82) 024101.
[29] Tsuru T, Kaji Y, Shibutani Y. Minimum Energy Motion and Core Structure of Pure Edge and Screw Dislocations in Aluminum. J Comp Sci Tech 2010 (4) 185-193.
[30] Kunz A, Pathak S, Greer JR. Size effects in Al nanopillars: single crystalline versus bicrystalline. Acta Mater 2011 (59) 4416-4424.
[31] Ng KS, Ngan AHW. Deformation of micron-sized aluminum bi-crystal pillars. Philos Mag 2009 (89) 3013-3326.
[32] Kheradmand N, Dake J, Barnoush A, Vehoff H. Novel methods for micromechanical examination of hydrogen and grain boundary effects on dislocations. Philos Mag 2012 (92) 3216-3230.
[33] Jang D, Greer JR. Transition from a strong-yet-brittle to a stronger-and-ductile

state by size reduction of metallic glasses. Nat Mater 2010 (9) 215-219.
[34] Jang D, Greer JR. Size-induced weakening and grain boundary-assisted deformation in 60nm-grained Ni nano-pillar. Scr Mater 2011 (64) 77-80.
[35] Volkert CA, Donohue A, Spaepen F. Effect of sample size on deformation in amorphous metals. J Appl Phys 2008 (103) 083539.
[36] Kuzmin O, Pei Y, Chen C, De Hosson JTM. Intrinsic and extrinsic size effects in the deformation of metallic glass nanopillars. Acta Mater 2011 (60) 889-898.
[37] Schuster BE, Wei Q, Hufnagel TC, Ramesh KT. Size-independent strength and deformation mode in compression of a Pd-based metallic glass. Acta Mater 2008 (56) 5091-5100.
[38] Tang H, Schwarz KW, Espinosa HD. Dislocation-source shutdown and the plastic behavior of single-crystal micropillars. Phys Rev Lett 2008 (100) 185503.
[39] Zhang X, Pan B, Shang, FL. Scale-free behavior of displacement bursts: Lower limit and scaling exponent, Europhys Lett 2012 (100) 16005.
[40] Zhang X, Shang FL. A continuum model for intermittent deformation of single crystal micro pillars, Int J Solids Struct 2014 (51) 1859–1871.
[41] Zhang X, Shang FL, Yu Y, Yan YB, Yan SP. A stochastic model for the temporal aspects of flow intermittency in micro pillar compression, Int J Solids Struct Vol.51, 2014 (51) 4519–4530.
[42] Gao Y, Liu ZL, You, XC et al. A hybrid multiscale computational framework of crystal plasticity at submicron scales. Comput Mater Sci 2010 (49) 672-681.
[43] Gao Y, Zhuang Z, Liu ZL et al. Characteristic sizes for exhaustion-hardening mechanism of compressed Cu single-crystal micropillars. Chin Phys Lett 2010 (27) 086103.
[44] Gao Y, Zhuang Z, Liu ZL et al. Investigations of pipe-diffusion-based dislocation climb by discrete dislocation dynamics. Int J Plast 2011 (27) 1055-1071.
[45] Zhao M, Li M. Comparative study of elastoplastic constitutive models for deformation of metallic glasses. Metals 2012 (2) 488-507.

Chapter 3

Physical modeling on size dependent yielding and yield surface on crystals

Recent research has explained that the steeply increasing yield strength in metals depends on decreasing sample size. The size dependent yield strength of single crystals has been found in Chapter 2, this phenomenon will be physically discussed in this chapter. First, we consider the effect of inner dislocation motion- “pile-up” effect, and derive a statistical physical model of the yield strength of finite single-crystal micro-pillars that depends on single-ended dislocation pile-up inside the micro-pillars. We show that this size effect can be explained almost completely by considering the stochastic lengths of the dislocation source and the dislocation pile-up length in the single-crystal micro-pillars. Our quantitative conclusions suggest that the number of dislocation sources and pile-ups are significant factors for the size effect. Moreover, we investigated the explicit relationship between the stacking fault energy and the dislocation “pile-up” effect inside the sample: materials with low stacking fault energy exhibit an obvious dislocation pile-up effect. And then, the influence of the surface energy and surface elasticity upon the size-dependent yield strength of single-crystalline hollow micro- and nanopillars is considered quantitatively. An analytical expression of the size-dependent yield strength is established that considers the surface energy and the inner defects and by the principle of minimum potential

energy. The predicted yield strength of our model as a function of the pillar size is more precise than that of the well-known single arm source model when comparing the predictions with the experimental results of pillars made of Al or Ni. Finally, in order to describe more complicated stress condition, a size-dependent yield function for a single crystal is developed by considering defect effects, including dislocation pile-up, dislocation starvation and source exhaustion, especially for micro-pillars.

3.1 Effect of dislocation pile-up on size-dependent yield strength in finite single-crystal micro-samples

3.1.1 Model

In the micro-pillars, the critical resolved shear stress (CRSS), which can be treated as the initial yield strength when considering macroscopic plasticity, predominantly depends on the stress required to initiate and to maintain dislocation multiplication [1-4]. Plastic flow of the micro-pillars requires the CRSS to be initiated by activating the dislocation multiplication from the weakest dislocation source[1-3, 5, 6], and then to be maintained by hardening stresses [3, 4, 7]. Finite micro-pillars contain double-pinned Frank–Read sources and/or SAS, which occurs because finite micro-pillars have much larger volume than nano-pillars, in which there are nearly no dislocation sources. Mobile dislocations can move from the interior of the sample to the surface, according to the single arm source (SAS) model by Parthasarathy et al [1, 8]. These dislocations can annihilate at the free surface, possibly causing “starvation” of mobile dislocations[9, 10]. In the SAS model, however, the pile-up mechanism is not considered, and the strength (CRSS) includes the friction stress τ_0 , back stress τ_{back} , and activation stress τ_{activate} of the dislocation source, which can be expressed as [1]

$$\mathrm{CRSS} = \tau_0 + \tau_{\mathrm{back}} + \tau_{\mathrm{activate}} = \tau_s + \tau_{\mathrm{activate}} = \tau_0 + 0.5\mu b\sqrt{\rho} + \frac{\mu b}{\bar{\lambda}_{\max}}, \tag{3.1}$$

where $\tau_s = \tau_0 + 0.5\mu b\sqrt{\rho}$ represents an field stress on the slip plane including τ_0 and τ_{back}, ρ is the total initial dislocation density, μ is the shear modulus, ν is Poisson's ratio, b is the magnitude of the Burgers vector, λ is the dislocation source length shown in Figure 3-1, and $\bar{\lambda}_{\max}$ is the average longest effective length [1].

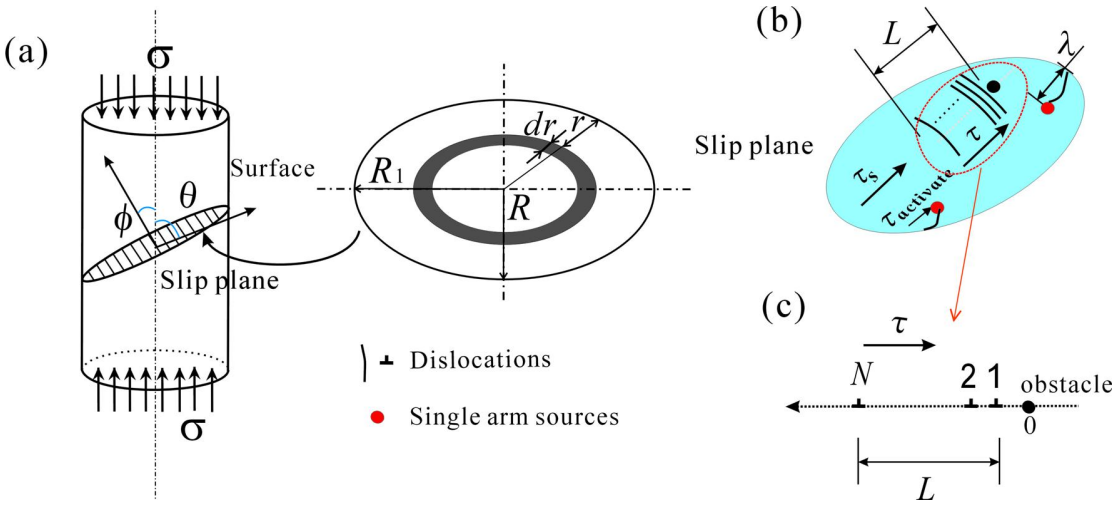

Figure 3-1. Schematic of dislocations piling up behind obstacles in a cylindrical micro-pillar in a critical configuration. (a) Illustration of the primary slip plane in a cylindrical pillar: the dislocation sources are distributed randomly on this slip plane with width dr; (b) dislocation configurations and stress states with a pile-up already formed on the slip plane: the external stress σ provides the applied field stress τ_s, the activation stress τ_{activate}, and/or the applied shear stress τ to the dislocation pile-up on the slip plane; (c) a sketch of the pile-up field.

As the basis for our investigation, we use the SAS model's configuration accompanying the already-formed pile-up. First, consider a compressed cylindrical pillar with radius R, as shown in Figure 3-1a, and a primary slip plane oriented at an

angle ϕ with respect to the loading axis. Figure 3-1b shows a pile-up already formed on the slip plane and the critical shear stress required to activate the SAS (initial yielding state). The external stress σ provides the applied field stress τ_s, activation stress τ_{activate}, and applied shear stress τ on the dislocation pile-up region on the slip plane. In the SAS model, because there is no pile-up field, the CRSS is given by Eq. (3.1). In Figure 3-1c, under an applied shear stress τ, an inner defect or junction caused by slight crystal rotation can be regarded as an obstacle at x=0. Here, the obstacle represents a local resistance to motion of mobile dislocations on the slip plane. Some mobile dislocations stop gliding and pile up behind obstacles on the slip plane, as shown in Figure 3-1c. N is the number of pile-up dislocations, and L is the length of the dislocation pile-up, as shown in Figure 3-1c). According to dislocation elasticity theory [11], the critical stress τ_p at the tip of the dislocation pile-up and L are

$$\tau_p = N\tau, \tag{3.2}$$

$$L = x_N \approx \frac{a_0 N}{\tau}\frac{\mu b}{2\pi(1-\nu)} = \frac{\pi^2}{8\tau}\frac{\tau_p}{\tau}\frac{\mu b}{2\pi(1-\nu)} \quad (a_0 = \frac{\pi^2}{8}). \tag{3.3}$$

The value of L is difficult to define, even using in situ microscopy. However, L is proportional to the specimen geometry R [12], and the statistical value of the dislocation source length λ is ~0.3 times as long as the radius according to a simulation by Parthasarathy et al [1]. Thus, in Eq. (3.3) the length L can be assumed to be $L = m\lambda,\ (m > 0)$. In terms of a pile-up SAS model, $L = m\lambda,\ (m > 0)$ is used to describe the pile-up effect in the following analysis.

The dislocation sources distribute randomly on the slip plane, and the number of sources is related to dislocation density and the volume [1]. The obstacles inside the pillars may be the junctions caused by rotation of the crystal or the dislocation source.

The motion of mobile dislocations at the position of obstacles has two possibilities: first, they bow and continue going through the obstacle, or they stop behind the obstacle. Both of these possibilities are shown in Figure 3-2. When a dislocation passes through the obstacles or climbs to another slip plane, the back stress and the stress to activate the dislocation source are considered in the SAS model [1, 8]. However, if the mobile dislocation stops behind the obstacle, there are two cases for pile-up: first, when there is a dislocation source near the tip of dislocation pile-up, which is shown as Case 1 in Figure 3-2; second, when that dislocation sources are far from the tip of pile-up, which is shown as Case 2 in Figure 3-2.

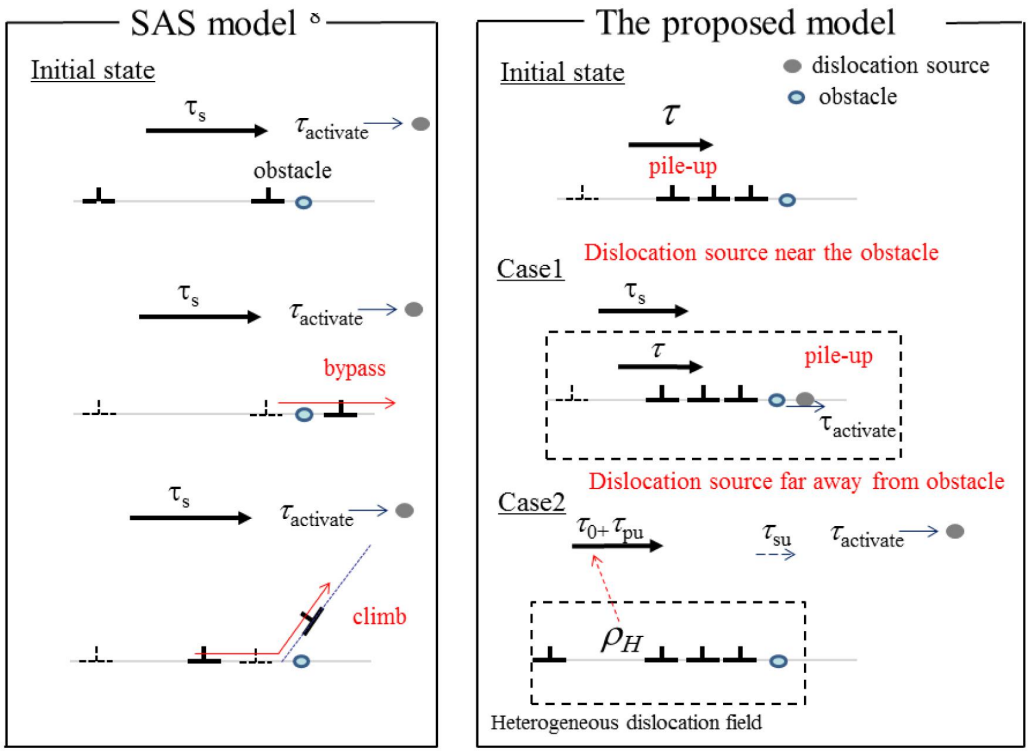

Figure 3-2. Schematic comparing the physical background between the SAS model and proposed model, showing the relative positions of the dislocation source and pile-up. The motion of mobile dislocations at the position of obstacles has two possibilities: first, the mobile dislocations bow and continue going through the obstacle or climb to another slip plane, which is considered by the SAS model [1, 8];

second, the mobile dislocations stop behind the obstacle. If a dislocation source is near the obstacle or is regarded as the obstacle, the concentration shear stress at the tip of the dislocation pile-up would activate the dislocation source, as shown in Case 1 of the proposed model. If the dislocation source is far from obstacles, the back stress from dislocation pile-up τ_{pu} would affect the field stress [13, 14], as shown in Case 2. As there will be almost no dislocations in the low-dislocation-density field, $\rho_L \approx 0$, leading to a back stress from the low-density field of $\tau_{\mathrm{su}} \approx 0$.

In the following analysis, we consider the SAS model's configuration accompanying the already-formed pile-up. Derived from the original Eq. (3.1), we propose two kinds of contributions of the already-formed pile-up: first, in Case 1 where the stress concentration caused by the pile-up activates the dislocation source close to the pile-up; second, in Case 2 where the pile-up contributes to the CRSS of the dislocation source far from the pile-up as the back stress.

A. Case 1:

First, we consider a single arm dislocation source on the slip plane. If the dislocation source is near the tip of the dislocation pile-up, the stress back of the pile-up τ_B [12] is the stress behind the last dislocation of the pile-up, which is similar to the back stress τ_{back} in the SAS model associated with a prior surrounding dislocation density ρ_s, which is extremely small for a micro-pillar ($\rho_s \approx 0$). As shown in Figure 3-2, the applied shear stress τ to the dislocation pile-up region provides the concentration stress at the pile-up tip, and the concentration stress can be the activation stress τ_{activate}. In Case 1 (Figure 3-2), the CRSS should overcome the friction stress and back stress, so it provides the applied shear stress τ to form the stress concentration at the dislocation pile-up tip, which activates the dislocation source. Thus, the CRSS can be expressed as

$$\mathrm{CRSS} = \tau_0 + \tau_{\mathrm{back}} + \tau = \tau_0 + 0.5\mu b\sqrt{\rho_s} + \tau \ . \tag{3.4}$$

According to Eq. (3.3) and $L = m\lambda,\ (m > 0)$ discussed before and according to the literature [1, 12], the applied shear stress to the dislocation pile-up region can be expressed as

$$\tau = k_y \lambda^{-0.5} = Ak\lambda^{-0.5},\ A = \sqrt{\frac{\pi}{32m(1-\nu)}},\ k = \sqrt{2\mu b\tau_p} \ . \tag{3.5}$$

where k is equivalent to the strengthening factor of a polycrystalline material, $k_y = Ak$. Actually, $\tau = \mathrm{CRSS} - \tau_s$ .Then, Eq. (3.4) can be expressed as

$$\mathrm{CRSS} = \tau_0 + 0.5\mu b\sqrt{\rho_s} + Ak\lambda^{-0.5} = \tau_s + k_y\lambda^{-0.5} \ . \tag{3.6}$$

In Eq. (3.6), a Hall–Petch-type relationship, which is strongly affected by the dislocation source length, is observed even in single crystals. The Hall–Petch effect does operate in polycrystalline materials and leads to yield strength scaling as $d^{-0.5}$, where d is the grain size.

Some experts believe that the SAS plays a more important role than other sources in the multiplication of dislocations in micro-dimensional samples[1-3, 5, 6, 8, 15, 16]. The critical stress required to activate the SAS can be taken as $\tau_{\mathrm{C}} = \dfrac{\mu b}{\lambda}$ [1]. In the SAS model, the SAS is activated by the applied stress on the slip plane in Eq. (3.4) ($\tau = \tau_{\mathrm{activate}}$) with $\tau_{\mathrm{activate}} = \tau_{\mathrm{C}} = \dfrac{\mu b}{\lambda}$, and mobile dislocations do not pile up. We accept the SAS condition in the present study. In Eq. (3.6), the CRSS is a function of τ_p , and τ_p is much larger than the applied stress in this field. In finite single-crystal micro-pillars, τ_p should equal the critical stress $\tau_p = \tau_{\mathrm{C}} = \dfrac{B\mu b}{\lambda}(B = 1)$, if a

dislocation source is near the tip of the dislocation pile-up and this source becomes the weakest source to be activated, as shown in Figure 3-2. The statistic mechanics theory [8] calculates $\bar{\lambda}_{\max}$ the maximum distance from these sources to the surfaces, and it uses $\bar{\lambda}_{\max}$ to replace λ. Thus, the critical stress should be written as $\tau_C = \frac{\mu b}{\bar{\lambda}_{\max}}$. Substituting $\tau_p = \tau_C = \frac{\mu b}{\bar{\lambda}_{\max}}$ into Eq. (3.6), we obtain

$$\text{CRSS} = \tau_0 + 0.5\mu b\sqrt{\rho_s} + \frac{\alpha_1 \mu b}{\bar{\lambda}_{\max}}, \alpha_1 = \sqrt{\frac{\pi}{16m(1-\nu)}}. \tag{3.7}$$

B. Case 2

If dislocation sources are far from the tip of the dislocation pile-up on the slip plane, the pile-up exerted is applied on the back stress τ_{back} [16-19]. The stress to activate the dislocation source is the applied stress, similar to the condition of the SAS model shown in Eq. (3.1). By considering the critical condition here, CRSS need not consider τ because it does not affect the activation of the dislocation source. Thus, as shown in Case 2 (Figure 3-2), the CRSS includes τ_0, the back stress from pile-up τ_{pu}, the back stress from surrounding dislocations τ_{su} ($\tau_{\text{back}} = \tau_{\text{pu}} + \tau_{\text{su}}$), and the activation stress τ_{activate}:

$$\text{CRSS} = \tau_s + \tau_{\text{activate}} = \tau_0 + \tau_{\text{back}} + \tau_{\text{activate}} = \tau_0 + \tau_{pu} + \tau_{su} + \frac{\mu b}{\bar{\lambda}_{\max}}. \tag{3.8}$$

where the back stress τ_{back} is the surrounding stress applied on the slip plane[16, 19]. The whole region of the slip plane is divided into two parts: the high-dislocation-density field (the field of dislocation pile-up in this study, with a dislocation density of ρ_H) and the low-dislocation-density field (dislocation density of ρ_L), as shown in Figure 3-2. Thus, we discuss the average effect of the pile-up and treat the pile-up field as a high-dislocation-density field according to the literatures [20, 21]. From this analysis, the average applied field stress τ_s on the slip

plane can be expressed as in the literature [20, 21]:

$$\tau_s = f_H \tau_H + (1 - f_H)\tau_L , \tag{3.9}$$

where τ_H is the applied field shear stress in the high-dislocation-density field, τ_L is the applied field stress in another region, and f_H is the average area fraction of the high-dislocation-density field ($f_H = L/2R$) [20]. The shear stresses of τ_H and τ_L are related to their local dislocation densities [21], which can be obtained according to Feaugas et al. as follows [20]:

$$\tau_H = \tau_0 + 0.5\mu b\sqrt{\rho_H} , \tag{3.10}$$

$$\tau_L = \tau_0 + 0.5\mu b\sqrt{\rho_L} . \tag{3.11}$$

Eq. (3.9) can be rewritten as

$$\tau_s = \tau_0 + (1 - f_H)0.5\mu b\sqrt{\rho_L} + 0.5 f_H \mu b\sqrt{\rho_H} = \tau_0 + \tau_{su} + \tau_{pu} . \tag{3.12}$$

It refers $\rho_L = 0 \sim 10^{12}/\mathrm{m}^2$, $\rho_H = 10^{12} \sim 10^{15}/\mathrm{m}^2$ [21]. There are very few dislocations inside micro-pillars: perhaps one, two, or few. If this limited number of dislocations piles up behind the obstacle, there will be almost no dislocations elsewhere. We set $\rho_L \approx \rho_s \approx 0$ and $\rho_H \approx \rho$, and Eq. (3.12) can be rewritten as

$$\tau_s = \tau_0 + 0.5 f_H \mu b\sqrt{\rho_H} = \tau_0 + \tau_{\mathrm{pu}} . \tag{3.13}$$

In Eq. (3.13), τ_{pu} is the back stress of dislocation pile-up in small volumes regarding length scale effects, the formulation of which is similar to literatures [16, 18-20]. Thus, Eq. (3.8) can be expressed as

$$\mathrm{CRSS} = \tau_0 + \tau_{\mathrm{back}} + \tau_{\mathrm{activate}} = \tau_0 + 0.5 f_H \mu b\sqrt{\rho} + \frac{\mu b}{\bar{\lambda}_{\max}}, f_H = \frac{m\bar{\lambda}_{\max}}{2R} . \tag{3.14}$$

C. General CRSS model to describe single-crystal micro-pillars

When considering one pillar, it is hard to determine whether the obstacle on the slip plane is near the dislocation source. Here, we wish to obtain a general statistical

model to describe the pile-up effect in micro-pillars of one material. By examining a series of micro-pillars of one material, we can consider the average behavior of dislocation pile-up. Thus, we consider both constitutions Eq. (3.7) and Eq. (3.14). When we assume the percent of specimens with dislocation sources far from the obstacle is p (the CRSS is described in Eq. (3.14)), the percent with a dislocation source near the obstacle becomes $1-p$ (the CRSS is described in Eq. (3.7)). In this study, we try to describe the average CRSS of this series of micro-pillars of one material. And the general CRSS model can be shown as

$$\mathrm{CRSS}=\tau_0+pf_H 0.5\mu b\sqrt{\rho}+[(1-p)\alpha_1+p]\frac{\mu b}{\bar{\lambda}_{\max}},\alpha_1=\sqrt{\frac{\pi}{16m(1-\nu)}},f_H=\frac{m\bar{\lambda}_{\max}}{2R}. \tag{3.15}$$

In finite single-crystal micro-samples, which have dimensions on the same order of magnitude as the length of the dislocation sources, the longest source length $\lambda_{\max}$ determines the CRSS required for initiating plastic strain or dislocation multiplication. This effect has been observed in micro-samples[1-3, 5, 6]. As shown in Figure 3-1a, the slip plane is an ellipse with the major axis $R_1=R/\cos\phi$ and the minor axis R. If the dislocation pins are distributed randomly on this slip plane with width $\mathrm{d}r$ (the width of the shadowed area), the statistical mechanics method in the SAS model can be used. Thus, the mean and standard deviation of the longest effective source length can be given as [1]

$$\begin{aligned}\bar{\lambda}_{\max}&=\int_0^R\lambda_{\max}p(\lambda_{\max})\mathrm{d}\lambda_{\max}=\int_0^R\lambda_{\max}[1-\frac{\pi(R-\lambda_{\max})(R_1-\lambda_{\max})}{\pi R_1R}]^{n-1}\\&\times(\frac{\pi[(R-\lambda_{\max})+(R_1-\lambda_{\max})]}{\pi R_1R})n\,\mathrm{d}\lambda_{\max}.\end{aligned} \tag{3.16}$$

$$\begin{aligned}S_{\lambda_{\max}}&=[\int_0^R\lambda_{\max}^2p(\lambda_{\max})\mathrm{d}\lambda_{\max}-\bar{\lambda}_{\max}^2]^{1/2}\\&=[\int_0^R\lambda_{\max}^2[1-\frac{\pi(R-\lambda_{\max})(R_1-\lambda_{\max})}{\pi R_1R}]^{n-1}\times(\frac{\pi[(R-\lambda_{\max})+(R_1-\lambda_{\max})]}{\pi R_1R})n\mathrm{d}\lambda_{\max}-\bar{\lambda}_{\max}^2]^{1/2}.\end{aligned} \tag{3.17}$$

where the number of pins n depends on the sample dimensions and the initial dislocation density [1], and n can be given by

$$n=\text{Integer}[\rho_{mob}\frac{\pi R^2 h}{L_{seg}}],\ \rho_{mob}=\frac{\rho}{s}. \tag{3.18}$$

where ρ and ρ_{mob} are the total and mobile initial dislocation densities, respectively, h is the specimen height, L_{seg} is the average length of the dislocation segments, and s is the number of slip systems. We selected ϕ=51° for the loading axis direction of [126], s=12 for face-centered cubic (fcc) crystals, $L_{\text{seg}}=R$, and h=2.5R [1, 8, 15]. Moreover, to distinguish micro-pillars from metal whiskers that contain fewer dislocations and can be treated as ideal crystals, we assumed the samples had a dislocation density of 10^{12}–10^{13} /m^2 and took the lower bound for n to be unity.

3.1.2 Discussion for pile-up effect

Because of the concentrated stress around the tip of pile-up dislocations, the stress at the tip τ_p is larger than the applied stress τ on the slip plane. In Case 1 of our model, τ_p will activate the SAS and is $\tau_p=\tau_{\text{C}}=\frac{\mu b}{\bar{\lambda}_{\max}}$. In this case, the applied stress τ is smaller than $\frac{\mu b}{\bar{\lambda}_{\max}}$ because of the stress concentration. According to Eqs. (3.4), (3.7), and (3.15), the parameter m must be over 0.28 because dislocation pile-up must be effective in the samples: in the condition $[(1-p)\alpha_1+p]\frac{\mu b}{\bar{\lambda}_{\max}}\le\frac{\mu b}{\bar{\lambda}_{\max}}$, then $\alpha_1\le 1$, $m\ge 0.28$, where $\frac{\mu b}{\bar{\lambda}_{\max}}$ is the stress to activate the dislocation source in the SAS model in Eq. (3.1) [1, 8]. If $m<0.28$, the SAS model should be considered.

At first, we used a least-squares method with Eq. (3.15) to simulate the characteristics of Au, Cu, Al, and Ni and found the values of (p, m) for them with the

conditions of $0 \le p \le 1$ and $m>0$, where p is the percent of of specimens with dislocation sources far from the pile-up. From Eqs. (3.15) and (3.16), we get the functions of $\overline{\lambda}_{\max} = \overline{\lambda}_{\max}(R)$ and $\mathrm{CRSS} = \mathrm{CRSS}(p, m, \overline{\lambda}_{\max})$, respectively. Thus, we get $\mathrm{CRSS} = \mathrm{CRSS}(p, m, R)$. The least-squares value y can be obtained as

$$y = \sum_i (\mathrm{CRSS}(p, m, R_i) - \mathrm{CRSS}_i)^2 \quad n = \mathrm{Integer}[\rho_{mob} \frac{\pi R^2 h}{L_{seg}}], \ \rho_{mob} = \frac{\rho}{s}, \tag{3.19}$$

where CRSS_i is the experimental data and R_i is the corresponding radius of the experimental data. Then, (p, m) can be obtained using the following method:

$$\begin{cases} \dfrac{\partial y}{\partial p} = 0 \\ \dfrac{\partial y}{\partial m} = 0 \end{cases}, \ 0 \le p \le 1 \text{ and } m > 0 . \tag{3.20}$$

We selected the parameters used here from the literatures [1, 3, 8, 10, 22-27]: $\rho = 4 \times 10^{12}/\mathrm{m}^2$; τ_0 = 11 MPa (Ni), 13 MPa (Au), 10 MPa (Al), 12 MPa (Cu); $\nu = 0.3$; s=12; h=2.5R; μ=76 GPa (Ni), 27 GPa (Au), 48 GPa (Cu), 32.7 GPa (Al); b=0.24 nm (Ni), 0.288 nm (Au), 0.283 nm (Al), 0.361 nm (Cu). The obtained (p, m) are Au (0.47, 1.62), Cu(0.58, 0.89), Al(0.67, 0.35), and Ni(0.99, 0.002). Figure 3-3 shows the relationships between the stacking fault energy (SFE) [3] and the parameters m and p. For fcc crystals, materials with low SFE more easily exhibit dislocation pile-up. This behavior suggests that a smaller SFE corresponds to a larger m in Eq. (3.15), as shown in Figure 3-3a. Because Au has a lower SFE (0.06 J/m^2) than Ni (0.40 J/m^2), the dislocation pile-up effect is more likely in Au than in Ni, and this suggests there would be more dislocation pile-ups in Au than in Ni. The value p of Au should be smaller than that of Ni, which is shown in Figure 3-3b. In Figure 3-3 the value p of Ni is 0.99 nearly equal to 1, and m is much smaller than 0.28; that is, there is no source

near the pile-up and almost no pile-up effect inside the pillar. Experiments by Frick et al [28]. showed no evidence of dislocation pile-ups in compression studies of Ni micro- and nano-pillars ranging from 160 nm to 2000 nm in diameter. In other words, Eq. (3.15) cannot be applied to Ni; the SAS model should be used. Consequently, the pile-up SAS model of Eq. (3.15) can be used to describe the yield strength of a material with a strong dislocation pile-up effect, especially for materials with low SFE such as Au and Cu. In Figure 3-3a, there is a line at m=0.28. If the material has a larger m, the pile-up SAS model should be used; if not, the SAS model should be used. From the previous discussion, once these formulations of the proposed model are established, their parameters (p, m) must be fixed when applying the models to the specific material, and we believe that the results obtained in Figure 3-3 support the applicability of our proposed model.

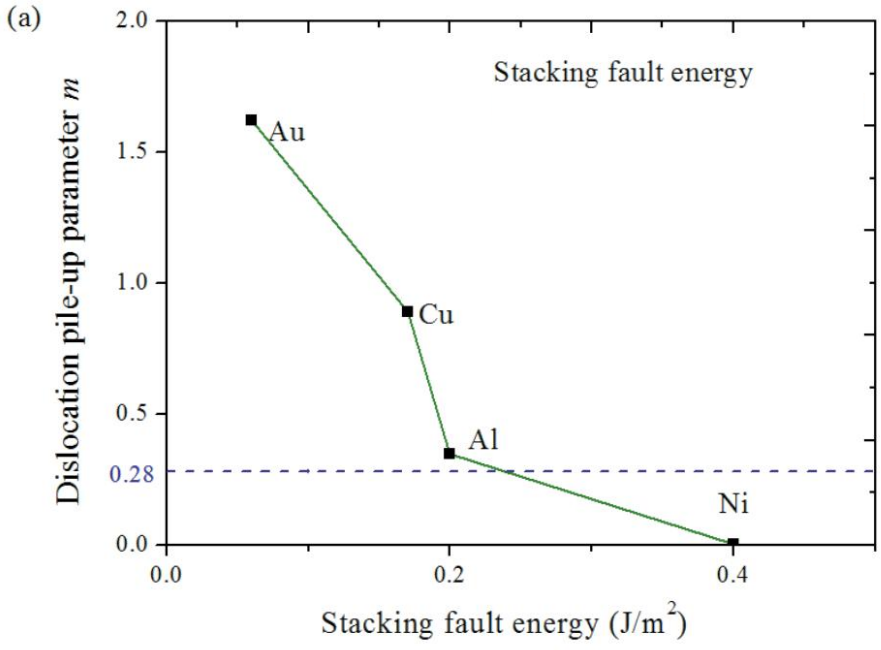

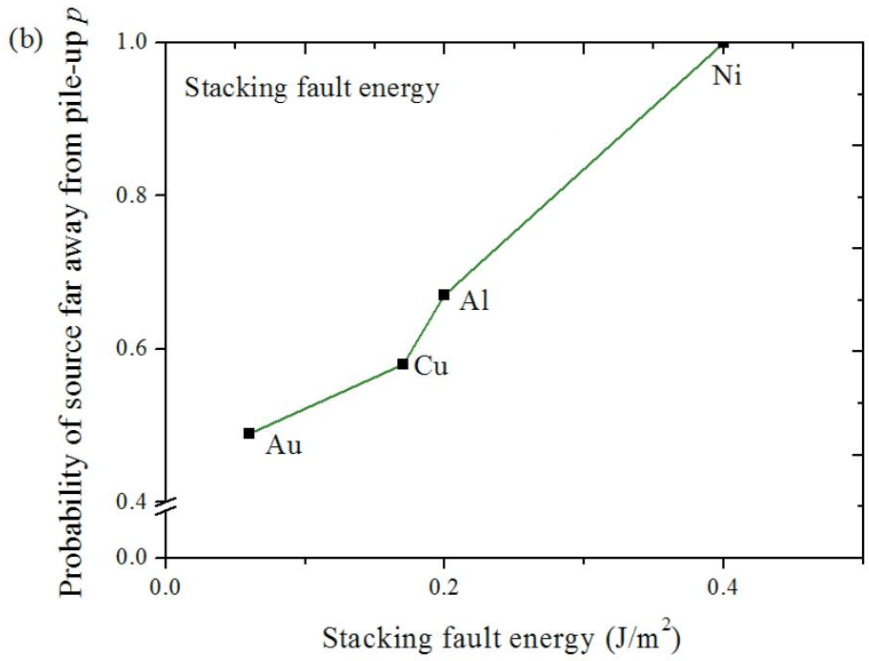

Figure 3-3. Relationship among the stacking fault energy and the parameters *m* and *p*; (a) the corresponding relation of the dislocation pile-up parameter *m*; (b) the corresponding relation of the probability of the source being far from the pile-up *p*.

3.1.3 Size effect of the single crystal micro-pillars

Figure 3-4 plots the experimental data reported so far [10, 22, 23], the predictions of our pile-up SAS model shown in Eq. (3.15), and those of the original SAS model. The predicted critical results were based on $\overline{\lambda}_{\max}$, and the upper and lower bounds were based on ($\overline{\lambda}_{\max} - S_{\lambda_{\max}}$) and ($\overline{\lambda}_{\max} + S_{\lambda_{\max}}$). Equations (3.13) to (3.15) indicate that the CRSS for a finite micro-sample depends on the number of pins *n*, the length of dislocation pile-ups *L*, and the initial dislocation density ρ. The influence of the initial dislocation density ρ has been sufficiently discussed in the literature [1, 8, 15]. In Figure 3-4a, our pile-up SAS model agrees better than the original SAS model with the experimental data; that is, our pile-up SAS model gives a more precise prediction. Also, compared the computational results of Au, the interval predicted by our model

is narrower than that predicted by the original SAS model. For Au, our pile-up SAS model is more suited to describing the size-dependent strength of the micro-pillars. As shown in Figure 3-4a and 3-4b, the size-dependent CRSS depends on the number of dislocation sources and the effective length of dislocation source. When the size is large enough, the effective length of the dislocation source would become large, as shown in Figure 3-4b, making the CRSS constant according to Eq. (3.15). For Ni, the original SAS model should be used, as demonstrated in Figure 3-4c and d. In micro-pillars, the pile-up field can form in the Au specimen, but hardly in the Ni specimen.

Figure 3-5 shows the predictions from our pile-up SAS model and the original SAS model for Al and Cu micro-pillars. For the Cu specimens, our pile-up SAS model agrees better than the original SAS model with the experimental data, showing that our pile-up SAS model gives a more precise prediction. The effective length of the dislocation source affects the size-dependent CRSS in Figure 3-5b and 3-5d. For the Al specimens, there is little difference between our pile-up SAS model and the original SAS model.

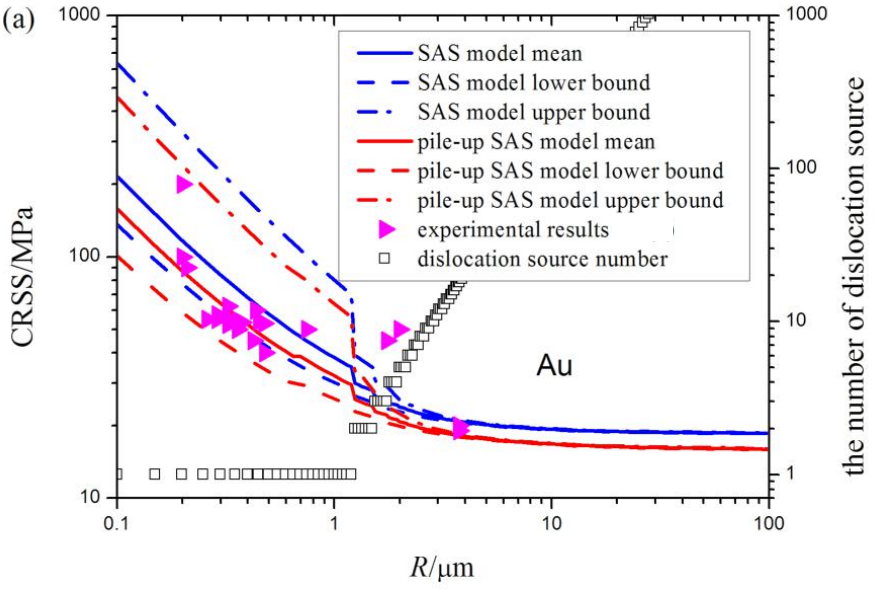

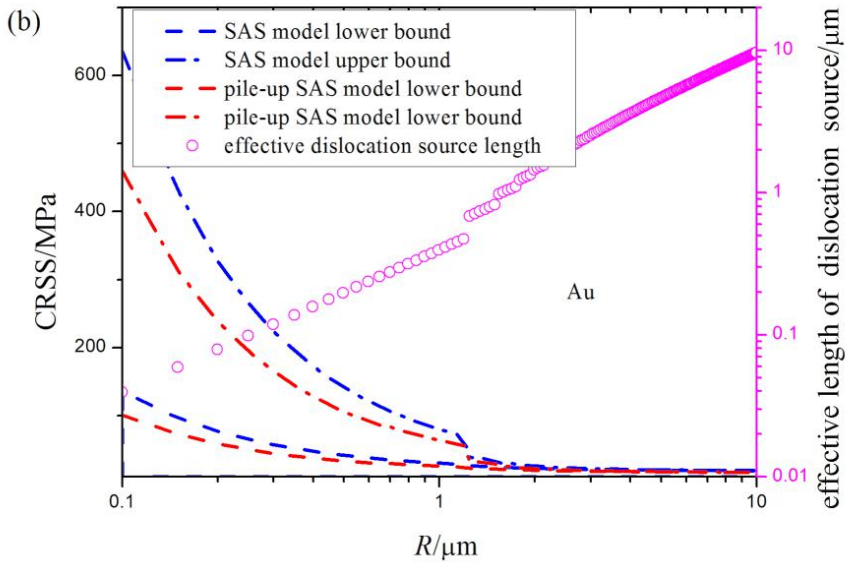
(b)
SAS model lower bound
SAS model upper bound
pile-up SAS model lower bound
pile-up SAS model lower bound
effective dislocation source length
Au
CRSS/MPa
effective length of dislocation source/μm
R/μm
600
400
200
10
1
0.1
0.01
0.1
1
10

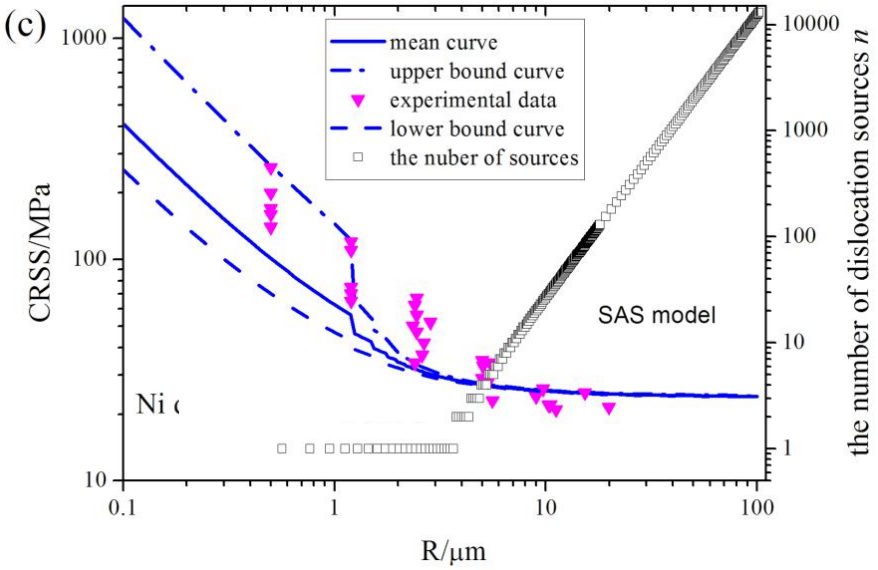
(c)
mean curve
upper bound curve
experimental data
lower bound curve
the nuber of sources
SAS model
Ni
CRSS/MPa
the number of dislocation sources n
R/μm
1000
100
10
10000
1000
100
10
1
0.1
1
10
100

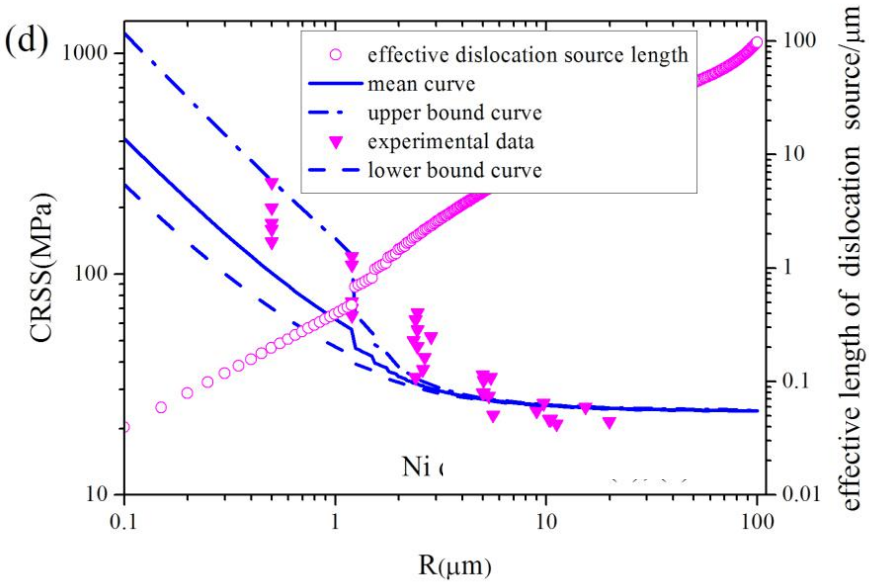

Figure 3-4 Experimental data of Au and Ni with 0.2% plastic strain and the yield stress predicted by our proposed model. The mean, upper, and lower bound curves correspond to $\overline{\lambda}_{\max}$, ($\overline{\lambda}_{\max} - S_{\lambda_{\max}}$), and ($\overline{\lambda}_{\max} + S_{\lambda_{\max}}$).

Figures 3-4 and 3-5 show sudden drops in the CRSS at a sample radius of ~1.2 μm. According to the models shown by Eqs. (3.15), (3.16), and (3.18), the number of pins stays at unity at a sample radius below 1.2 μm. Figures 3-4 and 3-5 show that the strength obviously increases by decreasing the radius below 1.2 μm. In other words, the size effect is obvious when the radius is below 1.2 μm, but not obvious when the radius is more than 1.2 μm. However, in Parthasarathy's model [1], the integer number of dislocation pins was not obtained, so there was no sudden drop in their plotted curves. Compared with the predictions in Figures 3-4 and 3-5 based on our pile-up SAS model, the size effect of the yield stress is more obvious when the number of pins is unity. Figures 3-4 and 3-5 indicate that, with increasing sample radius, the number of dislocation sources increases and the yield strength deceases. Thus, the size-dependent yield stress depends on the number of sources. According to Eqs. (3.13), (3.14), and (3.16), the number of dislocation sources decreases as the

sample size decreases, so the starvation of dislocation sources is one reason for the observed size effect. Moreover, with fewer dislocation sources, dislocation multiplication becomes more difficult, and dislocations will tend to slip to the surface. This discussion agrees well with dislocation starvation theory [1, 8, 10, 24].

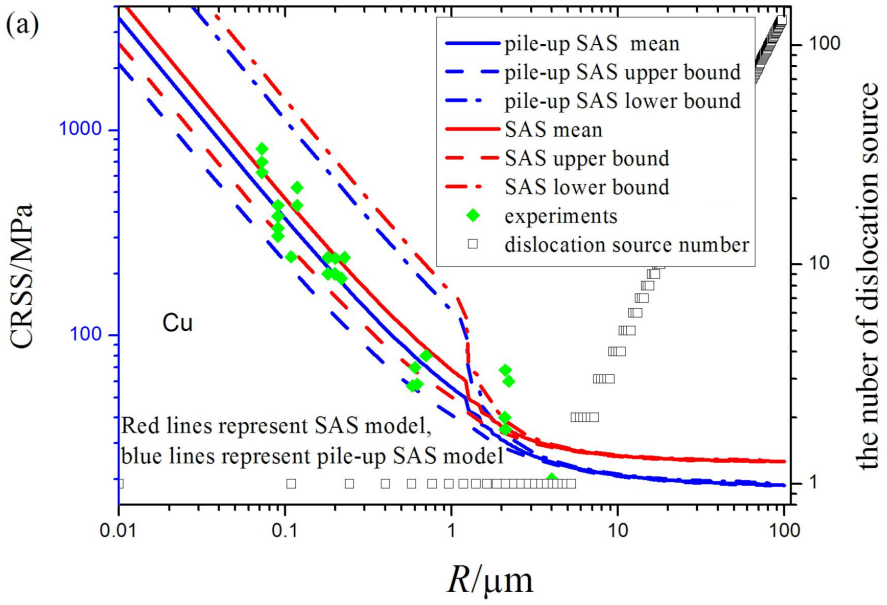

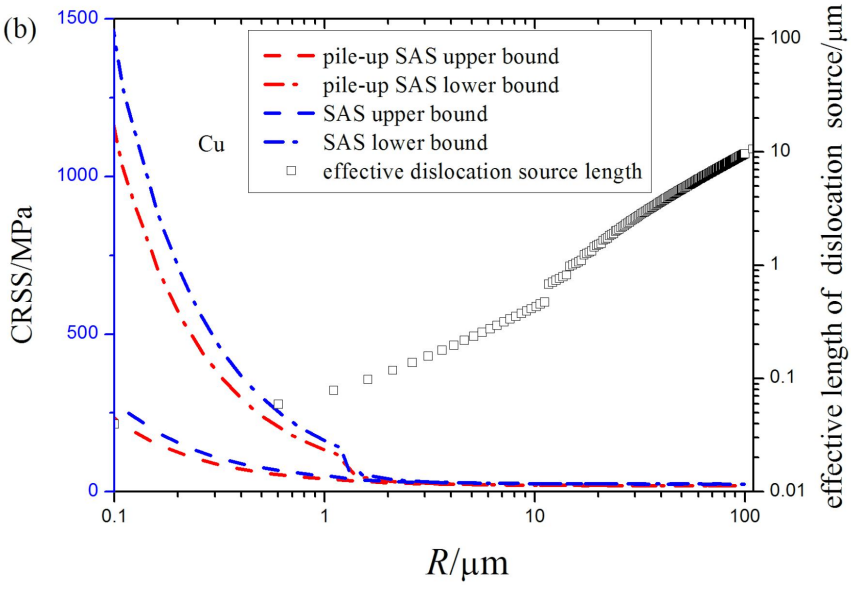

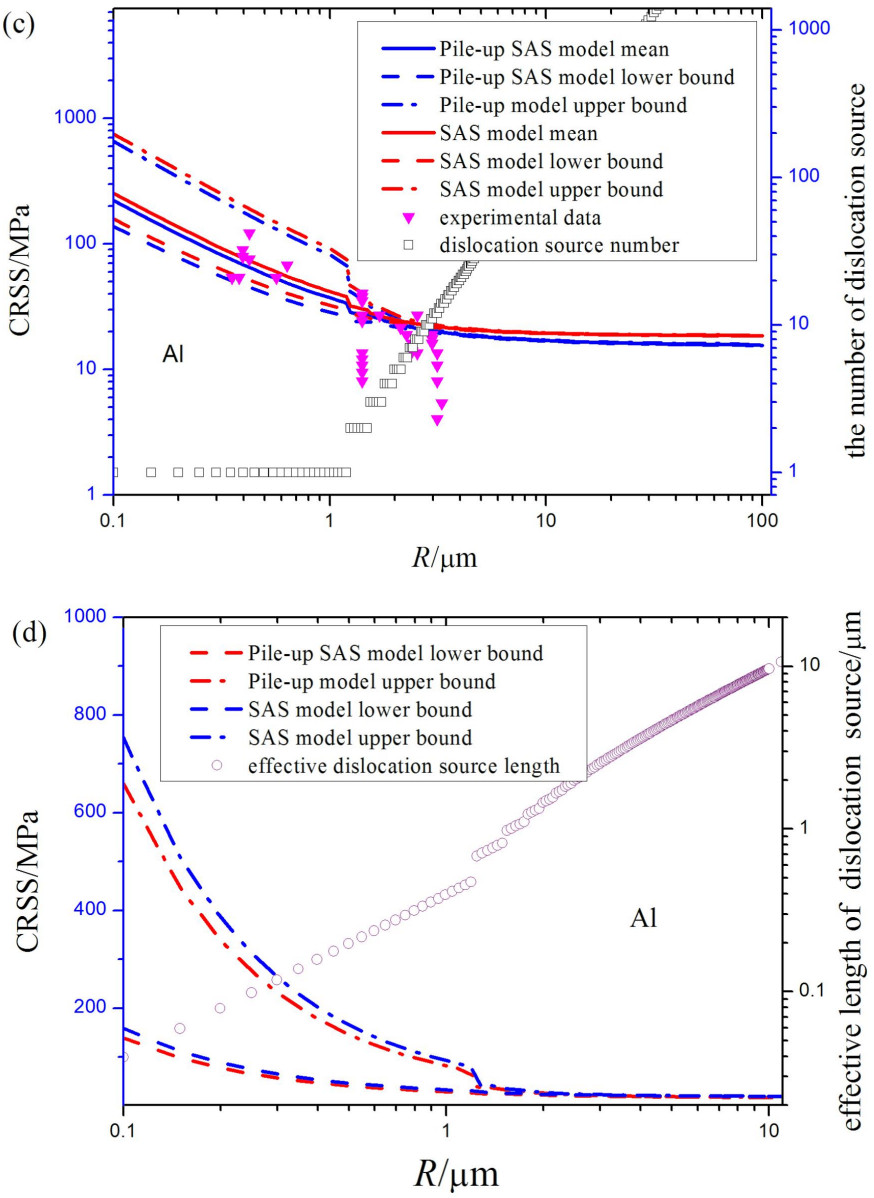

Figure 3-5 Experimental data of Al and Cu with 0.2% plastic strain and the yield stress predicted by various models. The mean, upper, and lower bound curves correspond to $\overline{\lambda}_{\max}$, ($\overline{\lambda}_{\max} - S_{\lambda_{\max}}$), and ($\overline{\lambda}_{\max} + S_{\lambda_{\max}}$).

When the dislocations distribute near the surface, the image stress would drive the dislocations to the surface. This is one explanation of the theory of dislocation starvation. For micro-pillars, it is reasonable that plasticity commences via the activation of internal dislocation sources [1, 8] (i.e., single-arm or Frank–Read

sources) rather than surface sources [29, 30]. Sun et al. investigated the small-scale effect of image force and showed that the image stress for dislocations within 20–30 nm from the free surface is stronger than the applied stress [4]. Thus, most of dislocations inside the micro-pillars are less affected by the image stresses.

3.2 Surface energy effect on the size dependent strength

3.2.1 Modeling on the surface energy

All of the recent experimental and theoretical research on the size effect of micro- and nanopillars show that the critical resolved shear stress (CRSS) results from inner defects, including back stresses from the interactive effect among the dislocations and the activation stress of dislocation sources [3, 16, 22, 31-34]. The CRSS that is the main result of inner defects, as reported in the literature [1, 31], is usually represented as the inner stress, σ^{inner}. Besides all of the inner defect factors, the surface energy can also play a role in the yield stress of micro- or nanopillars, where the stress induced by the surface energy is expressed as $\sigma^{surface}$ [35], and a schematic of this physical description is shown in Figure 3-6. For the case of uniaxial stress state, the total stress σ ($\sigma = \mathrm{CRSS} / SF$, SF is the Schmid Factor) equal to the external stress is the summation of σ^{inner} and $\sigma^{surface}$. Thus, the total stress can be written as

$$\sigma=\sigma^{inner}+\sigma^{surface}. \tag{3.21}$$

If the external stress is equal to zero, $\sigma^{surface}$ can be regarded as the residual stress that influences inner defects. In conventional solid mechanics, the yield strength is determined by the phenomenological theory [31], which doesn't involve the defects inside the pillars. Recently, σ^{inner} has been expressed by the inner defects in the SAS model as [1, 15, 31, 36]. Even the pile-up SAS model has been reported by Pan et al [3] and stated in Chapter 2, in this section the original SAS model will be chosen

in order to estimate the surface energy effect and compare with the existing theoretical models:

$$\sigma^{inner} = (\frac{\alpha\mu b}{\bar{\lambda}_{\max}} + \tau_0 + 0.5\mu b\sqrt{\rho_0}) / SF,\ \alpha = \sqrt{\frac{\pi}{16(1-\nu)}}, \tag{3.22}$$

where μ is the shear modulus, v is Poisson's ratio, b is the magnitude of the Burgers vector, τ_0 is the Peierls-Nabarro force, $\bar{\lambda}_{\max}$ is the longest of the effective average lengths of dislocation sources (λ), and ρ_0 is the initial dislocation density. The SAS model has included the characteristic length of the defects $\bar{\lambda}_{\max}$ inside the pillars, which leads to the size-dependent mechanical properties. This model can be treated as an effective method to explain the size-dependent σ^{inner} in micro-pillars [3, 31]. The detailed process used to obtain $\bar{\lambda}_{\max}$ is given in Ref. [1, 3], and the number of pins, n, is related to the sample dimensions and the initial dislocation density [1, 3].

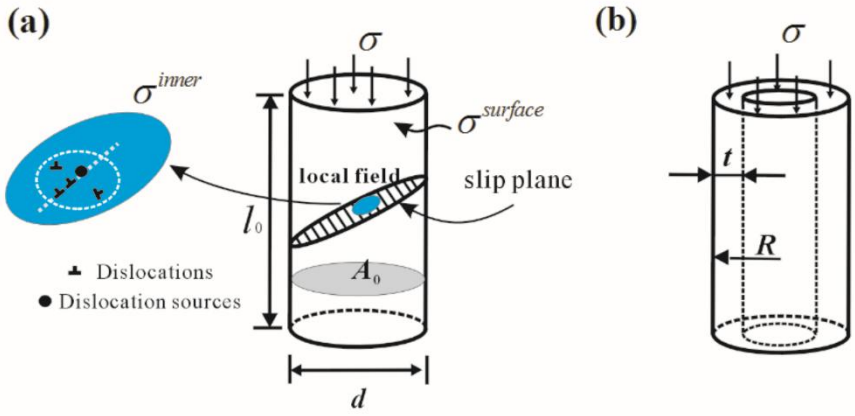

Figure 3-6. Schematics of the micro-pillar model. (a) Components of the stress state that considers the effects from both the surface and the inner defects. (b) Cylindrical hollow pillar with diameter d and thickness t.

In Figure 3-6, the length of the pillar in a longitudinal direction is l_0 and the current length of the deformed configuration l_1 is equal to $l_0 + \Delta l$, where Δl is the small elastic deformed increment of the length, and so the engineering strain can be expressed as $\varepsilon = (l_1 - l_0)/l_0$. As shown in the schematic sketch of the hollow pillars in

Figure 3-6b, the tensile rigidity D_0 should be considered as follows:

$$D_0=EA_0 = E\frac{\pi d^2 - \pi(d-2t)^2}{4} = E\pi(2Rt - t^2)\,, \tag{3.23}$$

where E is the elastic moduli, A_0 is the initial section area, d is the pillar diameter, R (=d/2) is the pillar radius and t is the thickness.

The yield stress is the critical stress between the elastic response and the plastic response of a material. Therefore, just before the critical yield condition, the material responses the linear elastic deformation and the strain energy can be written as a quadratic form. The total potential energy is estimated by Π , which is

$$\Pi = U_e + U_s - W\,, \tag{3.24}$$

where U_e is the elastic strain energy, U_s is the surface energy and W is the work done by the external force P. The elastic strain energy is estimated by

$$U_e = \int_v \int_0^{\varepsilon_{ij}} \sigma_{ij}\mathrm{d}\varepsilon_{ij}\mathrm{d}v = \frac{1}{2}D_0\varepsilon^2 l_0\,, \tag{3.25}$$

where v is the volume of the specimen in current state. And the total surface energy is approximated by

$$U_s = \gamma S\,, \tag{3.26}$$

where γ is the surface energy density and S is the surface area. Because the surface area is described by $S = S_0 + O_0\varepsilon l_0(1-\nu)$ under the isotropic assumption, following Ref. [35], Eq. (3.26) can be developed as

$$U_S = \gamma S_0 + \gamma O_0\varepsilon l_0(1-\nu)\,. \tag{3.27}$$

where O_0 is the perimeter of the initial cross-section and S_0 is the initial surface area. The work done by the external force P is given by displacement u

$$W = Pu = P\varepsilon l_0\,. \tag{3.28}$$

By substituting Eqs. (3.25), (3.27) and (3.28) into Eq. (3.24), the total potential energy

can be expressed as

$$\Pi = \frac{1}{2} D_0 \varepsilon^2 l_0 + \gamma S_0 + \gamma O_0 \varepsilon l_0 (1-\nu) - P\varepsilon l_0 . \tag{3.29}$$

Based on the principle of minimum potential energy, the final equilibrium state is determined by $\partial \Pi / \partial \varepsilon = 0$ with ignoring the high order small term including ε^2, according to the framework of Figure 3-6, the strain ε here can be expressed as

$$\varepsilon = (P - \gamma O_0 (1-\nu)) / EA_0 = \frac{P}{EA_0} - \frac{\gamma O_0 (1-\nu)}{EA_0} . \tag{3.30}$$

If the deformation is elastic, the term (P / A_0) is considered as the total external stress σ, and Eq. (3.30) can be rewritten as

$$\varepsilon = \frac{\sigma}{E} - \frac{\gamma O_0 (1-\nu)}{EA_0} . \tag{3.31}$$

If $\sigma = 0$, the strain in Eq. (3.31) will be in a compressive state owing to the residual surface strain. Based on Eqs. (3.23) and (3.31), σ can be obtained as $\sigma = E\varepsilon + \gamma O_0(1-\nu)/\pi(2Rt-t^2)$. In this study, the compressive strength and tensile strength are assumed to be equal ($\left|\sigma_{\text{compressive}}\right| = \left|\sigma_{\text{tensile}}\right| = \sigma$).Because the surface energy is independent of the elastic strain energy, the surface stress is equal to $\gamma O_0(1-\nu)/\pi(2Rt-t^2)$, and the first term $E\varepsilon$, therefore, represents the inner defects σ^{inner} of Eq. (3.21). The term σ^{inner} has been represented as that shown in Eq. (3.22) when the material is in the yield state, and the final model would be

$$\sigma = \sigma^{inner} + \sigma^{surface} = (\frac{\alpha \mu b}{\overline{\lambda}_{\max}} + \tau_0 + 0.5\mu b\sqrt{\rho_0}) / SF + \frac{\gamma O_0 (1-\nu)}{\pi(2Rt - t^2)} . \tag{3.32}$$

This demonstrates that the yield stresses would be affected by n, $\overline{\lambda}_{\max}$ and $\sigma^{surface}$. According to Cammarata [36], the surface stress tensor $\sigma_{ij}^{surface}$ is related to the surface energy density γ and the surface strain tensor $\varepsilon_{ij}^{surface}$ by

$$\sigma_{ij}^{surface} = \gamma\delta_{ij} + \frac{\partial\gamma}{\partial\varepsilon_{ij}^{surface}}. \tag{3.33}$$

The surface stress tensor can also be expressed in an alternative definition of the surface elasticity that is consistent with Eq. (3.33) [37, 38]

$$\sigma_{ij}^{surface} = \gamma\delta_{ij} + \frac{\partial\gamma}{\partial\varepsilon_{ij}^{surface}}\bigg|_{\varepsilon_{ij}^{surface}=0} + S_{ijkl}\varepsilon_{kl}^{surface}, \tag{3.34}$$

where S_{ijkl} is the fourth-order surface elastic tensor, which can be determined by atomistic simulations or experiments [38, 40]. For the uniaxial deformation of micro- and nanopillars, the stress component mainly related to the external force is only the normal stress to the surface, and so the surface stress tensor in Eqs. (3.33) and (3.34) can be expressed as the scalars:

$$\sigma^{surface} = \gamma + \frac{\partial\gamma}{\partial\varepsilon^{surface}}, \tag{3.35}$$

$$\sigma_{ij}^{surface} = \gamma\delta_{ij} + \frac{\partial\gamma}{\partial\varepsilon_{ij}^{surface}}\bigg|_{\varepsilon_{ij}^{surface}=0} + S_{ijkl}\varepsilon_{kl}^{surface}, \tag{3.36}$$

where E^s is the surface elastic modulus in the crystalline orientation direction normal to the surface of the pillar. In Eq. (3.32), the surface stress can be expressed as $\sigma^{surface} = \gamma[O_0(1-\nu)/\pi(2Rt-t^2)] = \gamma B_1$. Linking this equation to Eq. (3.35), we can obtain

$$\gamma B_1 = \gamma + \frac{\partial\gamma}{\partial\varepsilon^{surface}}. \tag{3.37}$$

Therefore, the surface energy density can be obtained as

$$\gamma = Ce^{(B_1-1)\varepsilon^{surface}}, \tag{3.38}$$

where the C is a constant of integration. Before the external force and/or damage is applied on the surface, the residual surface strain $\varepsilon_0^{surface}$ is related to the initial

surface energy density. Inserting Eq. (3.38) into Eq. (3.36) and taking the surface strain to be in the state of the initial condition without external outside damage, we can obtain the parameter C such that

$$C = \frac{E^s \varepsilon_0^{surface}}{(B_2 - 1)(B_1 - 1)}, \tag{3.39}$$

where B_2 = exp [(B_1-1) $\varepsilon_0^{surface}$]. In this way, the surface energy density can be expressed as

$$\gamma = \frac{E^s \varepsilon_0^{surface}}{(B_2 - 1)(B_1 - 1)} e^{(B_1-1)\varepsilon^{surface}}, \tag{3.40}$$

where the parameters E^s , B_1 and B_2 are only geometric and material characteristics, and have no relationship with the external force and/or damage.

3.2.2 Inner defects and surface stress of hollow pillars

The parameters for Cu pillars used in Figures 3-7, 3-8 and 3-9 are selected from Refs. [32-35] and are summarized in Table 3-1, and the crystallographic orientation normal to the pillar surface is set to [1 2 6] [3]. Figure 3-7 shows the relationship between the yield stress given by Eq. (3.32) and the thickness t of a Cu pillar whose radius R is 0.35 μm. As derived from Eq. (3.32) for a pillar with a constant diameter, it can be observed that the stress is larger with a small value of t than that with a large value of t. The same mechanics can be found in Figures. 3-8 and 3-9, which show identical plots of the CRSS ($=\sigma \cdot SF$) as a function of radius for Cu hollow micro- and nanopillars with varying wall thicknesses, wherein the CRSS decreases as the pillar radius R ($=d/2$) increases and a particularly sudden drop in the CRSS can be seen at a radius of approximately 1.2 to 2 μm. Examining the detailed process used to obtain $\bar{\lambda}_{\max}$ [3], Figure 3-8a also plots the number of dislocation sources in the pillars, which

remains at unity until the sample radius is greater than the critical size 1.2 to 2 μm. Therefore, this discontinuity is due to the transition from the unity to the continuous change. Further, Figure 3-8b shows that, when the radius reaches the critical size 1.2 to 2 μm, the $\bar{\lambda}_{max}$ suddenly increases, which is caused by the same reason.

Table 3-1. Parameter values used in the simulations

Parameters	Values
τ_0 (MPa)	7 (Al)[1], 11 (Ni)[2], 12 (Cu)[3]
ν	0.33
μ (GPa)	26.25 (Al)[1], 76 (Ni)[2], 48 (Cu)[3]
b (nm)	0.25 (Al)[1], 0.24 (Ni)[2], 0.26 (Cu)[3]
γ (J/m^2)	1.2 (Al)[1], 90 (Ni)[2], 1.6 (Cu)[3]
ρ_0	2×10^{12} /m^2

[1]Ref. [8, 26, 38, 41, 42]; [2]Ref. [2, 3, 43]; [3]Ref. [32-35]

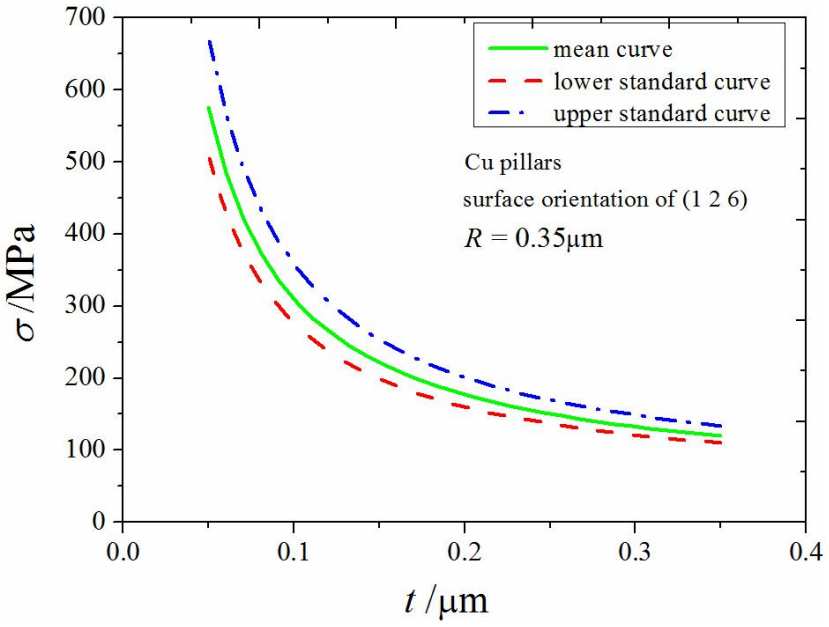

Figure 3-7. Theoretical relationship between yield stress (σ) and thickness (t) of a Cu hollow micro/nanopillar. The mean, upper and lower standard deviation curves

correspond to $\overline{\lambda}_{\max}$, ($\overline{\lambda}_{\max} - S_{\lambda_{\max}}$), and ($\overline{\lambda}_{\max} + S_{\lambda_{\max}}$), respectively, where $S_{\lambda_{\max}}$ is the standard deviation [1, 3].

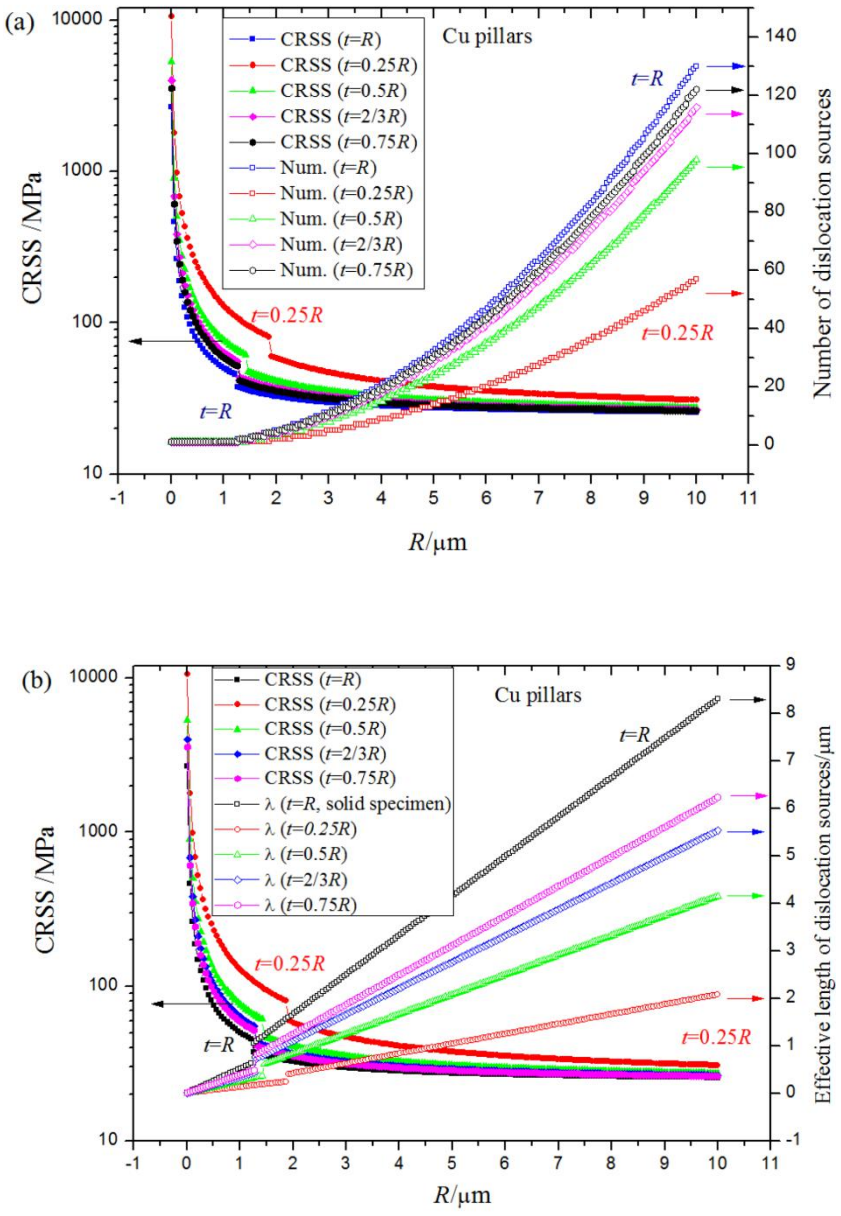

Figure 3-8. Relationship between the critical resolved shear stress (CRSS) and dislocation source number and effective length as a function of pillar radius. The effect of the inner surface (t) and size (R) of a hollow Cu micro/nanopillar upon its CRSS plotted along with the varying (a) number of dislocation sources and (b)

effective dislocation length of the dislocation sources. Solid marked lines represent CRSSs with different thicknesses t, and hollow marked lines represent the number of dislocation sources and effective length of dislocation sources with different thicknesses t, respectively.

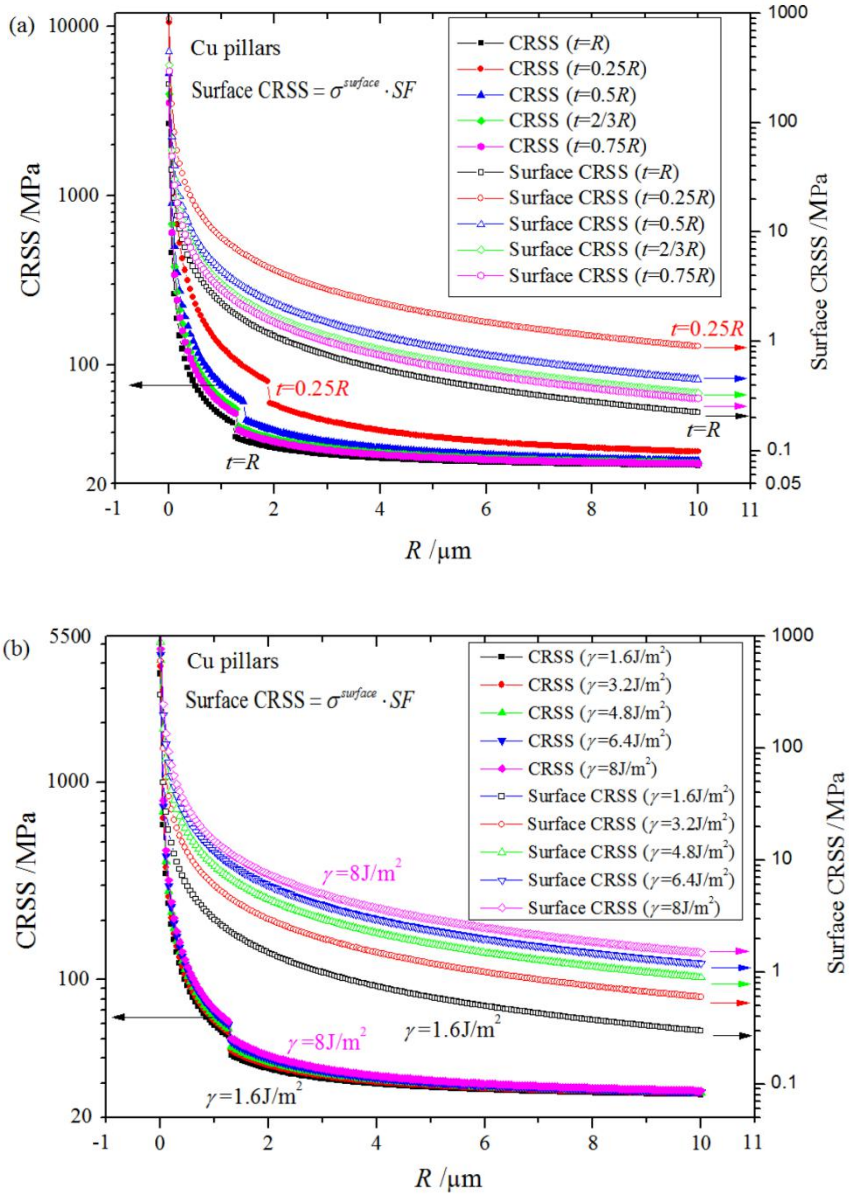

Figure 3-9. Relationship between the CRSS and the surface CRSS as a function of pillar radius. The critical resolved shear stress (CRSS) and the surface CRSS as a function of the pillar radius for (a) varying hollow pillar thicknesses and (b) varying

surface energy densities. Solid marked lines represent CRSSs and hollow marked lines represent the surface CRSSs ($\text{Surface CRSS} = \sigma^{surface} \cdot SF$) accompanying with different thickness t in (a) and with different surface energy densities γ in (b).

In Figure 3-8a, the pillars with a small value of t have fewer dislocation sources (n) than those with the same radius and larger t values. The variance of t (in the surface stress term) is accompanied by an across area variance, which means that the distribution of dislocation sources in σ^{inner} will be varied according to Ref. [3]. In Figure 3-8b, as was previously discussed, the increase of t is accompanied by a decrease of CRSS and an increase of $\overline{\lambda}_{\max}$, wherein the increase of $\overline{\lambda}_{\max}$ can cause a decrease of the σ^{inner} according to Eq. (3.32). The boundary/surface can truncate double-pinned Frank-Read sources and transform them into the single-arm sources, where the length of λ is the distance from the pin (dislocation) to the nearest surface [3]. When t is small, the two adjacent surfaces can effectively shorten the length of λ, which is to say, the boundary of the pillars limits the space to distribute λ. According to the discussion above, the variance of t affects the inner defects including n and $\overline{\lambda}_{\max}$ and acts on σ^{inner}. As a result, the variance of $\sigma^{surface}$ resulting from the varying t changes both σ^{inner} and σ, which is the reason why the yield stress of hollow pillars is larger than that of solid pillars, as shown in Figures 3-7 and 3-8.

Figure 3-9a shows that increasing the surface area of the Cu hollow pillars (i.e., decreasing t) corresponds with an increasing value of $\sigma^{surface}$, which comprises 4 to 6% of the total stress (i.e., σ of Cu solid pillars) in pillars with radius values of R = 1 to 4 μm with the value of γ = 1.6 J/m^2 [35]. In the subsequent comparison of these numerical results with experiments (refer to Figure 3-10), $\sigma^{surface}$ is found to provide nearly 10% of the total stress for Al solid pillars whose surface energy with R = 1 to 4

μm has a recommended value of γ = 1.2 J/m^2 [41, 42], and can provide over 50% of the total stress for the Ni solid pillars whose surface energy with R = 1 to 4 μm has a recommended value of γ = 90 J/m^2 [43]. That is to say, $\sigma^{surface}$ is important for describing the size-dependent yield stress. At present, there are less studies employed on the surface energy measurement of micro- and nanopillars to provide the exact values. Some studies focus on the surface effect by setting the surface energy empirically such as ref. [35, 43]. Actually, the surface energy densities of Ni between Refs. [41] and [43] are different. Therefore, the sensitivity analysis of surface energy densities is conducted to study the trends of surface energy effect in Figures 3-9b and 3-10. In Figure 3-9b, it is obvious that the surface stress value of the Cu hollow pillars can be made large by increasing the surface energy and, when the radius approaches 10 μm, all of the CRSSs for different surface energies are around the same value. All of these results mean that the proposed model can express the size-dependent characteristics of micropillars. The percent of surface stresses corresponding to total stresses of the Cu pillars whose radii R = 0.5, 2 and 10 μm are shown in Table 3-2, where it can be seen that the surface stress in small specimens has a large value and comprises nearly 10% of the total stress for R = 2 μm. If the surface energy density has a value five times the lowest value of γ = 1.6 J/m^2 [35], the $\sigma^{surface}$ will comprise up to nearly 20% of the total stress.

Table 3-2. $\sigma^{surface}$, σ and their ratio for different Cu pillar sizes and γ.

surface energy	R = 0.5 μm			R = 2 μm			R = 10μm		
density/ J/m^2	σ^{total}/MPa	$\sigma^{surface}$/MPa	$\sigma^{surface}/\sigma^{total}$	σ^{total}/MPa	$\sigma^{surface}$/MPa	$\sigma^{surface}/\sigma^{total}$	σ^{total}/MPa	$\sigma^{surface}$/MPa	$\sigma^{surface}/\sigma^{total}$
1.6	92.9	5.8	6.28%	35.3	1.5	4.19%	26.2	0.3	1.14%
3.2	98.7	11.7	11.82%	36.8	3.0	8.05%	26.5	0.6	2.25%
4.8	104.6	17.5	16.74%	38.3	4.4	11.60%	26.8	0.9	3.34%
6.4	110.4	23.3	21.14%	39.7	5.9	14.89%	27.1	1.2	4.41%
8	116.2	29.2	25.10%	41.2	7.4	17.95%	27.4	1.5	5.45%

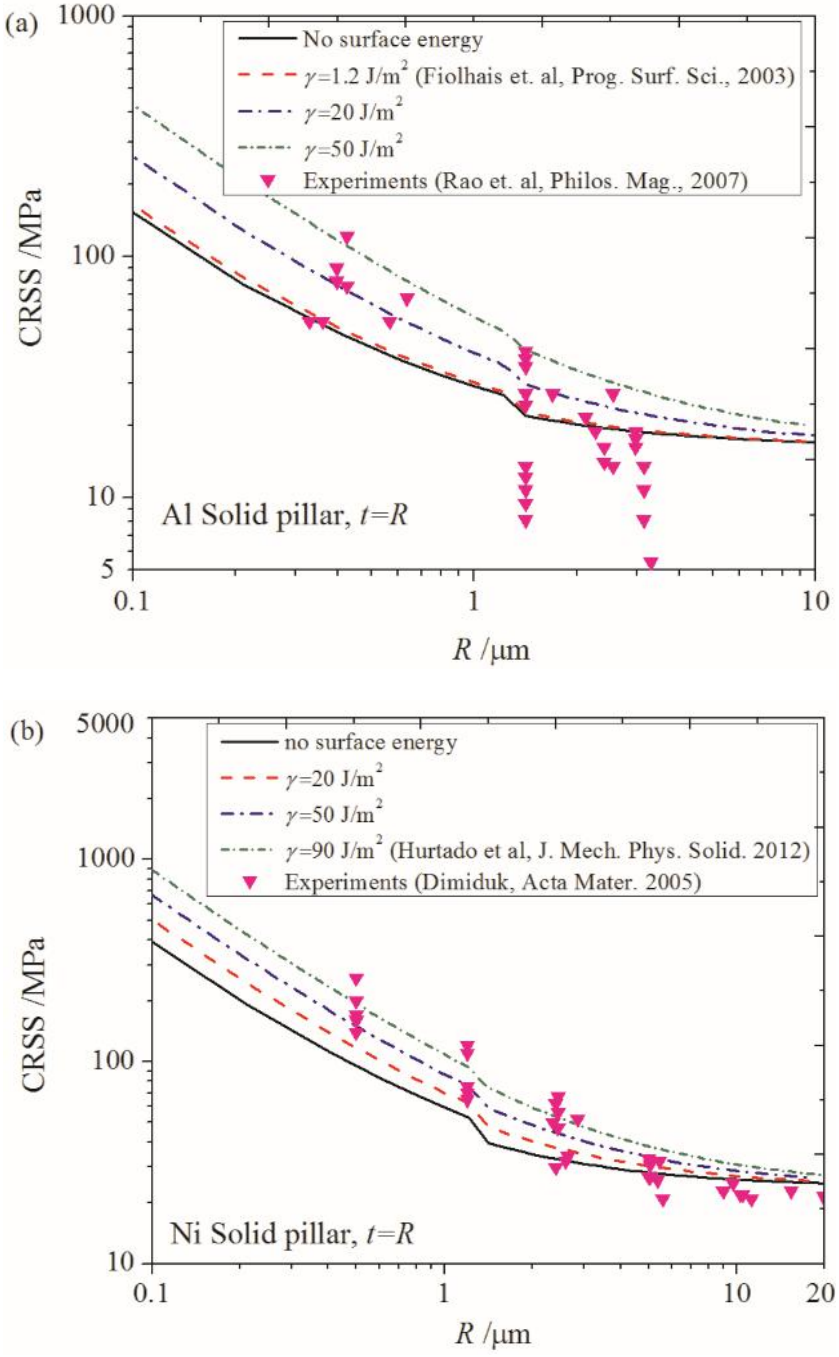

Figure 3-10. Comparison of the theoretical (lines) and experimental (points) results of the shear stress of solid pillars considering the surface energy effect. The numerical results use various surface energies for (a) solid Al pillars and are compared with experimental data [8, 42]; and for (b) solid Ni pillars and are compared with experimental data [2, 35].

3.2.3 Comparisons with experimental results of Al and Ni pillars

After discussing the relative characteristics of the proposed model, the necessary comparisons with experimental results should be made to prove the efficiency of the proposed model. Figure 3-10 shows the comparison of experimental results for solid pillars [2, 8] with these numerical results by considering the surface energy predicted according to Eq. (3.32) by setting $t = R$ (that is, solid pillar). The parameters of Al and Ni used for Figures 3-10 and 3-11 are obtained from Refs. [2, 3, 8, 26, 38, 41-43] and are tabulated in Table 3-1, and the direction of the loading axis is chosen as [1 2 6] in the simulation [3]. In Figure 3-10a, the numerical yield stresses of Al with different surface energies are plotted and compared with the experimental results [8], where it is shown that the calculated yield stress becomes larger as the surface energy increases from the case with no surface energy. The recommended calculated surface energy density of γ = 1.2 J/m^2 [41, 42] is chosen as a reference value and provides very little increase in the calculated yield stress from that with no surface energy, and the calculated curve is still far away from the experimental data for pillars whose radii are in the hundreds of nm range. In order to understand the trends of the surface energy effect, the sensitivity analysis of surface energy densities is conducted to describe the effect of surface energy. When γ is in large value, the numerical results can better express the yield stress for radius values in the range of hundreds of nm. When the radius becomes large enough, all of the calculated yield stress curves are almost constant and approach the same value because the surface stresses resulting from surface energy are very small. Similar results are obtained for Ni pillars, as shown in Figure 3-10b, where the numerical results using the recommended empirical surface energy density of γ = 90 J/m^2 [43] match the experimental data with the radius below 2 μm better than those without any surface energy effect. Based on the

calculation of sensitivity analyses of different surface energies, the large surface energy density makes the theoretical curve fitted better with the experimental data when considering the strength of micro- and nanopillars. Actually, for the case with no surface effect, Eq. (3.32) becomes the SAS model, and it suggests that the proposed model considering the surface energy provides a better prediction than the SAS model.

At present, there are practically no experiments focusing on hollow pillars to examine the size effects, though Ng and Ngan have conducted compression experiments on micron-sized Al crystalline pillars with a loading axis direction of [3 $\bar{1}$ 5] to examine the effects of trapping dislocations [26], where some hollow pillars were used for comparison in their studies. The experimental pillars produced by focused-ion beam (FIB) milling have the radiuses of ~3, 1.1 and 0.6 μm. The calculated yield stresses (calculated by Eq. (3.32)) and experimental data of pillars are shown in Figure 3-11 by setting γ = 1.2 J/m^2 (for Al solid and hollow pillars) [42], and it can be seen that the experimental and numerical results for the yield stress of the solid and hollow pillars both reveal size-dependent characteristics. In Figure 3-11, the experimental values for solid pillars are smaller than those for hollow pillars whose thickness t is R/3, and the numerical results exhibit a similar tendency. Compared with the predicted curve with γ = 1.2 J/m^2 shown in Figure 3-10a, the difference between them in Figures 3-10a and 3-11 results from the thickness of the hollow/solid pillars. The surface energy effect is amplified by increasing the area of the surface when a central hole that runs deeply along the pillar axis is added up to the hollow pillar. There are still some differences between the experiments and numerical results shown in Figure 3-11, because the experiments were conducted in a high strain rate that may, in addition to the thickness, have an influence on the yield stress.

However, thickness is only the varying factor in the experiment. Therefore based on the discussion above, the thickness actually plays an important role in the size-dependent yield stress of hollow pillars. As discussed in section 3.2.2, the two adjacent surfaces of the hollow pillars can effectively shorten the length of λ. When the internal surface increases, the thickness t and effective dislocation length λ in Eq. (3.32) would decrease, thus the total stress increases in our model. This conclusion agrees with the experiments of Ng and Ngan [26].

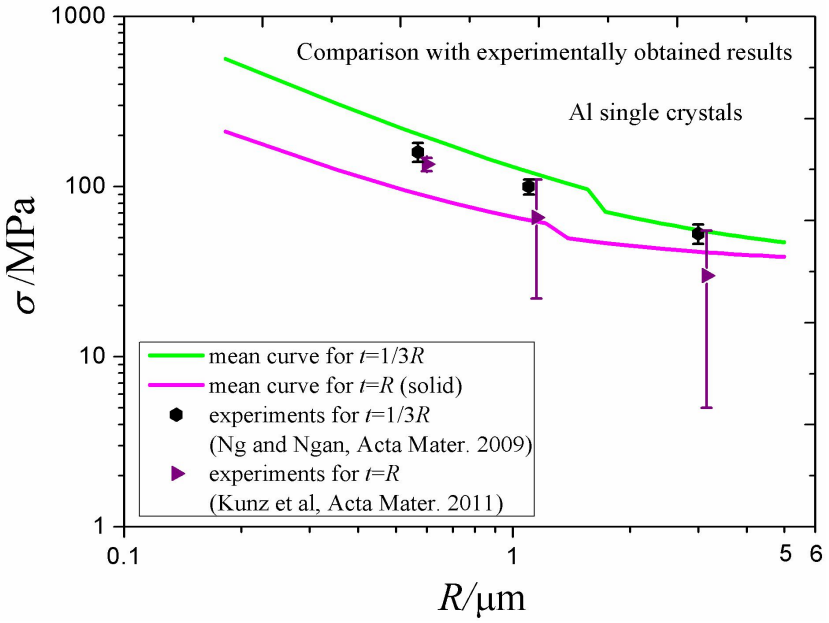

Figure 3-11. Comparison of the theoretical (lines) and experimental (points) results of the total stress in solid and hollow Al single-crystal pillars. The theoretical data are from this work, and the experimental data are taken from [20, 26].

According to the comparison of theory and experiment, the surface stress induced by the surface energy with the consideration of a hollow pillar is important for the size-dependent yield stress. In the above comparison, the thickness variance would also affect the yield stress, which results from the inner defects discussed above.

The present model in section 3.2 shows the surface energy plays an effect on the size dependent strength of the single crystalline micro-pillars. Compared with the original SAS model without consideration of this effect, the present model shows an advance than the original one. Linking to the content in section 3.1, the dislocations pile-up inside the pillars also results in the influence on the size dependent strength. That is to say, the inner and external physics both affects the size effect.

3.2.4 Surface energy

It is suggestive that a large surface energy should be used for micro- and nanopillars, even 45 times that of the bulk specimen [42, 43]. We note in closing that the surface properties of micro- and nano-scale specimens appear to have received scant attention. In particular, exact values of the surface energy in micro- and nano-scale specimens are not given in literature. However, a surface energy on the outer layer owing to external damage will generate an available effect on the strength, and Eqs. (3.38) and (3.39) show this relationship between the surface energy and the surface strain. The parameters E^s, B_1 and B_2 are related only to the geometry and the material and are not a function of the external force/damage, and thus these parameters determine the surface energy affected only by the material and the structural dimensions. In Eq. (3.38), if the residual surface strain $\varepsilon_0^{surface}$ is varied because of external damage, the surface energy will be changed, which means that external damage plays a role in the variance of the surface strain. If the external damage provides compressive damage on the surface and the residual surface strain is also in a compressive state in a small scale, the external damage will increase the compressive stress. Figure 3-12 shows the variances of the surface stress and surface

energy density corresponding to the effective surface strain $\varepsilon = \varepsilon^{surface} - \varepsilon_0^{surface}$, where the surface energy and stress will be proportional to the effective surface strain. The machining process in the preparation of pillars by focus-ion-beam, for example, would input additional energy on the surface of the pillar specimen and thereby affect the surface strain, and in this way the surface energy and stress will be varied.

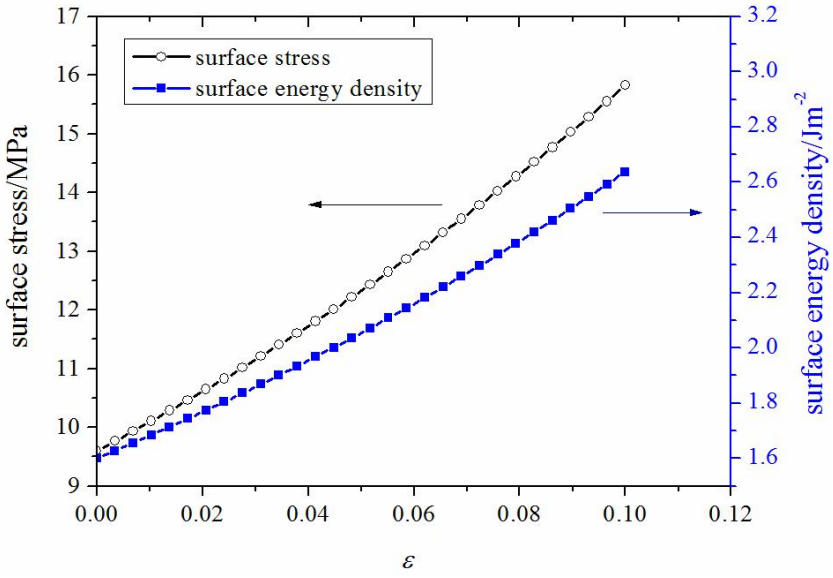

Figure 3-12. The relationships between the surface stress vs. effective strain and the surface energy density vs. effective strain. The effective strain is given as $\varepsilon = \varepsilon^{surface} - \varepsilon_0^{surface}$.

3.3 Size-dependent yield function for single crystals with a consideration of defect effects

3.3.1 Dislocation-based model of single-crystal yield surface

In order to describe the mechanical response of the small scaled micron crystalline material under complicated loading conditions besides uniaxial tension or compression, the corresponding yield function should be provided. The above sections have further studied the physical factors influencing the size dependent

strength of the single crystalline materials. In this section, the general yield function of single crystalline materials with size effect will be provided.

3.3.1.1 Single-crystal yield function derived from combined constraint optimization method

The plastic deformation after initial yielding in a normal isotropic material can usually be defined by a single smooth yield function; however, in some materials, like soil and rock, the deformation is expressed by several smooth yield surfaces, which intersect non-smoothly [44, 45].

In a single crystal, the overall plastic deformation consists of a series of shear strains as a result of dislocation slips on multiple slip systems. Considering the case of crystal plasticity, as the overall plastic deformation has to bypass multiple slip planes where the plastic behavior is defined by several yield surfaces, the yield function depends on the number of slip systems in the crystal. Assuming the validity of the Schmid law for the plastic deformation of a single crystal, then for any slip system a yield function can be defined as

$$f_\alpha(\boldsymbol{\sigma},\boldsymbol{q}) = \frac{\left|\boldsymbol{\sigma} : \boldsymbol{P}^\alpha\right|}{\mathrm{CRSS}} - 1, \tag{3.41}$$

where $\boldsymbol{q}$ is a vector containing the internal variables that affect the yield surface, $\boldsymbol{\sigma}$ is the Cauchy stress tensor, CRSS is the critical shear stress on the slip planes, α is the number of slip planes, and $\boldsymbol{P}^\alpha$ is a matrix showing the orientation of a slip system as:

$$\boldsymbol{P}^\alpha = \frac{1}{2}(\boldsymbol{s}_\alpha^* \otimes \boldsymbol{m}_\alpha^* + \boldsymbol{m}_\alpha^* \otimes \boldsymbol{s}_\alpha^*), \tag{3.42}$$

where $\boldsymbol{s}_\alpha$ and $\boldsymbol{m}_\alpha$ are the unity direction vector normal to the slip plane and the unity sliding direction vector in the α sliding system. α , β is represented as the active slip system and $\boldsymbol{m}_\alpha^* = \boldsymbol{m}_\alpha \cdot \boldsymbol{F}_e^{-1}$, $\boldsymbol{s}_\alpha^* = \boldsymbol{F}_e \cdot \boldsymbol{s}_\alpha$, where $\boldsymbol{F}_e$ is the elastic deformation gradient tensor.

In single-crystal plasticity, the increment objective function $l(\mathbf{x})$ of the plastic work and released internal energy in the [j, j+1]-th step is solved by the following constrained minimization solution [46]:

$$(\boldsymbol{\sigma}_{j+1},\ \boldsymbol{q}_{j+1}) = \begin{cases} Min(l(\mathbf{x})) \\ Subject\ to: f_\alpha(\boldsymbol{\sigma},\boldsymbol{q}) \le 0,\ \alpha = 1,...,s \end{cases}. \tag{3.43}$$

where $\boldsymbol{x}$ contains the variables related to the objective function $l(\boldsymbol{x})$ denoting the incremental release of elastic stored energy due to the plastic work and the incremental plastic work. Both should be minimized to find the equilibrium point. The constraints in Eq. (3.43) correspond to the yield function shown in Eq. (3.41).

To avoid singularity and computational ambiguity, a combined constraint optimization method is proposed. To explain the combined constraint method, the following optimization problem with several inequality constraints ($f_i(\boldsymbol{x}) \ge 0$, $i = 1,...,s$) is considered:

$$\begin{cases} Min(g(\boldsymbol{x})) \\ Subject\ to: f_i(\boldsymbol{x}) \ge 0,\ i = 1,...,s \end{cases} or \begin{cases} Min(g(\boldsymbol{x})) \\ Subject\ to:\ y_i(\boldsymbol{x}) = -f_i(\boldsymbol{x}) \le 0,\ i = 1,...,s \end{cases}. \tag{3.44}$$

The constraints of Eq. (3.44) can be combined and replaced by an equivalent single constraint function $h(\boldsymbol{x})$ defined as [47]

$$h(\boldsymbol{x}) = -\frac{1}{\varphi}\ln\{\sum_{i=1}^{s}\exp[\varphi(-f_i(\boldsymbol{x}))]\} = -\frac{1}{\varphi}\ln\{\sum_{i=1}^{s}\exp[\varphi(y_i(\boldsymbol{x}))]\}\ . \tag{3.45}$$

where φ is a parameter related to the SFE, and determines the closeness of $h(\boldsymbol{x})$ to the smallest inequality, $min[\ f_i(\boldsymbol{x})\ ]$. $h(\boldsymbol{x})$ is usually known as the *KS*-function. $h(\boldsymbol{x})$ is always convex and always more positive for any positive φ . Compared with the cases of Eq. (3.43) and Eq. (3.44), the constraints in Eq. (3.45) can be written as

$$y_i(\boldsymbol{\sigma},\boldsymbol{q}) = f_\alpha(\boldsymbol{\sigma},\boldsymbol{q}) = \frac{\left|\boldsymbol{\sigma}:\boldsymbol{P}^\alpha\right|}{\mathrm{CRSS}} - 1 \le 0\ . \tag{3.46}$$

Therefore, the combined constraint function $h(\boldsymbol{\sigma},\boldsymbol{q})$ can rewritten as

$$h(\boldsymbol{\sigma},\boldsymbol{q}) = -\frac{1}{\varphi}\ln\{\sum_{\alpha=1}^{s}\exp[\varphi(f_\alpha(\boldsymbol{\sigma},\boldsymbol{q}))]\} = -\frac{1}{\varphi}\ln\{\sum_{\alpha=1}^{s}\exp[\varphi(\frac{\left|\boldsymbol{\sigma}:\boldsymbol{P}^\alpha\right|}{\mathrm{CRSS}} - 1)]\}\ . \tag{3.47}$$

Then, the equivalent optimization problem for the crystal plasticity in Eq. (3.43) will be

$$(\boldsymbol{\sigma}_{j+1},\ \boldsymbol{q}_{j+1}) = \begin{cases} Min(l(\boldsymbol{x})) \\ Subject\ to:\ h(\boldsymbol{\sigma},\boldsymbol{q}) = -\dfrac{1}{\varphi} ln\{\sum_{\alpha=1}^{s} exp[\varphi(\dfrac{\left|\boldsymbol{\sigma}:\boldsymbol{P}^{\alpha}\right|}{\mathrm{CRSS}} - 1)]\} \geq 0 \end{cases} . \tag{3.48}$$

The parameter φ is introduced into Eq. (3.47) to give additional flexibility to the shape of the yield function [45].

Based on the combined constraint optimization method, a new single-crystal yield function is established with the final form defined as:

$$h(\boldsymbol{\sigma},\boldsymbol{q}) = -\frac{1}{\varphi}\ln\{\sum_{\alpha=1}^{s}\exp[\frac{\varphi}{\Omega}(\frac{\left|\boldsymbol{\sigma}:\boldsymbol{P}^{\alpha}\right|}{\mathrm{CRSS}} - 1)]\} . \tag{3.49}$$

where for most cases one may consider that Ω = 1 [45].

3.3.1.2 Dislocation-based single-crystal yield surface

Let us consider the yield function of a plastic case:

$$h(\boldsymbol{\sigma},\boldsymbol{q}) = -\frac{1}{\varphi}\ln\{\sum_{\alpha=1}^{s}\exp[\frac{\varphi}{\Omega}(\frac{\left|\boldsymbol{\sigma}:\boldsymbol{P}^{\alpha}\right|}{\mathrm{CRSS}} - 1)]\} = 0 . \tag{3.50}$$

With some simple manipulations of Eq. (3.50), the following relationship can be obtained:

$$\sum_{\alpha=1}^{s}\exp[\frac{\varphi}{\Omega}(\frac{\left|\boldsymbol{\sigma}:\boldsymbol{P}^{\alpha}\right|}{\mathrm{CRSS}})] = \exp(\frac{\varphi}{\Omega}) . \tag{3.51}$$

Based on the model of Zamiri and Pourboghrat [45], the following approximate relationship between the closeness parameter φ and the SFE of the material is suggested:

$$\varphi = \frac{C\Gamma}{\mu b} , \tag{3.52}$$

where Γ is the SFE of the material and C is a geometrical parameter. Considering the pile-up SAS model shown in Eq. (3.15) and surface energy effect shown in Eq. (3.32), the single-crystal yield surface model based on the physics of dislocation is finally given by

$$\sum_{\alpha=1}^{s}\exp[\frac{\varphi}{\Omega}(\frac{\left|\boldsymbol{\sigma}:\boldsymbol{P}^{\alpha}\right|}{\tau_0+pf_H 0.5\mu b\sqrt{\rho}+[(1-p)\alpha_1+p]\frac{\mu b}{\bar{\lambda}_{\max}}+SF\frac{\gamma O_0(1-\nu)}{\pi(2Rt-t^2)}})]=\exp(\frac{\varphi}{\Omega}). \tag{3.53}$$

Eq. (3.53) can describe arbitrary stress conditions and slip systems.

3.3.2 Yield surfaces of different materials

As an example application of the proposed model, we first consider the case in which σ_3 aligns with the (0 0 1) orientation. A plane stress condition (σ_x, σ_y, τ_{xy}) allows a straightforward evaluation of the effects of the yield function parameters shown in Eq. (3.53). The problem is simplified by setting the principal stress space (σ_1, σ_2) to overlap with the crystalline axis, while the directions of σ_1 and σ_2 are set to align with the (1 0 0) and (0 1 0) orientations, respectively. Therefore, Eq. (3.53) becomes a function of the undetermined parameters (σ_1, σ_2):

$$\begin{aligned}k(\sigma_1,\sigma_2)=\sum_{\alpha=1}^{s}\exp[\frac{\varphi}{\Omega}(\frac{\left|\boldsymbol{\sigma}:\boldsymbol{P}^{\alpha}\right|}{\tau_0+pf_H 0.5\mu b\sqrt{\rho}+[(1-p)\alpha_1+p]\frac{\mu b}{\bar{\lambda}_{\max}}+SF\frac{\gamma O_0(1-\nu)}{\pi(2Rt-t^2)}})]\\ -\exp(\frac{\varphi}{\Omega}),\end{aligned} \tag{3.54}$$

If the combination (σ_1, σ_2) can be made to satisfy the inequality $k(\sigma_1,\sigma_2)\le 1\times 10^{-3}$, a simple yield surface with principal stress space can be obtained as shown in Figure 3-13.

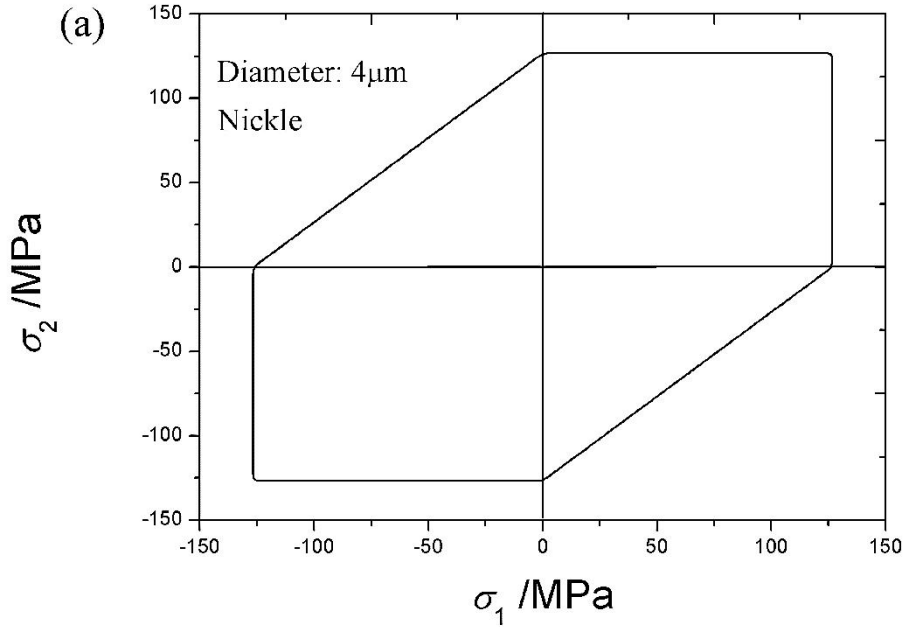
(a)
Diameter: 4μm
Nickle
150
100
50
0
-50
-100
-150
-150
-100
-50
0
50
100
150
σ2 /MPa
σ1 /MPa

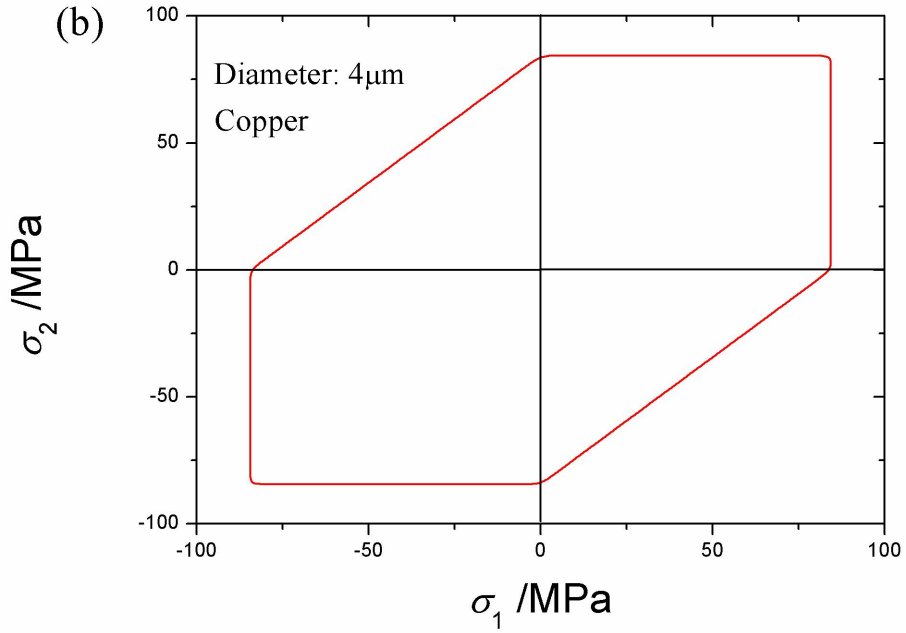
(b)
Diameter: 4μm
Copper
100
50
0
-50
-100
-100
-50
0
50
100
σ2 /MPa
σ1 /MPa

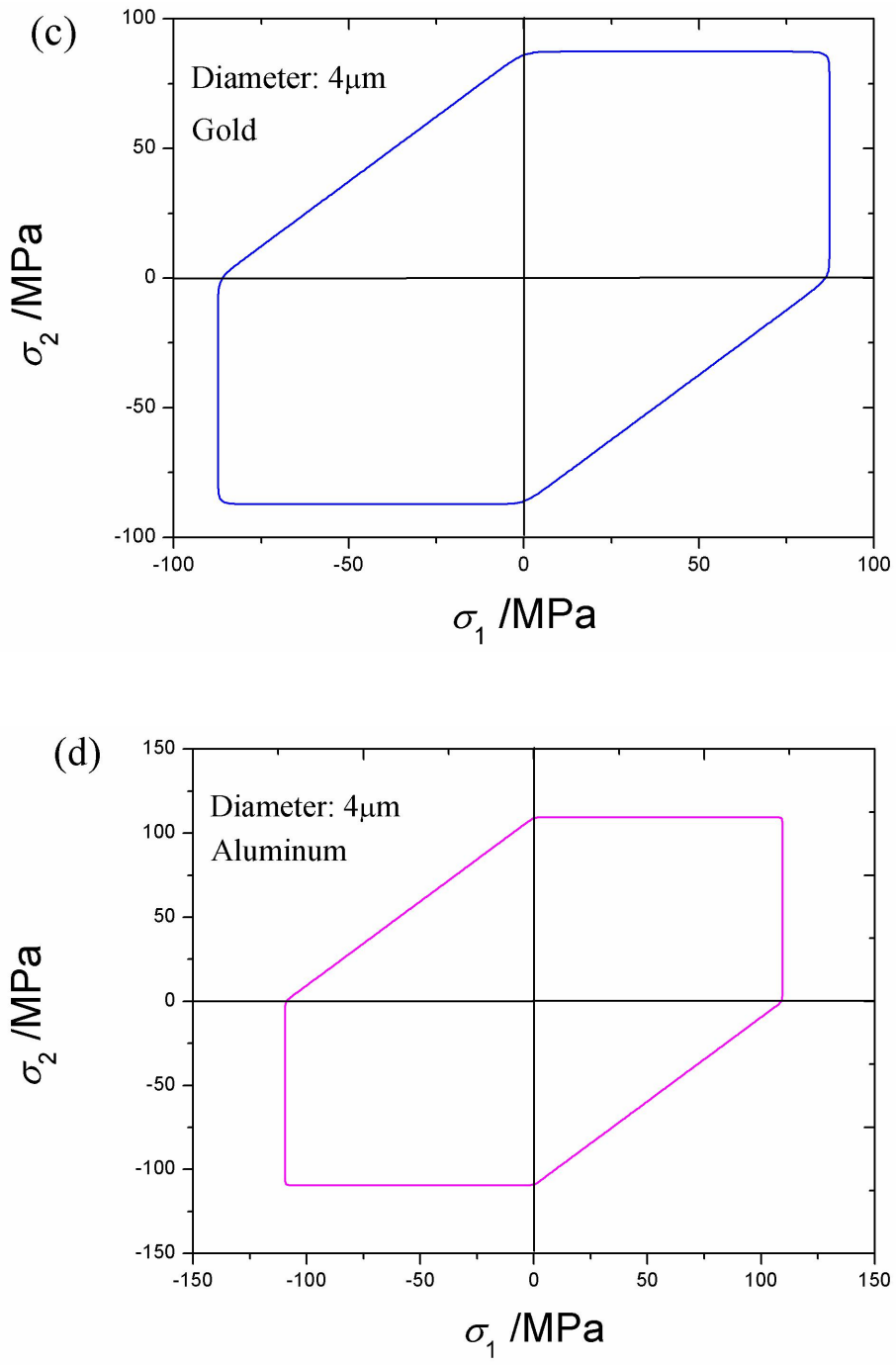

Figure 3-13. Shape of single-crystal yield surfaces for micro-pillars of different metals: (a) Nickel; (b) Copper; (c) Gold; (d) Aluminum. The yield surfaces are for single crystals with {1 1 1} slip systems.

In the following example, we select parameters the same as Sections 3.1 and 3.2: $\rho = 4\times10^{12}\ /\ \mathrm{m}^2$; $C = 0.6372$; $\tau_0 = 11$ MPa (Ni), 13 MPa (Au), 10 MPa (Al), 12 MPa (Cu); $\upsilon = 0.3$; $s = 12$; $h = 2.5R$; $\mu = 76$ GPa (Ni), 48 GPa (Cu), 32.7 GPa (Al); $b =$

0.24 nm (Ni), 0.288 nm (Au), 0.283 nm (Al), 0.256 nm (Cu); γ = 2.0 J/m^2(Ni), 1.2 J/m^2 (Al), 1.6 J/m^2 (Cu), 1.5 J/m^2 (Au). The values of (p, m) are Au (0.47, 1.62), Cu (0.58, 0.89), Al (0.67, 0.35), and Ni (0.99, 0.002), obtained by fitting the experiments using a least-squares method [3]. Figure 3-13 shows the shapes of the proposed single-crystal yield surfaces for fcc crystals. The proposed yield surfaces show Tresca yield-criterion-type shapes, in agreement with refs. [45, 48-57]. The edge value for each side of the yield surface is determined by the CRSS shown in Eqs. (3.51) and (3.53), and is not only material-dependent but also size-dependent. By considering the dislocation pile-up effect, the CRSS of the pile-up SAS model shown in Eq. (3.15) and surface energy effect shown in Eq. (3.32) can more effectively describe the size-dependent strength than the original SAS model [1], especially for materials with low values of the SFE. For fcc crystals, materials with low SFE more easily exhibit dislocation pile-up. The surface energy can provide some few percent of the total strength if the surface energy density is in small value. However, if the external damage enlarges the initial surface strain, the increasing surface energy will improve the influence of the surface stress, which has been discussed in section 3.2. That is to say, the yield function combined with the considerations in sections 3.1 and 3.2 can describe the size-dependent characteristics of single-crystal materials, as will be discussed in the following section.

If the stresses σ_1 and σ_2 are normalized by the CRSS as shown in Figure 3-14, the differences among the yield surface shapes can be found. First, the yield surfaces of Ni and Al, with large values of the closeness parameter φ, display larger and sharper edges than those of Au and Cu. Meanwhile, the surfaces of Ni and Al are coincident because their closeness parameters φ are almost identical. Figure 3-15 shows the effect of the closeness parameter φ on the shape of the proposed Cu

single-crystal yield surface. With increasing φ, the yield surfaces dramatically change their shape and display sharp vertices. With sufficiently small φ, e.g., $\varphi = 5$, the yield surface resembles the Mises yield-criterion-type shape and displays small edges. Above all, φ is dominant for the yield shape.

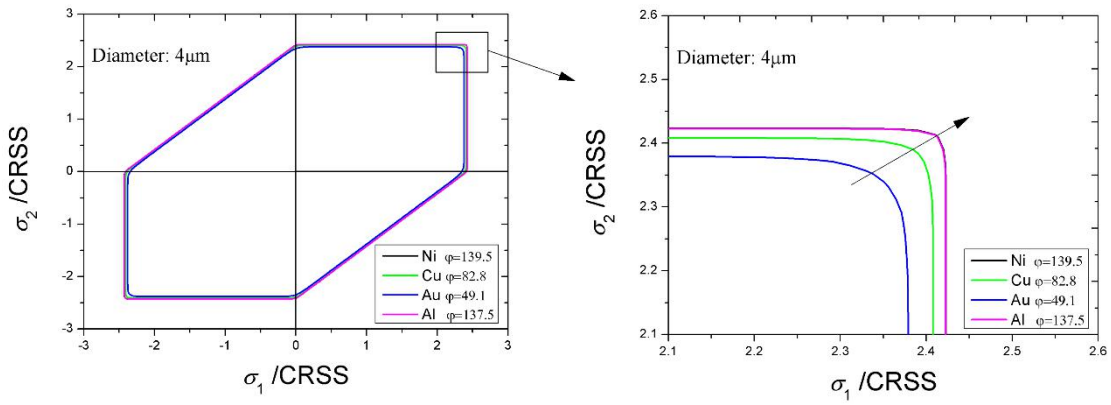

Figure 3-14. Non-dimensionalized shape of the proposed single-crystal yield surface for different materials. The yield surfaces are for single crystals with {1 1 1} slip systems.

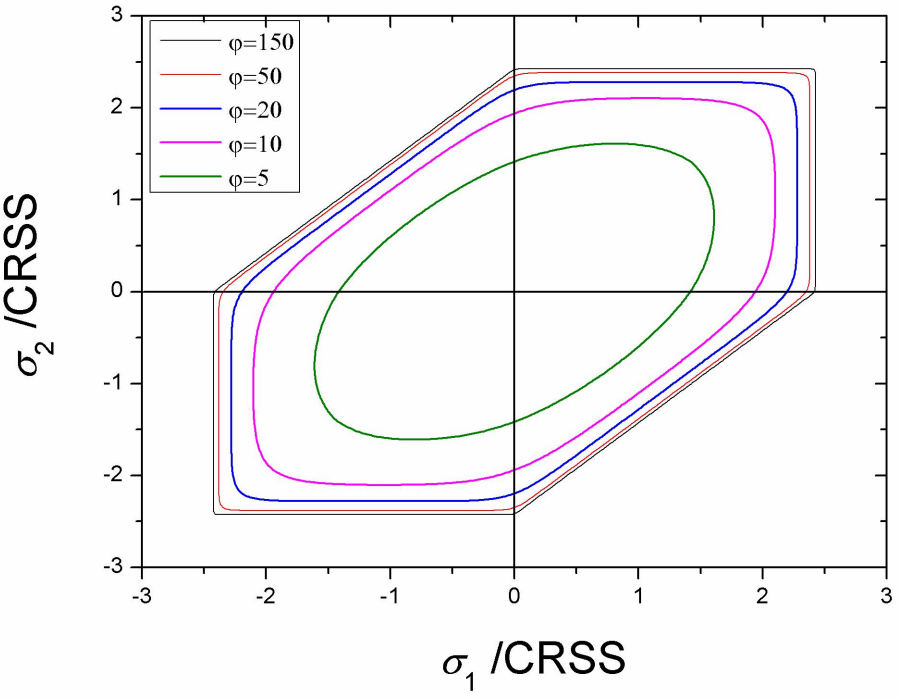

Figure 3-15. Effect of φ on the shape of proposed Cu single-crystal yield surfaces. The yield surfaces are for single crystals with {1 1 1} slip systems.

3.3.3 Relationship among SFEs, φ and (m, p)

Quantitative analyses of the relationship among SFEs, φ and (m, p) were conducted, as shown in Figures 3-3 and 3-16. In the pile-up SAS model, the value of m, related to the dislocation pile-up length, is used to estimate the magnitude of the dislocation effect [3]. A large value of m indicates a large dislocation pile-up length. Meanwhile, as mentioned above, the CRSS is determined by the activation of the weakest dislocation source. The stress concentration resulting from the pile-up zone may affect the weakest dislocation source, which will in turn affect the CRSS. The value of p represents the extent to which the pile-up is ineffective on the weakest dislocation source. That is, the parameters (m, p) represent the effect of dislocation pile-up. For fcc crystals, materials with low SFE more easily exhibit dislocation pile-up. This behavior suggests that a smaller SFE corresponds to a larger m in Eq. (3.15), as shown in Figure 3-3a. Because Au has a lower SFE (0.06 J/m^2) than Ni (0.40 J/m^2), the dislocation pile-up effect is more pronounced in Au than in Ni. In Figure 3-3b, the value of p for Ni is 0.99, nearly equal to 1, and m is much smaller than 0.28; that is, there is no source near the pile-up and almost no pile-up effect inside the pillar [3]. Experiments by Frick et al. [28] showed no evidence of dislocation pile-ups in systematic studies of Ni micro- and nano-pillars ranging from 160 nm to 2000 nm in diameter. Here, the SFE and (m, p) represent the extent of the influence of dislocation pile-up on the CRSS of SCMs.

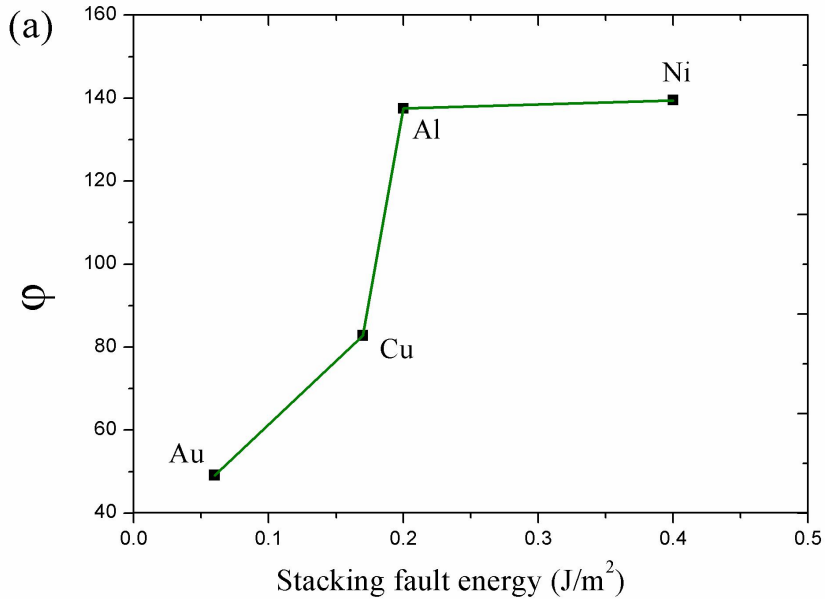

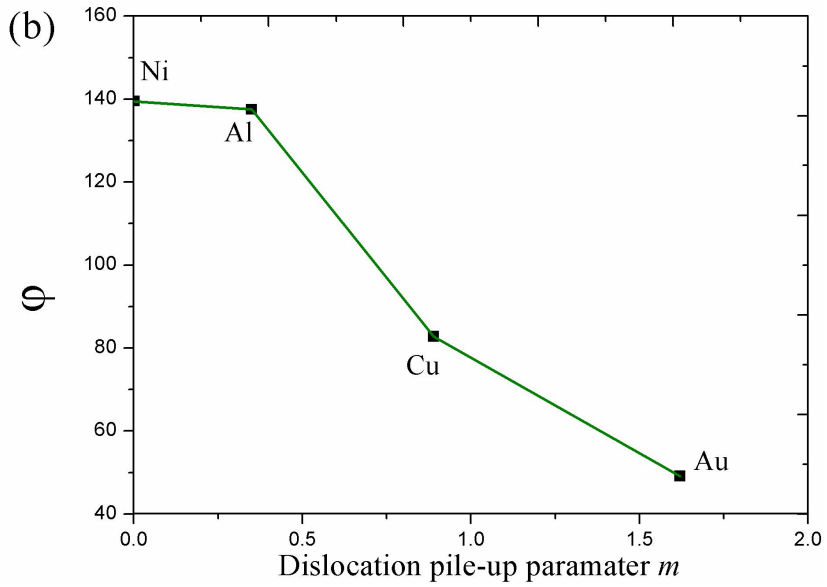

Figure 3-16. Relationship among the stacking-fault energy (SFE), the parameters (*m, p*), and the closeness parameter φ ; (a) SFE as a function of the closeness parameter φ ; (b) the relationship between the dislocation pile-up parameter m and the closeness parameter φ .

In Figure 3-16a, increasing values of SFE are accompanied by larger φ , even though Cu and Ni have nearly identical values of φ . According to Eq. (3.52), φ is

defined by the SFE, therefore the SFE is related to the shape of the yield surface. Specifically, materials with high SFE, such as Al, have yield surfaces with sharp vertices, related to the high mobility of the dislocations [56]. Conversely, for materials with low SFE, such as silver, the yield surface displays rounded corners as per the Mises yield criterion [56, 58]. The plots in Figures 3-14 and 3-15 are therefore consistent with these principles. This is illustrated by Figure 3-3a, which shows that the dislocation pile-up affects the shape of the yield surface. The corresponding result for φ is shown in Figure 3-16b, in which m increases as φ decreases. That is, the dislocation pile-up rounds the corners and contracts the edges of the yield surface.

3.3.4 Size effect on yield surface

For SCMs, the CRSS varies with the pillar diameter, which is an example of the size effects found in previous studies [2, 22-24]. In the SAS model and pile-up SAS model, the CRSS depends on the effective length of the dislocation source and the number of dislocation sources, as described by Eqs. (3.16) and (3.17). ($\bar{\lambda}_{\max} - S_{\lambda_{\max}}$) and ($\bar{\lambda}_{\max} + S_{\lambda_{\max}}$) give the upper and lower bounds, respectively, of the CRSS. In Eq. (3.53), the yield surface is also related to the effective length of the dislocation source $\bar{\lambda}_{\max}$ and the number of dislocation sources n. Therefore, the yield surface is also size-dependent, as shown in Figure 3-17. It can be seen that, with decreasing size, the edge of the yield surface of the SCMs increases. As the SFE and material parameters (μ, b) are not size-dependent, the shape of the yield surface is size-independent given a constant φ for a particular material. In Figure 3-17, the edge of 8.2 μm is close to that of 10.4 μm. As discussed in ref. [3], when the diameter size is large enough (> 10 μm), large values of $\bar{\lambda}_{\max}$ reduce the extent to which τ_{activate}, which is dominant

for the size effect, determines the total CRSS. In this case, the proposed yield surface becomes the original yield surface, without the consideration of defects introduced by this study, and it describes the bulk SC material in the same way as other yield functions [45, 48-57].

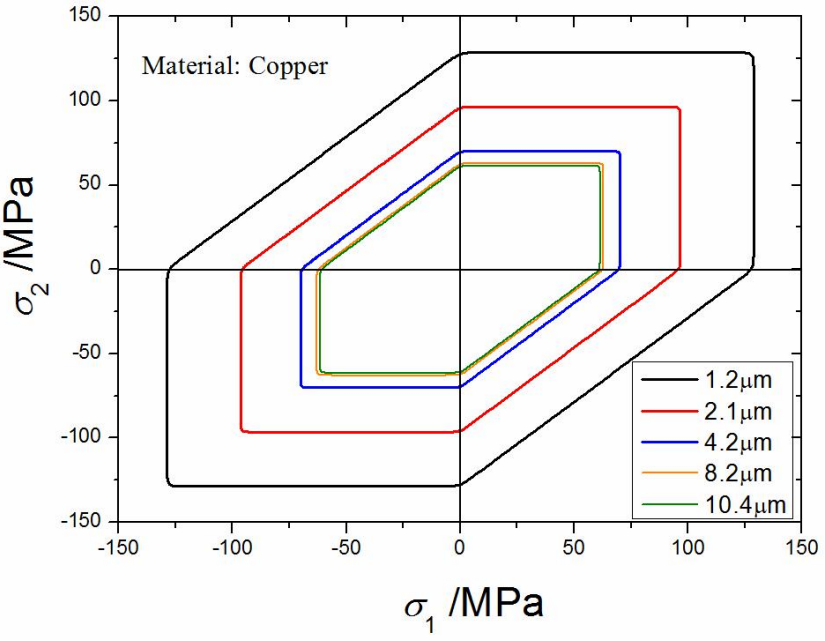

Figure 3-17. Yield surfaces of Cu single-crystal micro-pillars with different diameters. The yield surfaces are for single crystals with {1 1 1} slip systems.

3.4 Conclusion

In summary, we consider two physical factors the inner dislocations pile-up effect and external surface energy effect to explain the size dependent strength of single crystalline micro-pillars. We first provide pile-up SAS model to describe the pile-up effect, and establish a mixed model combining the surface energy and inner defects to describe surface effect. At least, we provide a size dependent single crystalline yield function to describe the size dependent strength under complicated loading condition.

First, our proposed pile-up SAS model provides a dimensional model that can be used to better understand the size effect in crystals in a physical framework that incorporates dislocation pile-up and size-dependent plasticity effects. Our model agrees well with experimental data, showing that it can effectively describe the size-dependent strength in finite micro-pillars. Our pile-up SAS model agrees better

than the original SAS model with the experimental data, especially for Au and Cu. Our results reveal that the Hall–Petch effect can be observed even in the single crystals, and that the length of dislocation pile-up is an important factor in the CRSS. Moreover, the number of dislocation sources greatly affects the observed size effect, which makes the size effect more obvious in smaller samples. Our pile-up SAS model can be used to describe the yield strength of materials that exhibit strong dislocation pile-up effects, especially for materials with low SFE.

Secondly, we have established a mixed model combining the surface energy and inner defects to describe the yield stress of hollow micro- and nanopillars based on the principle of minimum potential energy. The experimental results show good agreement with these numerical results, and the proposed model is seen to provide a better prediction than the SAS model, which does not consider the surface energy. Therefore, the main influences on the size-dependent yield stress results from both the surface stress, which is mainly dominated by the geometry and the surface energy, and the inner defects arising from the effective dislocation length and the number of dislocation sources. Meanwhile, an analytical form of the relationship between the surface energy and the surface strain is obtained. The surface energy is determined by the geometric structure, the surface modulus and the surface strain, though the machining process in the preparation of pillars would input additional energy on the specimen surface to affect the surface strain, and in this way the surface energy and stress will be varied.

Finally, the size-dependent yield surface of a single-crystalline micro-pillar was developed with a logarithmic-exponential form by considering defect effects, including dislocation pile-up, dislocation starvation and source exhaustion. Our proposed model provides the following results: materials with low stacking-fault energy exhibit clear dislocation pile-up effects and their yield surfaces tend to display rounded vertices, as per the Mises yield criterion; those with high stacking-fault energy show typical Tresca criterion-type yield surfaces displaying sharp vertices. It is concluded that the dislocation pile-up rounds the corners and contracts the edges of the yield surface. We also show that this yield function can completely describe the size-dependent yield surface by considering the stochastic lengths of the dislocation source and the dislocation pile-up length in single-crystalline micro-pillars.

Reference

[1] Parthasarathy TA, Rao SI, Dimiduk DM, Uchic MD, Trinkle DR. Contribution to size effect of yield strength from the stochastics of dislocation source lengths in finite samples. Scr Mater 2007 (56) 313-316.
[2] Dimiduk DM, Uchic MD, Parthasarathy TA. Size-affected single-slip behavior of pure nickel microcrystals. Acta Mater 2005 (53) 4065-4077.
[3] Pan B, Shibutani Y, Zhang X, Shang F. Effect of dislocation pile-up on size-dependent yield strength in finite single-crystal micro-samples. J Appl Phys 2015 (118) 014305.
[4] Sun Q, Guo Q, Liao X, Greer JR, Sun J. Size effects in strength and plasticity of single crystalline titanium micro-pillars with prismatic slip orientation. Scr Mater 2011 (65) 473–476.
[5] Shan ZW, Li J, Cheng YQ, Minor AM, Syed Asif SA et al. Plastic flow and failure resistance of metallic glass: Insight from in situ compression of nanopillars. Phys Rev B 2008 (77) 155419.
[6] Senger J, Weygand D, Gumbsch P, Kraft O. Discrete dislocation simulations of the plasticity of micro-pillars under uniaxial loading. Scr Mater. 2008 (58) 587-590.
[7] Dehm G. Miniaturized single-crystalline fcc metals deformed in tension: New insights in size-dependent plasticity. Prog Mater Sci 2009 (54) 664-688.
[8] Rao SI, Dimiduk DM, Tang M, Uchic MD, Parthasarathy TA, Woodwar C. Estimating the strength of single-ended dislocation sources in micron-sized single crystals. Philos Mag 2007 (87) 4777-4794.
[9] Greer JR, De Hosson JTM. Plasticity in small-sized metallic systems: Intrinsic versus extrinsic size effect. Prog Mater Sci 2011 (56) 654 – 724.
[10] Greer JR, Oliver WC, Nix WD. Size dependence of mechanical properties of gold at the micron scale in the absence of strain gradients. Acta Mater 2005 (53) 1821-1830.
[11] Hirth JP, Lothe J. Theory of Dislocation (1982), John Wiley.
[12] Huang Y, Gao H, Nix WD, Hutchinson JW. Mechanism-based strain gradient plasticity—II. Analysis. J Mech Phys Solids 2000 (48) 99-128.
[13] Kiener D, Grosinger W, Dehm G, Pippan R. A further step towards an understanding of size-dependent crystal plasticity: in situ tension experiments of miniaturized single-crystal copper samples. Acta Mater 2008 (56) 580-592.
[14] Kiener D, Motz C, Dehm G. Micro-compression testing: a critical discussion of experimental constraints. Mater Sci Eng A 2009 (505) 79-87.
[15] Fan H, Li Z, Huang M. Size effect on the compressive strength of hollow micropillars governed by wall thickness, Scr Mater 2012 (67) 225-228.

[16] Motz C, Weygand D, Senger J, Gumbsch P. Micro-bending tests: A comparison between three-dimensional discrete dislocation dynamics simulations and experiments. Acta Mater 2008(56) 1942-1955.
[17] Senger J, Weygand D, Gumbsch P, Kraft O. Discrete dislocation simulations of the plasticity of micro-pillars under uniaxial loading. Scr Mater. 2008 (58) 587-590.
[18] Roy A, Peerlings RHJ, Geers MGD, Kasyanyuk Y. Continuum modeling of dislocation interactions: Why discreteness matters? Mater Sci Eng A 2008(486) 653-661.
[19] Fan H, Aubry S, Arsenlis A, El-Awady JA. Orientation influence on grain size effects in ultrafine-grained magnesium. Scr Mater 2015 (97) 25-28.
[20] Feaugas X. On the origin of the tensile flow stress in the stainless steel AISI 316L at 300 K: back stress and effective stress. Acta Mater 1999 (47) 3617-3632.
[21] Mughrabi H. Dislocation wall and cell structures and long-range internal stresses in deformed metal crystals. Acta Metall 1983 (31) 1367-1379.
[22] Uchic MD, Shade PA, Dimiduk DM. Plasticity of micrometer-scale single crystals in compression. Annu Rev Mater Res 2009 (39) 361-386.
[23] Uchic MD, Dimiduk DM, Florando JN, Nix WD. Sample dimensions influence strength and crystal plasticity. Science 2004 (305) 986-989.
[24] Greer JR, De Hosson JTM. Plasticity in small-sized metallic systems: Intrinsic versus extrinsic size effect. Prog Mater Sci 2011 (56) 654-724.
[25] Hirouchi T, Shibutani Y. Mechanical Responses of Copper Bicrystalline Micro Pillars with $\Sigma 3$ Coherent Twin Boundaries by Uniaxial Compression Tests. Mater Trans 2014 (55) 52-57.
[26] Ng KS, Ngan AHW. Effects of trapping dislocations within small crystals on their deformation behavior. Acta Mater 2009 (57) 4902-4910.
[27] Hartford J, Von-Sydow B, Wahnström G, Lundqvist BI. Peierls barriers and stresses for edge dislocations in Pd and Al calculated from first principles. Phys Rev B 1998 (58) 2487-2496.
[28] Frick CP, Clark BG, Orso S, Schneider AS, Arzt E. Size effect on strength and strain hardening of small-scale [1 1 1] nickel compression pillars. Mater Sci Eng A 2008 (489) 319-329.
[29] Gao Y, Zhuang Z, Liu ZL et al. Characteristic sizes for exhaustion-hardening mechanism of compressed Cu single-crystal micropillars. Chin Phys Lett 2010 (27) 086103.
[30] El-Awady JA, Wen M, Ghoniem NM. The role of the weakest-link mechanism in controlling the plasticity of micropillars. J Mech Phys Solids 2009 (57) 32-50.
[31] Norfleet DM, Dimiduk DM, Polasik SJ, Uchic MD, Mills MJ. Dislocation structures and their relationship to strength in deformed nickel microcrystals, Acta Mater 2008 (56) 2988–3001.
[32] Bei H, Shim Pharr SGM, George EP. Effects of pre-strain on the compressive stress–strain response of Mo-alloy single-crystal micropillars. Acta Mater 2008 (56) 4762–4770.
[33] Kiener D, Motz C, Rester M, Jenko M, Dehm G. FIB damage of Cu and possible consequences for miniaturized mechanical tests. Mater Sci Eng A 2006 (459)

262-272.
[34] Dubach A, Raghavan R, Löffler JF, Michler J, Ramamurty U. Micropillar compression studies on a bulk metallic glass in different structural states. Scr Mater 2009 (60) 567-570.
[35] Wang D, Wang G. Influence of surface energy on the stiffness of nanosprings. Appl Phys Lett 2011(98) 083112.
[36] Kiener D, Grosinger W, Dehm G. On the importance of sample compliance in uniaxial microtesting. Scr Mater 2009 (60) 148-151.
[37] Cammarata C. Surface and Interface Stress Effects in Thin Films. Prog Surf Sci 1994 (46) 1-38.
[38] Kunz A, Pathak S, Greer JR. Size effects in Al nanopillars: Single crystalline vs. bicrystalline Acta Mater 2011 (59) 4416-4424.
[39] Wang G, Yang F. Post buckling analysis of nanowires with surface effects. J Appl Phys 2011 (109) 063535.
[40] Cuenot S, Fretigny C, Demoustier-Champagne S, Nysten B. Surface tension effect on the mechanical properties of nanomaterials measured by atomic force microscopy. Phys Rev B 2004 (69) 165410.
[41] Shenoy VB, Atomistic calculations of elastic properties of metallic fcc crystal surfaces. Phys Rev B 2005 (71) 094104.
[42] Fiolhais C, Almeida LM, Henriques C. Extraction of aluminium surface energies from slab calculations: perturbative and non-perturbative approaches. Prog Surf Sci 2003 (74) 209-217.
[43] Hurtado DE, Ortiz M. Surface effects and the size-dependent hardening and strengthening of nickel micropillars. J Mech Phys Solid 2012 (60) 1432-1446.
[44] Montheillet F, Gilormini P, Jonas JJ. Relation between axial stresses and texture development during torsion testing: a simplified theory. Acta Metall 1985 (33) 705-718.
[45] Zamiri A, Pourboghrat F. A novel yield function for single crystals based on combined constraints optimization. Int J Plast 2010 (26) 731-746.
[46] Simo JC, Hughes TJR. Computational Inelasticity. Interdisciplinary Applied Mathematics. Springer-Verlag, Inc.: New York, USA, 1998; p10.
[47] Kreisselmeier G, Steinhauser R. Systematic control design by optimizing a vector performance index. In: Proceedings of IFAC Symposium on Computer Aided Design of Control Systems, Zurich, Switzerland, 1979.
24-33[48] Montheillet F, Gilormini P, Jonas JJ. Relation between axial stresses and texture development during torsion testing: a simplified theory. Acta Metall 1985 (33) 705-718.
[49] Houtte PV. Calculation of the yield locus of textured polycrystals using the Taylor and the related Taylor theories. Texture Microstruct 1987 (7) 29-72.
[50] Lequeu Ph, Gilormini P, Montheillet F, Bacroix B, Jonas JJ. Yield surfaces for textured polycrystals – I. Crystallographic approach. Acta Metall 1987 (35) 439-451.
[51] Lequeu Ph, Gilormini P, Montheillet F, Bacroix B, Jonas JJ. Yield surfaces for textured polycrystals – II. Analytical approach. Acta Metall 1987 (35) 1159-1174.
[52] Arminjon M. A regular form of the Schmid law. Application to the ambiguity problem. Texture Microstruct 1991 (14-18) 1121-1128.

[53] Darrieulat M, Piot D. A method of generating analytical yield surfaces of crystalline materials. Int J Plast 1996 (12) 575-610.
[54] Gambin W. Plasticity of crystals with interacting slip systems. Eng Trans 1991 (39) 303-324.
[55] Gambin W. Refined analysis of elastic-plastic crystals. Int J Solids Struct 1992 (29) 2013-2021.
[56] Gambin W, Barlat F. Modeling of deformation texture development based on rate independent crystal plasticity. Int J Plast 1997 (13) 75-85.
[57] Zamiri A, Pourboghrat F, Barlat F. An effective computational algorithm for rate-independent crystal plasticity based on a single crystal yield surface with an application to tube hydroforming. Int J Plast 2007 (23) 1126-1147.
[58] Kowalczyk K, Gambin W. Model of plastic anisotropy evolution with texture-dependent yield surface. Int J Plast 2004 (20) 19–54.

Chapter 4

Dislocation-based constitutive model of crystal plasticity for the size effect of single crystalline and Bi-crystalline micro pillar samples

In the last chapter, the size dependent yielding has been investigated physically. In this chapter, a constitutive model with the CPFE framework that accounts for dislocation physics is developed to describe the size-dependent deformation of single crystalline or bi-crystalline micro pillars. The relationship between the dislocation density and the plastic strain is derived based on the Orowan equation and the principle of Bergstrom dislocation evolution, and the physical model of yield stress is provided from the SAS model and the crystalline material yield function. We then redefined the original Peirce, Asaro, and Needleman (PAN) hardening model by considering the effective dislocation length and dislocation evolution. Finally, the yield stresses and redefined PAN model are included in the CPFE model. The dislocation evolution parameters are determined by fitting to the experimental data, and they are used to describe the size-dependent characteristics of plastic flow. Further discussion about the friction effect between the punch and the top surface of the pillar under uniaxial compression is given based on the stress–strain response and shear band deformation inside the pillar.

4.1 Description of plastic strain based on dislocation evolution

4.1.1 Relationship between plastic strain and dislocation density under uniaxial compression

The total dislocation density can be expressed as

$$\rho_{\text{total}} = \rho_{\text{mobile}} + \rho_{\text{trapped}}, \tag{4.1}$$

where ρ_{total} is the total dislocation, ρ_{mobile} is the mobile dislocation and ρ_{trapped} is the trapped dislocation. The rate of plastic shear strain $\dot{\gamma}_p$ in any slip system can be expressed according to the Orowan equation as

$$\dot{\gamma}_p = \rho_{\text{mobile}} b \bar{v}, \tag{4.2}$$

where $\bar{v}$ is the average velocity of dislocations and b is the Burgers vector. Assuming that the mobile dislocation density is not dependent to time because of the dislocation movement in a short time, Eq. (4.2) can be integrated simply according to time. By averaging the quantities for the whole single crystalline pillar with one or a few active slip systems, Eq. (4.2) is reformulated using the uniaxial plastic compressive strain ε_p of the whole single crystalline pillar and the average total length of mobile dislocation $\bar{L}_m$ as follows:

$$\varepsilon_p = \rho_{\text{mobile}} b \bar{L}_m, \tag{4.3}$$

$\bar{L}_m$ can be expressed by the average length of the mobile dislocation and the number of mobile dislocation as [1]

$$\bar{L}_m = n\overline{d_m} = n / \sqrt{\rho_{\text{mobile}}}, \tag{4.4}$$

where n is the number of mobile dislocations and $\overline{d_m}$ is the average length of the mobile dislocations. n is related to the sample dimensions and initial dislocation density for the case of micro-sized pillars [2]:

$$n = \text{Integer}[\frac{\rho_0 \pi R^2}{s}], \tag{4.5}$$

where R is the radius of the pillar specimen, and s is the number of slip systems. In this paper, the parameters are selected to be s = 12 for face-centered cubic (fcc) crystals. In this case, by substituting Eq. (4.4) into Eq. (4.3), the following equation can be obtained:

$$\rho_{\text{mobile}} = (\varepsilon_p / bn)^2 . \tag{4.6}$$

According to the principle of Bergstrom dislocation evolution [1], the trapped dislocation density can be expressed as

$$\rho_{\text{trapped}} = \frac{1}{\Omega^2}\{k^* - \frac{k^* - \Omega\sqrt{\rho_0}}{\exp(\Omega\varepsilon_p / 2)}\}^2 . \tag{4.7}$$

where ρ_0 is the initial dislocation density, and k^* and Ω are the parameters of dislocation evolution on the increase of trapped dislocation and the dislocation annihilation, respectively. We assume that the initial dislocation is only the initial trapped dislocation, because there are very few initial mobile dislocations for the micro pillars [2, 3].

Therefore, the total dislocation density can be obtained by substituting Eqs. (4.7) and (4.6) into Eq. (4.1):

$$\rho_{\text{total}} = \rho_{\text{mobile}} + \rho_{\text{trapped}} = (\varepsilon_p / bn)^2 + \frac{1}{\Omega^2}\{k^* - \frac{k^* - \Omega\sqrt{\rho_0}}{\exp(\Omega\varepsilon_p / 2)}\}^2 . \tag{4.8}$$

The dislocation evolution parameters (k^* and Ω) are determined from the

experimental data, which will be introduced in the next section.

4.1.2 Initial yield stress and constitutive equation of the extended SAS model

According to the theory of dislocation starvation and exhaustion, the statistical behavior of dislocations is used to describe the strength [2, 4-7]. Based on this view, the SAS model derived from statistical mechanics can be used to describe the size-dependent strength of SCMs [2].

The critical resolved shear stress (CRSS) of micropillars is related to the effective dislocation source length λ. Thus, it can be expressed as the SAS model [2]:

$$\tau_{\mathrm{SAS}}^{0} = \tau_0 + 0.5\mu b\sqrt{\rho_0} + \frac{\alpha\mu b}{\overline{\lambda}_{\max}}, \tag{4.9}$$

where μ is the shear modulus, τ_0 is the Peierls–Nabarro stress, α is the constant and $\overline{\lambda}_{\max}$ is the effective average longest length of the dislocation sources (remind that $\overline{\lambda}_{\max}$ is dependent to the radius of pillar, as written in ref. [5]). Equation (4.9) is used to describe the initial yield stress accounting for the initial dislocation density ρ_0.

If the subsequent plastic process is represented, the SAS model can be extended to express the function of the dislocation density ρ and the plastic strain ε_p instead. In this case, Eq. (4.8) should be used to describe the evolution of dislocations in the micro pillars according to the plastic strain. Therefore, substituting Eq. (4.8) into Eq. (4.9), the shear stress on the slip plane is

$$\tau_{\mathrm{SAS}}^{f} = \tau_0 + 0.5\mu b\left[(\varepsilon_p / bn)^2 + \frac{1}{\Omega^2}\left\{k^* - \frac{k^* - \Omega\sqrt{\rho_0}}{\exp(\Omega\varepsilon_p / 2)}\right\}^2\right]^{0.5} + \frac{\alpha\mu b}{\overline{\lambda}_{\max}}, \tag{4.10}$$

where $\overline{\lambda}_{\max}$ can be simulated using the statistics method [2].

The τ_{SAS}^{0} and τ_{SAS}^{f} values are used to describe the CRSS and the subsequent yield shear stress of the micro pillars, respectively. The τ_{SAS}^{0} in Eq. (4.9) agrees well with experimental data [2]. However, the values of the parameters k^* and Ω in Eq. (4.10) are still unknown. In the following, the values of these parameters will be determined by fitting to the experimental data.

4.1.3 Determination of k^* and Ω

By substituting Eq. (4.10) into the equation $\sigma = M_\sigma \tau_{\mathrm{SAS}}^{f}$ under uniaxial compression, where M_σ is Taylor-like factor which phenomenologically links the local shear stress to the global uniaxial stress [8, 9], the hardening ratio θ can be expressed by differentiation as

$$\theta = \frac{d\sigma}{d\varepsilon_p} = \frac{M_\sigma \mu b}{4\sqrt{\rho_{\mathrm{total}}}} \frac{2}{nb} (\varepsilon_p / nb) + \frac{M_\sigma \mu b}{4\sqrt{\rho_{\mathrm{total}}}} (k^* \sqrt{\rho_{\mathrm{trapped}}} - \Omega \rho_{\mathrm{trapped}}) = \theta^m + \theta^t . \tag{4.11}$$

θ^m and θ^t are the hardening rate affected by mobile dislocations and the hardening rate affected by trapped dislocations, respectively. That is,

$$\theta^m = \frac{M_\sigma \mu b}{4\sqrt{\rho_{\mathrm{total}}}} \frac{2}{nb} (\varepsilon_p / nb), \tag{4.12}$$

When $\varepsilon_p = 0$, θ_y is the hardening rate at the initial yielding, which can be obtained as $\theta_y = \theta\ (\varepsilon_p = 0)$. Thus,

$$\theta_y = \frac{M_\sigma \mu b}{4} (k^* - \Omega \sqrt{\rho_0}), \tag{4.13}$$

Differentiating Eq. (4.7) with respect to plastic strain ε_p, it gives

$$\frac{d\rho_{\text{trapped}}}{d\varepsilon_p} = k^* \sqrt{\rho_{\text{trapped}}} - \Omega\rho_{\text{trapped}} \,. \tag{4.14}$$

Integrating Eq. (4.14), the relationship between the plastic strain and the trapped dislocation density is

$$\varepsilon_p = \frac{2}{\Omega}\ln\left(\frac{k^* - \Omega\sqrt{\rho_0}}{k^* - \Omega\sqrt{\rho_{\text{trapped}}}}\right) = \frac{2}{\Omega}\ln\left(\frac{\sqrt{\rho_{\text{trapped}}}\theta_y}{\sqrt{\rho_{\text{total}}}\theta^t}\right), \tag{4.15}$$

where

$$\theta^t = \frac{\sqrt{\rho_{\text{trapped}}}}{\sqrt{\rho_{\text{total}}}}\theta_y \exp(-\frac{\Omega\varepsilon_p}{2}) \,. \tag{4.16}$$

The stress σ can be obtained by substituting Eqs. (4.16) and (4.12) into Eq. (4.11) and then integrating:

$$\sigma - \sigma_0 = \frac{2\theta_y}{\Omega}\frac{\sqrt{\rho_{\text{trapped}}}}{\sqrt{\rho_{\text{total}}}}[1 - \exp(-\frac{\Omega\varepsilon_p}{2})] + \frac{M_\sigma \mu b}{4\sqrt{\rho_{\text{total}}}}(\varepsilon_p / nb)^2 \,. \tag{4.17}$$

where σ_0 is the experimental initial yield stress. Equations (4.8), (4.11), and (4.17) can be used to obtain the dislocation evolution parameters (k^* and Ω) by fitting to the experimental data with the least-squares method.

The fitted results of SCMs are shown in Figures 4-1 and 4-2. In Figure 4-1, Eq. (4.17) was used to fit the Ni experiment data [10, 11] with the least-squares method, and the determined parameters are given in Table 4-1. In Figure 4-2, the same method was used to obtain the parameters of Cu by comparing with the experiments for the pillars with diameter d ~ 1 μm and d ~ 4 μm [12], and the results are also given in Table 4-1. In Figures. 4-1a and b, the hardening flows for d ~ 10 μm and ~ 20 μm involving a series of small strain bursts are close to that of the bulk material [10]. In Figure 1c, the hardening flow for d ~ 5 μm specimens includes obvious strain bursts,

and the hardening process shows different evolution of dislocations from the bulk material, which is the size effect of hardening flow [10]. In Figure 4-2, the hardening flow for $d \sim 1$ μm is more than twice as strong as that for $d \sim 4$ μm. In Table 1, the k^* and Ω values for $d \sim 10$ and ~ 20 μm in Ni are nearly the same. Meanwhile, the k^* value for $d \sim 5$ μm in Ni is larger than that for $d \sim 10$ μm, and the Ω value for $d \sim 5$ μm in Ni is smaller than that for $d \sim 10$ μm. The same conclusion can be obtained by comparing the data of Cu in Table 4-1. That is, the material of the smaller micro pillars has a larger k^* value and a smaller Ω value, which suggests more active dislocation evolution.

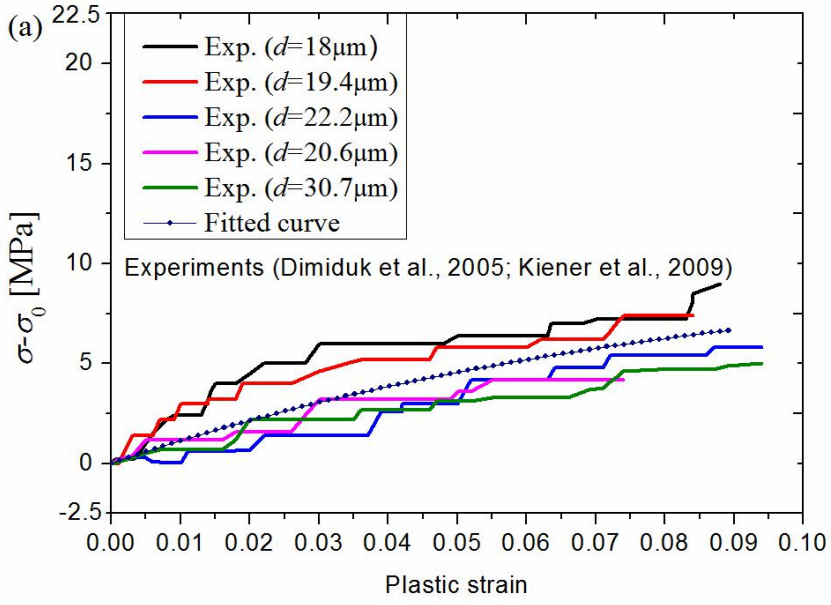

(a) diameter $d \sim 20$ μm

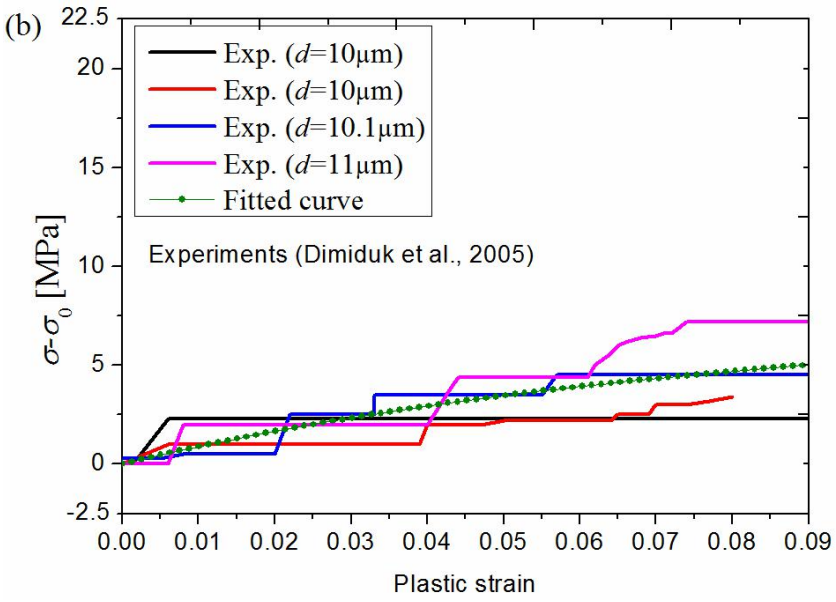

(b) diameter $d \sim 10$ μm

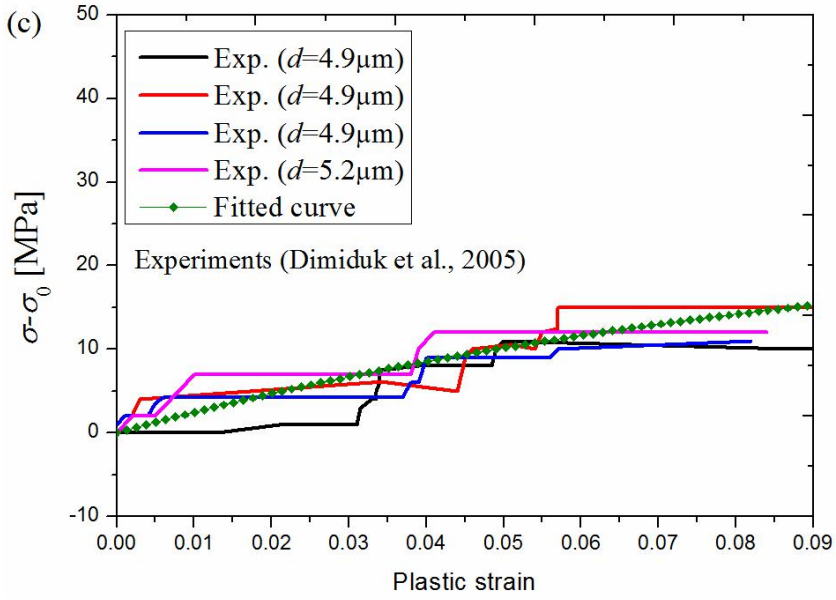

(c) $d \sim 5$ μm

Figure 4-1. Parameter determination of dislocation evolution from the experimental results of Ni with (a) diameter $d \sim 20$ μm, (b) $d \sim 10$ μm, and (c) $d \sim 5$ μm [10, 11].

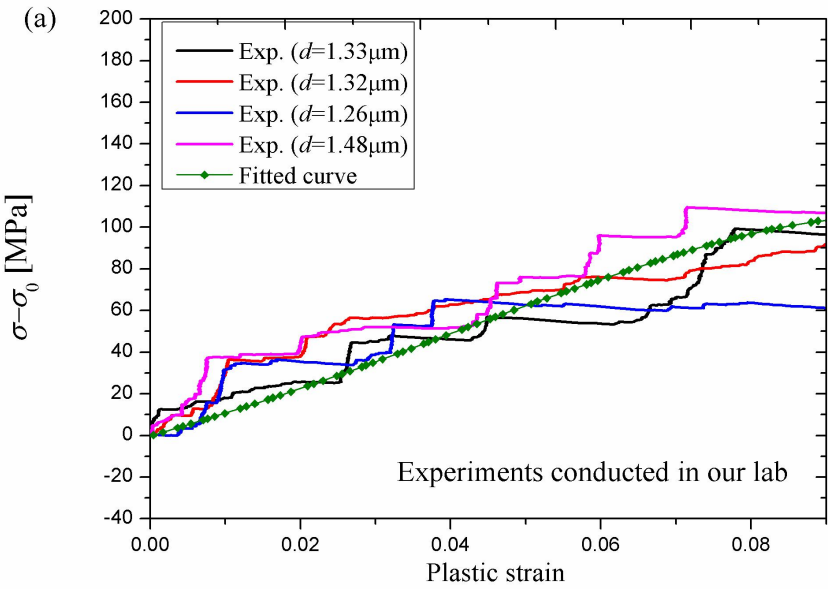

(a) diameter $d \sim 1$ μm

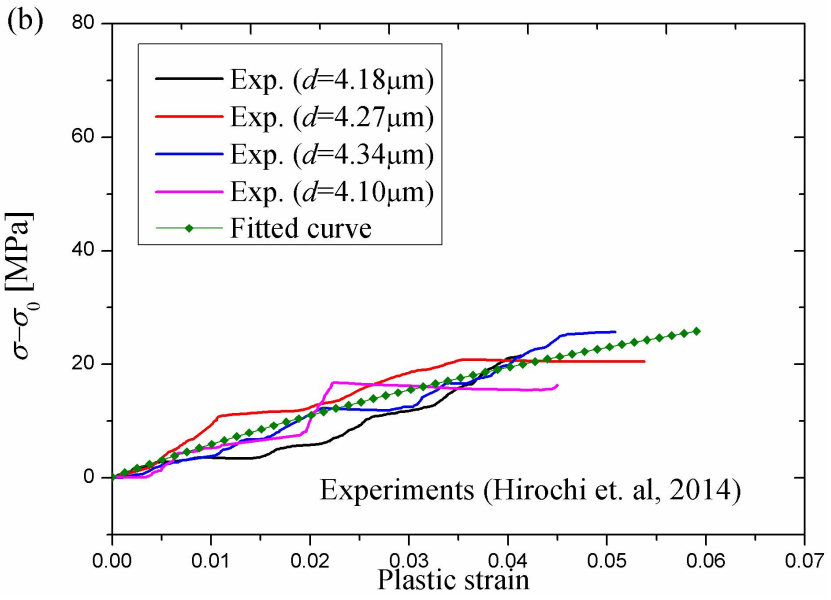

(b) $d \sim 4$ μm

Figure 4-2. Parameter determination of dislocation evolution from the experimental results of Cu with (a) diameter $d \sim 1$ μm and (b) $d \sim 4$ μm [12].

Table 4-1 Dislocation evolution parameters fitted to experimental data.

	θ_y [MPa]	k^* [μm^{-1}]	Ω
Ni (5 μm)	276	56.2	20.3
Ni (10 μm)	85.7	45.6	25.6
Ni (20 μm)	129	47.1	23.3
Cu (1 μm)	1420	176	12.5
Cu (4 μm)	394	68.2	17.4

4.2 Continuum Crystal plasticity model

The kinematics of FCC crystals described below is well-established and the detailed formulations are given in literature [13]. The total deformation gradient tensor $\boldsymbol{F}$ can be decomposed into the elastic tensor $\boldsymbol{F}_e$, and the plastic tensor $\boldsymbol{F}_p$:

$$\boldsymbol{F} = \boldsymbol{F}_e \boldsymbol{F}_p, \tag{4.18}$$

where $\boldsymbol{F}_e$ represents the rotation and stretching of the lattice, $\boldsymbol{F}_p$ represents the plastic shear of the materials that do not change the lattice orientation and spacing. The plastic velocity gradient is defined as

$$\boldsymbol{L}_p = \boldsymbol{F}_e \cdot \dot{\boldsymbol{F}}_p \cdot \boldsymbol{F}_p^{-1} \cdot \boldsymbol{F}_e^{-1} = \sum_{\alpha=1}^{n} \dot{\gamma}^{\alpha} \boldsymbol{s}_{\alpha}^{*} \otimes \boldsymbol{m}_{\alpha}^{*}, \tag{4.19}$$

where $\boldsymbol{s}_\alpha$ and $\boldsymbol{m}_\alpha$ are the unity normal direction vector and the sliding direction vector in the α sliding system, and

$$\boldsymbol{m}_{\alpha}^{*} = \boldsymbol{m}_{\alpha} \cdot \boldsymbol{F}_e^{-1}, \tag{4.20}$$

$$\boldsymbol{s}_{\alpha}^{*} = \boldsymbol{F}_e \cdot \boldsymbol{s}_{\alpha}. \tag{4.21}$$

The symmetric tensor $\boldsymbol{P}^{\alpha}$ and the skew-symmetric tensor $\boldsymbol{Q}^{\alpha}$ are introduced here.

$$\boldsymbol{P}^{\alpha} = \frac{1}{2}(\boldsymbol{s}_{\alpha}^{*} \otimes \boldsymbol{m}_{\alpha}^{*} + \boldsymbol{m}_{\alpha}^{*} \otimes \boldsymbol{s}_{\alpha}^{*}), \tag{4.22}$$

$$\boldsymbol{Q}^{\alpha} = \frac{1}{2}(\boldsymbol{s}_{\alpha}^{*} \otimes \boldsymbol{m}_{\alpha}^{*} - \boldsymbol{m}_{\alpha}^{*} \otimes \boldsymbol{s}_{\alpha}^{*}). \tag{4.23}$$

The plastic stretching tensor $\dot{\boldsymbol{D}}_p$ and the plastic spin $\dot{\boldsymbol{\omega}}_p$ can be represented as:

$$\dot{\boldsymbol{D}}_p = \sum_{\alpha=1}^{n} \dot{\gamma}^{\alpha} \boldsymbol{P}^{\alpha}, \tag{4.24}$$

$$\dot{\boldsymbol{\omega}}_p = \sum_{\alpha=1}^{n} \dot{\gamma}^{\alpha} \boldsymbol{Q}^{\alpha}, \tag{4.25}$$

in which the strain rate $\dot{\gamma}^{\alpha}$ in the α sliding system is shown in the Eqs. (4.24) and (4.25). The Eq. (4.19) can be expressed as

$$\boldsymbol{L}_p = \dot{\boldsymbol{D}}_p + \dot{\boldsymbol{\omega}}_p. \tag{4.26}$$

The Jaumann stress rate $\hat{\boldsymbol{\sigma}}$ can be expressed as

$$\hat{\boldsymbol{\sigma}} = \boldsymbol{L} : \dot{\boldsymbol{\varepsilon}} - \sum_{\alpha=1}^{n} \boldsymbol{\Gamma}^{\alpha} \dot{\gamma}^{\alpha}, \tag{4.27}$$

in which

$$\boldsymbol{\Gamma}^{\alpha} = \boldsymbol{C} : \boldsymbol{P}^{\alpha} + \boldsymbol{Q}^{\alpha} \cdot \boldsymbol{\sigma} - \boldsymbol{\sigma} \cdot \boldsymbol{Q}^{\alpha}, L_{ijmn} = C_{ijmn} - \sigma_{ij}\delta_{mn} \tag{4.28}$$

where $\boldsymbol{C}$ is the elastic modulus tensor, $\boldsymbol{\sigma}$ is the Cauchy stress, and $\dot{\boldsymbol{\varepsilon}}$ is the strain rate tensor. The constitutive equation can be represented in Eq. (4.27). The mixed shear component of Kirchhoff stress $\boldsymbol{\tau}$ on coordinates which convert the lattice:

$$\dot{\boldsymbol{\tau}} = \boldsymbol{m}_{\alpha}^{*} \cdot (\boldsymbol{L} : \dot{\boldsymbol{\varepsilon}} - \sum_{\alpha=1}^{n} \boldsymbol{\Gamma}^{\alpha} \dot{\gamma}^{\alpha}) \cdot \boldsymbol{s}_{\alpha}^{*} \tag{4.29}$$

4.3 Hardening law accounting for the size effect in fcc pillars

The strain hardening is characterized by the evolution of the current resistant

strength $\dot{\tau}_c^\alpha$ for describing the variance of the dislocations on that slip system:

$$\dot{\tau}_c^\alpha = \sum_{\beta=1}^{n} h_{\alpha\beta}\dot{\gamma}^\beta \tag{4.30}$$

where $h_{\alpha\beta}$ is the hardening modulus and the sum includes all activated slip systems. The diagonal components $h_{\alpha\alpha}$ and the off-diagonal components $h_{\alpha\beta}$ represent the self-hardening and latent-hardening effects, respectively. Accordingly, the gliding dislocation under the action of the resolved shear stress τ^α is obtained by the Schmid's law:

$$\tau^\alpha = \boldsymbol{P}^\alpha : \boldsymbol{\sigma} \tag{4.31}$$

For FCC metals, one commonly-used phenomenological hardening law is the Pierce-Asaro-Needleman (PAN) model suggested by Pierce, Asaro and Needleman [14]. In this model, the hardening modulus $h_{\alpha\beta}$ takes the form:

$$h_{\alpha\beta}(\gamma) = H_{\alpha\beta}(\gamma) + \frac{1}{2}(\boldsymbol{\beta}^\beta : \boldsymbol{P}^\alpha - \boldsymbol{\beta}^\alpha : \boldsymbol{P}^\beta) \tag{4.32}$$

where

$$\boldsymbol{\beta}^\alpha = \boldsymbol{Q}^\alpha \cdot \boldsymbol{\tau} - \boldsymbol{\tau} \cdot \boldsymbol{Q}^\alpha \tag{4.33}$$

In this model, the hardening matrix $H_{\alpha\beta}$ in Eq. (4.32) takes the form

$$H_{\alpha\beta}(\gamma) = H_{\beta\beta}(\gamma)[q + (1-q)\delta_{\alpha\beta}] \tag{4.34}$$

where

$$H_{\beta\beta}(\gamma) = H_0 \operatorname{sech}^2\left(\frac{H_0\gamma}{\tau_s - \tau_0}\right) \text{ and } \gamma = \sum_{\alpha=1}^{n} \left| \gamma_p^{(\alpha)} \right|. \tag{4.35}$$

Here, q describes the latent hardening effect and is assumed to be 1.0 for coplanar and 1.4 for non-coplanar slip systems [13]. In this study, we chose q = 1 to describe the micro pillars according to the recommendation of ref. [15]. $H_{\alpha\beta}$ is a symmetric tensor,

and in their model, H_0 is the initial hardening modulus, n = 12 for fcc materials, τ_0 is the initial value of the yield stress, and τ_s is the saturated shear stress at the stage of finite plastic deformation. A number of experimental compression tests on micro pillars have found that their stress–strain curves appear to remain in the easy glide stage throughout the tests, and this is supported by the observation of postmortem transmission electron microscopy of nickel specimens [16]. It thus seems to be appropriate to use the strain hardening model to characterize the experimental stress–strain curve. The PAN hardening laws for bulk materials have been widely discussed [17]. However, there is no physical analysis of the hardening at the microscale.

In the PAN model, τ_0 and τ_s are provided by the experimental data without any physical parameters related to the size, and they cannot provide a physical understanding. The values of the current strength and the initial yield shear stress are provided in an appropriate way, such as based on experimental data or simulation definitions [3, 15]. However, the hardening behavior in the micro pillars is different from the bulk material, including multiplication of dislocations, boundary annihilation [18, 19], and displacement burst [15, 20]. Here, we attempt to add the effect of dislocation evolution and size-dependent yield stress into the hardening model.

In the PAN hardening model, τ_s is the saturated shear stress at the stage of finite plastic deformation. If we replace τ_0 and τ_s by τ_{SAS}^0 and τ_{SAS}^f, τ_{SAS}^f should be the saturated shear stress of the micropillars, and then $\varepsilon_p = \varepsilon_s$, where ε_s is the strain corresponding to τ_s. The revised form of the PAN hardening model can be written as

$$H_{\beta\beta}(\gamma) = H_0 \mathrm{sech}^2\left(\frac{H_0\gamma}{\tau_{\mathrm{SAS}}^f - \tau_{\mathrm{SAS}}^0}\right). \tag{4.36}$$

$$\tau_{\mathrm{SAS}}^{f}-\tau_{\mathrm{SAS}}^{0}=0.5\mu b\left[(\varepsilon_p/bn)^2+\frac{1}{\Omega^2}\left\{k^*-\frac{k^*-\Omega\sqrt{\rho_0}}{\exp(\Omega\varepsilon_p/2)}\right\}^2\right]^{0.5}-0.5\mu b\sqrt{\rho_0} \tag{4.37}$$

In Eq. (4.37), the hardening model includes the dislocation evolution parameters (those are k^* and Ω). The initial yield stress is replaced by τ_{SAS}^{0}, which can express the size-dependent properties. The difference between τ_{SAS}^{0} and τ_{SAS}^{f} in Eq. (4.37) is shown in Figure 4-3 by setting k^* and Ω constant to examine the effect of n.

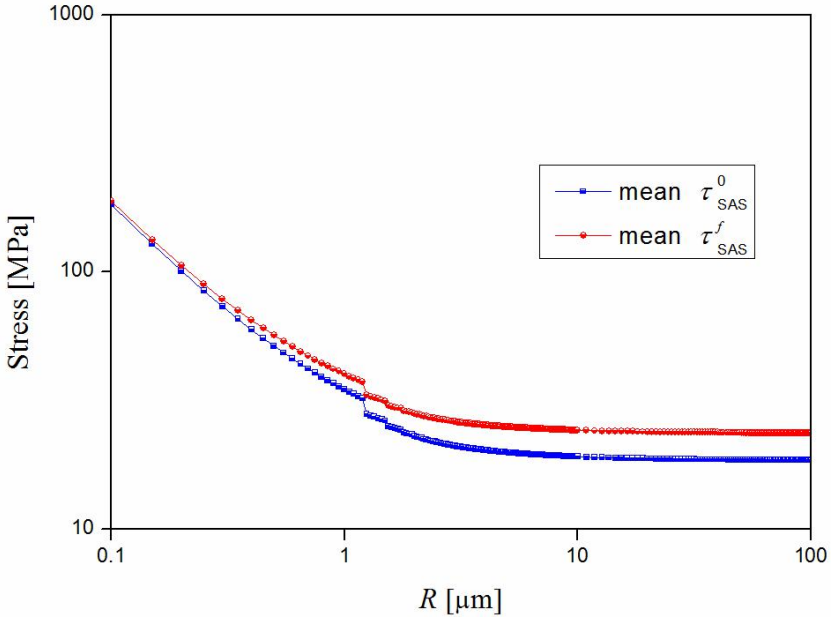

Figure 4-3. Comparison of τ_{SAS}^{0} and τ_{SAS}^{f} for different R values.

When R > 10 μm, the difference between τ_{SAS}^{0} and τ_{SAS}^{f} is nearly constant because the value of n is large enough to make the term $(\varepsilon_p/bn)^2$ be nearly 0. This presents that the hardening modulus is size independent when the diameter is sufficiently large. In this range, the original PAN hardening model without considering the size effect is reasonable. However, if R < 10 μm, the size-dependent difference of τ_{SAS}^{0} and τ_{SAS}^{f} makes the hardening modulus size-dependent as the

value of n is small in the range of 10^0~10^1.

From Eqs. (4.36) and (4.37), the hardening modulus is related to the dislocation evolution parameters. The parameters are selected from the articles of [2, 5, 8], and they are given in Table 4-2. Figure 4-4 shows that the hardening modulus of Cu is affected by the characteristics of dislocation evolution by k^* and Ω. The parameters of the original PAN model are $H_0 = 56.8\text{MPa}$, $\tau_0 = 41.1\text{MPa}$, and $\tau_s = 1.53\tau_0$ [20]. In Figure 4-4a, the original PAN hardening model is compared with the revised PAN hardening model with different k^* and $\Omega = 17.4$. Figure 4-4b shows the hardening modulus of Cu with different Ω values and $k^* = 68.2\ \mu\text{m}^{-1}$. The dislocation evolution parameters result in different hardening modulus, as shown in Figure 4-4. As shown in Table 4-1, k^* and Ω are size dependent. That is, the hardening modulus should be different to account for the different size by using different values of k^* and Ω.

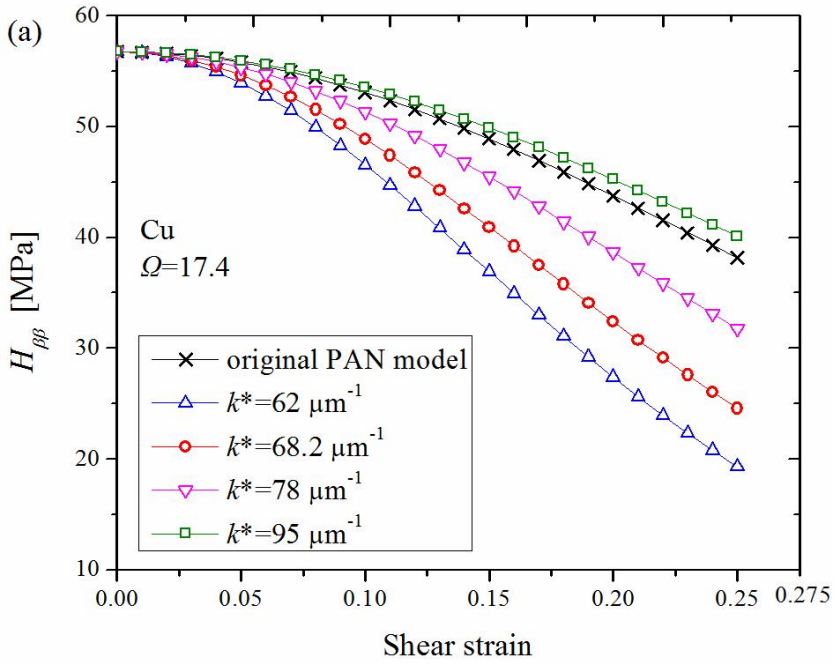

(a) the effect of k^*

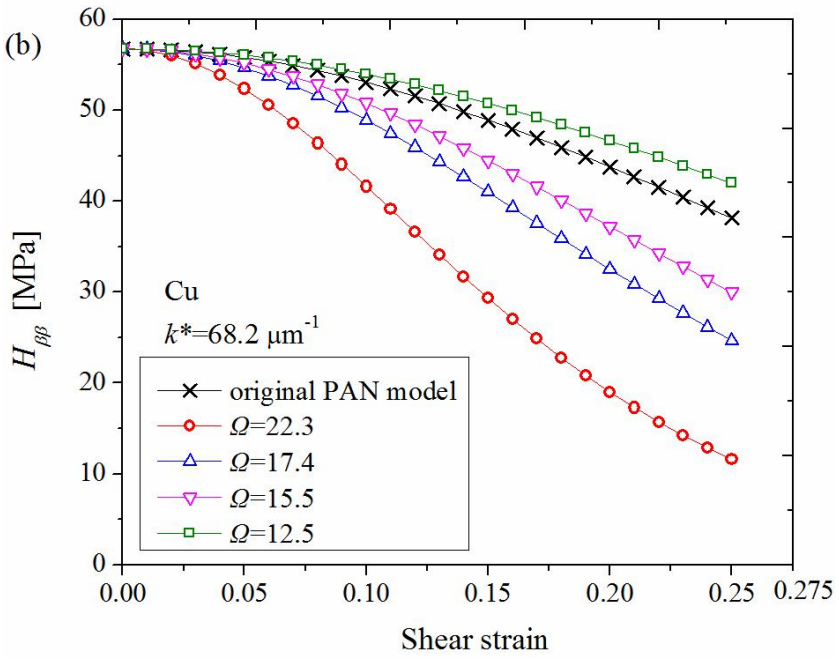

(b) the effect of Ω

Figure 4-4. Effect of dislocation evolution on the hardening modulus for (a) different k* and (b) different Ω.

Table 4-2 Parameters used in the extended SAS model and CPFE

Parameters	Values	Parameters	Values
ρ_0 [m^{-2}]	2×10^{12}	b [nm]	0.255
τ_0 [MPa] Eq. (4.10)	12	k* [μm^{-1}]	176 (d = 1 μm) 68.2 (d = 4 μm)
μ [GPa]	48		
υ	0.3	Ω	12.5 (d = 1 μm) 17.4 (d = 4 μm)

4.4 Finite element model of Cu single crystalline micro pillar compression test

We performed finite element (FE) analyses using a user material subroutine (UMAT) in the commercial code ABAQUS/Standard (2012). In UMAT, initial yield

stresses and subsequent yield stresses, which are introduced in Section 4.1.2, and the present redefined hardening model, which is introduced in Section 4.3, are implemented in the CPFE framework introduced in Section 4.2. The normal micro pillar axes are set to the [6 11 5] and [6 1 5] surface orientations, which are the same as experiments [12]. In the calculations, we performed the compression tests with a flat punch, which is treated as the rigid body, as shown in Figure 4-5. In addition, isothermal conditions were assumed and the specimens were kept at room temperature. Pillars with diameters of 1 and 4 μm were simulated, and the height-to-diameter aspect ratio was fixed at 2.5 in all of the simulations. For simplicity, the FE model consisted of a single 8-node brick-type element (C3D8). The displacements were applied along the *y* direction associated with a constant strain rate of 1.0×10^{-4} s^{-1}. A base material at the bottom of the pillar was included to simulate to the real boundary condition of the samples.

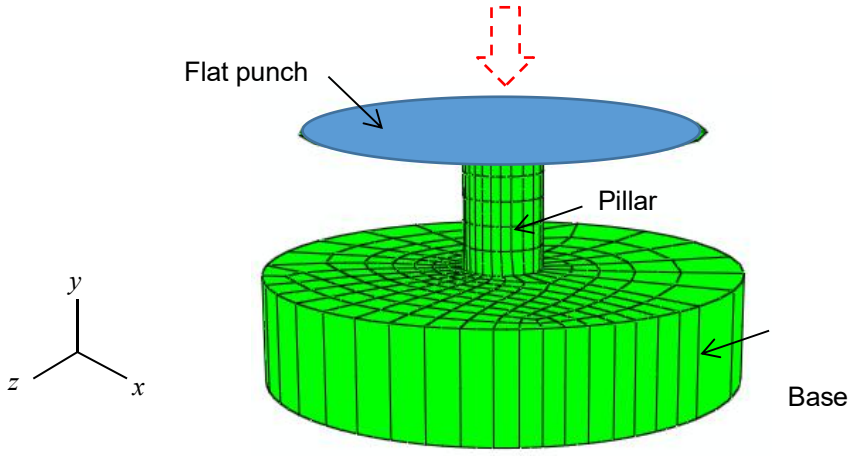

Figure 4-5. Finite element model of micro pillar and the boundary conditions.

The material parameters used in the simulations are given in Table 4-2. The elastic moduli [21] and the related parameters of the FEM simulations are given in Table 4-3. The CRSS was chosen as τ^{0}_{SAS} in Eq. (4.9), which is dependent on the scale. The

initial hardening moduli H_0 was determined using a similar approach to a previously published method [15, 20].

Table 4-3 CPFE parameters.

Parameters	Values
c_{11} [GPa]	168.4
c_{12} [GPa]	121.4
c_{22} [GPa]	75.4
ε_s	0.3
H_0 [MPa]	283.8 (d = 1 μm), 78.5 (d = 4 μm)

4.4.1 Stress–strain responses

Figure 4-6 shows the relationship between compressive stress and plastic strain obtained from the FEM simulations using the original PAN hardening model and the revised PAN hardening model. Because the size-dependent yield stress is based on the initial distribution of dislocations, the initial yield stress might not agree well with the experimental results. Therefore, we compare the net stress $\sigma - \sigma_{\mathrm{SAS}}^{0}$. Compression of Cu pillars was performed for the samples with diameters of $d \sim 4$μm for the [6 11 5] surface axis and $d \sim 1$μm for the [6 1 5] surface axis using the dislocation evolution parameters k^* = 68.2 μm^{-1} and Ω = 17.4, and k^* = 176 μm^{-1} and Ω = 12.5, respectively. The original PAN hardening model chooses $\tau_s = 1.53\tau_0$ [20]. In Figure 4-6, the flow stress of the original PAN hardening model is almost the same as that of the revised PAN hardening model when the strain is small. However, the flow stress of the original PAN hardening model is larger than that of the revised PAN hardening model when the strain is large. The reason is that the original PAN hardening modulus is much larger than the revised PAN modulus when the strain is large, as shown in

Figure 4-4. Compared with the curves of revised PAN model in Figures 4-6a and b, the flow stresses are quite different because of the different sets of k^* and Ω, as shown in Figure 4-4.

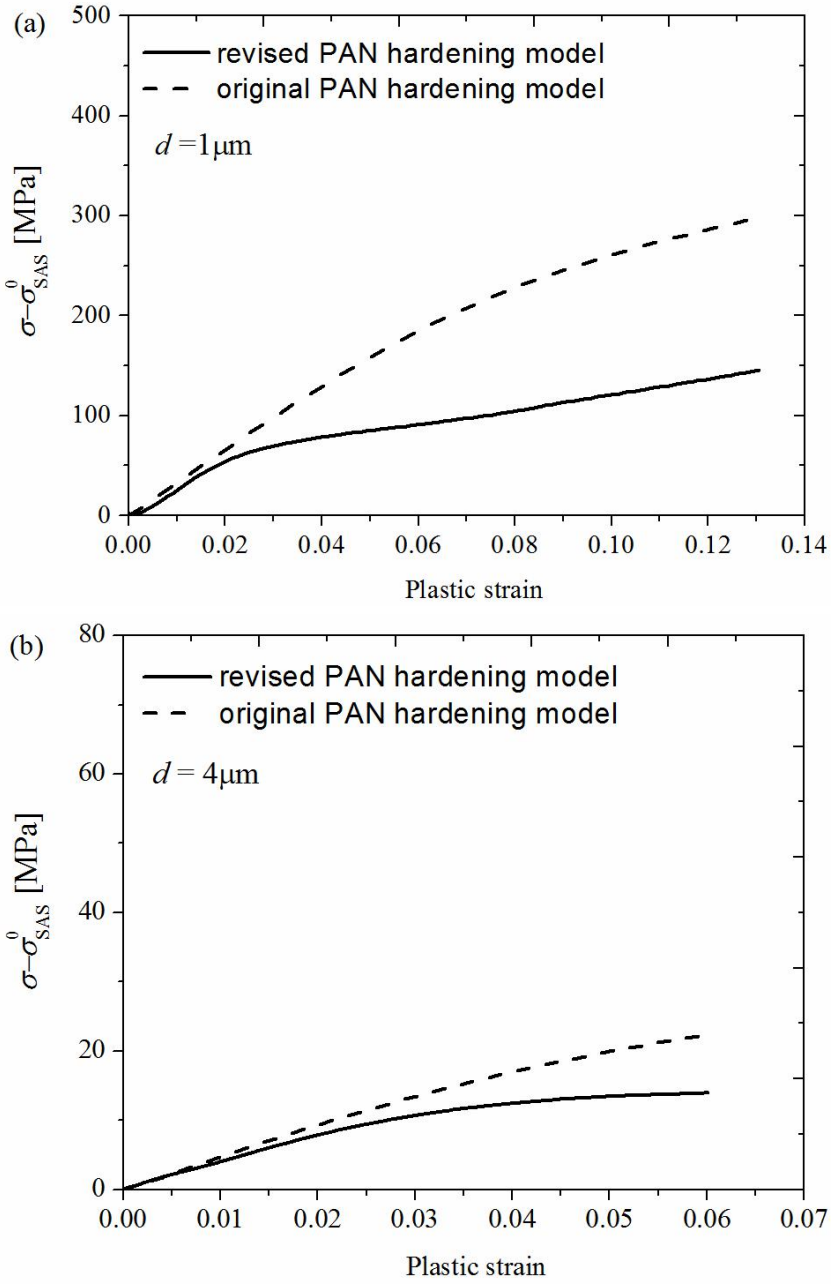

Figure 4-6. Comparisons of the hardening flows between the revised PAN and the original PAN models for the compression tests of [6 11 5] and [6 1 5] copper pillars with diameters of (a) 1 μm and (b) 4 μm, respectively.

In the CPFE model, size-dependent hardening is dominated by the

dislocation-based hardening model (Eq. (4.36)). In Figure 4-2, the hardening flows of the experiments show several bursts, which have been studied by the FEM analyses [15]. However, it is very hard to determine the time when a displacement burst will occur and the magnitude of the displacement burst. How to provide the exact response considering such a displacement is still an open issue, which needs more investigation. In this study, the average value of the plastic response is used for discussion.

Figure 4-7a shows the stress–strain responses with different k^* values and Ω = 17.4. The stress with a high k^* value is larger than that with a small k^* value. Compared with Figure 4-4a, a higher hardening modulus results in a larger stress–strain response. Similar results were obtained with different Ω values and k^* = 68.2 μm^{-1} because the larger stress–strain response is dominated by the hardening modulus (see Figure 4-7b). In this part, the friction between the flat punch and top surface of pillar is considered by setting the friction coefficient f equal to 0.2. The influence of friction coefficient will be discussed in section 4.4.3.

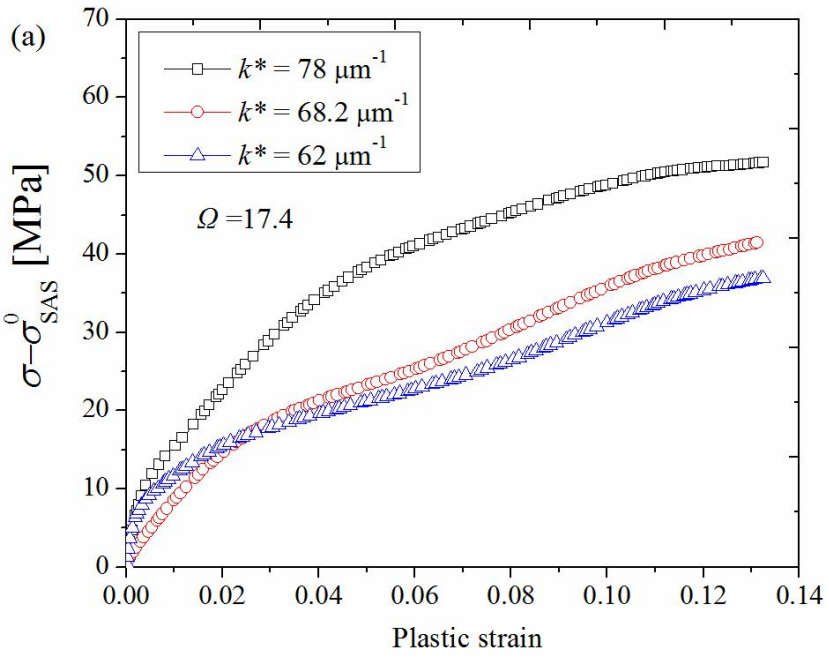

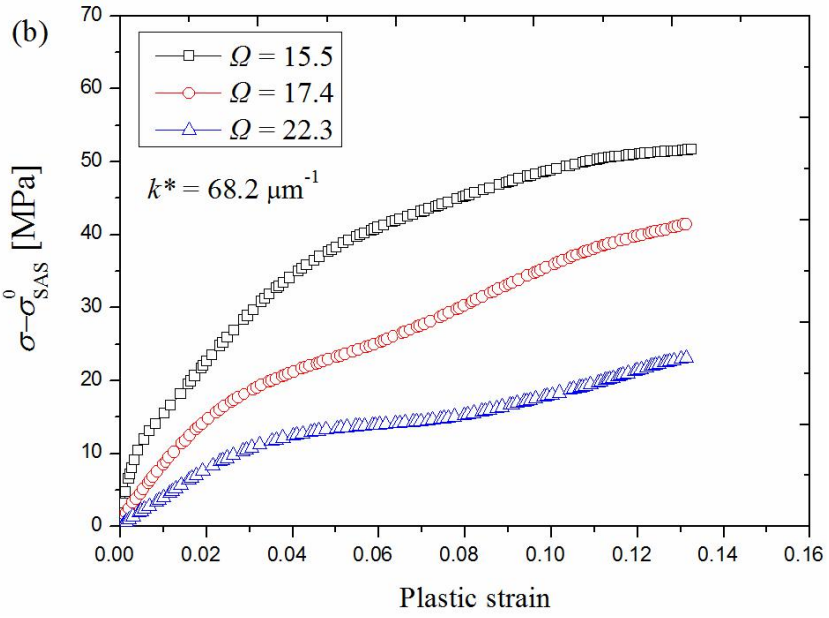

Figure 4-7. Dislocation evolution effect on hardening for (a) different k^* and (b) different Ω.

4.4.2 Shear deformations inside the pillar

Figure 4-8 shows a comparison of the scanning electron microscopy (SEM) image of the compressed pillar with the crystalline orientation [6 11 5] and the FEM deformed mesh image. In the FEM deformed image, the color represents the scaled magnitude of displacement in the micropillars for displaying. The slip band in the SEM image has an angle of around 50° with respect to the normal axis and occurs along the $(1\ 1\ \bar{1})$ [0 1 1] slip plane, which is the crystalline system with the maximum Schmid factor. The deformation band is similar to the experimental results.

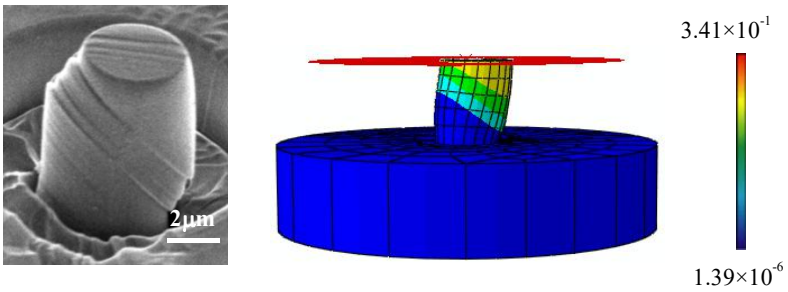

Figure 4-8. Comparison of the SEM image and the FEM deformed mesh image (displacement image) at normal compressive strain of $\varepsilon = 0.134$. The color of the FEM image indicates the scaled magnitude of displacement in the micro pillar.

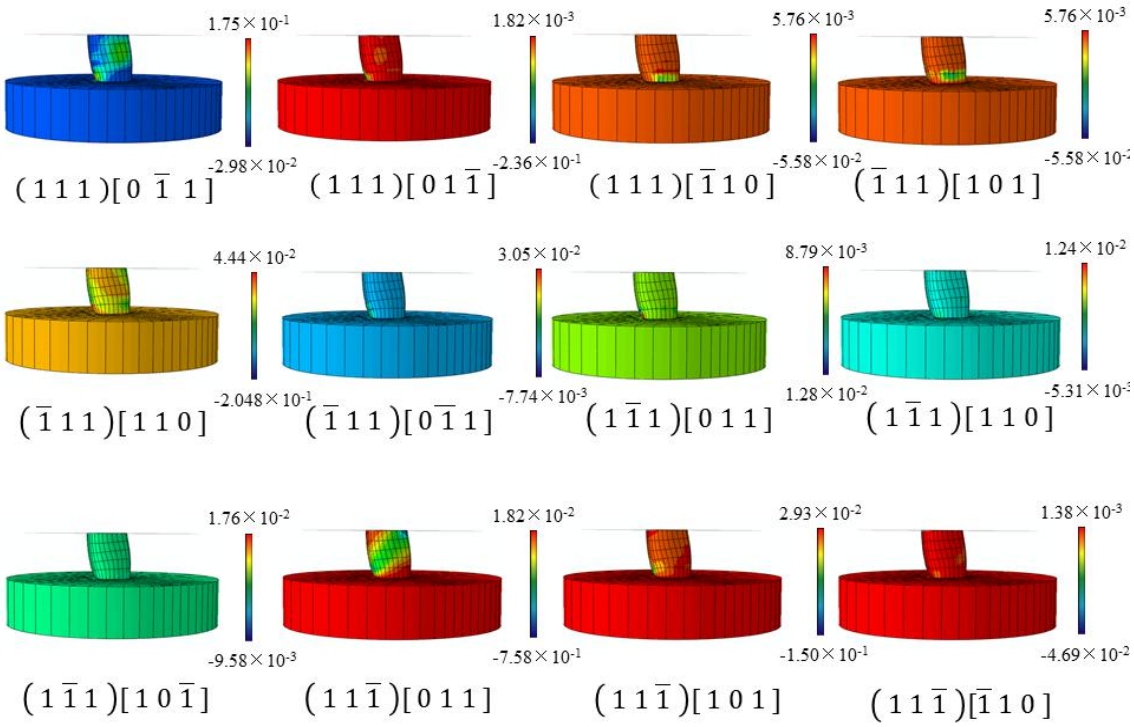

Figure 4-9. Shear strains $\gamma_p^{(\alpha)}$ in Eq. (4.35) on different slip planes with orientation of [6 11 5] at normal compressive strain of $\varepsilon = 0.134$.

Figures 4-9 and 4-10 show the shear strains $\gamma_p^{(\alpha)}$ in Eq. (4.35) on 12 slip planes

with crystalline orientations of [6 11 5] and [6 1 5], respectively. In Figure 4-9, the (1 1 $\bar{1}$) [0 1 1] slip plane has the maximum Schmid factor (0.431) and the maximum shear strain. The shear band is clear and the same as the experimental SEM image in Figure 4-8. In Figure 4-9, there is a shear strain on the (1 1 1) [0 $\bar{1}$ 1] slip plane with the Schmid factor 0.296. Compared with shear strain on the (1 1 $\bar{1}$) [0 1 1] slip plane, its shear strain is smaller than that of the system. In other words, the shear deformation is uniformly distributed on the slip plane with the maximum Schmid factor.

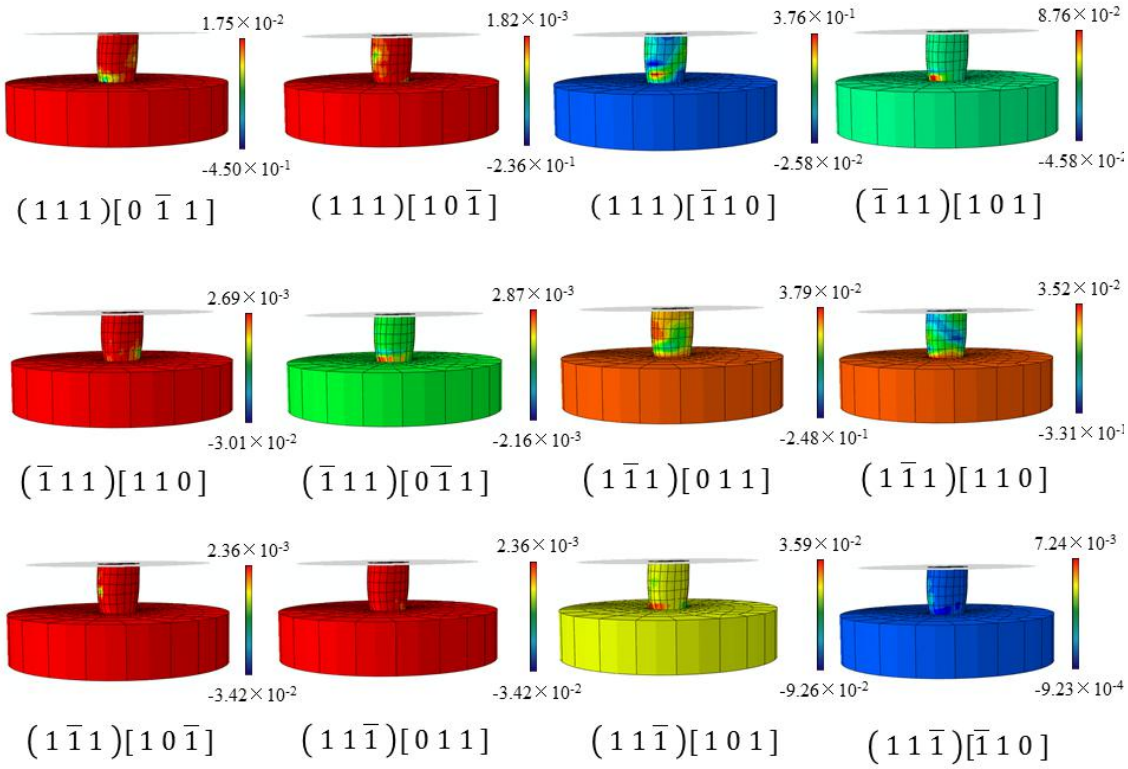

Figure 10. Shear strains $\gamma_p^{(\alpha)}$ in Eq. (4.35) on different slip planes with orientation of [6 1 5] at normal compressive strain of $\varepsilon = 0.134$.

A similar phenomenon is seen in Figure 4-10. In Figure 4-10, the (1 $\bar{1}$ 1) [1 1 0] slip

plane has the maximum Schmid factor (0.461) and the maximum shear strain. Strain localization can also be found on the slip plane with the second largest Schmid factor (0.395), but the value is much smaller than that on the (1 $\bar{1}$ 1) [1 1 0] slip plane. In summary, the shear band in the micro pillar is mainly on the slip plane with the largest Schmid factor. The shear strains on the other slip planes can also be found because the crystal orientation would change during deformation, but they are still small.

4.4.3 Friction effect on shear band and hardening

Most of the previous simulations of micropillars [15, 20, 22] did not include the friction between the flat punch and the top surface of the pillar. Shear deformation inside the pillar with the non-friction condition was discussed in Section 4.4.2. As mentioned before, the shear band in the micropillar was mainly on the slip system with the maximum Schmid factor. If the friction effect is considered in the model, the deformed image of the pillar with [6 11 5] surface orientation in Figure 4-11 also shows the shear band, which is slightly different from that in Figure 4-8. Figure 4-12 shows the distribution of the nonzero shear strains in the slip planes with the largest three Schmid factors, and the information about the slip systems is given in Table 4-4. Except for the slip planes shown in Figure 4-12, the shear strains on the other slip planes are almost zero. In Figure 4-12, the local slip deformations in green or light blue on the #5, #10, and #11 slip planes are activated by external compression. In Figure 4-9, the shear strain is only on the slip plane with the maximum Schmid factor. However, the shear band shown in Figure 4-11 is due to multiple slip planes.

Table 4-4 Slip system in FEM

#	slip plane	slip direction	SF with friction	SF without friction
1	(1 1 1)	[0 $\bar{1}$ 1]	-0.296	-0.296
2	(1 1 1)	[1 0 $\bar{1}$]	0.049	0.049
3	(1 1 1)	[$\bar{1}$ 1 0]	0.247	0.247
4	(1 1 1)	[1 0 1]	0.222	0.222
5	($\bar{1}$ 1 1)	[1 1 0]	0.343	0.343
6	($\bar{1}$ 1 1)	[0 $\bar{1}$ 1]	-0.121	-0.121
7	(1 $\bar{1}$ 1)	[0 1 1]	0	0
8	(1 1 1)	[1 1 0]	0	0
9	(1 $\bar{1}$ 1)	[1 0 1]	0	0
10	(1 1 $\bar{1}$)	[0 1 1]	0.431	0.431
11	(1 1 $\bar{1}$)	[1 0 1]	0.296	0.296
12	(1 1 $\bar{1}$)	[$\bar{1}$ 1 0]	0.134	0.134

Red words represent the active slip systems

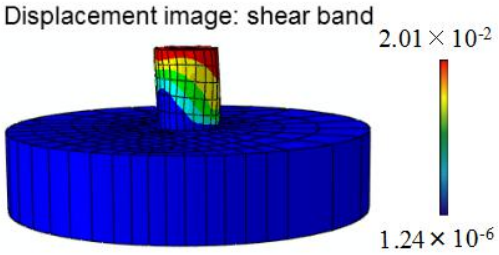

Figure 4-11. Slip system and displacement deformed shear band image at normal compressive strain of $\varepsilon = 0.134$.

The friction between the flat punch and the top surface of the pillar makes the local deformation near the punch different from that in the middle of the pillars [10, 23]. Accompanied by global plastic strain, dislocations near the punch would pile up and climb from the maximum Schmid factor slip plane to the other slip planes [5, 22] which are the green parts near the punch on the #5 and #11 slip planes shown in Figure 4-12. The constrained deformation resulting from the local dislocation pile-up and climb makes the external compression activate the other slip planes. Because the dislocations on the slip plane with maximum Schmid factor might move to the surface and form the single slip bands shown in Figure 4-8, the non-friction case in this study is reasonable.

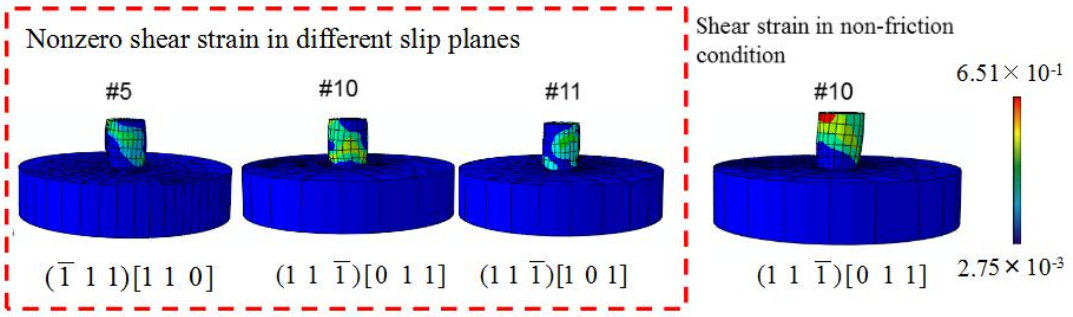

Figure 4-12. Friction effect on shear deformation on the slip plane at normal compressive strain of $\varepsilon = 0.134$.

Figure 4-13 shows the results of the stress–strain responses of the pillars with Coulomb's friction model. The friction coefficient f was set to 0, 0.3, or 0.5. The results show that the hardening stress versus plastic strain curve is steeper for the largest friction coefficient (f = 0.5) than without friction (f = 0). In the friction case, constrained deformation resulting from local dislocation pile-up and climb makes the external compression activate the other slip planes. According to the Schmid law of $\tau^{\alpha} = \boldsymbol{P}^{\alpha} : \boldsymbol{\sigma}$, the shear stress τ^{α} on a slip plane with small a Schmid factor needs a larger external stress than that with the maximum Schmid factor. Moreover, dislocation pile-up and climb alter the crystalline structure and even distort the crystal lattice, and this increases the $h_{\alpha\beta}$ term in Eq. (4.32). The distorted crystal lattice results in the multiple slip planes being activated when the plastic strain is generated. However, activating and generating multiple slip planes requires more stress, which represents more obvious hardening [3, 13]. The experiments also show that multiple slips are more difficult than a single slip [12]. To understand this phenomenon, the effect of friction on the hardening modulus $h_{\alpha\beta}$ is shown in Figure 4-14. The results show that the $h_{\alpha\beta}$ value in the simulation considering friction is larger than the value without friction, and $h_{\alpha\beta}$ for the large friction coefficient (f = 0.5) is larger than that for the small friction coefficient (f = 0.3). This means that the hardening stress with a large friction coefficient would be large, which agrees with the results shown in Figure 4-13.

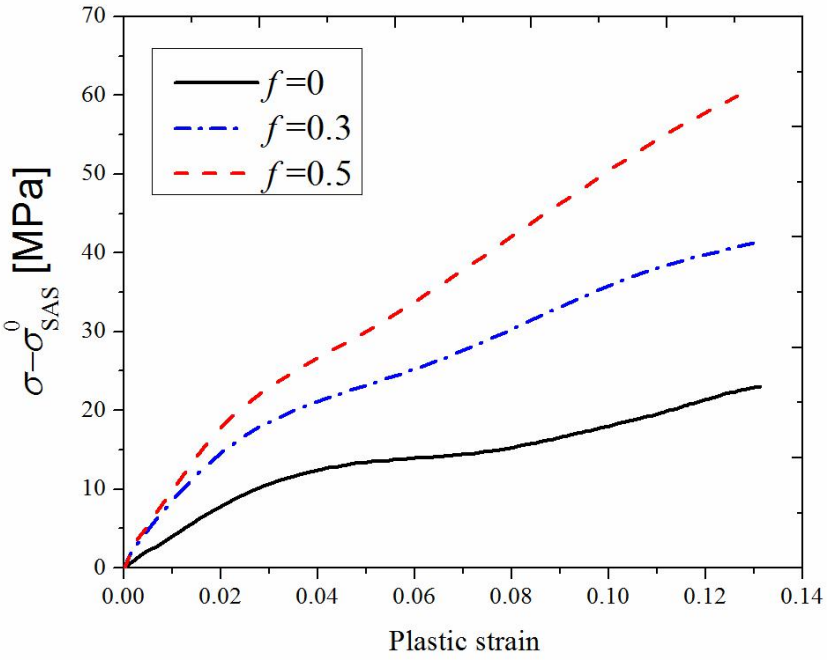

Figure 4-13. Effect of friction on the hardening stress of micro pillars with the crystalline orientation [6 11 5].

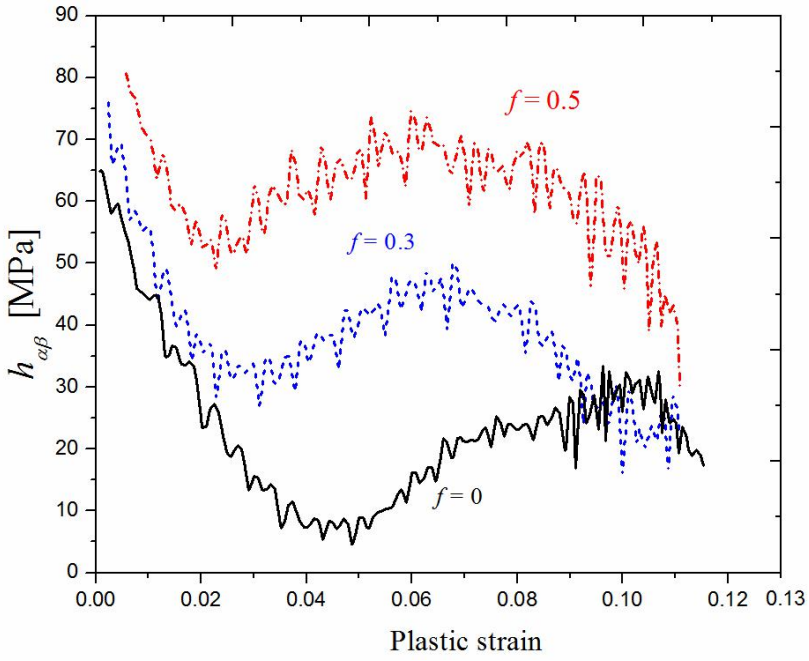

Figure 4-14. Friction effect on the hardening modulus. The friction between the punch and the pillar constrains rotation of the pillar, which affects the hardening flow increments during the simulation.

4.5 Finite element model of Cu bi-crystalline micro pillar compression test

We performed finite element (FE) analyses of the Bi-crystalline micro pillar (BCM) using a user material subroutine (UMAT) in the commercial code ABAQUS/Standard (2012). In UMAT, initial yield stresses and subsequent yield stresses, which are introduced in Section 4.1.2, and the present redefined hardening model, which is introduced in Section 4.3, are implemented in the CPFE framework introduced in Section 4.2. The orientations of BCM are defined based on the experiments in Chapter 2, the Group C in Table 2-1. The FEM model and the corresponding experimental pillar are shown in Figure 4-16. The SCMs of each grains with the orientations [$\overline{25}$ $\overline{16}$ $\bar{9}$] (SCM (L)) and [4 7 $\overline{11}$] (SCM(R)) are simulated as described as Section 4.4 for comparison. In addition, isothermal conditions of the simulation of BCM were assumed and the specimens were kept at room temperature. Pillars with diameters of 7 μm were simulated, and the height-to-diameter aspect ratio was fixed at 3.5 in all of the simulations. For simplicity, the FE model consisted of a single 8-node brick-type element (C3D8). The displacements were applied along the *y* direction associated with a constant strain rate of 1.0×10^{-4} s^{-1}. A base material at the bottom of the pillar was included to simulate to the real boundary condition of the samples.

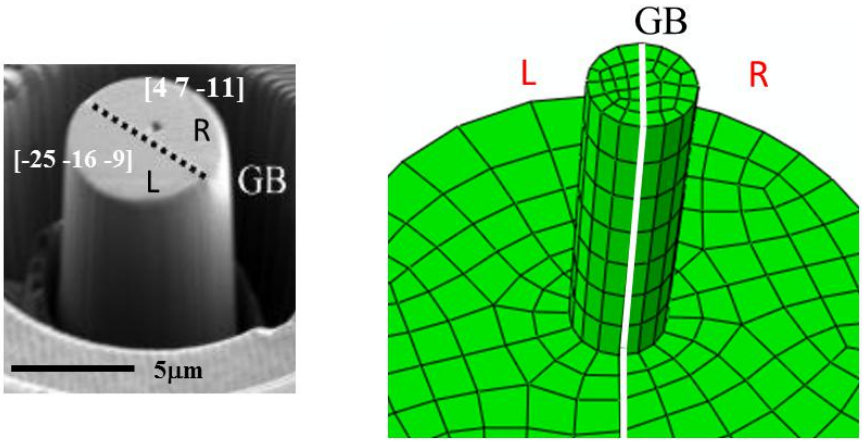

Figure 4-15. The SEM image of the BCM in Group C in Table 2-1, and the FEM model defined based on the experimental information.

4.5.1 Stress-strain response of BCM and corresponding SCMs

The material parameters used in the simulations are given in Table 4-5. The elastic moduli [21] and the related parameters of the FEM simulations are given in Table 4-5. The same method introduced in Section 4.1.3 is used to determine (k^*, Ω). Eq. (4.17) is used to fit the experiments of SCMs (L) and SCMs (R) of the same grains of BCM simultaneously to obtain the average value of the dislocation evolution parameters of the corresponding BCM. Finally, the fitting parameter can be obtained with the approximate value (62 μm^{-1}, 20.2). The initial hardening moduli H_0 was set as 68.4 MPa. The friction condition is considered here and the friction coefficient is set to f = 0.2.

Table 4-5 Parameters used in the extended SAS model and CPFE

Parameters	Values	Parameters	Values
ρ_0 [m^{-2}]	2×10^{12}	b [nm]	0.255
τ_0 [MPa] Eq. (4.10)	12	k^* [μm^{-1}]	62 (d = 7 μm)
μ [GPa]	48		
υ	0.3	Ω	20.2 (d = 7 μm)

Figure 4-16 shows the comparison of the FEM simulated results based on the set value of (k^*, Ω, f, H_0) shown in Table 4-5 and 4-6, and the experimental results shown in Figure 2-6. It is shown that the simulated results compare well with the experimental results. That is to say, the values of (k^*, Ω, f, H_0) are reasonable for SCMs. In the following, the same values of (k^*, Ω, f, H_0) are applied for the BCM with two orientations shown in Figure 4-15.

Table 4-6 CPFE parameters.

Parameters	Values
c_{11} [GPa]	168.4
c_{12} [GPa]	121.4
c_{22} [GPa]	75.4
ε_s	0.3
f	0.2
H_0 [MPa]	68.4 (d = 7 μm)

Figure 4-17 shows the comparison of the FEM simulated results and the experimental results of BCM in Table 2-1. Because the size-dependent yield stress is based on the initial distribution of dislocations, the initial yield stress might not agree well with the experimental results. Therefore, we use the net stress $\sigma - \sigma_{\mathrm{SAS}}^{0}$ (call it "stress" for short in Figure 4-17) to describe the effective stresses of the mechanical response. It is shown that the simulated results are nearly coincident to the experiments at the beginning of the plastic flow, and a little bit smaller than the experimental data when the plastic strain is above 3%. The rotation of the slip plane and the possible variance of dislocation configuration may change the local stress field and result in the larger stress-strain response. Globally, the FEM method based on the revised hardening model and crystal plasticity can describe the mechanical response of the BCM effectively.

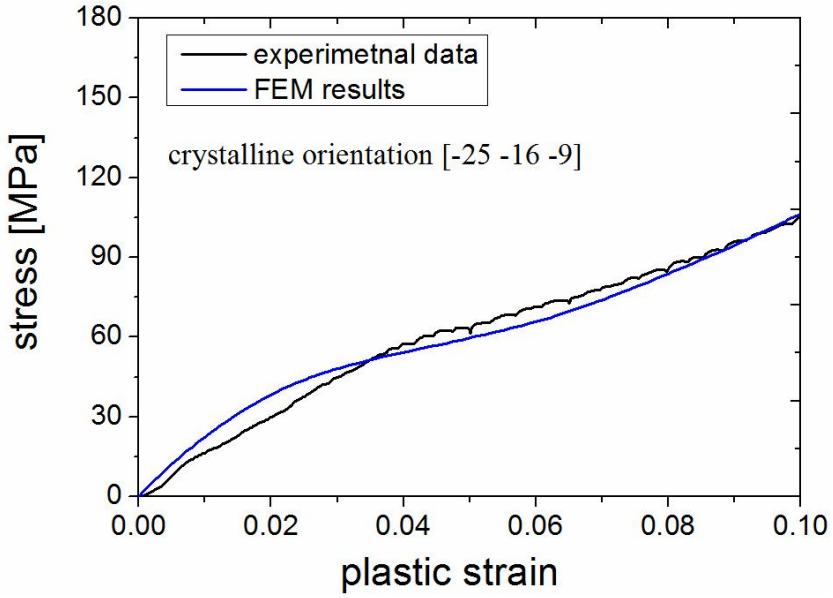

(a) SCM (L) of Group C

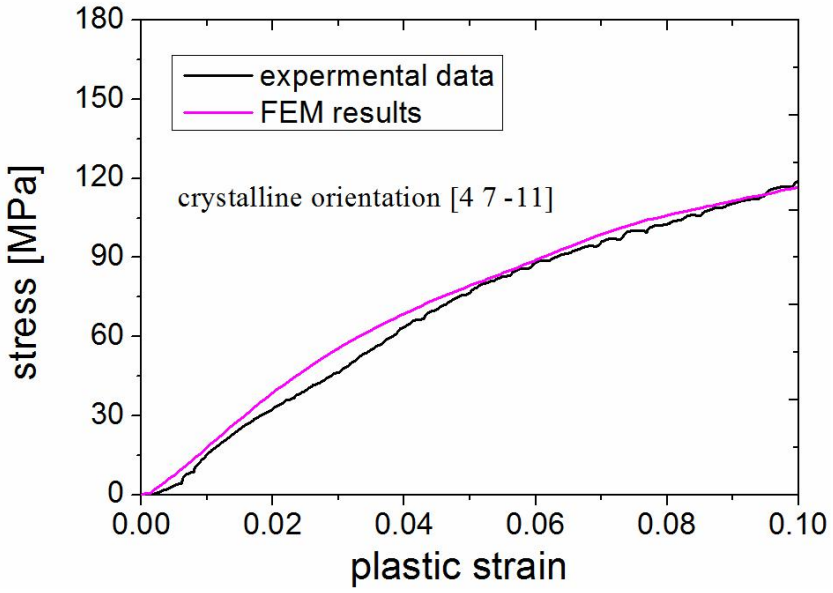

(b) SCM (R) of Group C

Figure 4-16. The comparison of the FEM simulated results and the experimental results of the SCMs of Group C: (a) SCM (L) and (b) SCM (R).

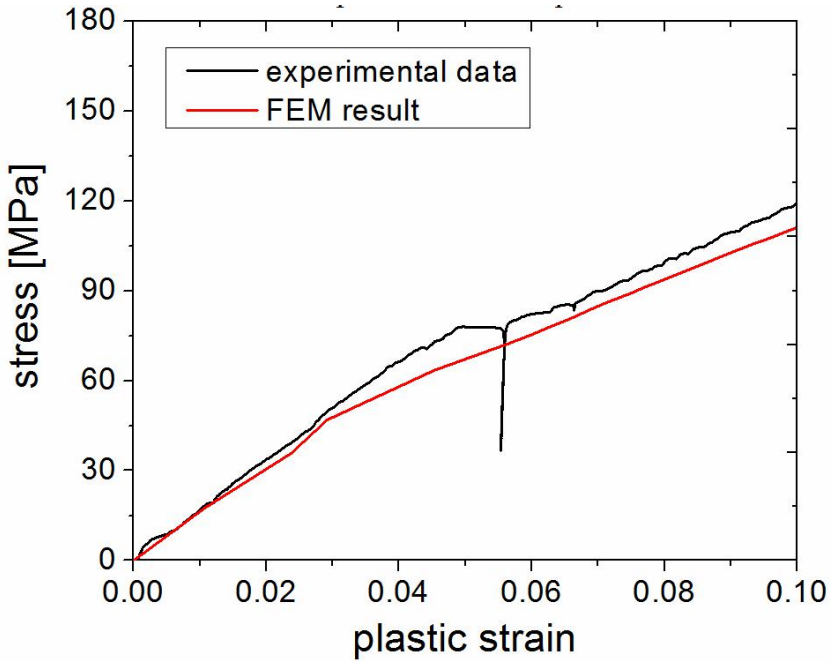

Figure 4-17. The comparison of the FEM simulated results and the experimental results of the BCM of Group C.

4.5.2 Shear deformation inside the BCM

Figure 4-18 shows a comparison of the scanning electron microscopy (SEM) image of the compressed BCM with the crystalline orientation [$\bar{2}5\ \bar{1}6\ \bar{9}$] left side of BCM (BCM (L)) and [4 7 $\bar{1}1$] right side of BCM (BCM (R)) and the FEM deformed mesh image. In the FEM deformed image, the color represents the scaled magnitude of displacement in the micro pillars for displaying. The slip band in the SEM image has an angle of around 50° with respect to the normal axis and occurs along the (1 1 $\bar{1}$) [1 0 1] slip plane of BCM (L) and (1 1 1) [1 0 $\bar{1}$] slip plane of BCM (R). The information of the slip systems of the BCM is shown in Table 4-7. The red words represent the slip plane with the maximum SF. The FEM displacement image of the BCM shows the BCM exists shear deformation along the maximum SF slip plane and parallel to the GB. This result is the same as the shape deformation of Group A in Table 2-1, and is similar to the shape deformation of Group C shown in Figure 4-18.

The red arrow in Figure 4-18 shows the global slip deformation in the BCM, and it represents the shear deformation is almost along the GB. It can be found that few dislocations transfer across the GB. This compares the results shown in FEM.

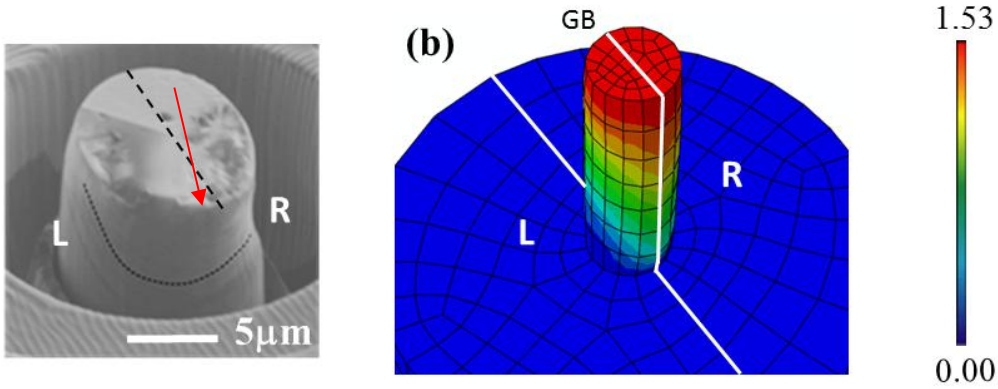

Figure 4-18. Comparison of the SEM image and the FEM deformed mesh image (displacement image) of BCM at normal compressive strain of $\varepsilon = 0.134$. The color of the FEM image indicates the scaled magnitude of displacement in the micro pillar.

Table 4-7 slip systems of the BCM

#	slip plane	slip direction	SF for SCM (L)	SF for SCM (R)
1	$(1\ \bar{1}\ 1)$	[0 1 1]	0.191	0.123
2	$(1\ 1\ \bar{1})$	[0 1 1]	0.339	-0.193
3	$(\bar{1}\ 1\ 1)$	[1 0 1]	0	-0.123
4	$(1\ 1\ \bar{1})$	[1 0 1]	0.462	0.338
5	$(\bar{1}\ 1\ 1)$	[1 1 0]	0	-0.193
6	$(1\ \bar{1}\ 1)$	[1 1 0]	0.313	-0.338
7	$(1\ 1\ 1)$	$[0\ \bar{1}\ 1]$	-0.149	0
8	$(\bar{1}\ 1\ 1)$	$[0\ \bar{1}\ 1]$	0	0.316
9	$(1\ 1\ 1)$	$[1\ 0\ \bar{1}]$	0.339	0
10	$(1\ \bar{1}\ 1)$	$[1\ 0\ \bar{1}]$	0.122	0.461
11	$(1\ 1\ 1)$	$[\bar{1}\ 1\ 0]$	-0.191	0
12	$(1\ 1\ \bar{1})$	$[\bar{1}\ 1\ 0]$	-0.122	0.145
Red words represent the active slip system				

Figures 4-19 and 4-20 show the shear strains $\gamma_p^{(\alpha)}$ in Eq. (4.35) on 12 slip planes with crystalline orientations of $[\ \bar{25}\ \ \bar{16}\ \ \bar{9}\ ]$ (BCM (L)) and $[4\ 7\ \bar{11}\ ]$ (BCM (R)),

respectively. In Figure 4-19, the (1 1 $\bar{1}$) [1 0 1] slip plane has the maximum Schmid factor (0.461) and the maximum shear strain. The shear band is clear and the same as the experimental SEM image in Figure 4-18. In Figure 4-19, the (1 1 $\bar{1}$) [1 0 1] slip plane has the maximum Schmid factor (0.462) and the maximum shear strain. Strain localization can also be found on the slip planes with the second largest and third largest Schmid factor (0.339, 0.319), but the value is much smaller than that on the (1 1 $\bar{1}$) [1 0 1] slip plane. The flat punch touches the top surface of the BCM, the dislocations may result in the pile-up zone and crystalline rotation [5, 7]. The local deformation represents the touch effect of the uniaxial compression test. Above all, the shear deformation is uniformly distributed on the slip plane with the maximum Schmid factor.

A similar phenomenon is seen in Figure 4-20. In Figure 4-20, there is a shear strain on the ($\bar{1}$ 1 1) [0 $\bar{1}$ 1] slip plane with the Schmid factor 0.316. Compared with shear strain on the (1 $\bar{1}$ 1) [1 0 $\bar{1}$] slip plane, its shear strain (the order is ~10^{-3}) is smaller than that of the (1 $\bar{1}$ 1) [1 0 $\bar{1}$] system (the order is ~10^{-1}). There are also some local deformation on the ($\bar{1}$ 1 1) [0 $\bar{1}$ 1] slip plane and the (1 $\bar{1}$ 1) [1 1 0] slip plane. In summary, from the outside view, the shear band in the micro pillar is mainly on the slip plane with the largest Schmid factor. The shear strains on the other slip planes can also be found because the crystal orientation would change during deformation, but they are still small. However, the deformation near the GB is still unknown. In the following, the $\gamma_p^{(\alpha)}$ near the GB of different slip planes of BCM (L) and BCM (R) is discussed.

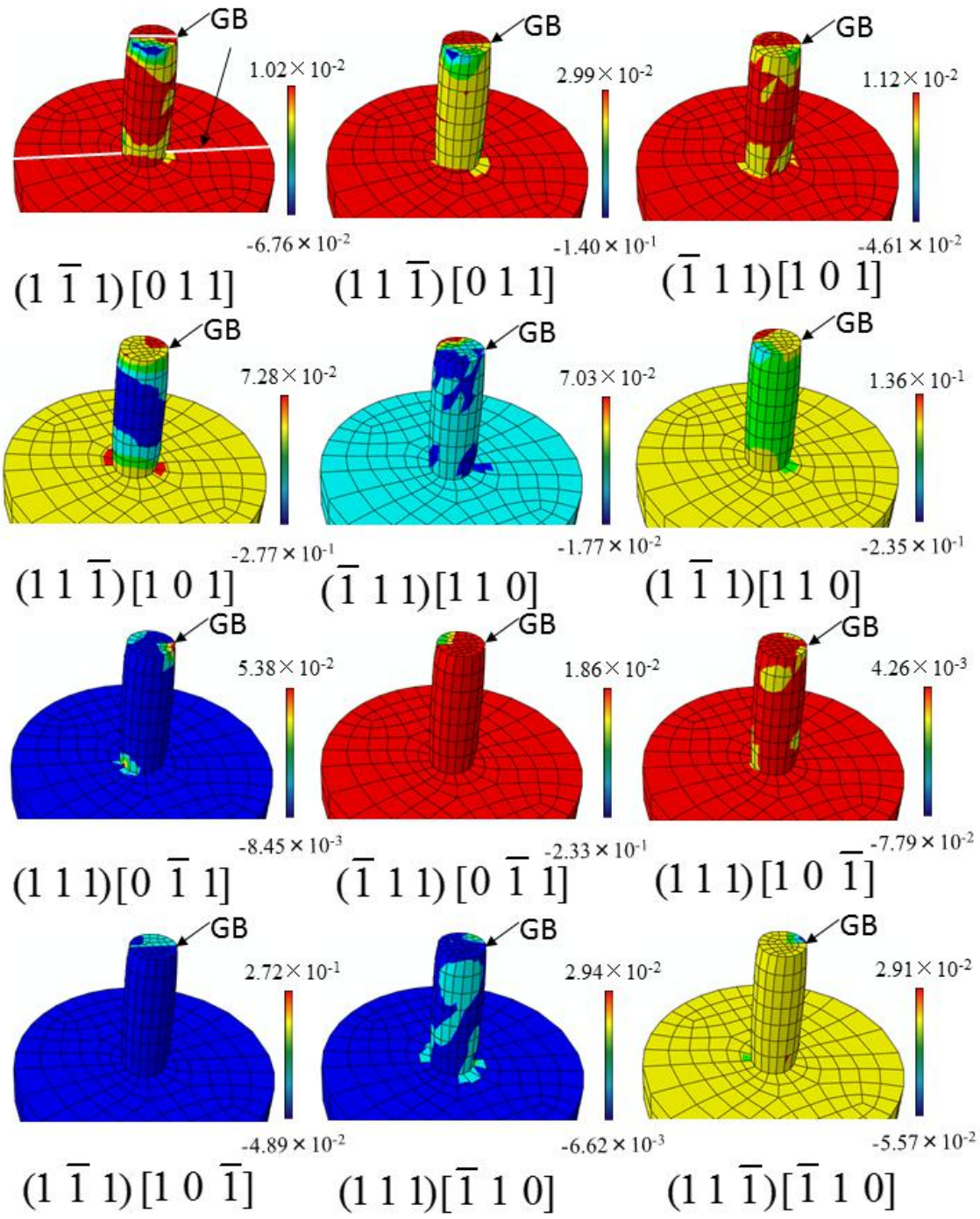

Figure 4-19. Shear strains $\gamma_p^{(\alpha)}$ in Eq. (4.35) on different slip planes of the left side of the BCM with orientation of $[\bar{25}\ \bar{16}\ \bar{9}]$ at normal compressive strain of $\varepsilon = 0.134$.

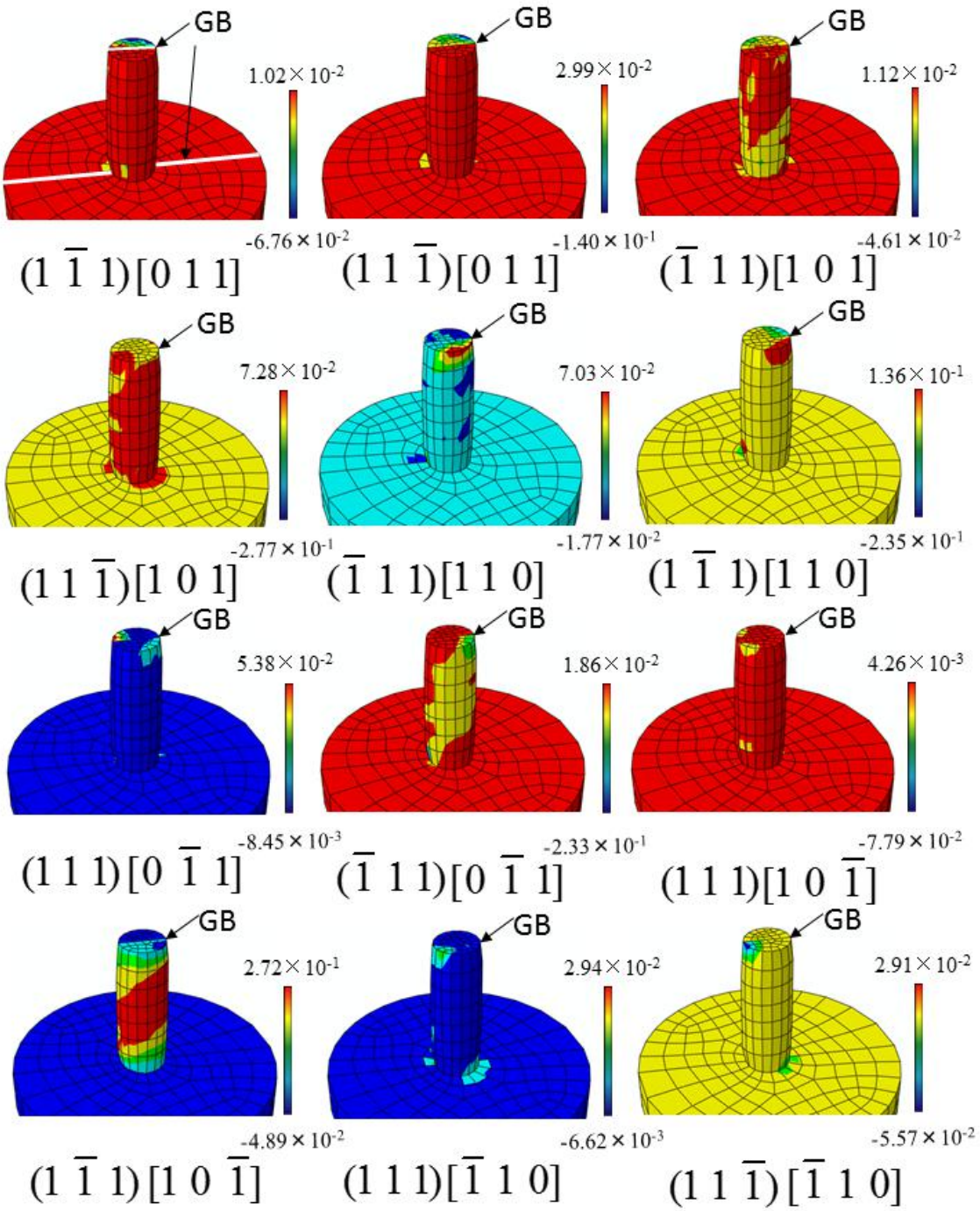

Figure 4-20. Shear strains $\gamma_p^{(\alpha)}$ in Eq. (4.35) on different slip planes of the right side of the BCM with orientation of $[4\ 7\bar{1}1]$ at normal compressive strain of $\varepsilon = 0.134$.

The deformation near the GB is shown in Figure 4-21 and Figure 4-22. They provide the information of the local deformation of different slip planes in BCM (L) and BCM (R), respectively. In Figure 4-21, the slip band is also clear on the maximum SF slip plane ((1 1 $\bar{1}$) [1 0 1]), but the third largest SF slip plane shows some shear deformation. The value of the shear strain on (1 1 $\bar{1}$) [1 0 1] slip plane is maximum in the order of ~10^{-1}, and much larger than the local deformation on other slip planes. In Figure 4-22, the slip band is clear on the (1 $\bar{1}$ 1) [1 0 $\bar{1}$] slip plane, and value of the shear strain is maximum in the order of ~10^{-1}. It is much larger than the local deformation on other slip planes. The second largest SF ($\bar{1}$ 1 1) [0 $\bar{1}$ 1] slip plane also shows some shear band, but is not obvious compared with that on the (1 $\bar{1}$ 1) [1 1 0] slip plane.

Compared with Figures 4-21 and 4-22, the shear deformation only exists on one side of the GB, and no deformation on the other side. That means there are no dislocations transferring across the GB on this kind of the GB. However, on the #2 (1 1 $\bar{1}$) [0 1 1] and #6 (1 $\bar{1}$ 1) [1 1 0] slip planes, there are some small value of deformation on both sides of the GB. And the positions of the existing deformations are corresponding to each other. That means few dislocations transferring cross the GB. The transferring motion doesn't exist on the maximum SF slip plane. Meanwhile, there are some local deformations found at the bottom of the BCM, and localized deformation also deeps into the base of the BCM. This is the effect of the base of the pillars. The base can limit the deformation of the BCM and also localize the dislocation motion. From this view, the modeling here considering the base effect is reasonable.

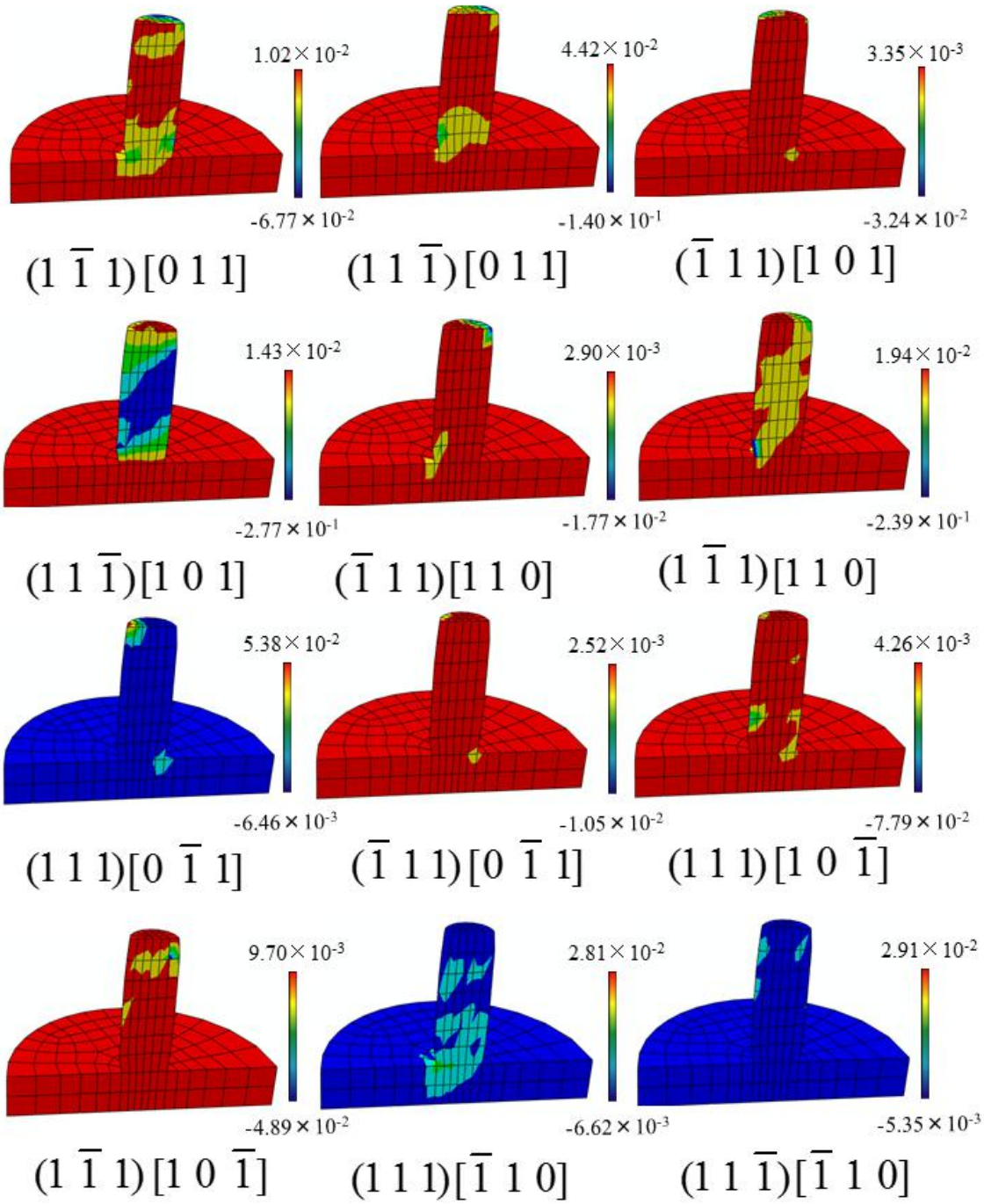

Figure 4-21. Shear strains $\gamma_p^{(\alpha)}$ in Eq. (4.35) on the cross section in different slip planes of the right side of the BCM with orientation of [$\bar{25}$ $\bar{16}$ $\bar{9}$] at normal compressive strain of $\varepsilon = 0.134$.

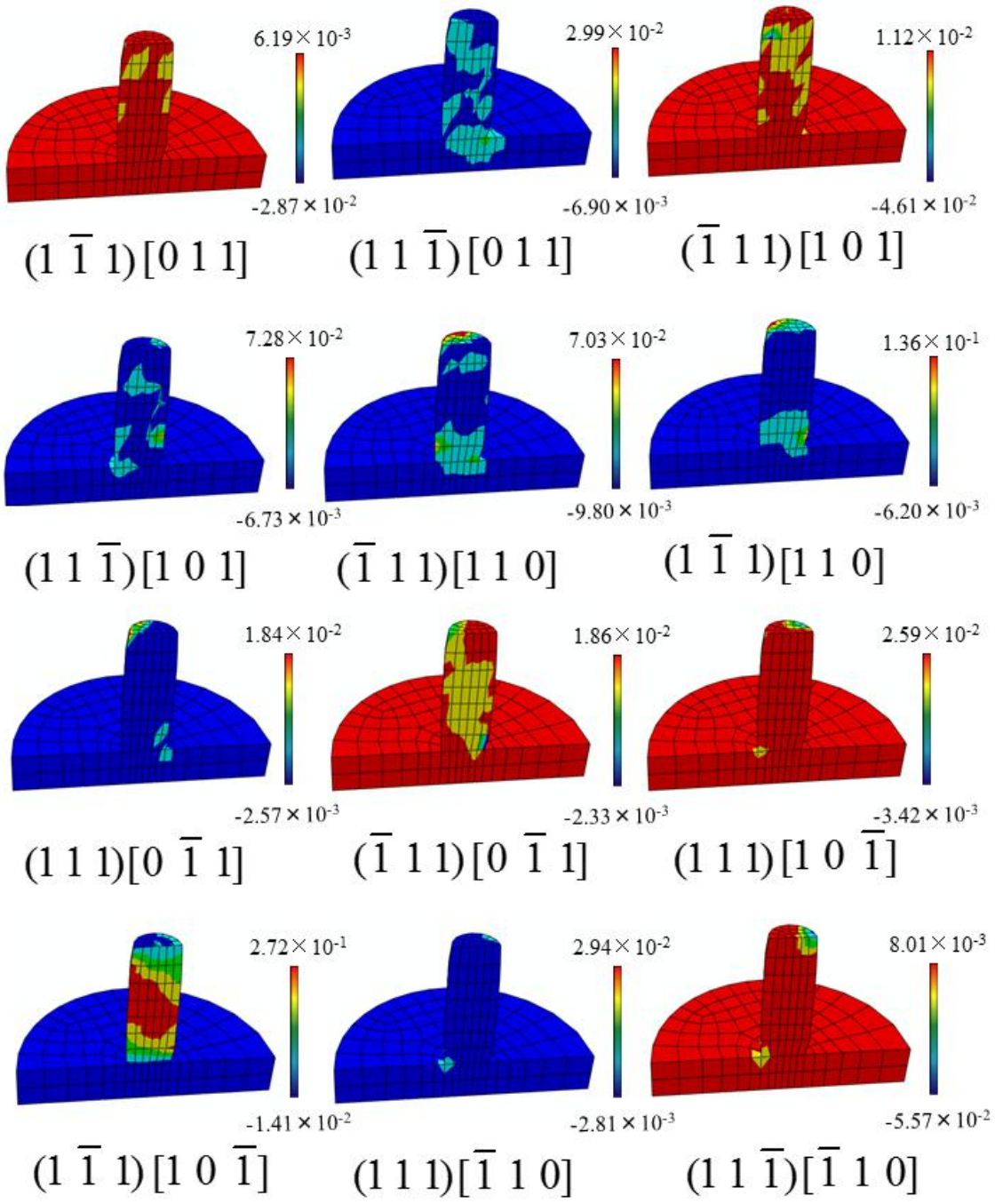

Figure 4-22. Shear strains $\gamma_p^{(\alpha)}$ in Eq. (4.35) on cross section in different slip planes of the left side of the BCM with orientation of [4 7 $\bar{1}$ 1] at normal compressive strain of $\varepsilon = 0.134$.

According to the molecular dynamic simulation result [24-26], the dislocations emitted from sources can traverse the grain interior and be absorbed by GBs or just only stay in grain interior. In micro scale sample, once the strain burst occurs, the newly generated immobile dislocations can be transformed into mobile dislocations, absorbed by GBs and/or annihilated at free surface [27, 28]. According to the model of statistical absorption of dislocations by GBs (SAD), the probability of a dislocation being absorbed by the GBs, P_{dis}, can be expressed as

$$P_{dis} = [1-(1-p)^N]^J = \{1-[1-\exp(\frac{-(\Delta G+\tau_0 b^3)}{k_B T})]^{\frac{SFbv}{\dot{\varepsilon} d}}\}^J , \quad (4.37)$$

where $p = \exp(-(\Delta G+\tau_0 b^3)/k_B T)$ is the probability of an atom successfully jumping into the GB/surface in a single attempt; N is the number of attempted jumps by dislocation core atoms to the GB/surface during a given time; J is the total number of atoms on the dislocation core jumping into the GB; ΔG is the activation energy for atomic migration (or dislocation nucleation), varying within the range of ~0.6–0.95 eV [27]; k_B = 1.38 × 10^{-23} J/K is Boltzmann's constant; T is temperature; $\dot{\varepsilon}$ is strain rate; v is Debye frequency; τ_0 is resolved shear stress; b is Burgers vector; d is the grain size/diameter of sample. The case $P_{dis}=1$ means GBs are transparent, and do easily absorb dislocations to transfer across them. In contrast, $P_{dis}=0$ implies that GBs are opaque and inhibit mobile dislocations traverse the GB. By using τ_0 =11MPa, b=0.2556nm, T=300K, v=7.2×10^{12}Hz [27], d=sample diameter (3500~8000nm), J=6.5d [27], ΔG =0.73eV [28], $\dot{\varepsilon}$ =0.08/s. We can obtain the probability $P_{dis}=0$ shown in Figure 4-23. For BCMs Cu pillars, upon loading, the lower is the probability of dislocation absorption P_{dis}, the more dislocations pile-up against the barrier. Moreover, $P_{dis}=0$ makes the dislocations difficult to transfer across the GB. As known, GB can be treated as the barrier to inhibit the dislocation

motion which is shown in Figures 2-7, 2-8 and 4-18. The external loading cannot make the dislocations bypass the GBs like them in single crystalline. Therefore, the GBs in BCMs of 3500~8000nm size inhibit the dislocations transfer and slide across the GB, and result in the slide direction along GB. When the strain burst occurred in the plastic deformation, the $\dot{\varepsilon}$ would be higher as the tip of the sample suddenly escaped from the flat-punch. In Figure 4-23, it is obvious that the P_{dis} will be lower at a higher $\dot{\varepsilon}$. That means the GB provides a barrier wall to inhibit the instable dislocation evolution in the near filed of GB, and decreases the probability of dislocation transfer across the GB. In this case, the dislocations just pile-up or slide along the grain boundary. However, some special local energy conditions make some local parts in the state of $P_{dis}=1$, which is the reason of that some few dislocations transfer the GB shown in Figures 4-21 and 4-22.

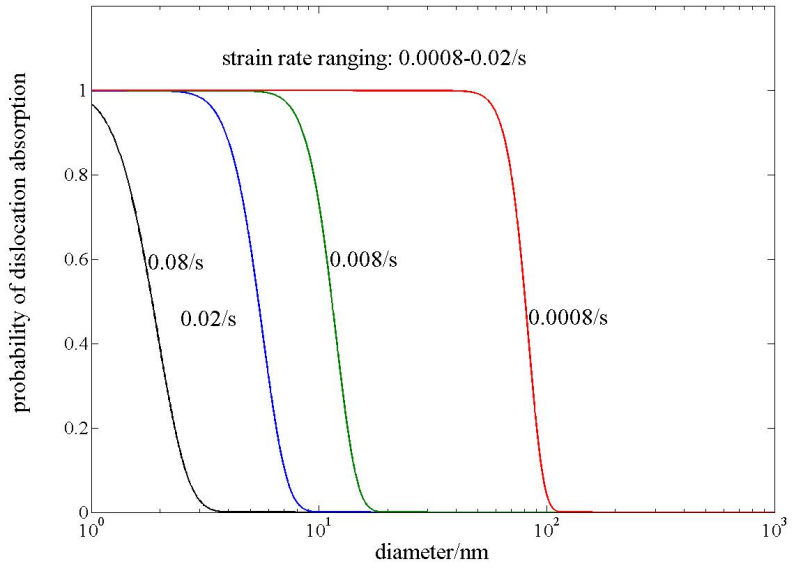

Figure 4-23. The probability P_{dis} of dislocation absorbed by GBs as a function of d or $\dot{\varepsilon}$.

4.6 Conclusion

In this chapter, we propose a physical constitutive model with the framework of the

CPFE method that accounts for the dislocation physics to describe the size-dependent plastic deformation of single crystalline and bi-crystalline micro pillars. To predict the variation of the plastic state owing to size-dependent internal microstructures, such as dislocation sources, dislocation source length, mobile dislocations, and trapped dislocations, information about these defects is introduced by providing dislocation evolution based on the Orowan equation and the principle of Bergstrom dislocation evolution , and the extended SAS model. Our conclusions are as follows:

(1) The present formulation suggests that the dislocation evolution equation includes both mobile dislocations and trapped dislocations, and the total dislocation density is a function of the plastic strain, the number of dislocation sources, and the dislocation evolution parameters.

(2) Based on the SAS model, a revised PAN hardening model is proposed that can describe size-dependent hardening flow.

(3) The physical constitutive equations combined with the SAS model, the revised PAN hardening model, and CPFE framework can describe the size-dependent plastic flow of single crystalline and bi-crystalline micro pillars.

(4) Size-dependent dislocation evolution is related to the hardening modulus of the micro pillars, and this makes the stress–strain response vary with the micro pillar size.

(5) The friction between the flat punch and the top surface of the pillar affects the stress–strain response of the plastic flow and the shear band deformation of the micro pillars. Hardening with friction is greater than that under the non-friction condition. Friction makes the shear strain on the slip plane much more complicated.

(6) The GB in bi-crystalline micro pillars can inhibit the dislocation transfer across the each grains, and dislocations pile up after the GB and slip along the GB on the maximum Schmid factor slip planes of the each sides of the bi-crystalline micro pillar.

(7) The model of statistical absorption of dislocations by GBs is provided to explain the dislocation motion near the GB. It is found that the GB effect on the dislocation motion is related to the size of the specimen: the small size make the GB become transparent.

Reference

[1] Hill R, Rice, JR. Constitutive analysis of elastic-plastic crystals at arbitrary strain. J Mech Phys Solids 1972 (20) 401–413.
[2] Parthasarathy TA, Rao SI, Dimiduk DM, Uchic MD, Trinkle DR. Contribution to size effect of yield strength from the stochastics of dislocation source lengths in finite samples. Scr Mater 2007 (56) 313–316.
[3] Gao Y, Liu ZL, You X. C. and Zhuang Z. A hybrid multiscale computational framework of crystal plasticity at submicron scales, Comp Mater Sci 2010 (49) 672–681.
[4] Bei H, Shim S, Pharr GM, George EP. Effects of pre-strain on the compressive stress–strain response of Mo-alloy single-crystal micropillars, Acta Mater 2008 (56) 4762–4770.
[5] Pan B, Shibutani Y, Zhang X, Shang FL. Effect of dislocation pile-up on size-dependent yield strength in finite single-crystal micro-samples. J Appl Phys 2015 (18) 014305.
[6] Schneider AS, Kiener, D, Yakacki CM, Maier HJ, Grube PAR, Tamura N, Kunz M, Minor AM, Frick CP. Influence of bulk pre-straining on the size effect in nickel compression pillars, Mater Sci Eng A 2013 (559) 147–158.
[7] Shan ZW, Mishra RK, Asif SAS, Warren OL, Minor AM. Mechanical annealing and source-limited deformation in submicrometer-diameter Ni crystals, Nat Mater 2008 (7) 115–119.
[8] Beyerlein IJ, Tomé CN. A dislocation-based constitutive law for pure Zr including temperature effects, Int J Plast 2008 (24) 867–895.
[9] Hirth JP, Lothe J. Theory of Dislocation (1982), John Wiley.
[10] Dimiduk DM, Uchic MD, Parthasarathy TA. Size-affected single-slip behavior of pure nickel microcrystals. Acta Mater 2005 (53) 4065–4077.
[11] Kiener D, Grosinger W, Dehm G. On the importance of sample compliance in uniaxial microtesting. Scr Mater 2009 (60) 148–151.
[12] Hirouchi T, Shibutani Y. Mechanical responses of copper bicrystalline micro pillars with ∑3 coherent twin boundaries by uniaxial compression tests. Mater Trans 2014 (55) 52–57.
[13] Asaro RJ, Lubarda VA. Mechanics of Solids and Materials (2006), Cambridge University Press.
[14] Peirce D, Asaro RJ, Needleman A. An analysis of nonuniform and localized deformation in ductile single crystals, Acta Metall 1982 (30) 1087–1119.
[15] Zhang X, Shang FL. A continuum model for intermittent deformation of single

crystal micro pillars, Int J Solids Struct 2014 (51) 1859–1871.
[16] Norfleet DM, Dimiduk DM, Polasik SJ, Uchic MD, Mills MJ. Dislocation structures and their relationship to strength in deformed nickel microcrystals. Acta Mater 2008 (56) 2988–3001.
[17] Roters F, Eisenlohr P, Hantcherli L, Tjahjanto D, Bieler T, Raabe D. Overview of constitutive laws, kinematics, homogenization and multiscale methods in crystal plasticity finite-element modeling: Theory, experiments, applications. Acta Mater 2010 (58) 1152–1211.
[18] Evers LP, Brekelmans WAM, Geers MGD. Scale dependent crystal plasticity framework with dislocation density and grain boundary effects. Int J Solids Struct 2004 (41) 5209–5230.
[19] Gurtin ME, Anand L, Lele SP, Gradient single-crystal plasticity with free energy dependent on dislocation densities, J Mech Phys Solids 2007 (55) 1853–1878.
[20] Zhang X, Shang FL, Yu Y, Yan YB, Yan SP. A stochastic model for the temporal aspects of flow intermittency in micro pillar compression. Int J Solids Struct 2014 (51) 4519–4530.
[21] Freund LB, Suresh S. Thin Film Materials: Stress, Defect Formation and Surface Evolution (2003), Cambridge University Press.
[22] Gerken JM Dawson PR. A crystal plasticity model that incorporates stresses and strains due to slip gradients. J Mech Phys Solids 2008 (56) 1651–1672.
[23] Uchic MD, Dimiduk DM, Florando J, Nix WD. Sample dimensions influence strength and crystal plasticity. Science 2004 (305) 986–989.
[24] Tsuru T, Kaji Y, Shibutani Y. Incipient plasticity of twin and stable/unstable grain boundaries during nanoindentation in copper. Phys Rev B 82 (2010) 024101.
[25] Tsuru T, Kaji Y, Shibutani Y. Minimum Energy Motion and Core Structure of Pure Edge and Screw Dislocations in Aluminum. J Comp Sci Tech 4 (2010) 185-193.
[26] Kunz A, Pathak S, Greer JR. Size effects in Al nanopillars: single crystalline versus bicrystalline. Acta Mater 2011 (59) 4416-4424.
[27] Carlton CE, Ferreira PJ. What is behind the inverse Hall – Petch effect in nanocrystalline materials? Acta Mater 2007 (55) 3749-3756.
[28] Zhang JY, Liu G, Lei SY, Niu JJ, Sun J. Transition from homogeneous-like to shear-band deformation in nanolayered crystalline Cu/amorphous Cu–Zr micropillars: Intrinsic vs. extrinsic size effect. Acta Mater 2012 (60) 7183-7196.

Chapter 5

Size dependent plasticity of metallic glass materials

In this chapter, the size dependent elastic limit of MG micro-pillars will be studied experimentally first. And then the explanation of this size effect will be provided based on the shear band energy theory. The comparison of the size dependent strengths of the metallic glass (MG) and the crystalline material is conducted to study the mechanism of the size dependent strength. Moreover, the plastic deformation of MG bulk/micro-pillars at room temperature and near the glass transition temperature will be described by establishing the FEM framework based on the free volume model and Drucker-Prager model. The homogeneous and inhomogeneous deformation mechanism will be studied by the "flow defects". The propagation of shear bands is dominant for the deformation form and strength presentation.

5.1 Size dependent elastic limit of metallic glass micro-pillars

5.1.1 Experimental results of the size dependent elastic limit of metallic glass micro-pillars

The uniaxial compression tests on the MG micro-pillars with a flat punch have been conducted and their result has been shown in Chapter 2. The experimental elastic limits of the MG micro-pillars are collected in Figure 5-1. It is shown that the specimen in small scale has a smaller elastic limit than those in large scale. The elastic

limits in 1μm and 2μm are in the value of 1200MPa. And then their values of largely scaled pillars increase nonlinearly. Over 6μm, the values hold around 1700 MPa, which is close to value of 1650MPa of the bulk [1, 2].

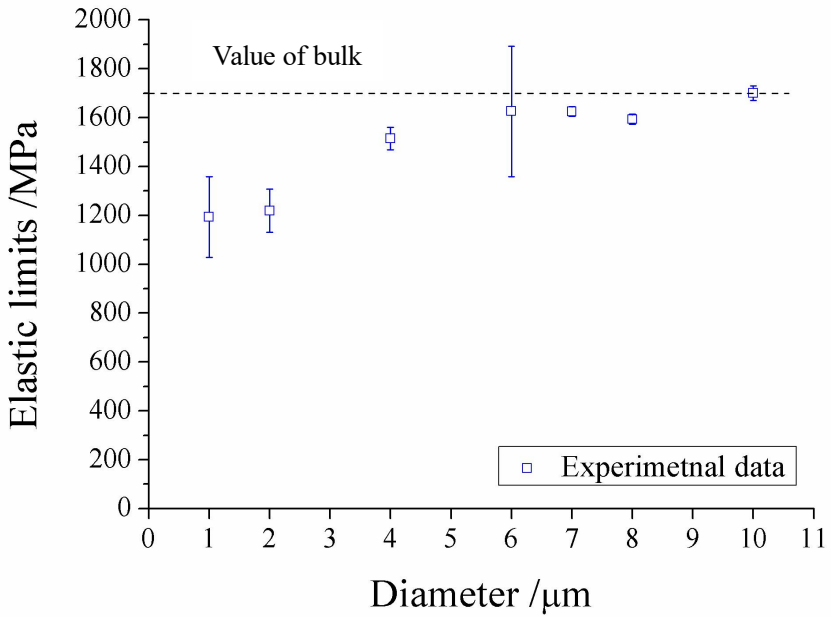

Figure 5-1. The size dependent elastic limits of Zr-based metallic glass micro-pillars.

5.1.2 Explanation on size effect of metallic glass micro-pillars

The value of the yield strength of metallic glass pillars shown in Figure 5-1 turns out that there is slight increase dependence of the yield stresses on diameter increasing tendency. But as is well known, the high yield strength is due to the lack of an "easy" flow mechanism like "dislocation sliding" in the crystalline materials. As a consequence measured from experiments shown in Figure 5-1, in the metallic glass, one cannot express a "smaller is stronger" relationship observed in the micro- and nano- crystalline materials due to dislocation nucleation, multiplication control, dislocation starvation and source starvation mechanism. The strength of metallic glass is essentially affected by the inter-atomic bonding. Until now, for the MG pillars at

the nano scale, the surface stress is used to explain the strength variance. However, the experimental data to prove the theoretical prediction and simulation test has not been found as the limitation of the experimental facility. For the MG pillars at sub-micron and micron scale, shear banding is the dominant plastic deformation mechanism, and an energetic model is provided to evaluate the stress for the shear band propagation [1, 2]:

$$\sigma = \sqrt{\frac{2\sqrt{2}\Gamma E}{\beta D}} . \tag{5.1}$$

where Γ is the shear band energy density per unit area, E the Young's modulus, D diameter of the sample and β the aspect ratio of the sample, respectively. For the load-controlled mode in this study, the strain energy of one displacement burst stage accumulated in the volume is uV, where V is the volume ($\pi D^2 L/4$ for a cylinder specimen), u is the strain energy density, for uniaxial deformation $u = \sigma_i(\varepsilon_{i+1} - \varepsilon_i)$, σ_i being the stress of the ith burst, ε_i, ε_{i+1} being the strains before and after the ith burst. The generation energy of shear band ($\sqrt{2}\pi D^2 \Gamma / 4$ for a cylinder specimen) is released from strain energy [2, 3]. When a burst occurs under compression, the energy released is approximately

$$\Gamma = \frac{\sqrt{2}}{2}\sigma_i(\varepsilon_{i+1} - \varepsilon_i)L . \tag{5.2}$$

where L is the specimen size (height of a cylinder pillar scaling linearly with the diameter (= β D)). And the strain resulting released shear band energy can be expressed $\Delta\varepsilon_i = \varepsilon_{i+1} - \varepsilon_i$, thus the strain before the and after ith burst involves two parts: the ideal elastic strain ε_0 for each deformation condition without any shear bands corresponding to the elastic stress σ_{c0}, with the form $\varepsilon_i = \varepsilon_0 + \sum_{i=1}^{i-1}\Delta\varepsilon_i$. For the

initial yield stress σ, it can be regarded as the stress σ_1 involving the elastic stress without any shear band and the component stress to active the first burst, Eq. (5.2) can be expressed as

$$\Gamma=\frac{\sqrt{2}}{2}\sigma_{c0}(\varepsilon_1-\varepsilon_0)L. \tag{5.3}$$

In Eq. (5.3), σ_{c0} and σ_1 are both in the elastic state, thus $\varepsilon_0=\sigma_{c0}/E$ and $\varepsilon_1=\sigma_1/E$, E the Young's modulus. Therefore, we can obtain

$$\sigma_1=\frac{\sqrt{2}E\Gamma}{\sigma_{c0}L}+\sigma_{c0}. \tag{5.4}$$

If the initial shear band is controlled by the shear stress, the propagation of shear band is governed by the release of the stored shear band energy of a nearly 45° angle unique sliding [2]. For the high temperature case and nano-scaled case, the homogeneous deformation is derived by the multiple small cross shear bands with different angles or no release of stored elastic energy. Averagely, the homogeneous condition (with the multiple small cross shear bands and no shear bands) implements the few release of shear band energy. If we also use Eq. (5.4) to describe this homogeneous condition with few release of shear band energy, Γ is defined as Γ_h for the homogeneous deformation condition. Correspondingly, Γ is defined as Γ_i for the absolutely inhomogeneous condition of large-scaled samples with at least one obvious single shear band generated through the surface. The shear band energy Γ can be redefined in a general form:

$$\Gamma=\alpha_i\Gamma_i+\alpha_h\Gamma_h,\ \alpha_i+\alpha_h=1, \tag{5.5}$$

where α_i, α_h are the percent/probability of the inhomogeneous and homogeneous condition, respectively. As shown in Figure 2-10, the deformations in the samples at

1μm and 2μm are totally in the homogeneous condition α_h=1, and for the samples in the size larger than 10μm and bulk sample, the deformations are totally in the inhomogeneous condition α_i=1. From the 2μm to 10μm scale, it is assumed that the deformed samples are in the transitional condition between the homogeneous and inhomogeneous condition with a linear increase value of α_i= 0~1. Therefore, Eq. (5.4) can be expressed as

$$\sigma = \sigma_{c0} + \frac{\sqrt{2}E}{\sigma_{c0}L}[\alpha_i \Gamma_i + (1-\alpha_i)\Gamma_h]. \tag{5.6}$$

According to the definition of shear band energy Γ, Γ_h is much smaller than Γ_i, with the value nearly 0. The theoretical predicting of the transitional state (2μm~10μm) is shown in Figure 5-3. Here, σ_{C0} =1.2 GPa, Young's modulus E is taken as 78GPa and the aspect ratio β as 2.5 from our simulations, while Γ_i =80J/m^2. Compared with the experimental data, the theory provided here can effectively describe the tendency of the size dependent elastic limit.

For micro scaled MG pillars, the volume is large enough (compared with sub-micron MG pillars) and the shear band generation energy can be absorbed by the adjacent parts. As shear band formation is attributed to a required critical strained volume [2]. Thus, for the small MG micropillar, the strain volume is inefficient for propagation of single shear band. The more strain energy in large samples can be provided as the propagation energy of shear band. That means the propagation energy shear band is related to strain volume corresponding to size of micropillars, thus shear band in large scaled micropillar with efficient strain volume needs more stress to activate as shown in Eqs. (5.4) and (5.6). The change from shear band to

homogeneous deformation with decreasing pillar size results from the size (strain volume) dependent propagation of shear band.

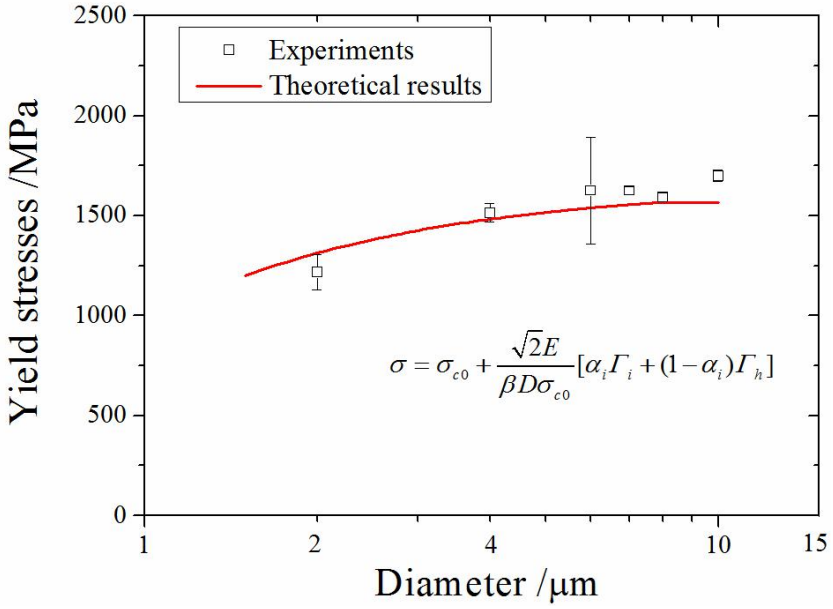

Figure 5-2. The comparison of the experimental data and theoretical predicted results.

5.1.3 Further discussion on size dependent strength

The present reported investigations of size dependent strength in fcc crystalline micro- and nano- pillars have resulted in the general agreement: the increase of strength accompanies with the decrease of the specimen size so called ”smaller is stronger ” tendency. Several theories have been provided to explain this size dependent phenomenon, but no agreement to establish a unified plastic model to state the physics inside the pillars. Two prominent deformation mechanisms have been proposed at present: one is the single arm source model, the other is the dislocation starvation with the surface dislocations nucleation. In the SAS model, the double pinned Frank-read dislocation sources are truncated into single arm sources, the truncated sources interplay the dislocations motion and source activation. For the

dislocation starvation theory, the surface nucleation of dislocations appear to be taken place in the small scaled pillars, and the dislocations annihilate at the free pillar surface. However, these mechanisms seem to be competing, both of them take place at different micron sizes from the inner defects view and surface influence view. This is also our origin to think about this problem, thus we consider the pile-up mechanism (defect distribution affects stress concentration) and surface energy effect (physics of surface) to further explain the size dependent strength.

However, there are no agreement of the size dependent strength of MG pillars, even for the tendency whether the strength with decreasing size is slight increase or decrease showing in Table 5-1. Then of course, there are no sufficient discussions on the plasticity to explain this uncertain phenomenon. Figure 5-3 shows the selected tendency of size dependent strength of MG pillars. It is shown that it is much more complicated than that of fcc crystalline materials. For the metallic glasses, the yield strength is determined by the cooperative shear motion of atomic clusters (also related to the shear transformation zones (STZs)) [14] and defect flows [15, 16]. But this local deformation doesn't build the direct correlation with the onset of the plastic deformation. A defect flow is a cluster of STZ and its propagation strength is controlled by the STZ nucleation stress (yield stress) but not directly related to size. And this local defect motion is relevant to the temperature, strain rate and even the alloying constituent [17]. The present reported studies have shown that the shear band energy, potential energy and surface energy may be effective on the strength of MG pillars. All these increase the complexity of understanding the size effect of MG materials. Our study focuses on exploring the size effect of MG pillars by experiments and trying to provide our explanation of this problem. Our results agree that the size effect of MG pillars results from the propagation of shear bands.

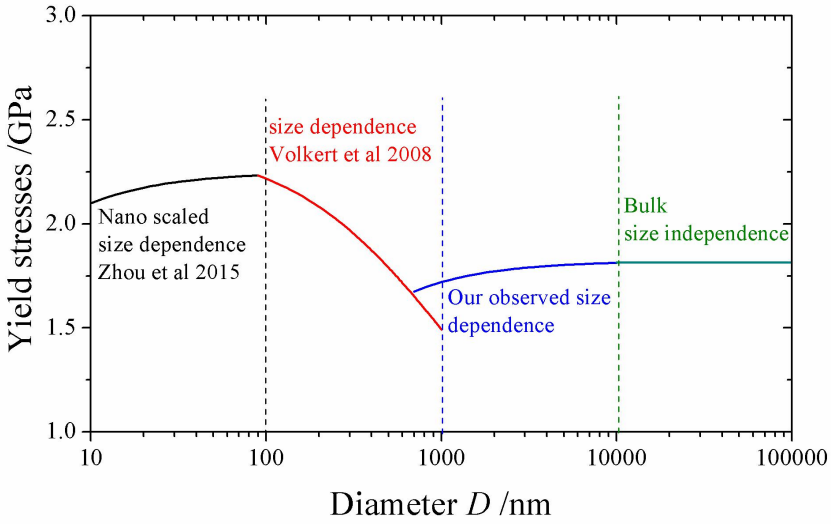

Figure 5-3. Schematic illustrated tendency of the size effect in MGs in three different size regimes, namely the size independence regime in bulk MGs [2, 3].

Besides the intrinsic factors like defect flow, there may be some extrinsic factors effective on the size dependent strength. One generous factor is the FIB damage. In the section 3.2, the surface energy effect is introduced by defining the initial surface strain. The FIB milling damage can affect the initial surface strain, and then change the surface energy. In this case, the FIB damage can be considered for the description of size effect of fcc crystalline materials. For the amorphous materials, the 3-4 nm FIB disordered thickness can generate a constrained shear bands [5]. But this unconstrained shear band cannot run away largely, or even cannot be observed as the limited energy damage. For the small volume pillars such as nano-pillars, the FIB damage should be discreetly considered. Another generous factor is the strain rate. For the crystalline materials, the effect from strain rate on the size effect has few reported. But for the amorphous material, the strain rate vastly affects the strength and deformation mechanism. Based on the free volume theory [18], the high strain rate would make the material tend to form the propagation of shear band, and extend the

elastic deformation. Generously, the strain rate should be controlled under 10^{-2}/s in order to avoid the influence from strain rate.

Table 5-1. Literature overview size effects in metallic glasses

References	Mode transition inhomogeneous	Strength size dependence with increasing size
Lee et al. [4]	No	Dramatic increase
Lai et al. [5]	No	Dramatic increase
Volkert et al. [2]	Yes	Slight decrease
Zhou et al. [3]	No	Slight increase
Schuster et al. [6, 7]	No	Slight increase
Dubach et al. [8]	No	No change
Jang and Greer [9, 10]	Yes	Slight increase
Bharathula et al. [11]	Yes	Slight increase/slight decrease
Chen et al. [12, 13]	Yes	No change

5.2 Elastoplastic constitutive models for plastic deformation of metallic glasses

In this section, we will try to quantificationally describe the plastic deformation of MG pillars shown in section 2.3.3, The free volume model and the Drucker-Prager (DP) model will be linked to the the constitutive formulations for the room temperature and high temperature (>0.7T_g, T_g is the glass transition temperature) conditions. Even though the size dependence of the plastic deformation in MG pillars is still an open issue, the theoretical description combining factors of the temperature dependence and size dependence is necessary to have an insight into the deformation mechanism. In this section, we implement the constitutive models into the finite element method (FEM) to simulate the deformation process under the uniaxial compressive test condition. The propagation of shear bands and the evolution details of the mechanical properties and free volume behaviors will be examined. We hope these trials can provide some help to understand the plastic deformation phenomenon of MG pillars.

5.2.1 Constitutive Theories

5.2.1.1 Yield criterion [19]

An alternative way to consider the hydrostatic stress $p = \frac{1}{3} tr(\boldsymbol{\sigma})$ or the volume dilatation effects through the Drucker-Prager (DP) model has been proved to be effective to describe the plastic deformation of MG pillars [20, 21]. The yield function can be expresses by the term of hydrostatic component of the stress,

$$f = \sqrt{J_2} + \frac{\kappa}{\sqrt{6}} I_1 - k, \tag{5.7}$$

where $J_2 = \boldsymbol{s} \cdot \boldsymbol{s} / 2$ with $\boldsymbol{s} = \boldsymbol{\sigma} - p\boldsymbol{I}$ is the deviatoric stress tensor, $\boldsymbol{I}$ is the identity tensor, $\boldsymbol{I}_1 = tr(\boldsymbol{\sigma})$ is the first invariant of the stress tensor, and κ represents the stress dependence. The relationship between the yield stress σ_0 (described in Eq. (5.6) theoretically) and *k* is shown as

$$\sigma_0 = k, \text{ (shear)} \tag{5.8}$$

$$\sigma_0 = \frac{\sqrt{3}k}{1 + \mu / \sqrt{2}}, \text{ (tensile)} \tag{5.9}$$

$$\sigma_0 = -\frac{\sqrt{3}k}{1 - \mu / \sqrt{2}}, \text{ (compressive)} \tag{5.10}$$

From the yield function (Eq. (5.7)), we can similarly define an equivalent stress, or DP stress $\bar{\sigma}$ as

$$\bar{\sigma} = \frac{\sqrt{J_2} + \frac{\kappa}{\sqrt{6}} I_1}{\frac{1}{\sqrt{3}} + \frac{\kappa}{\sqrt{6}}} = \sqrt{3J_2} + \frac{\kappa}{\sqrt{6}} I_1 = \bar{\sigma}_1 + \bar{\sigma}_2. \tag{5.11}$$

5.2.1.2 Associated flow rule

The flow rule is obtained by directly taking the stress derivative of the yield

function, namely associated flow.The plastic strain rate $\dot{\varepsilon}_{ij}^{p}$ is then defined by the associated function φ

$$\dot{\varepsilon}_{ij}^{p} = \frac{\partial \varphi}{\partial \sigma_{ij}} \dot{\lambda}, \tag{5.12}$$

where $\dot{\lambda}$ is the proportional coefficient providing the magnitude for the flow and σ_{ij} is the stress tensor.

According to the yield criterion shown in Eq. (5.7), the plastic strain rate $\dot{\varepsilon}_{ij}^{p}$ can be shown in the following:

$$\dot{\varepsilon}_{ij}^{p} = \dot{\lambda} \frac{\partial f}{\partial \sigma_{ij}} = \dot{\lambda} \left(\frac{1}{2\sqrt{J_2}} s_{ij} + \frac{\kappa}{\sqrt{6}} \delta_{ij} \right). \tag{5.13}$$

Thus, the proportional coefficient $\dot{\lambda}$ can be expressed as

$$\dot{\lambda} = \frac{\bar{\sigma}}{\sqrt{J_2} + \frac{\kappa}{\sqrt{6}} I_1} \dot{\bar{\varepsilon}}^{p} = \frac{\sqrt{3J_2} + \frac{\kappa}{\sqrt{6}} I_1}{\sqrt{J_2} + \frac{\kappa}{\sqrt{6}} I_1} \dot{\bar{\varepsilon}}^{p}. \tag{5.14a}$$

$$\dot{\bar{\varepsilon}}^{p} = \left(\frac{\sqrt{J_2} + \frac{\kappa}{\sqrt{6}} I_1}{\sqrt{3J_2} + \frac{\kappa}{\sqrt{6}} I_1} \right) \sqrt{\frac{2}{1+\kappa^2} \dot{\varepsilon}_{ij}^{p} \dot{\varepsilon}_{ij}^{p}}\, \bar{\sigma}. \tag{5.14b}$$

Above all, the strain rate $\dot{\varepsilon}_{ij}$ can be written as

$$\dot{\varepsilon}_{ij} = \dot{\varepsilon}_{ij}^{e} + \dot{\varepsilon}_{ij}^{p} = \{ \frac{1}{2\mu} \dot{\sigma}_{ij} - \frac{\lambda}{2\mu(3\lambda + 2\mu)} \delta_{ij} \dot{\sigma}_{kk} \} + \dot{\lambda} \left(\frac{1}{2\sqrt{J_2}} s_{ij} + \frac{\kappa}{\sqrt{6}} \delta_{ij} \right). \tag{5.15}$$

where λ and μ are Lamé constants.

5.2.1.3 Free volume theory

The defects in amorphous are often described by the free volume model [20]. Based

on the free volume model, the plastic deformation of amorphous metal occurs by the superposition of the shear localized groups of atoms, often referred as flow defects on STZ [22]. During the process of the superposition, an additional volume dilatation is formed and the moving atoms is accommodated accompanying with the increase of volume. This mechanism expresses the plastic strain

$$\dot{\gamma}^p = 2c_f k_f \left(\frac{\varepsilon_0 \omega_0}{\Omega}\right) \sinh\left(\frac{\varepsilon_0 \omega_0 \tau}{2k_B T}\right), \tag{5.16}$$

where $\dot{\gamma}^p$ is the plastic strain rate on STZ, τ the stress on the shear band, Ω the atomic volume, k_B the Boltzmann's constant, T the absolute temperature which is used to describe the condition temperature, the product $\varepsilon_0 \omega_0$ is the activation volume of the process, k_f the temperature-dependent rate parameter and c_f defect density. If the multiaxial stress condition is considered, τ and γ can be replaced by the equivalent stress $\bar{\sigma}$ and the corresponding plastic strain $\bar{\varepsilon}^p$ [18]:

$$\dot{\bar{\varepsilon}}^p = 2c_f k_f \left(\frac{\varepsilon_0 \omega_0}{\Omega}\right) \sinh\left(\frac{\varepsilon_0 \omega_0 \bar{\sigma}}{2k_B T}\right). \tag{5.17}$$

k_f and c_f can be expressed as

$$k_f = J \exp\left(-\frac{\Delta G^m}{k_B T}\right), \tag{5.18}$$

$$c_f = \exp\left(-\frac{\beta v^*}{v_f}\right), \tag{5.19}$$

where J is the vibrating number of atoms, ΔG^m the Gibbs energy of activation, β a geometrical overlap factor between 0.5~1, v_f the average free volume per atom and the density fluctuations with volume being greater than a critical value v^*. The relationship between the free volume v_f and defect density c_f is shown in the

Figure 5-4, where the increase value of v_f makes c_f close to 1.

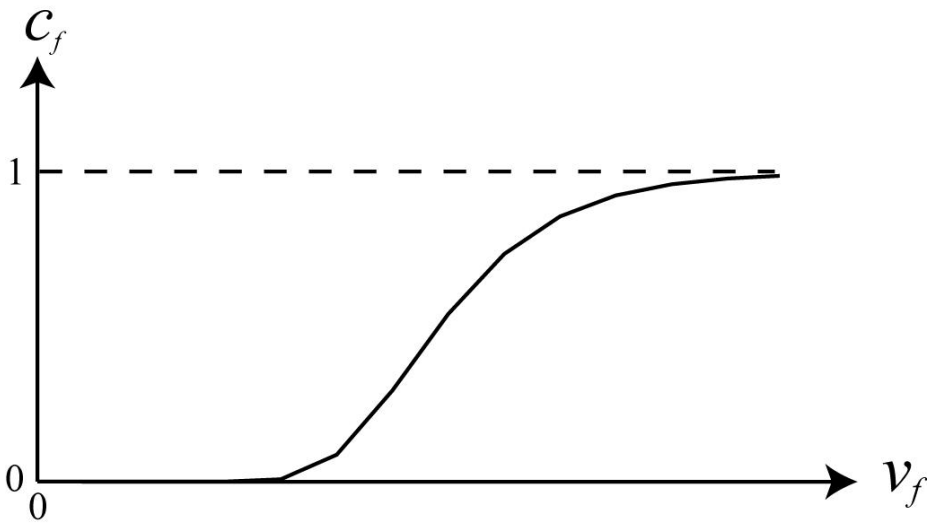

Figure 5-4. Relationship of defect density and free volume

The process of density evolution includes the generation and annihilation of the defects, the rate of which can be described as

$$\dot{c}_f = \dot{c}_f^+ - \dot{c}_f^- . \tag{5.20}$$

According to Eq. (5.19), the free volume v_f can be expressed as

$$v_f = -\frac{\beta v^*}{\ln c_f}, \tag{5.21}$$

and

$$\dot{v}_f = \frac{\beta v^*}{c_f \left(\ln c_f\right)^2} \dot{c}_f . \tag{5.22}$$

The deformation-driven creation of defects can be modeled through the free volume theory by considering the density fluctuations with volumes just smaller than the critical size v^*. The resulting expression for the creation of free volume is

$$\dot{v}_f = 2c_f k_f \frac{k_B T}{S} \frac{\beta \nu^*}{v_f} \left(\frac{\varepsilon_0 \omega_0}{\Omega} \right) \left\{ \cosh\left(\frac{\varepsilon_0 \omega_0 \sigma}{2k_B T} \right) - 1 \right\}, \tag{5.23}$$

in which

$$S = \frac{E}{3(1-\nu)}. \tag{5.24}$$

Linking Eq. (5.24) to Eq. (5.22),

$$\dot{v}_f = 2c_f k_f \frac{k_B T}{S} \frac{\beta \nu^*}{v_f} \left(\frac{\varepsilon_0 \omega_0}{\Omega} \right) \left[\cosh\left(\frac{\varepsilon_0 \omega_0 \bar{\sigma}}{2k_B T} \right) - 1 \right] = \frac{\beta \nu^*}{c_f \left(\ln c_f \right)^2} \dot{c}_f, \tag{5.25}$$

and generation rate of defects density can be obtained by considering the main process of the increase evolution

$$\dot{c}_f^+ = -6 \frac{k_f k_B T (1-\nu)}{E \beta \nu^*} c_f^{\,2} \left(\ln c_f \right)^3 \left[\cosh\left(\frac{\varepsilon_0 \omega_0 \bar{\sigma}}{2k_B T} \right) - 1 \right]. \tag{5.26}$$

The annihilation of the defects during structural relaxation takes place by a bimolecular process. The bimolecular nature is the annihilation occurs by the joining of two dangling bonds. The researchers have shown that during isothermal annealing at temperatures close to the glass transition temperature T_g, the viscosity of the amorphous metals reaches a saturation value. Since the viscosity is inversely proportional to the defect concentration c_f , the defect concentration then reaches a metastable equilibrium concentration $c_{f,\,eg}$ [18]. The annihilation rate of the defect density $\dot{c}_f^-$ can be described as

$$\dot{c}_f^- = k_r c_f^{\,2}, \tag{5.27}$$

where is the parameter of structural relaxation rate. The above equation cannot describe the equilibrium point with the value $c_{f,\,eg} \neq 0$. Therefore, Eq. (5.27) can be rewritten as

$$\dot{c}_f^- = k_r c_f \left(c_f - c_{f,eq} \right). \tag{5.28}$$

The relationship between $\dot{c}_f^-$ and c_f is shown in Figure 5-5.Thereby, the rate of density evolution can be written as

$$\dot{c}_f = -6\frac{k_f k_B T(1-\nu)}{E\beta v^*} c_f{}^2 \left(\ln c_f \right)^3 \left[\cosh\left(\frac{\varepsilon_0 \omega_0 \bar{\sigma}}{2k_B T} \right) - 1 \right] - k_r c_f \left(c_f - c_{f,eq} \right). \tag{5.29}$$

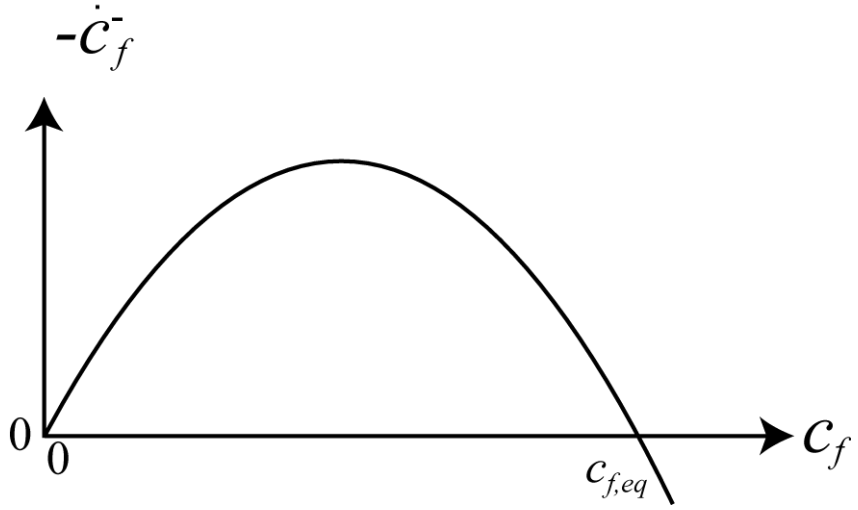

Figure 5-5. Relationship between structural relaxation rate and defect concentration.

5.2.2 Model and parameters

We performed finite element (FE) analyses using a user material subroutine (UMAT) in the commercial code ABAQUS/Standard (2012). In UMAT, yield stresses or yield strengths, which are shown in Eq. (5.6) introduced in Section 5.1, and the yield strengths are shown in Eqs. (5.8~5.10), are implemented in the CPFE framework introduced in Section 5.2.1. The room temperature (300K) and high temperature (around 655K) conditions of MG bulk specimens and MG micro pillars are simulated by FEM. In the calculations, we performed the compression tests with a flat punch, which is treated as the rigid body shown as Figure 5-6. In addition,

isothermal conditions were assumed and the specimens were kept for each temperature. Pillars with diameters of 8 and 10 μm were simulated, and the height-to-diameter aspect ratio was fixed at 2.5 in all of the simulations. For simplicity, the FE model consisted of a single 8-node brick-type element (C3D8). The displacements were applied along the *y* direction associated with a constant strain rate of 1.0×10^{-4} s^{-1}. A base material at the bottom of the pillar was included to simulate to the real boundary condition of the samples.

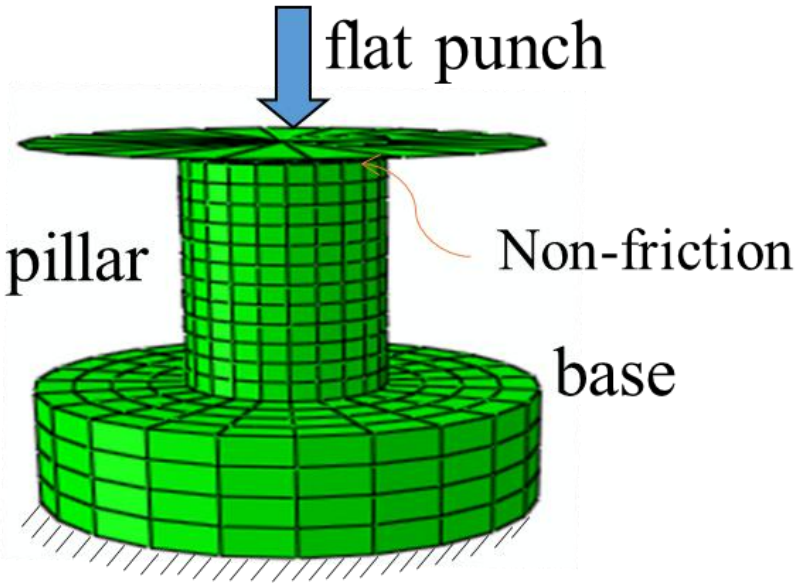

Figure 5-6. Finite element model of micro pillar and the boundary conditions.

As the experimental facilities cannot provide efficient high temperature conditions for micro uniaxial compressive test on the MG pillars, the bulk experiments conducted by Yoshikawa [23] are used to determine the simulation parameters which can be obtained by the method introduced by Mima [24]. The parameters for high temperature conditions obtained from bulk specimens is used to describe the deformation of MG pillars at high temperature. The parameter for room temperature condition obtained from bulk specimens can provide some reference for the similar

temperature case of MG pillars. The loading form and bulk specimen fracture shape is shown in Figure 5-7. The parameters of constitutive law fitted to experimental data of bulk specimens using DP yield criterion are shown in Table 5-2. And the results of the comparison between the experimental data and simulation curves are shown in Figure 5-8. It is shown that the selected parameters in Table 5-2 can make the simulation compare well with the experimental data. That means that the constitutive framework with these parameters can provide effective physics to describe the deformation of the bulk MG specimens. For the room temperature, the specimen shows no plastic deformation from experiments and extremely high elastic limit. But the specimen can also provide good plastic flow when the temperature is close to T_g. That is the reason for the name origin of metallic glass. The simulations holds that the constitutive framework in this thesis can not only provides room temperature simulations but also high temperature simulations. And the simulations can well fit the real conditions of the experiments. In this thesis, we focus on the study of the deformation behavior of MG pillars. Thereby, the further discussions on bulk specimens will not be shown here.

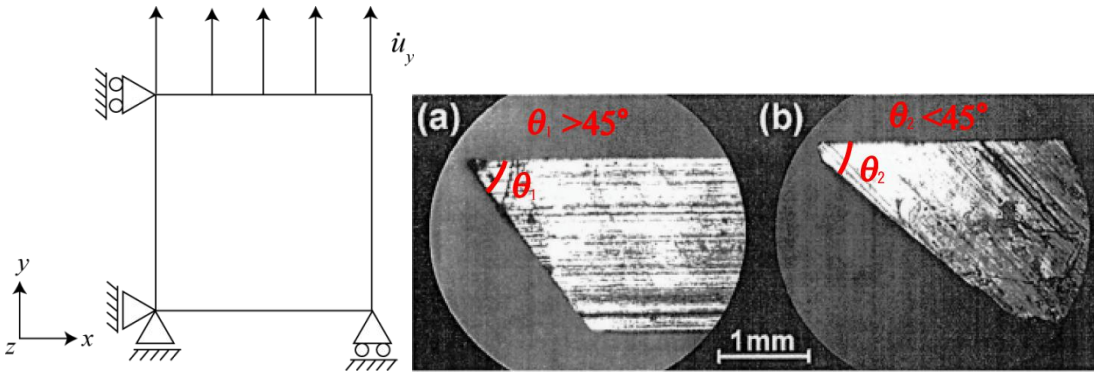

Figure 5-7. Fracture shape of $Zr_{55}Al_{10}Cu_{30}Ni_5$ BMG by (a) tensile test and (b) compressive test [23].

Table 5-2. Parameters of constitutive law fitted to experimental data of bulk specimens using DP yield criterion [24].

Parameters	Units	300K	645K	655K	667K
Ω	[m^3]	13.2×10^{-30}	13.2×10^{-30}	13.2×10^{-30}	13.2×10^{-30}
T	[K]	300	645	655	667
k_f	[s^{-1}]	2.10×10^{-1}	5.10×10^{6}	1.39×10^{7}	9.94×10^{7}
$\varepsilon_0\omega_0$	[m^3]	106×10^{-30}	106×10^{-30}	106×10^{-30}	106×10^{-30}
E	[GPa]	80.9	7.1	5.1	6.5
v		0.3	0.3	0.3	0.3
γv^*	[m^3]	9.00×10^{-30}	5.10×10^{-28}	7.10×10^{-27}	1.04×10^{-26}
k_r	[s^{-1}]	5.15×10^{5}	1.00×10^{10}	1.10×10^{10}	1.70×10^{9}
$c_{f,eq}$		2.00×10^{-15}	2.00×10^{-15}	2.00×10^{-15}	2.00×10^{-15}

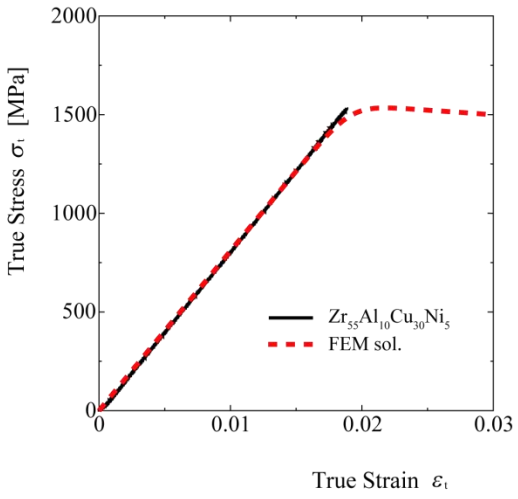

(a) T=300K

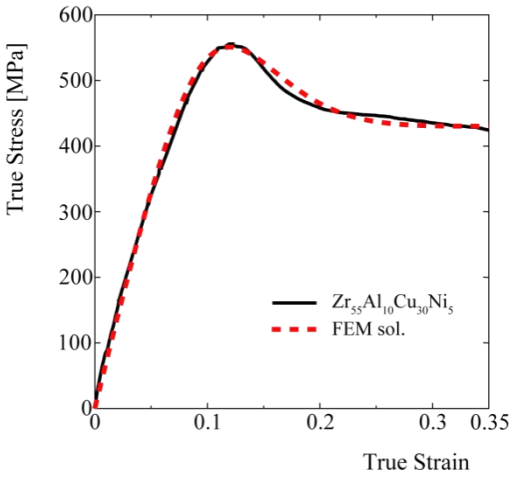

(b) T=645K

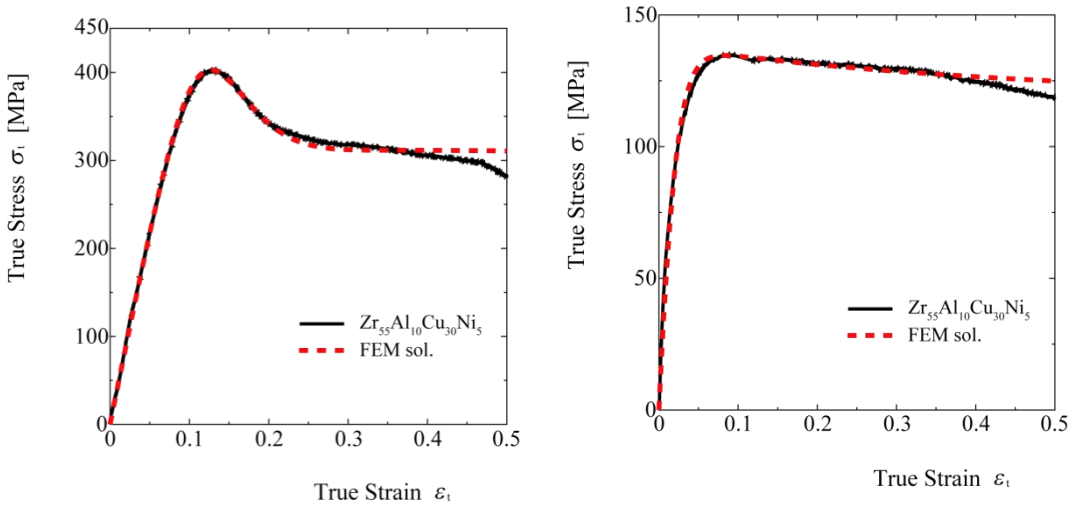

(c) T=655K (d) T=667K

Figure 5-8. True stress-true strain curve fitted to $Zr_{55}Al_{10}Cu_{30}Ni_5$ BMG for tensile test using DP yield criterion [24].

In order to describe the plastic deformation of the MG pillars which has been shown in Chapter 2, the FEM model is established as shown in Figure 5-6. The Table 5-3 shows the selected parameters of the MG pillars, which are referred from the parameters of bulk specimens shown in Table 5-2. Even though the MG pillars fabricated by FIB milling is affected with the surface damage or energy injection, the pillars with large scale make them similar to the bulk specimen. Or the external effect can be ignored by considering the surface/boundary effect averagely. For the micro-pillars with the diameter smaller than 10μm, the plastic flow can be obtained even at room temperature from the experiments. The plastic flow of micro-pillars shows some obvious small bursts, which is similar to the deformation of crystalline micro-pillars. It is different from the plastic behavior of bulk specimens. We redefine some parameters according to the experiments in Chapter 2 and those of bulk specimens in Table 5-2.

Table 5-3. Parameters of constitutive law fitted to experimental data of MG pillars using DP yield criterion

Parameters	Units	300K(bulk pillar)	300K(micro pillar)	655K
Ω	[m^3]	13.2×10^{-30}	13.2×10^{-30}	13.2×10^{-30}
T	[K]	300	300	655
k_f	[s^{-1}]	2.10×10^{-1}	2.00×10^{-1}	1.39×10^{7}
$\varepsilon_0\omega_0$	[m^3]	106×10^{-30}	106×10^{-30}	106×10^{-30}
E	[GPa]	80.9	58.7	5.1
v		0.3	0.3	0.3
γv^*	[m^3]	9.00×10^{-30}	9.00×10^{-30}	7.10×10^{-27}
k_r	[s^{-1}]	5.15×10^{5}	1.00×10^{6}	1.10×10^{10}
$c_{f,eq}$		2.00×10^{-15}	2.00×10^{-15}	2.00×10^{-15}

5.2.3 Results and discussions

Figure 5-10 shows that the simulated results of MG micro-pillars compare well with the experiments at room temperature (300K). That is to say, the selected parameters are reasonable for this simulation case. The simulated result of bulk pillars shows soften flow after the elastic limit, but in the experiments the bulk specimen shows fracture on the shear band. The experimental SEM deformed image in Figure 5-9 also provides shear band propagation with plastic flow except rather than the sudden fracture. The FEM deformed images tell us that the equivalent strain and the equivalent strain rate provide the shear band similar to the experiments. Compared with the FEM results of micro-pillars and bulk specimens, the small size avoids the softening or fracture during the plastic deformation. Linking to the FEM deformed images in Figure 5-9, the equivalent strain rate affects this phenomenon directly. According to Eq. (5.17), the equivalent strain rate is relate to the defect density the

evolution of which may be changed largely.

Figure 5-10 shows the evolution of the defect densities of micro-pillars and bulk pillars. The rapid increase of the defect density accompanying with the plastic deformation results in the softening for the bulk pillars or specimens. The defect density of micro-pillars doesn't represent rapid increase accompanying with the plastic flow. This tendency avoids obvious softening or sudden fracture. We have cut the deformed pillars into pieces, the small scaled pillars shows that the center part of the pillars cannot generate the shear band which is resulting from the free volume (defect flow). The smaller the pillar is, the homogeneous part is larger. That means the slow speed of the defect evolution to propagate the shear band slow down the softening process or even avoid the fracture.

Figure 5-11 shows that large plastic flow of MG pillars at high temperature (655K), and the yield strength is much smaller than that at room temperature. Accompanying with the development of plastic flow, the softening tends to be slowed down. The equivalent strain image doesn't show an obvious shear band as shown at room temperature. According to Eq. (5.17), the defect density image should present the similar tendency. In order to compare with the difference of the deformation at room temperature (300K) and high temperature (655K), the mechanical responses of them are shown in Figure 5-12. In Figure 5-12, it is obvious that the plastic deformation at room temperature shows hardening tendency, but the case at high temperature provides softening process even though the softening rate is slowed down during the development of plastic deformation. The homogeneous deformation at high temperature shows some cross narrow shear bands but not obvious as the single shear bands along nearly 42° direction at room temperature.

In order to study the deformation mechanism, the defect density c_f images of

micro-pillars in 300K and 655K response to the points in Figure 5-12 is shown in Figure 5-13. For the room temperature case, the defect density distributes homogeneously when the strain is elastic as shown in Figure 5-13a. And then defects form and flow along the single shear band along nearly 42° direction during the plastic deformation as shown in Figure 5-13b and c. For the high temperature case, the defect also distributes homogeneously at elastic stage as shown in Figure 5-13d. But when the plastic deformation, defects first concentrate along some shear lines alone the same direction as shown in Figure 5-13e, and then some cross multi narrow shear bands form and evolve as shown in Figure 5-13f. These net shear lines make the deformation homogeneous globally. Moreover, the parts near the base have obvious defects distributions. It means that the base constraints the compressive deformation generate along the pillar, as the FEM images shown in Figure 5-9. This may be one reason for that there is no rapid decrease softening stage in the micro-pillars.

If the strain rate is set as 2.8×10^{-4} s^{-1} and 1.0×10^{2} s^{-1}, the stress-strain responses are varied as shown in Figure 5-14. The stress at high strain rate is much larger than that at low strain rate. According to Eq. (5.17), the increasing strain rate is equal to the decrease of the temperature. The increase of temperature can decrease the stress response, certainly the decrease of temperature can increase the stress response. The defect density evolution is shown in Figure 5-15. The defect of high strain rate case increases faster than that of low strain rate case, and then decease rather than the following increase as that of low strain rate case. Therefore, the stress-strain response of high strain rate case shows more obvious softening than that of low strain rate case at first. The equivalent strain and defect density condition are presented in Figure 5-16. The shear band of high strain rate case is much clearer than that of low strain rate case as the equivalent strain images showing. The reason is that the defects flow along the

shear band much more obviously. That means low temperature/high strain rate promotes the propagation of shear band.

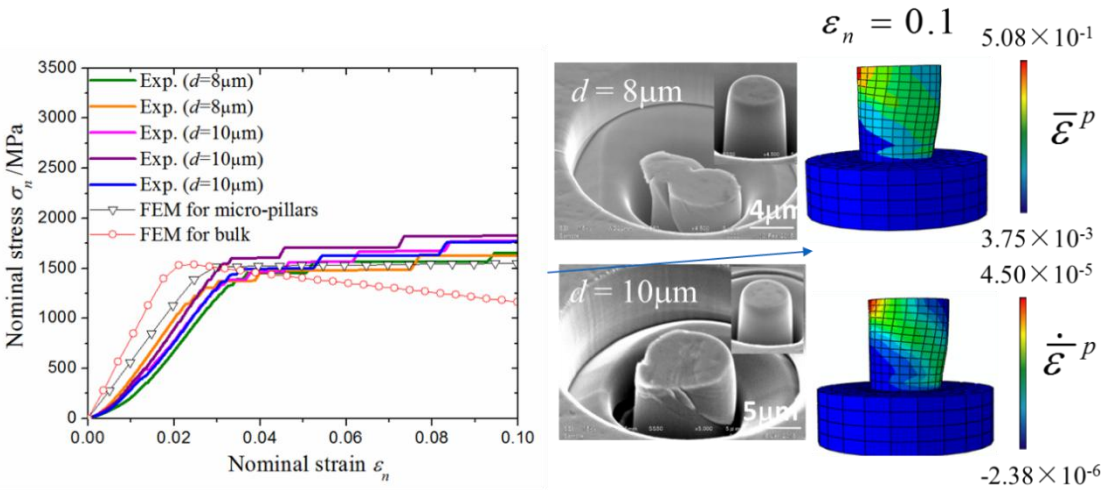

Figure 5-9. FEM and experimental results of micro-pillars of metallic glass

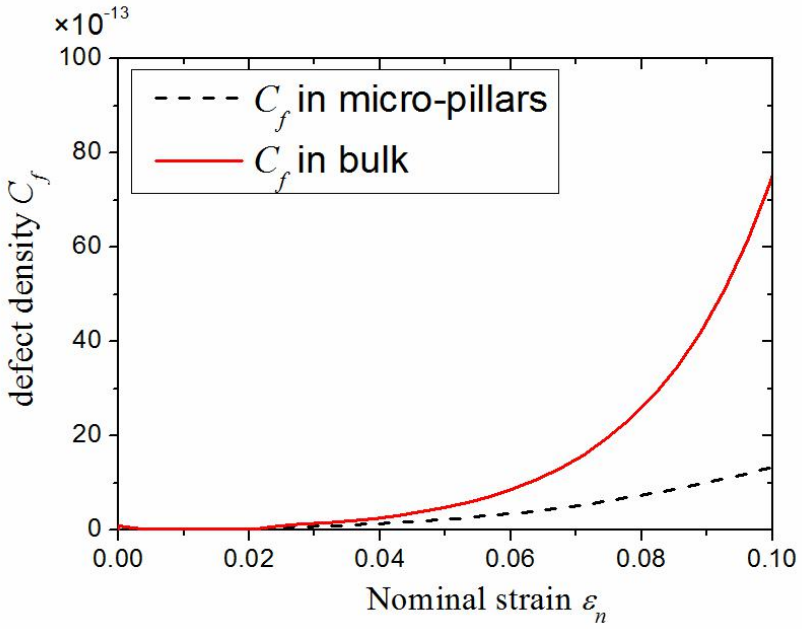

Figure 5-10. Defect density of micro-pillars and bulk-pillars at room temperature

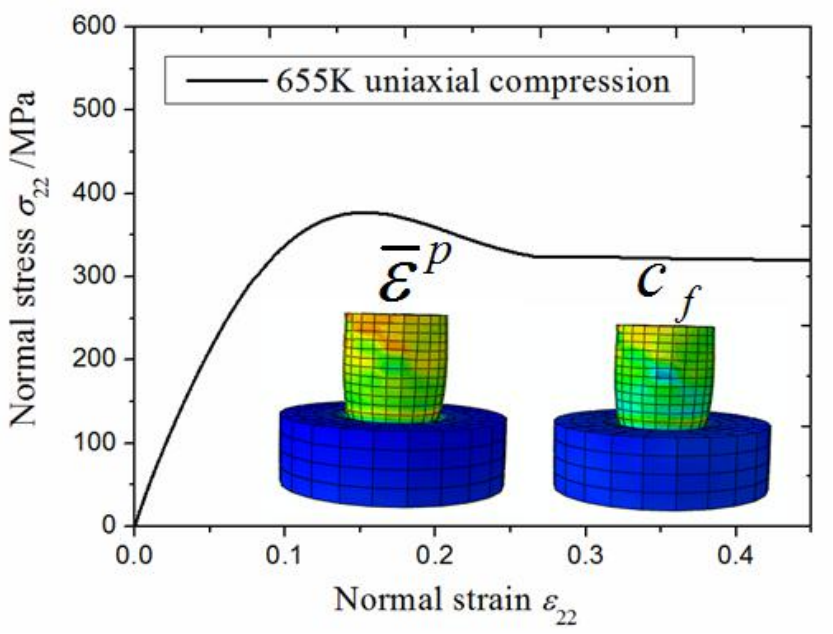

Figure 5-11. The relationship between the normal strain and normal stress at 655K, the equivalent strain image and defect density image of MG pillars.

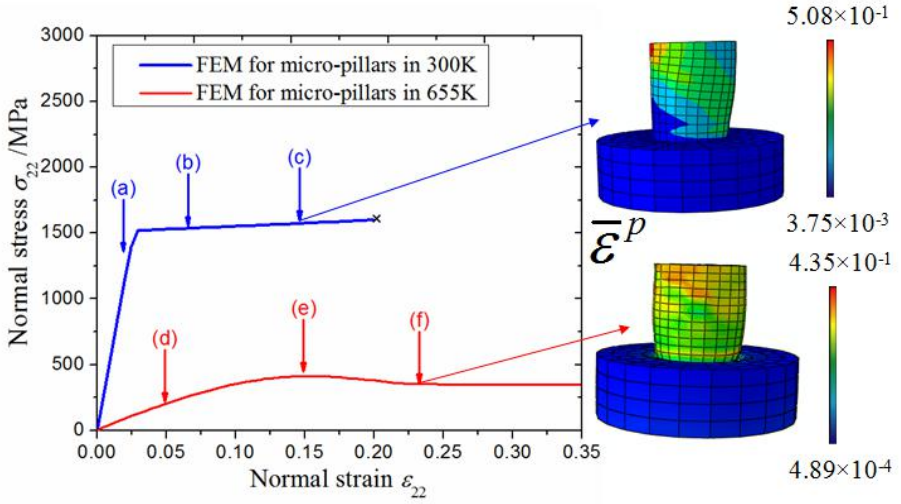

Figure 5-12. Stress-strain responses and FEM images of micro-pillars in 300K and 655K

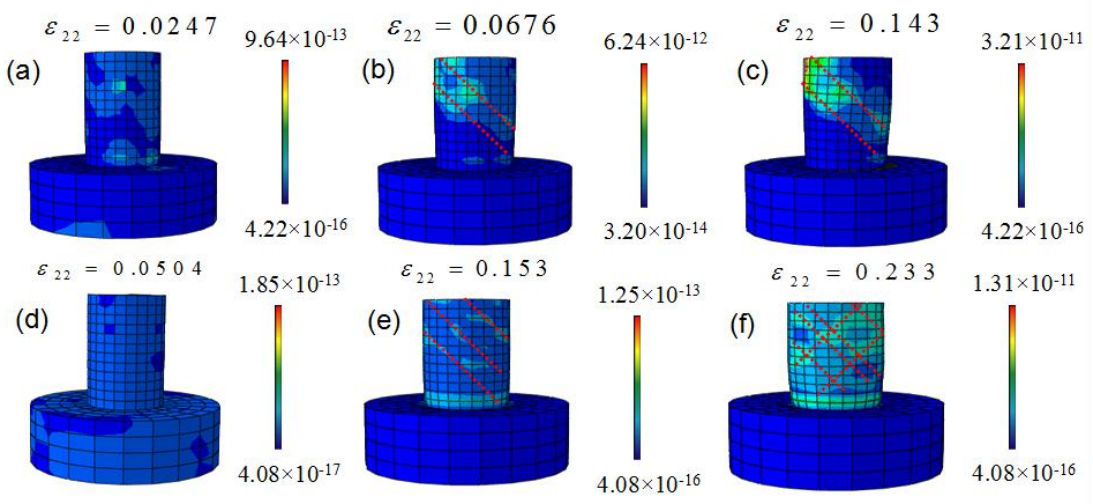

Figure 5-13. Defect density c_f images of micro-pillars in 300K and 655K response to the points in Figure 5-11.

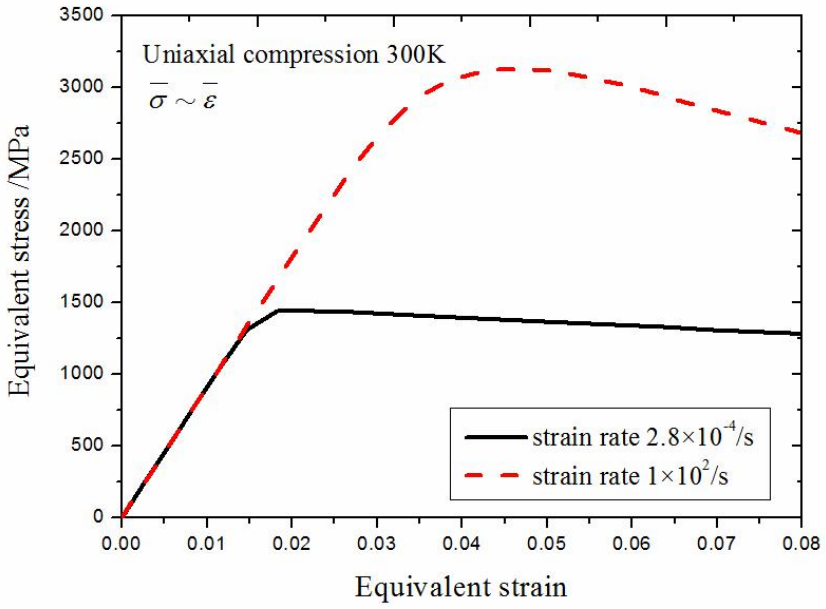

Figure 5-14. The stress-strain response of MG pillar with different strain rate.

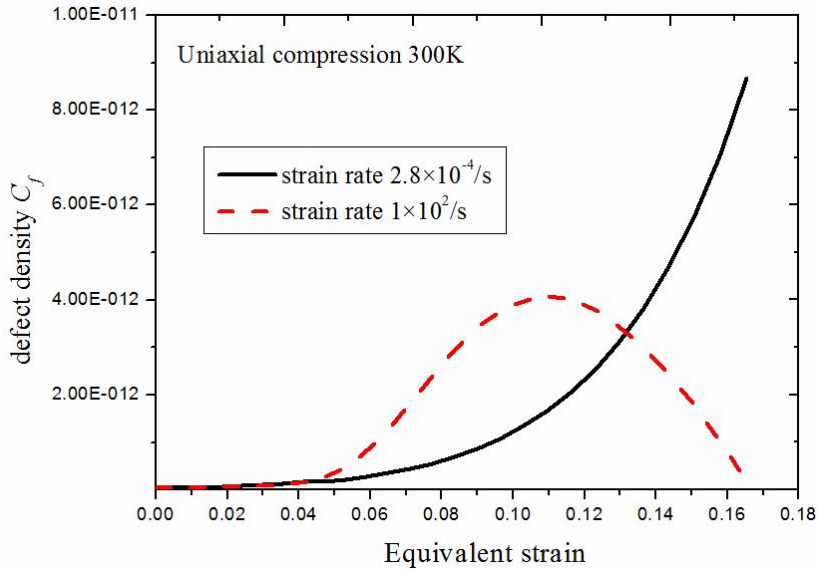

Figure 5-15. The defect density evolution of MG pillar with different strain rate.

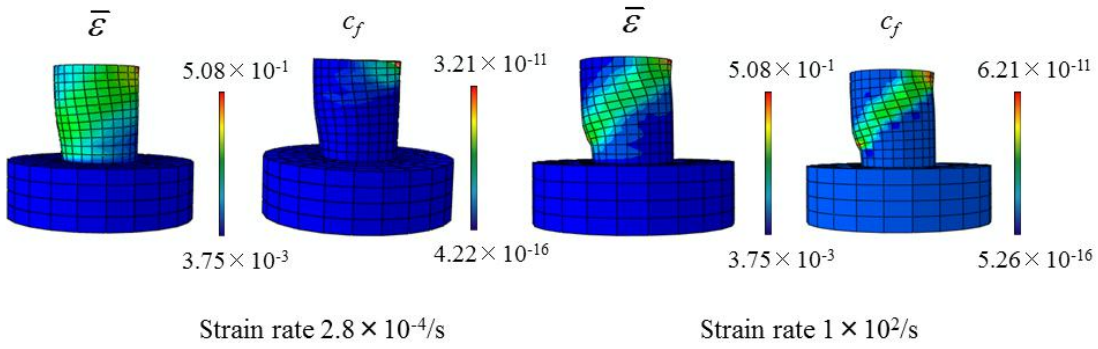

Figure 5-16. Equivalent strain $\bar{\varepsilon}$ and defect density c_f images of micro-pillars at different strain rate at ε_{22}=0.16.

5.2.4 Further discussion on plastic flow

The present reported investigations of plastic in fcc crystalline micro- and nano-pillars have resulted in the general agreement: the dislocation motion results in the plastic deformation; the crystalline orientation determines the propagation of the single or multi shear bands. The dislocation evolution play an important role on the plastic behavior which has been stated in Chapter 4. The interplay among the

dislocations, GB and surface is also significant for the generation of plastic deformation. The GB constraints or stores the defects, and varies the original defect distributions and the stress field. This part has also been studied in Chapter 4. The plastic deformation of micro-pillars represents strong hardening behavior and a series of small displacement bursts, which are size dependent and also different from the case of bulk specimens. These size dependences have been widely discussed and still a questionable topic for the researchers. We have presented our understanding on this topic and provided a trial to describe these size dependence physically. Even though the dislocation physics combined with solid mechanics is one choice for effective description, the inside local evolution of defects is still unknown by this method. The further study on this topic needs more physical considerations and experimental support.

Similar to the study on the size dependent plasticity of crystalline micro- and nano-pillars, the “flow defect” model (free volume theory) is considered. The atomic studies of metallic glasses provide their explanations of shear band propagation and extremely high strength. However, the global mechanical response of them is scarce to provide proof of mechanical design. The plastic behavior of MG is different from the crystalline specimens, holding not only size dependence but also temperature dependence. The flow defects influence the generation of shear bands largely, and dominantly. Even though the amorphous crystalline lattice makes the MG exhibit no crystalline orientations, the shear band without Schmid laws can be formed as necking effect in polycrystals. The classical strength theories are used to explain the shear localization. At present, DP model is much acceptable but still questionable. Some commons can be found by both considering the crystal plasticity and amorphous plasticity: the plastic deformation is based on the defects no matter that they are

dislocations or “flow defects”; size dependence is determined by the inner defect evolution. The further study may focus on the physical origin of “flow defects”, which is the key to understand the physics of the plastic deformation.

5.3 Conclusions

In this chapter, the size dependent strength of MG micro-pillars are summarized by experiments, and explained physically based on shear band energy theory. And then, the plastic deformation of MG bulk/micro-pillars at room temperature (300K) and high temperature near the glass transition temperature (655K) are described based on the FEM framework combined with the free volume model and Drucker-Prager model. Moreover, the homogeneous and inhomogeneous deformation characteristics are simulated by the “flow defects” in the above constitutive framework. The following conclusions can be obtained

(a) The micro scaled Zr-based MG pillars present a slight increase of elastic limit accompanying with the increase of specimen diameters based on the experimental data.

(b) The above phenomenon is not only related to the size variance, but also relevant to the generation energy of shear band.

(c) The different size dependent strength of MG micro-pillars from that of crystalline materials results from different physics: the truncated sources interplay the dislocations motion and source activation, and the small volume forms the starvation of dislocations in the crystalline micro-pillars; but in the MG micro-pillars, the “flow defects” in the globally homogeneous form or inhomogeneous shear localization affects the propagation energy of shear bands, which results in the size dependent strength.

(d) The plastic flow of MG bulk/micro-pillars can be well described in 300K and

655K. And the homogeneous and inhomogeneous deformation can also be presented by the current constitution based on the free volume theory.

(e) The size dependent plastic deformation is related to the defect evolution.

(f) The plastic deformation of MG specimens is related to the size, temperature and strain rate.

Reference

[1] Greer JR, De Hosson JTM. Plasticity in small-sized metallic systems: Intrinsic versus extrinsic size effect. Prog Mater Sci 2011 (56) 654-724.
[2] Volkert CA, Donohue A, Spaepen F. Effect of sample size on deformation in amorphous metals. J Appl Phys 2008 (103) 083539.
[3] Zhou X, Zhou H, Li X, Chen C. Size effects on tensile and compressive strengths in metallic glass nanowires. J Mech Phys Solids 2015 (84) 130-144.
[4] Lee CJ, Huang JC, Nieh TG. Sample size effect and microcompression of $Mg_{65}Cu_{25}Gd_{10}$ metallic glass. Appl Phys Lett 2007 (91) 161913.
[5] Lai YH, Lee CJ, Cheng YT, Chou HS, Chen HM, Du XH, et al. Bulk and microscale compressive behavior of a Zr-based metallic glass. Scr Mater 2008 (58) 890-893.
[6] Schuster BE, Wei Q, Hufnagel TC, Ramesh KT. Size-independent strength and deformation mode in compression of a Pdbased metallic glass. Acta Mater 2008 (56) 5091-5100.
[7] Schuster BE, Wei Q, Ervin MH, Hruszkewycz SO, Miller MK, Hufnagel TC, et al. Bulk and microscale compressive properties of a Pd-based metallic glass. Scr Mater 2007 (57) 517-20.
[8] Dubach A, Raghavan R, Löffler JF, Michler J, Ramamurty U. Micropillar compression studies on a bulk metallic glass in different structural states. Scr Mater 2009 (60) 567-570.
[9] Jang D, Greer JR. Size-induced weakening and grain boundary-assisted deformation in 60nm-grained Ni nano-pillar. Scr Mater 2011 (64) 77-80.
[10] Jang D, Cai C, Greer JR. Influence of homogeneous interfaces on the strength of 500 nm diameter Cu nanopillars. Nano Lett 2011 (11) 1743–1746.
[11] Bharathula A, Lee S-W, Wright WJ, Flores KM. Compression testing of metallic glass at small length scales: effects on deformation mode and stability. Acta Mater 2010 (58) 5789 – 5796.
[12] Chen CQ, Pei YT, De Hosson JTM. Effects of size on the mechanical response of metallic glasses investigated through in situ TEM bending and compression experiments. Acta Mater 2010 (58) 189–200.
[13] Chen CQ, Pei YT, De Hosson JTM. Strength of submicrometer diameter pillars of metallic glasses investigated with in situ transmission electron microscopy. Philos Mag Lett 2009 (89) 633–640.
[14] Falk ML, Langer JS. Dynamics of viscoplastic deformation in amorphous solids. Phys Rev E 1998 (57) 7192.
[15] Lee JY, Han KH, Park JM, Chattopadhyay K, Kim WT, Kim DH. Deformation and evolution of shear bands under compressive loading in bulk metallic glasses. Acta Mater 2006 (54) 5271–5279.
[16] Bengus V, Tabachnikova E, Csach K, Miskuf J, Ocelík V. Possible local

superplasticity of amorphous metallic alloys in the catastrophic shear band under low temperature ductile shear failure. Scr Mater 1996 (35) 781–784.
[17] Trexler MM, Thadhani NN. Mechanical properties of bulk metallic glasses. Prog Mater Sci 2010 (55) 759–839.
[18] Heggen M, Spaemen F, Feuerbacher M. Creation and annihilation of free volume during homogeneous flow of a metallic glass. J Appl Phys 2005 (97) 033506.
[19] Shibutani Y, Wakeda M, Yoshikawa T. Mechanics of Amorphous Metals (Elastic-Plastic Finite Element Analyses Using Inhomogeneous Defects Theory) [in Japanese]. Trans Jpn Soc Mech Eng Ser A 2013 (79) 1807-1817. (渋谷陽二，譯田真人，吉川高正，非晶性金属材料の材料力学 (不均質欠陥理論に基づく弾塑性有限要素解析).日本機械学会論文集（A 編），2013 (79) 1807-1817.)
[20] Zhao M, Li M. Comparative study of elastoplastic constitutive models for deformation of metallic glasses. Metals 2012 (2) 488-507.
[21] Zhao M, Li M. A constitutive theory and modeling on deviation of shear band inclination angles in bulk metallic glass. J Mater Res 2009 (24) 2688-2696.
[22] Spaepen F. Homogeneous flow of metallic glasses: A free volume perspective. Scr Mater 2006 (54) 363-367.
[23] Yoshikawa T. Experimental research on mechanical properties of Zr based bulk metallic glass. 2007. 3 Doctor thesis, Mie University. (吉川高正, Zr 基バルク金属ガラスの強度及び変形特性に関する実験的研究．2007 年 3 月，三重大学博士学位論文.)
[24] 美馬英人，平均応力依存の降伏関数と非連合流れ則の構成式を用いた金属ガラスの局所変形挙動．2013 年 2 月，大阪大学修士論文.

Chapter 6

Summary

In this dissertation, the focus is applied on providing an insight into the size dependent plasticity of the crystalline materials and amorphous materials.

In chapter 1, size dependent plasticity of crystalline materials and amorphous materials is reviewed. At present, there are some challenges to understand size dependent plasticity: (a) For the crystalline materials, even though there are some theories providing some trials to explain the size dependent yield strength, the physical origin of this size dependence is still a questionable topic, and some intrinsic length related to this size dependence is still few studied. (b) Meanwhile, the physics of the size dependent plastic deformation is still unknown for most cases. (c) Whether the yielding of small scaled metallic glasses (amorphous materials) is size dependent or not is still controversy. The experimental verification and theoretical explanation are both scarce. (d) The plastic deformation of metallic glasses is more questionable than that of crystalline materials in the case of size dependence and deformation mechanism. Summarizing these, the intrinsic defect scales, external geometrical scales, interaction of GB and defects and "flow defects" are necessary to be investigated to understand the physics of the deformation mechanism. The results and findings are shown in Chapter 2-5, respectively.

In chapter 2, the research background of the uniaxial compression test on the single crystalline micro-pillars (SCMs), bi-crystalline micro-pillars (BCMs) and metallic glass (MG) micro-pillars, the targets of our conducted experiments and the procedure of the experiments are introduced. The experimental data presents strong size

dependent mechanical response of SCMs and BCMs, interplay of grain boundary effect and strain-stress response of BCMs, and size dependent plastic response of MG micro-pillars. It provides the basis of study on the physics and mechanics of these phenomenon, stated in chapter 3, 4 and 5, respectively.

In chapter 3, we first propose pile-up SAS model in crystals in a physical framework that incorporates dislocation pile-up and size-dependent plasticity effects. And then we establish a mixed model combining the surface energy and inner defects to describe the yield stress of hollow micro- and nanopillars. Our pile-up SAS model and mixed model with surface energy agree better than the original SAS model with the experimental data. That means that the size effect is mainly dominated by the inner defects evolution and surface energy/stress. At least, we provide a size dependent single crystalline yield function to describe the size dependent strength under a multiaxial stress state by considering defect effects, including dislocation pile-up, dislocation starvation and source exhaustion. Our proposed model provides the following results: materials with low stacking-fault energy makes their yield surfaces tend to display rounded vertices, like the Mises yield criterion; those with high stacking-fault energy show typical Tresca criterion-type yield surfaces displaying sharp vertices.

In chapter 4, we propose a physical constitutive model with the framework of the CPFE method that accounts for the dislocation physics to well describe the size-dependent plastic deformation of single crystalline and bi-crystalline micro pillars. And dislocation evolution factors are used to extend the SAS model and revise the hardening model. It is shown that size-dependent dislocation evolution is related to the hardening modulus of the micro pillars, and this makes the stress–strain response vary with the micro pillar size. The GB in BCMs can inhibit the dislocation

transfer across the each grains, and dislocations pile up after the GB and slip along the GB on the maximum Schmid factor slip planes of the each sides of the bi-crystalline micro pillar.

In chapter 5, the size dependent strength of MG micro-pillars is summarized by experiments, and explained physically based on shear band energy theory. It is shown that the micro scaled Zr-based MG pillars present a slight increase of elastic limit accompanying with the increase of specimen diameters based on the experimental data. The above phenomenon is not only related to the size variance, but also relevant to the generation energy of shear band. The size dependent strength of MG micro-pillars different from that of crystalline materials results from different physics: the truncated sources interplay the dislocations motion and source activation, and the small volume forms the starvation of dislocations in the crystalline micro-pillars; but in the MG micro-pillars, the “flow defects” in the globally homogeneous form or inhomogeneous shear localization affects the propagation energy of shear bands, which results in the size dependent strength. And then, the plastic deformation of MG bulk/micro-pillars at room temperature (300K) and high temperature near the glass transition temperature (655K) are described based on the FEM framework combined with the free volume model and Drucker-Prager model. The plastic deformation of MG specimens is related to the size, temperature and strain rate.

All the above experimental and theoretical trials provide our understandings on the size dependent phenomenon of crystalline materials and amorphous materials based on our best knowledge. As this topic is still controversial, further insight needs more studies and discussions.

List of Contributions

A. Journals related to this thesis

1) **Bo Pan**, Yoji Shibutani, Xu Zhang, Fulin Shang, Effect of dislocation pile-up on size-dependent yield strength in finite single-crystal micro-samples. ***Journal of Applied Physics***. 118, 3(2015) 014305.
2) **Bo Pan**, Hiro Tanaka, Yoji Shibutani, Surface energy effect on the size dependent compressive strength of single- crystalline micro- and nano- hollow pillars, ***Material Science & Engineering A***, 659,6 (2016) 22-28.
3) **Bo Pan**, Yoji Shibutani, Hiro Tanaka, Dislocation-based constitutive model of crystal plasticity for the size effect of single crystalline micropillar samples, ***Mechanical Engineering Journal***, 3, 4 (2016) 15pages. DOI:10.1299/mej.15-00602

B. Conferences

1) **Bo Pan**, Yoji Shibutani, Influence of surface energy and dislocation pile-up on the size dependent strength of single-crystalline micro-pillars. 12th International Conference on the Mechanical Behavior of Materials, 2015. 5. 10-14, Germany, Karlsruhe.
2) **潘渤**, 渋谷陽二, 転位論に基づく単結晶構成式モデルによるマイクロピラーのサイズ効果. 2014 日本機械学会・第 27 回計算力学大会, 2014. 12. 25-27, 若手・盛岡.

3) **潘渤**，田中展，渋谷陽二，転位論に基づいて構成式モデルを用いた単結晶マイクロピラーの塑性流動の解析，日本機械学会・材料力学部門若手シンポジウム 2015，2015.8.10-11，三重・伊勢.

4) **Bo Pan**， Yoji Shibutani， Deformation behaviors of Zr-base Metallic Glass Micro- pillars by Elasto- plastic Finite Element Analyses， JSMS Annual Meeting, 2015.10.13-18, Kyoto.

5) 田中祐樹，岡崎貴広，**潘渤**，渋谷陽二，Zr 基金属ガラスマイクロピラーの圧縮塑性変形．2015 日本機械学会・関西学生会平成 26 年度学生員卒業研究発表講演会，2015.3.14，京都大学.

6) 横川龍世，**潘渤**，渋谷陽二，単結晶・双結晶・三重結晶マイクロピラーの圧縮塑性変形挙動. 関西学生会平成 27 年度学生員卒業研究発表講演会，2016.3.10，大阪電気通信大学

Acknowledgments

This dissertation is completed under the guidance of my supervisor, Professor Dr. Yoji Shibutani. He provides constructive advice, valuable instruction and financial support through my whole study from topic selection to experiment design, to theory consideration, to simulation modelling, to article submission, and to dissertation composition. He is my model in the future research as his effort, carved work, profound knowledge and extensive learning. At the time when this thesis is accomplished, I would like to express my deepest gratitude to him. The appreciation is then extended to the dissertation committee, Professor Dr. Katsuyoshi Kondoh, Professor Dr. Akihiro Nakatani and Professor Dr. Hiroyuki Hirakata for their valuable and constructive comments on this dissertation.

I want to transfer my gratefulness to Professor Dr. Ryuichi Tarumi, who provides me much valuable discussion and advice on my study. Also great thanks to Dr. Hiro Tanaka, he teaches me so much about how to write papers and how to deal with the hardest time during the doctoral study. I appreciate Dr. Yang Liu for his evaluable suggestion to my studies and career. I express my great thanks to Professor Dr. Daisuke Matsunaka and Professor Dr. Dai Okumura for their share of treasured research experience with me and valuable comments to my study. Then I would like to express my thankfulness to Professor Dr. Fulin Shang for farsighted comments to my study.

Special thanks are also sent to all staffs and students in Shibutani, Tarumi & Okumura Laboratory for their technical support and valuable suggestion in the research works and kind help to my daily life. Especially, I express my thanks to Mr. Eiji Sakaguchi, Mr. Tofu Nakanishi, Mr. Ryusei Yokokawa, Mr. Kenta Yukihiro and

Mr. Yuki Tanaka for their corporate effort of experiments and also thanks to Mr. Takahiro Okazaki for his help on simulations. Appreciations are given to Dr. Biao Chen and Dr. Lei Jia in the Joining and Welding Institute of Osaka University, for their help on the experiment study. Many thanks to my previous classmates Dr. Jingda Tang in Harvard University, Doctor Candidate Mr. Chao Lin in Mines Paris Tech, Doctor Candidate Mr. Xing Li in École Polytechnique Fédérale de Lausanne, Doctor Candidate Mr. Bo Ni in Brown University, Doctor Candidate Mr. Weixin Li and Xin Qin in Northwestern University for their sharing experiences on daily life of similar doctoral studying experience and study insight.

I acknowledge the Ministry of Education, Culture, Sports, Science and Technology (MEXT), Japan for the financial support to my studies as a Ph. D student. The staff in Shibutani Lab., Prof. Dr Tiejun Wang and Prof. Dr. Fulin Shang in Xi'an Jiaotong University give me great help to apply for it.

I thank my Japanese language teachers Mr. Ken Sugauchi, Mr. Kazuhito Shiomi and Mr. Ikukazu Enomoto, who are the volunteers of Suita International Friendship Association, for their two years' kind teaching.

I would like to express the great gratitude and respect to my family for the perpetual personal support and encouragement through all the years I have been abroad.

June 2016

B. Pan